



**Design, Growth and Characterisation of Resonant
Cavity Light Emitting Diodes (RCLEDs) for Mid-infrared
Applications**

Furat A. Mahdi Al-Saymari

B.Sc., M.Sc.

Supervisor: A. Krier

This thesis is submitted in fulfilment of the requirements for the degree of

Doctor of Philosophy

In physics

Department of Physics

Lancaster University

United Kingdom

September 2020

Declaration

I declare that the contents of this thesis, titled '**Design, Growth and Characterisation of Resonant Cavity Light Emitting Diodes for Mid-infrared Applications**', are the result of my own independent work. I confirm that this work has not been submitted in whole or in any part for any other degree or qualification at this university or at any other academic institution. This thesis documents work carried out between March 2016 and September 2020 at Lancaster University, UK, under supervision of Prof. Anthony Krier and funded by Ministry of Higher Education and Scientific Research (MOHESR) of Iraq in partnership with university of Basrah, Iraq.

Furat A. Al-Saymari

September 2020

Design, Growth and Characterisation of Resonant Cavity Light Emitting Diodes for Mid-infrared Applications

By

Furat A. Al-Saymari

September 2020

Abstract

There is a growing requirement for high brightness light emitting diodes which can operate in the technologically important mid-infrared spectral range (3-5 μm), for applications such as environmental monitoring, industrial process control and spectroscopy. To date, mid-infrared ($\lambda > 4 \mu\text{m}$) LEDs exhibit a poor 300 K external efficiency with broadband emission spectra, resulting in low available output power at the target wavelength. The resonant cavity structure is an attractive solution to improve the performance of these LEDs by locating the active region inside a Fabry-Perot cavity which is formed between two distributed Bragg reflectors (DBRs). In this thesis, we demonstrated four novel mid-infrared resonant cavity LED (RCLED) structures operating near 4.0 μm , 4.2 μm , 4.5 μm , and 4.6 μm at room temperature. Three samples were grown on GaSb substrate and one on InAs substrate using molecular beam epitaxy (MBE). Different III-V semiconductor materials; bulk InAsSb, AlInAs/InAsSb strained multi quantum wells (MQWs), and InAs/GaAsSb superlattices (SLs) were used as active regions, positioned at the antinode of the electric field inside the micro-cavity. The 1λ -thick cavities, containing the active regions, were sandwiched between two high contrast lattice-matched AlAs_{0.08}Sb_{0.92}/GaSb DBR mirrors for GaSb-based RC structures and lattice-matched AlAs_{0.16}Sb_{0.84}/GaAs_{0.08}Sb_{0.92} DBR mirrors for the InAs-based RC structure respectively. The RC

structures were first designed theoretically, where the thickness of the micro-cavity layers and the DBR layers were evaluated corresponding to the target wavelength of RC emission spectra. Then, the reflectivity of the top and bottom mirror were investigated to achieve high emission enhancement as determined by the number of layers in the DBR. The simulated results show that 13.5 pairs in the bottom DBR mirror with reflectivity ($R > 98\%$) and 5 pairs in the top DBR mirror with reflectivity ($R > 83\%$) are sufficient to achieve very high enhancement factors.

The temperature dependence of the transmission spectra of the RC samples was measured over the range from 77 K to 300 K. It was found that the position of the optical cavity mode and the DBR stopband centre shift towards longer wavelength very slowly as the temperature increases at a rate of < 0.4 nm/K and < 0.3 nm/K, respectively. At room temperature the optical modes exhibit a narrow linewidth in the transmission spectrum ($\Delta\lambda < 100$ nm). The room temperature quality factors were found to be in the range from ~ 60 to ~ 100 , predicting that the emission of the RCLEDs should have a strong enhancement. Although all the RC samples exhibit some detuning, between the wavelength of the DBR stopband centre and the position of the optical cavity mode, the simulated results show that the spectral linewidth remains narrow and the emission enhancement factors are still high.

Two entirely new GaSb-based mid-infrared RCLEDs were fabricated, (i) using bulk InAsSb operating at ~ 4.2 μm and (ii) with AlInAs/InAsSb MQWs operating at ~ 4.5 μm . The temperature dependence of the electroluminescence spectra and I-V characterization of both these RCLEDs and their reference LEDs were measured experimentally over the range from 20 K to 300 K. The RCLEDs show significantly better temperature stability, narrower emission linewidth, and high enhancement factors. The bulk InAsSb RCLED exhibits a significantly narrower (10x) spectral linewidth, (6x) superior temperature stability, (70x) higher peak intensity, (33x) higher integrated output power compared to that of the reference without a resonant cavity. For the MQWs RCLED, the peak intensity and the integrated emission were enhanced by a factor of ~ 85 and ~ 13 , respectively. It also shows a superior temperature stability

of ~ 0.35 nm/K and a narrow emission linewidth of ~ 70 nm (which are less than that of the reference LED by 7x and 16x, respectively). The optical and electrical properties of the RCLEDs without top DBR mirror were also investigated. The results show that the intensity and integrated enhancement are still achieved, but somewhat less than that of the full RCLED structures, due to low reflectivity ($\sim 33\%$) of the interface semiconductor/air top mirror.

The high brightness, better spectral purity, narrow linewidth and superior temperature stability, of the RCLEDs developed in this work are rather attractive features, enabling these devices to be readily implemented in the next generation of optical gas sensor instrumentation.

Acknowledgement

First and foremost, I am sincerely grateful to my supervisor Prof Anthony Krier for being a kind, wise and encouraging supervisor during my PhD studies. Giving me the opportunity to be part of his research team and the freedom to choose my research project was one of the most important events in my life.

Special thanks to Dr Andy Marshall for working with me as one of his students and for giving me all the technical and motivational support which I would have never been this far without.

Sincere gratitude to my closest friend and lab partner Dr Adam Craig who was never hesitant to share his experience and provide the technical training that I needed to become independent with executing my projects.

I would like also to thank Drs. Peter Carington, Yasir Noori, Lu Qi, Eva, Veronica Lekta, and Laura Hanks, who share their experience with me for some periods of my research.

I would like to thank the technical staff at Lancaster University who provided the necessary equipment maintenance and services that I needed to continue my research in a smooth manner. These are the cleanroom manager Dr Kunal Lulla, the cryogenics technician Alan Stokes, the safety officer Shona Ions, the IT supporter Rob Lewsy, Dr Sara Baldock for providing technical support in obtaining SEM images, and Steve Holt and his teams at the electronics and mechanical workshops.

I would like to acknowledge the financial support that I received from the University of Basra, and the Iraqi ministry of Higher Education and Scientific Research which gave me a once in a lifetime opportunity to pursue my PhD in the UK.

Lastly, but most importantly, a special thank goes to my family in Iraq for being extremely patient with me and for provided me the emotional support that I needed while being thousands of miles away during my studies.

List of Publications

- [1] [Furat A. Al-Saymari](#), Adam P. Craig, Qi Lu, Andrew R. J. Marshall, Peter J. Carrington and Anthony Krier, “Mid-infrared resonant cavity light emitting diodes operating at 4.5 μm ,” *Optics Express* **28**, 23338 (2020). (paper)
- [2] [F. A. Al-Saymari](#), A. P. Craig, Y. J. Noori, Q. Lu, A. R. J. Marshall, A. Krier, “Electroluminescence enhancement in mid-infrared InAsSb resonant cavity light emitting diodes for CO₂ detection,” *Appl. Phys. Lett.* **114**, 171103 (2019). (paper)
- [3] A. Craig, [F. Al-Saymari](#), M. Jain, A. Bainbridge, G. Savich, T. Golding, A. Krier, G. Wicks, and A. Marshall, “Resonant cavity enhanced photodiodes on GaSb for the mid-wave infrared,” *Appl. Phys. Lett.* **114**, 151107 (2019). (paper)
- [4] V. Letka, A. Bainbridge, A. P. Craig, [F. Al-Saymari](#), A. R. J. Marshall, “Resonant cavity-enhanced photodetector incorporating a type-II superlattice to extend MWIR sensitivity,” *Optics Express* **27**, 23970 (2019). (paper)
- [5] Bainbridge, Andrew; Mamic, Katarina; Hanks, Laura; [Al-Saymari, Furat](#); Craig, Adam; Marshall, Andrew "Resonant Cavity Enhanced Photodiodes in the Short-Wave Infrared for Spectroscopic Detection" submit to ACS Applied Electronic Materials. (paper)
- [6] Abdelazim, Nema; Fong, Matthew; McGrath, Thomas; Woodhead, Christopher; [Al-Saymari, Furat](#); Bagci, Ibrahim; Jones, Alex; Wang, Xintai; Young, Robert "Hotspot Generation for Unique Identification with Nanomaterials" submit to Scientific reports. (paper)
- [7] Krier, A., Repiso, Menendez, E., [Al-Saymari, F.](#), Marshall, A., Lu, Q., Krier, S., Lulla Ramrakhiyani, K., Steer, M., MacGregor, C., Broderick, C., Arkani, R., O'Reilly, E., Sorel, M., Molina, S. & de la Mata, M., 18/10/2019, Mid-infrared Optoelectronics Materials, Devices, and Applications. Tournié, E. & Cerutti, L. (eds.). Elsevier. (Chapter)
- [8] Savich, G. R., Wicks, G. W., Jamison, K., Fredin, L., Golding, T. D., Carmichael, M., Reilly, J., Craig A. P., [Al-Saymari, F.](#) & Marshall A. R., 2019, “Mid-wavelength infrared resonant cavity enhanced photodiodes for infrared spectroscopic sensing of chemicals and other narrow-band optical signals” In : Proceedings of SPIE. 11002, 13 p. (conference paper)

Conferences

- [1] [Furat A. Al-Saymari](#), A. P. Craig, Y. J. Noori, Q. Lu, A. R. J. Marshall, A. Krier, Mid infrared (3-5 μm) InAsSb resonant cavity light emitting diode (RCLED), Semiconductor and Integrated Optoelectronics (SIOE) Conference 2018, Cardiff, UK. Talk.
- [2] [Furat A. Al-Saymari](#), A. P. Craig, Y. J. Noori, Q. Lu, A. R. J. Marshall, A. Krier, Mid infrared InAsSb resonant cavity light emitting diode (RCLED), UK Semiconductors (UKSC) Conference 2018, Sheffield, UK. Talk
- [3] [Furat A. Al-Saymari](#), A. P. Craig, Y. J. Noori, Q. Lu, A. R. J. Marshall, A. Krier, Mid Infrared InAsSb Resonant Cavity Light Emitting Diode (RCLED), PROMIS conference, 2018, Windermere, UK. Talk.

Contents

| | | |
|-----------|---|----|
| 1 | Introduction | 1 |
| 2 | Background theory and fundamental concepts | 5 |
| 2.1 | Fundamental concepts of semiconductor materials | 5 |
| 2.1.1 | Band structure of semiconductor | 5 |
| 2.1.2 | Temperature dependence of band structure | 6 |
| 2.1.3 | III-V band gap alignment | 6 |
| 2.1.3.1 | Type I band alignment | 7 |
| 2.1.3.2 | Type II band alignment | 7 |
| 2.1.4 | Band gap of III-V semiconductor materials | 8 |
| 2.1.5 | Strained layer | 9 |
| 2.1.5.1 | Critical thickness | 10 |
| 2.1.5.2 | Effect strain on the energy levels | 11 |
| 2.1.6 | Radiative and non-radiative recombination | 14 |
| 2.1.6.1 | Radiative electron–hole recombination | 15 |
| 2.1.6.2 | Non-radiative recombination | 16 |
| 2.1.6.2.1 | Shockley-Read-Hall (SRH) recombination | 17 |
| 2.1.6.2.2 | Auger recombination | 18 |
| 2.2 | Light emitting diodes | 19 |
| 2.2.1 | Electrical properties | 19 |
| 2.2.2 | Optical properties | 23 |
| 2.2.2.1 | Efficiency | 23 |
| 2.2.2.2 | Emission spectrum | 24 |
| 2.3 | Resonant cavity light emitting diodes (RCLEDs) | 25 |
| 2.3.1 | Spontaneous emission | 25 |
| 2.3.2 | Fabry-Perot resonator | 26 |

| | |
|---|-----------|
| 2.3.3 Optical mode density in a one-dimensional resonator | 28 |
| 2.3.4 Spectral emission enhancement | 31 |
| 2.3.5 Integrated emission enhancement | 32 |
| 2.3.6 Distributed Bragg Reflector (DBR) | 33 |
| 2.3.7 RCLED design rules | 35 |
| 3 Literature review | 39 |
| 3.1 Introduction | 39 |
| 3.2 Mid infrared light emitting diodes (MIR LEDs) | 39 |
| 3.2.1 Bulk MIR LEDs | 39 |
| 3.2.1 Single quantum well (SQW), multi quantum well (MQWs), and super lattice (SL) MIR LEDs | 42 |
| 3.3 Inter-band cascade mid infrared light emitting diodes (MIR ICLEDs) | 46 |
| 3.4 Infrared-resonant cavity light emitting diode (I-RCLED) | 48 |
| 3.4.1 Near-Infrared 850-980 nm RCLEDs | 48 |
| 3.4.2 Mid-infrared 2.5-4.3 μm RCLEDs | 50 |
| 3.5 Mid-Infrared vertical-cavity surface-emitting lasers (MIR-VCSELs) | 53 |
| 3.5.1 Mid-Infrared VCSELs emitting at 3 μm , 3.4 μm , and 4 μm | 53 |
| 3.6 Summary | 55 |
| 4 Experimental procedures | 59 |
| 4.1 Molecular beam epitaxy (MBE) | 59 |
| 4.2 X-ray diffraction | 61 |
| 4.3 Photoluminescence experimental setup | 62 |
| 4.4 Transmission setup | 63 |
| 4.5 Scanning electron microscopy (SEM) | 64 |
| 4.6 Device Fabrication | 65 |
| 4.7 Electroluminescence setup | 73 |
| 4.8 Photo-response experimental setup | 74 |

| | |
|--|-----------|
| 4.9 Current-voltage (I-V) experimental setup | 74 |
| 5 Resonant cavity structures for mid infrared applications: theoretical and experimental study | 76 |
| 5.1 Introduction | 76 |
| 5.2 Theoretical analysis | 77 |
| 5.2.1 Fabry-Perot transmission | 77 |
| 5.2.2 Optical parameters of the Fabry-Perot cavity | 78 |
| 5.2.3 Temperature-dependent transmission of the DBR mirror | 81 |
| 5.3 Mid-infrared resonant cavity (RC) structures: Design and growth | 83 |
| 5.3.1 Growth of GaSb-based 4.3 μm bulk RC structure with InAsSb cavity | 84 |
| 5.3.2 Growth of GaSb-based 4.5 μm MQW RC structure with InAsSb cavity | 85 |
| 5.3.3 Growth of GaSb-based 4.0 μm MQWs RC structure with GaSb cavity | 87 |
| 5.3.4 Growth of InAs-based 4.6 μm InAs/GaAsSb SLs RC structure | 88 |
| 5.4 Optical characteristics of the resonant cavity (RC) structures | 89 |
| 5.4.1 GaSb-based RC structures with InAsSb active region | 89 |
| 5.4.2 GaSb-based RC structure with GaSb material cavity | 91 |
| 5.4.3 InAs-based RC structure with InAs active region | 92 |
| 5.5 Comparison between the experimental and simulated results | 93 |
| 5.6 Discussion | 95 |
| 6 Bulk InAsSb resonant cavity light emitting diode for mid-infrared applications | 98 |
| 6.1 Introduction | 98 |
| 6.2 Fabrication of the GaSb-based bulk InAsSb RCLED | 99 |
| 6.3 Optical Characterisation | 100 |
| 6.3.1 Electroluminescence emission of the high detuning RCLED device with and without top DBR | 100 |
| 6.3.2 Optical characterization of the low detuning resonance cavity structure | 103 |
| 6.3.2.1 Current injection and duty cycle effects on the electroluminescence spectra of the low detuning RCLED | 105 |
| 6.3.2.2 Temperature dependence of the Electroluminescence Spectra | 108 |
| 6.4 Electrical Characterisation of the low detuning InAsSb RCLED | 111 |

| | | |
|----------|--|------------|
| 6.5 | Photo-response of the low detuning InAsSb RCLED-M1 | 113 |
| 6.6 | Discussion | 115 |
| 7 | AllInAs/InAsSb MQWs resonant cavity light emitting diode for N₂O detection | 118 |
| 7.1 | Introduction | 118 |
| 7.2 | AllInAs/InAsSb MQWs RCLED | 119 |
| 7.2.1 | Fabrication of the MQWs RCLED and the reference LED | 119 |
| 7.2.2 | Optical Characterisation | 120 |
| 7.2.2.1 | Micro-cavity enhancement of mid-infrared electroluminescence ... | 120 |
| 7.2.2.2 | Temperature dependence of the electroluminescence spectra | 123 |
| 7.2.2.3 | Peak emission intensity and integrated emission enhancement | 129 |
| 7.2.2.4 | Duty cycle effect on the electroluminescence emission | 130 |
| 7.2.2.5 | Injection current effect on the electroluminescence emission | 131 |
| 7.2.3 | Temperature dependence of the current-voltage characteristics | 133 |
| 7.2.4 | Mesa area effect | 134 |
| 7.3 | AllInAs/InAsSb MQWs RCLED without top DBR mirror | 136 |
| 7.3.1 | Device fabrication | 136 |
| 7.3.2 | Electroluminescence measurements | 137 |
| 7.3.3 | Current and duty cycle effect on the electroluminescence | 139 |
| 7.3.4 | Area mesa effect on the optical and electrical characteristics | 141 |
| 7.4 | Discussion | 143 |
| 8 | Conclusion and Future Work | 147 |
| 8.1 | Conclusion | 147 |
| 8.2 | Suggested future work | 152 |
| | References | 154 |

Index of Figures and Tables

| | |
|--|----|
| Figure 1.1: Absorption bands (normalized intensity) of relevant gas species in the 2–6 μm range (data from SpectralCalc.com based on HITRAN database). | 1 |
| Figure 2.1: Schematic diagram of the band structure in the conductors, semiconductors, and insulators. | 5 |
| Figure 2.2: Schematic diagram of type I band alignment. | 7 |
| Figure 2.3: (a) and (b) Schematic diagrams illustrate the type II band alignments. | 7 |
| Figure 2.4: Schematic diagrams of broken type II band alignment. | 8 |
| Figure 2.5: Direct Γ -valley energy gap as a function of lattice constant for the zinc blende form of 12 III–V binary compound semiconductors (points), and some of their ternary alloys (curves) at zero temperature. | 8 |
| Figure 2.6: Schematic diagram of tensile strain, lattice matched, and compressive strain heteroepitaxial layers, where a_{\parallel} and a_{\perp} are the lattice constant of the grown material in the direction of growth for the tensile and compressive strain, respectively. | 9 |
| Figure 2.7: Example of the Burgers vector of edge and screw dislocations. | 10 |
| Figure 2.8: The effect of strain on the energy levels of the semiconductor material. (a) unstrained, (b) compressive strain, (c) tensile strain. | 12 |
| Figure 2.9: Schematic of the recombination processes (a) Shockley-Read-Hall (SRH) non-radiative recombination. (b) non-radiative Auger recombination. (c) radiative recombination. | 14 |
| Figure 2.10: Schematic of the radiative recombination processes (a) band-to-band, (b) donor to valence band, (c) conduction band to acceptor, (d) donor to acceptor and (e) excitonic. The solid arrows and dashed lines indicate radiative processes and non-radiative processes, respectively. | 15 |
| Figure 2.11: Schematic diagram of the three common non-radiative Auger recombination processes (a) CHCC, (b) CHLH, (c) CHSH. | 18 |
| Figure 2.12: p-n junction under (a) zero bias and (b) forward bias. Under forward-bias conditions, minority carriers diffuse into the neutral regions where they recombine. | 20 |
| Figure 2.13: Effect of series and parallel resistance (shunt) on I-V characteristic. | 22 |
| Figure 2.14: Parabolic dispersion relations of electrons and holes, showing electron-hole recombination and the resulting photon emission. | 24 |
| Figure 2.15: Theoretical emission spectrum of an LED. | 25 |
| Figure 2.16: Schematic illustration of a spontaneous emission process. | 26 |
| Figure 2.17: Schematic of a Fabry-Perot cavity consisting of two reflectors. Allowed mode and disallowed mode is also illustrated. | 27 |
| Figure 2.18: A one-dimensional optical mode density of a planar microcavity (solid line). | 30 |

| | |
|---|----|
| Figure 2.19 Schematic of a distributed Bragg reflector (DBR) consisting of a periodic multilayer. | 35 |
| Figure 2.20: Schematic illustration of a resonant cavity structure consisting of two DBR mirrors with reflectivity R_1 and R_2 . | 36 |
| Figure 2.21: Density of optical cavity mode for (a) short cavity and (b) long cavity with same cavity finesse (F). (c) Spontaneous emission spectrum (natural emission) of the active region. | 37 |
| Figure 3.1: (a) Demonstration of the application of an InAsSb light emitting diode as a CO ₂ sensor. The emission spectrum of the LED contained a single emission band with a peak at 4.3 μm at room temperature. | 40 |
| Figure 3.2: (a) 300 K electroluminescence spectrum measured from one of the InAsSbP/InAsSb LEDs. (b) Room temperature electroluminescence spectra of the LED measured at different currents. | 41 |
| Figure 3.3: (a) The room temperature electroluminescence emission of the QinetiQ LEDs measured at various Sb composition. (b) Schematic diagram of the InAsSb LED structure grown on Si, and (c) Temperature dependent normalized EL emission spectra obtained using 190 mA, 1 kHz and 50% duty cycle. | 41 |
| Figure 3.4: (a) Temperature-dependent EL spectra at $I = 40$ mA reported in. (b) LED emission at 80K and 300K from a 10 stage -5 period SLS-LED reported in. | 43 |
| Figure 3.5: (a) Schematic diagram of SLS LED, and (b) Room-temperature electroluminescence spectra of samples A (with a barrier) and B (without a barrier) showing atmospheric CO ₂ ~ 4.2 μm and C-H ~ 3.5 μm absorption features caused by a 1.1 m unevacuated beam path. | 44 |
| Figure 3.6: (a) Room temperature emission spectra at various injection currents from the InAsSb/InAs LED. The inset is the schematic diagram of the InAsSb/InAs MQW LED. (b) The temperature-dependent electroluminescence emission spectra measured using 100mA and 1 kHz, 50% duty cycle. | 44 |
| Figure. 3.7: (a) Schematic of the LED structure containing the InAs/InAsSb SLS active region, and (b1) and (b2) normalised (7–300 K) electroluminescence spectra of the InAs/InAsSb SLS LEDs with Sb composition of 4% and 6%, respectively. | 45 |
| Figure 3.8: Stack diagrams of SLED devices developed on (a) an n-doped (100) GaSb substrate, and (b) on a semi-insulating (100) GaAs substrate, (c) Radiance vs. current density for SLED devices grown on GaAs and GaSb substrates collected at 77 K and a 50% duty cycle. The 77 K electroluminescence spectrum of the devices measured at 50 mA is in the inset. | 46 |
| Figure 3.9: (a) Schematic illustration of the ICLED structure, and (b) output power and WPE dependence on current injection at 20–300 K for the 5-stage ICLED with a mesa size of 400 \times 400 μm . | 47 |
| Figure 3.10: (a) Schematic layer sequence of the resonant cavity light-emitting diode (RCLED). (b) Optical output power vs injection current of a resonant cavity light-emitting diode at room temperature. | 48 |
| Figure 3.11: (a) Comparison between the emission spectrum of a 880 nm range RCLED and a commercial LED in the same wavelength range for two bias currents. (b) Schematic illustrations of the fabricated resonant cavity light emitting diodes. | 49 |
| Figure 3.12: Schematic diagram of the Cd _{0.51} Hg _{0.49} Te/HgTe RCLED device. | 51 |

| | |
|---|-------|
| Figure 3.13: (a) Schematic of the InAs/InAs _{0.91} Sb _{0.09} SLS RCLED, and (b) Measured electroluminescence spectra from the device, at various temperatures. | 51 |
| Figure 3.14: Schematic of the AlGaAsSb/GaInAsSb RCLED structure with and without tunnel junction. | 52 |
| Figure 3.15: (a) Sketch of conduction and valence band alignment and the layer structure of the 3.5 μm InP-based RCLED device. The bottom Au contact serves also as heat sink and pseudo substrate. (b) Measured spectral emission from a bulk AlInSb RCLED, showing a 3-fold enhancement compared to a reference non-resonant device. | 53 |
| Figure 3.16: (a) Schematic structure of the GaSb-based VCSEL with undoped bottom DBR and intracavity contact, and (b) Power-current-voltage characteristic of a VCSEL at different temperatures in CW. (c) Schematic of the interband cascade VCSEL structure, and (b) Pulsed output power at various temperature. | 54 |
| Figure 3.17: (a) Power-current-voltage characteristics of a 4 μm VCSEL in (a) CW operation, and (b) pulsed operation. | 55 |
| Table 3.1: Summary of the literature review on LEDs, RCLEDs and VCSEL. | 56-58 |
| Figure 4.1: Simplified schematic diagram of the MBE system used in this work. | 59 |
| Figure 4.2: Schematic diagram showing the representation of Bragg's Law. | 61 |
| Figure 4.3: Schematic diagram of X-ray diffraction system. | 61 |
| Figure 4.4: Schematic diagram of the FTIR photoluminescence system, the red dashed line is the laser beam and grey line is the photoluminescence emission from the sample. | 62 |
| Figure 4.5: Schematic diagram of the FTIR system configured to measure the transmission of the samples. | 64 |
| Figure 4.6: Scanning electron microscope (SEM) tool. | 65 |
| Figure 4.7: Device patterns of varying mesa dimension of (a) mask No.1 and (b) Mask No.2. | 66 |
| Figure 4.8: Schematic illustration of the fabrication steps for the definition of RCLEDs (using mask No.1). | 66-67 |
| Figure 4.9: Schematic illustration of the fabrication steps for the definition of RCLEDs (using mask No.2). | 71-72 |
| Figure 4.10: Schematic diagram of FTIR electroluminescence system. The red dashed arrow represent the electroluminescence emission of the device. | 73 |
| Figure 4.11: Schematic diagram of FTIR photo-response system. | 74 |
| Figure 4.12: Experimental setup of the I-V measurements. | 75 |
| Figure 5.1: Transmission spectrum of Fabry-Perot cavity, (a) at different reflectivities of R_1 and R_2 (for cavity thickness = 1λ), and (b) at different cavity thickness. The cavity refractive index $\bar{n} = 3.8$. | 77 |
| Figure 5.2: Room temperature simulation results of the Fabry-Perot cavity parameters, (a) the distribution of the electric field inside the cavity. (b) Quality factor, Q , (c) the internal angle (on axis lobe), θ_{FWHM} , (d) Linewidth of the optical mode emission, (e) and (d) The resonant emission (G_e) enhancement factor, and the integrated emission (G_{int}) enhancement factor as a function of the top and bottom | 78 |

DBR mirror reflectivity, R_1 and R_2 , respectively. The refractive index of the cavity is $\bar{n} = 3.8$ and the cavity thickness = 1λ .

Figure 5.3: (a) The reflectivity peak of the DBR as a function of the number of layer pairs (N). The inset shows simulations of the DBR reflectivity as a function of the wavelength for 13.5 pairs (bottom DBR) and 5 pairs (top DBR). (b) The resonance condition between the optical mode and the DBR stopband center as a function of the cavity thickness and the DBR period layer thickness, respectively. (c) and (d) Room temperature simulations of the optical mode linewidth ($\Delta\lambda_{\text{cav}}$) and the quality factor (Q) as a function of the DBR stopband center and the peak emission of the cavity mode, respectively. The white dashed-dotted line represents the resonance case between the optical cavity mode and the DBR stopband center.

80

Figure 5.4: (a) Experimental transmission spectra of the 13 pairs DBR mirrors at 77 K and 300 K. (b) Temperature coefficient of the lattice constants for the DBR layers. (c) Temperature dependence of the InAsSb and GaSb DBR layers. (d) Temperature coefficient of the refractive index of the InAsSb and GaSb layers. (e) Simulated transmission spectra of the 13 pairs DBR mirrors at 77 K and 300 K. (f) Our experimental results of the DBR stopband center compared to the fitted results calculated from the values of da/dT and dn/dT].

83

Figure 5.5: (a) A schematic diagram of the GaSb-based 4.3 μm bulk InAsSb RC structure showing the details of the i-InAsSb/p-InAsSb in the active region of the p-i-n diode within the AlAsSb/GaSb DBRs, which form the microcavity, (b) The energy band diagram of the cavity layers calculated using nextnano, showing the electron-blocking barrier.

84

Figure 5.6: (a) A schematic diagram of the GaSb-based 4.5 μm MQWs RC structure showing the details of the AlInAs/InAsSb MQW in the active region of the p-i-n diode within the AlAsSb/GaSb DBRs, which form the microcavity, (b) The energy band diagram of the cavity layers calculated using nextnano, showing the electron-blocking barrier. Details of the type I band alignment in the MQW are highlighted in the inset.

86

Figure 5.7: (a) A schematic diagram of the GaSb-based 4.0 μm MQWs RC structure showing the details of the AlInAs/InAsSb MQW in the active region of the p-i-n diode within the AlAsSb/GaSb DBRs, which form the microcavity, (b) The energy band diagram of the cavity layers calculated using nextnano, showing the electron-blocking barrier. Details of the type I band alignment in the MQW are highlighted in the inset.

87

Figure 5.8: (a) A schematic diagram of the InAs-based 4.6 μm SLs RC structure showing the details of the InAs/GaAsSb SLS in the active region of the p-i-n diode within the AlAsSb/GaAsSb DBRs, which form the microcavity, (b) The energy band diagram of the cavity layers calculated using nextnano, showing the electron-blocking barrier. Details of the broken type II band alignment in the MQW are highlighted in the inset.

88

Figure 5.9: (a) Temperature dependence of the transmission spectra of the GaSb-based 4.3 μm bulk InAsSb RC sample. (b) Temperature dependence of the optical mode transmission. (c) The position of the optical cavity mode and the DBR stopband center of the sample as a function of temperature. (d) Temperature dependence of the transmission spectra of the GaSb-based 4.5 μm MQWs RC sample. (e) Temperature dependence of the optical mode transmission. (f) The position of the optical cavity mode and the DBR stopband center of the sample as a function of temperature.

90

| | |
|---|-----|
| Figure 5.10: (a) Temperature dependence of the transmission spectra of the GaSb-based 4.0 μm MQWs RC sample. (b) Temperature dependence of the optical mode transmission. (c) The position of the optical cavity mode and the DBR stopband center of the sample as a function of temperature. | 92 |
| Figure 5.11: (a) Temperature dependence of the transmission spectra of the InAs-based SLs RC sample. (b) Temperature dependence of the optical mode transmission. (c) The position of the optical cavity mode and the DBR stopband center of the sample as a function of temperature. | 92 |
| Figure 5.12: The position of the optical cavity mode for all RC samples as a function of temperature. | 94 |
| Figure 5.14: Temperature dependence of the detuning values for all RC samples. | 96 |
| Figure 5.15: Room temperature simulations of (a) the resonance emission (G_e) and (b) the integrated emission (G_{int}) enhancement factor, as a function of the DBR stopband center and the peak emission of the cavity mode, respectively. The white dashed line represents the resonance case between the optical cavity mode and the DBR stopband center. Square (GaSb-based 4.0 μm MQWs RC), Diamond (GaSb-based 4.3 μm bulk RC), triangle (GaSb-based 4.5 μm MQWs RC), circle (InAs-based 4.6 μm SLs RC). | 96 |
| Figure 5.16: SEM cross-section of the (a) bulk RCLED and (b) MQWs RCLED. | 97 |
| Table 5.1: Room temperature optical properties of the RC samples. | 97 |
| Figure 6.1: Schematic structure of the (a) bulk RCLED-M1 (b) bulk RCLED-M2. | 99 |
| Figure 6.2: (a) Temperature dependence of the EL spectra of the high detuning RCLED, (b) The peak intensity of the main resonance mode and the side mode as a function of temperature. The open triangles represent the relative intensity, (c) Temperature dependence of the peak position of the side modes (at 3.8 μm and 4.5 μm). | 101 |
| Figure 6.3: (a) Temperature dependence of the EL spectra of the high detuning RCLED without top DBR mirror, (b-e) The electroluminescence spectra of the RCLED with top DBR compared to that of the RCLED without top DBR at various temperature, (f) Peak intensity of the emission of the RCLED with top DBR compared to that of the RCLED without top DBR. Dash-dot line represents the relative intensity, (g) Optical output power of the emission of the RCLED with top DBR compared to that of the RCLED without top DBR. Dash-dot line represents the relative output power. | 102 |
| Figure 6.4: (a) Experimentally measured transmittance spectrum of the RC structure at room temperature, showing that the optical cavity mode occurs at 4.295 μm , and the DBR stopband is centred at 4.180 μm . (b) Comparison of the RCLED-M1 (solid line), RCLED-M2 (dashed line), and the reference LED (dotted line) electroluminescence emission spectra at 300 K using the same injection current (100 mA at 1 kHz with 20% duty cycle). The dip in the reference LED spectrum originates from atmospheric CO ₂ absorption in the optical path. Also shown are the fundamental fingerprint absorptions of CO ₂ gas. | 104 |
| Figure 6.5: (a) and (b) Room temperature electroluminescence spectra of the RCLED-M1 and RCLED-M2 at various duty cycle using 100 mA injection current, respectively. (c) Peak intensity of the RCLED-M1 and RCLED-M2 emission as a function of duty cycle. (d) Total integrated emission of the RCLED-M1 and RCLED-M2 as a function of duty cycle. | 105 |

| | |
|--|-----|
| Figure 6.6: Integrated emission of the main resonance mode for RCLED-M1 compared to that of the RCLED-M2 as a function of duty cycle using 100 mA injection current. | 106 |
| Figure 6.7: (a) Peak intensity of the RCLED-M1 emission as a function of injection current. (b) Optical output power of the RCLED-M1 emission as a function of injection current. | 107 |
| Figure 6.8: Far field angular profile of the RCLED emission, which shows a half power solid angle of 60° . | 108 |
| Figure 6.9: Temperature dependence of the EL spectra for (a) the RCLED-M1 and (b) the reference LED. (c) Intensity peak values of the EL spectra for the RCLED and reference LED. The dashed-dotted line represents the relative intensity. (d) The position of the EL peaks as a function of the temperature. The dashed line represents the theoretical results of the EL intensity peak of the RCLED. | 109 |
| Figure 6.10: (a) Temperature dependence of the EL spectra for the RCLED-M2. (b) and (c) Peak emission intensity and the output power for the RCLED-M1 and RCLED-M2 as a function of temperature, respectively. The dashed-dotted line represents the relative values. | 110 |
| Figure 6.11: (a)-(c) Current-Voltage (I-V) characteristics of the RCLED-M1, RCLED-M2, and the reference LED measured as a function of temperature, respectively. (d) Temperature dependence of the series resistance of the RCLED-M1, RCLED-M2, and the reference LED. | 111 |
| Figure 6.12: (a) Room temperature photo-response spectra of the RCLED-M1 at various bias voltage. (b) Peak intensity of the photo-response spectra as a function of the bias voltage measured at 300 K. | 113 |
| Figure 6.13: (a) Photo-response spectra of the RCLED-M1 measured at 200 K at various bias voltage. (b) and (c) Spectral photo-response at 300 K compared to that at 200 K at 0 bias and -200 mV, respectively. | 114 |
| Figure 6.14: (a) Photo-response spectra of the RCLED-M1 measured at 260 K at various reverse bias voltage. | 114 |
| Figure 6.15: (a) Transmission spectra of the high detuning RC sample at 77 K and 300 K. | 115 |
| Figure 7.1: Schematic structure of the (a) AlInAs/InAsSb QWs RCLED. (b) reference LED. | 119 |
| Figure 7.2: (a) Experimentally measured transmittance spectrum and EL emission spectrum of the RCLED structure, showing that the wavelength of the main EL emission peak at room temperature occurs at $4.462 \mu\text{m}$, which corresponds to the cavity resonance wavelength. (b) Comparison of the RCLED (solid line) and the reference LED (dashed line) electroluminescence emission spectra at 300 K using the same injection current (100 mA at 1 kHz with 30% duty cycle). The dip in the reference LED spectrum originates from atmospheric CO ₂ absorption in the optical path. Also shown are the fundamental fingerprint absorptions of greenhouse gases of interest in this spectral range. | 121 |
| Figure 7.3: The spectral intensity of two RCLEDs of different diameter vs current density, measured at room temperature using a 1 kHz injection current with 1% duty cycle. The MQW reference LED is also shown (x30) together with other results from the literature measured under similar conditions. The ICLED made in our | 122 |

laboratory is $400\ \mu\text{m} \times 400\ \mu\text{m}$ [1]. The conventional $4.6\ \mu\text{m}$ LED spectral intensity was estimated from the peak power given in the Roithner Lasertechnik data sheet.

Figure 7.4: Far field angular profile of the RCLED emission, which shows a half power solid angle of 45° . 123

Figure 7.5: Temperature dependence of the EL spectra for (a) the RCLED and (b) the reference LED. (c) Intensity peak values of the EL spectra for the RCLED and reference LED. The dashed-dotted line represent the relative intensity. (d) The position of the EL peaks as a function of the temperature. The dashed line represent the theoretical results of the EL intensity peak of the RCLED. 125

Figure 7.6: Temperature dependence of (a) The linewidth of the EL spectra for RCLED and reference LED, (b) the Quality factor (Q) of the RCLED, (c) The internal angle and solid angle of the RCLED. 126

Figure 7.7: (a) Peak energy of the EL emission for the reference LED and the fitting using Varshni equation. (b) Arrhenius plot of the integrated EL intensity for the reference LED indicating an activation energy of $52\ \text{meV}$. 127

Figure 7.8: (a) Temperature dependence of the intensity peak for the resonance emission spectra of RCLED and the emission spectra of LED. (b) Temperature dependence of the output power for the emission spectra of the RCLED and LED. (c) The difference between the peak wavelengths (spectral detuning) as a function of temperature. (d)-(g) EL spectra of the RCLED and LED at different temperature, $140\ \text{K}$, $200\ \text{K}$, $240\ \text{K}$ and $300\ \text{K}$, respectively. 129

Figure 7.9: (a) Room temperature electroluminescence emission spectra of the RCLED as a function of the wavelength at different duty cycles using $100\ \text{mA}$ injection current. (b) The peak intensity and the output power of the RCLED as a function of duty cycle. (c) The peak position of the electroluminescence emission vs the duty cycle. (d) The linewidth (FWHM) and the Q-factor of the electroluminescence spectra as a function of the duty cycle. 131

Figure 7.10: (a) Room-temperature power dependence of the electroluminescence emission spectra of the RCLED using different injection currents at 30% duty cycle. The inset is the peak position of the electroluminescence versus injection current. (b) The linewidth and the quality factor of the RCLED dependence on injection current. (c) Output power of the RCLED and reference LED as a function of injection current. The dashed-dotted line represents the power enhancement factor (the relative power). (d) Peak intensity of the RCLED and the reference LED as a function of injection current. The dashed-dotted line represents the intensity enhancement factor (the relative intensity). 132

Figure 7.11: (a) and (b) The forward and reverse current-voltage characteristics of the RCLED and the reference LED over the temperature range $20\ \text{K}$ - $300\ \text{K}$. (c) The series resistance of the RCLED and reference LED as a function of temperature. (d) Forward current-voltage characteristic of the RCLED against the temperature. There is a clear trend of decreasing the turn on voltage with increasing the temperature. (e) Schematic diagram illustrates the path of the current through the DBR and cavity layers. 133

Figure 7.12: (a) Room temperature EL emission spectra of the RCLED as a function of the wavelength at different mesa size using $100\ \text{mA}$ injection current. (b) The emission intensity of the RCLED as a function of mesa area. (c) The intensity peak position of the emission spectra of the RCLED as a function of mesa area. (d) Measured forward I-V characteristics of the RCLED at three different mesa size. (e) Measured forward J-V curves for devices with different mesa width. The current 135

was normalized to the mesa area. (f) The current density values at $V_{\text{bias}} = 3 \text{ V}$ are extracted and plotted against the mesa area. A log dependence over the mesa area is shown for comparison.

Figure 7.13: Schematic diagram of the RCLED device structure without top DBR mirror. 137

Figure 7.14: (a) Temperature dependence of the EL spectra for the RCLED without top DBR. (b) Room temperature electroluminescence emission of the RCLEDs with and without the top DBR mirror, and the reference LED. (c) Peak position of the EL emission spectra of the RCLED without top DBR versus temperature. (d) The linewidth and the quality factor of the EL spectra of the RCLED without top DBR as a function of temperature. 138

Figure 7.15: (a) and (d) Room temperature EL emission spectra of the RCLED without top DBR as a function of the wavelength at different injection current and at different duty cycle, respectively. (b) and (e) The emission intensity peak of the RCLED with and without top DBR as a function of the current and duty cycle, respectively. (c) and (f) The integrated emission of the RCLED with and without top DBR as a function of the current and duty cycle, respectively. 140

Figure 7.16: (a) Room temperature EL emission spectra of the RCLED without top DBR as a function of the wavelength at different mesa size using 100 mA injection current. (b) The emission peak intensity and the integrated emission of the EL spectra as a function of the mesa area. (c) The peak intensity position of the emission spectra as a function of mesa area. (d) Measured forward J-V curves for devices with different mesa width. (e) The current density values at $V_{\text{bias}} = 1 \text{ V}$ are extracted and plotted against the mesa area. A $1/r^{1.3}$ dependence over the mesa area is shown for comparison. 141

Figure 7.17: Room temperature external efficiency of the MQWs RCLED and reference LED as a function of current density. 143

Figure 7.18: The calculated variation in RCLED wavelength and emission intensity dependence on cavity thickness or DBR period thickness. Also shown are the absorption spectra of key greenhouse gases to illustrate the accessible tuning range, which encompasses CO₂, N₂O and CO. 144

Figure 7.19: Photoluminescence spectra of the AlInAs/InAsSb MQWs at various Sb composition. 145

Table 7.1: Room temperature optical properties of the RCLEDs samples compared to that of the reference LED. 146

Table 7.2: Room temperature optical properties of the RCLED full structure compared to that of the RCLED without top DBR for different area mesa. 146

Figure 8.1: Room temperature electroluminescence spectra of the four RCLEDs. We grow and fabricate these devices at physics department in Lancaster University. The emission spectra were under quasi-CW condition using 100 mA injection current and 30% Duty Cycle. 152

Chapter 1

Introduction

There are many applications including environmental gas detection and monitoring, medical diagnostics, military security and defense, space technology, and thermal imaging, which makes developing optoelectronic devices for the mid-infrared (3 – 5) μm spectral region of great research interest. In particular, infrared absorption spectroscopy is an attractive technique for monitoring greenhouse gases such as methane CH_4 (3.3 μm), carbon dioxide CO_2 (4.2 μm), N_2O (4.5 μm) and carbon monoxide CO (4.6 μm) because they have strong fingerprint absorptions in this spectral range (see Figure 1.1), enabling gas specific detection and remote sensing. Therefore, there is an increasing demand for mid-infrared light sources and detectors at these key wavelengths.

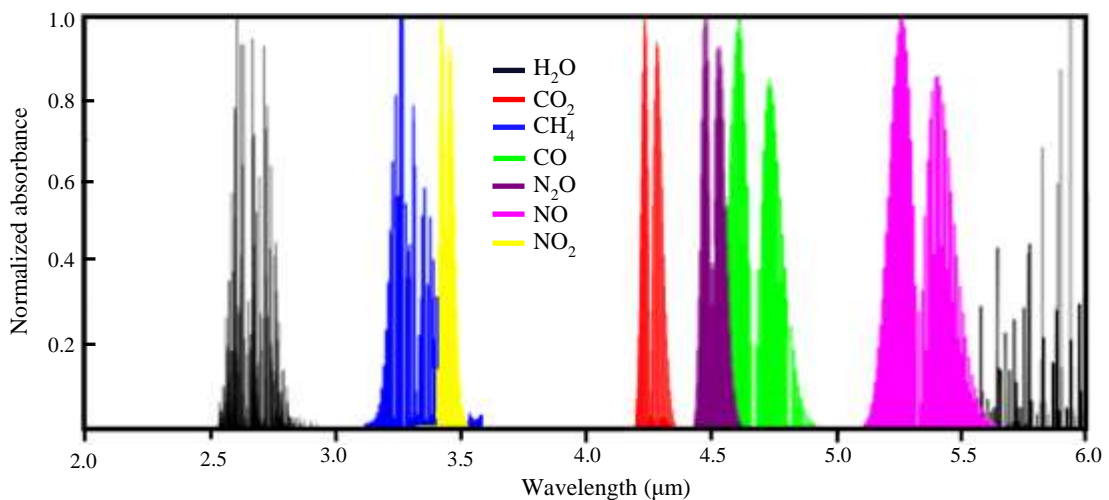


Figure 1.1: Normalized intensity of the absorption bands of relevant gas species in the 2–6 μm range (data from SpectralCalc.com based on HITRAN database)

For many applications mid-infrared LEDs are an attractive alternative to semiconductor laser especially for widespread distributed sensing applications requiring many point sensors. This is attributed to the operating properties of the LEDs such as, lower complexity, temperature stability, cost-effective, and lower power.

CO₂ and CO are greenhouse gases, emitting and absorbing mid-infrared radiation corresponding to the vibration transition of the gas molecules [1]. The concentration of these gases have risen due to human activities, especially burning fossil fuels, causing an increase in the global temperature. Therefore many research groups have investigated and developed LEDs for monitoring these two gases [2-16]. In particular, the ternary alloy InAs_{1-x}Sb_x with an antimony composition ~9% is conveniently lattice matched to GaSb substrates and LEDs and detectors with light emission at the CO₂ absorption wavelength have been demonstrated [17-20]. This material was also investigated with Sb=11% to detect CO gas [16]. The device was fabricated based on a InAs_{0.55}Sb_{0.15}P_{0.30}/InAs_{0.89}Sb_{0.11}/InAs_{0.55}Sb_{0.15}P_{0.30} symmetrical double heterostructure with large band offsets. Additionally, various LED structures have been developed for CO₂ monitoring at 4.2 μm, including bulk heterostructures of AlInSb [21], as well as InSb/InAs quantum dots [22], InAs/InAsSb quantum wells, and superlattices [23,24,25,26]. Recently, GSS Ltd has developed commercially available devices (gas sensors) for the monitoring of CO₂ [27, 28]. The LED and photodiode (PD) (light source/detector) based non-dispersive infrared CO₂ sensor was designed to provide low power consumption, low cost, longevity, and fast stabilization time. [28]

N₂O is well-known as a greenhouse gas and is nowadays the single most important ozone-depleting agent.[29] Although present at much lower levels than CO₂, it has 298 times the global warming potential (over a period of 100 years). N₂O in the atmosphere originates from a number of sources including agriculture, where for example N₂O is released in silage gas [30], and as a by-product of fossil fuel burning, as well as in car exhaust emissions [31-33]. Atmospheric N₂O (~330 ppb) monitoring is possible but it requires complex and expensive laser based systems. However, simpler gas sensors based on mid-infrared LEDs and detectors could provide an attractive means of widespread monitoring of localised N₂O sources. Some LEDs have already been developed, but so far these exhibit low spectral intensity at the target wavelength [34,35]. More recently interband quantum cascade LEDs have been demonstrated [36] with higher output power, but spread over a broad emission spectrum (~700 nm) with a limited fraction of *useable* photons within the N₂O absorption band (4.425-4.619 μm).

However, the efficiency of these devices (mid-infrared LEDs) is less than that of the visible and near-infrared LEDs. This is attributed to the increase in the rate of the non-radiative Auger recombination processes when the emission wavelength increases [37]. Furthermore, the devices typically exhibit 300 K optical output powers of a few microwatts, with an emittance of $\sim 1\text{--}14 \text{ mW/cm}^2$, but with broadband emission spectra resulting in low available power at the target wavelength. However, although many researchers have developed light emitting diodes (LEDs), the light extraction efficiency is still limited. This is due to the large refractive index mismatch between the semiconductor (n_s) and air (n_{air}). Thus, according to Snell's law ($\phi_c = \arcsin[n_{\text{air}}/n_s]$), the critical angle of total internal reflection (ϕ_c) which is defined as the light escape cone is quite small. As a result, the most of the generated light is trapped inside the device and only a small percentage can be extracted [38, 39]. One solution to this problem involves the use of a resonant cavity (RC) to enhance the light emission from the LED. This is typically achieved at shorter wavelengths by locating the active region, at the antinode of the standing wave optical field, inside a Fabry–Perot microcavity consisting of two distributed Bragg reflectors (DBRs) to form a resonant cavity light emitting diode (RCLED) structure [40]. RCLEDs offer many advantages including; higher brightness than their conventional LED counterparts, improved directionality, increased spectral purity and power efficiency [41,42]. Consequently, there has been some research effort devoted towards resonant cavity light emitting diodes (RCLEDs) and vertical cavity surface emitting lasers (VCSELs) for mid-infrared applications [43-49]. However, there are only a limited number of reports of RCLEDs and VCSELs operating in the 4-5 μm spectral range [44,49,50]. The RCLED structures, reported in [44] and [49] consisted of a gold top-mirror with reflectivity $\sim 95\%$ and bottom DBR mirror with low reflectivity ($<70\%$), showing a relatively modest resonant cavity emission enhancement ($<5x$). These two devices were designed to emit at a wavelength of $\sim 4.2 \mu\text{m}$ through the substrate. Meanwhile, the mid-infrared VCSEL reported in [50] was designed to emit at a wavelength of $\sim 4.0 \mu\text{m}$ and achieved single-mode CW operation up to $-7 \text{ }^\circ\text{C}$ and room temperature operation under pulsed conditions.

In this thesis we designed and fabricated mid-infrared RCLEDs, consisting of a bottom high reflectivity (>98%) DBR mirror and a top DBR mirror with reflectivity of >82%. The structures were designed to emit the light from the top surface and were grown by molecular beam epitaxy (MBE). In chapter two, we demonstrate the fundamentals and theoretical concepts of semiconductors, light emitting diodes (LEDs), and resonant cavity LEDs (RCLEDs). An up to date literature review about the mid-infrared LEDs, RCLEDs, and VCSELs is presented in chapter three. Then the experimental tools and techniques which are used to carry out the study in this thesis as well as the fabrication processes of the devices are described in details in chapter four. Our results and discussion are demonstrated in three chapters. The design, growth and characterization of the resonance cavity (RC) samples are investigated in the chapter five, including the results of the temperature dependence of the transmission spectra of four samples grown on GaSb and InAs substrates using molecular beam epitaxy (MBE). Two of those samples were fabricated, having bulk and MQWs RCLEDs. The optical and electrical properties of the bulk InAsSb RCLEDs and the AlInAs/InAsSb MQWs RCLEDs are discussed in details in chapters six and seven, respectively. The electroluminescence spectra of the bulk and MQWs RCLEDs are compared to that of the reference LEDs, exhibiting high emission enhancement factors, superior temperature stability and narrow emission linewidth. Finally, the conclusion of our results and the future work are included in chapter eight.

Chapter 2

Background theory and fundamental concepts

2.1 Fundamental concepts of semiconductor materials

2.1.1 Band structure

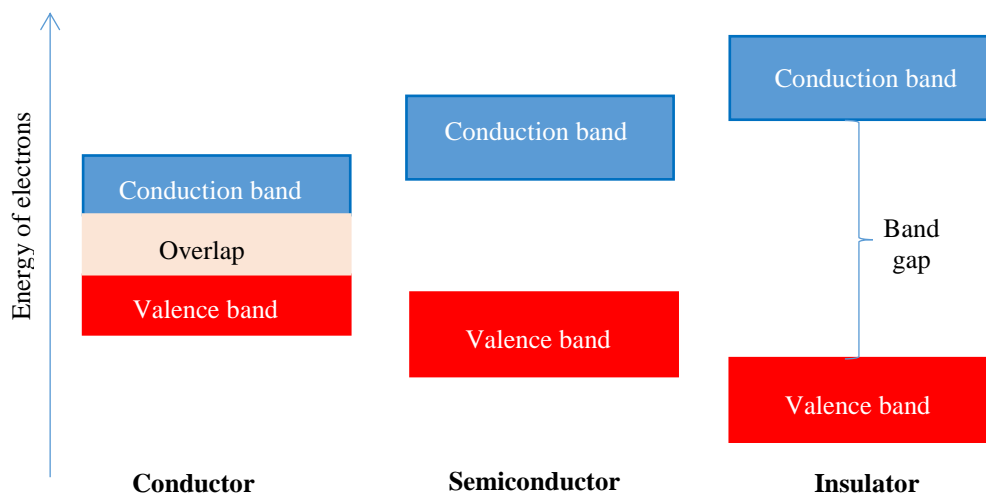


Figure 2.1: Schematic diagram of the band structure in conductors, semiconductors, and insulators [51].

When atoms and molecules form solid materials, the discrete energy levels of these atoms and molecules combine to form energy bands. These bands are formed when N number of atoms are brought very close and then the electrons in the orbits of these atoms interact and give N number of discrete band of allowed energy levels. The highest filled energy band is known as the valence band, and the next highest (empty) energy band is known as the conduction band. In the case of a conductor the valence band and conduction band overlap, while in the insulator materials there is a wide energy spacing (band gap) between the two bands. In comparison with insulators, semiconductors have a significantly narrower energy band gap. The schematic diagram of the energy bands of the inductors, insulators, and semiconductors are illustrated in [Figure 2.1](#). At 0 K, the semiconductor valence band is fully occupied and when the temperature increases the thermal energy increases, enabling a small portion of the electrons to be excited to the conduction band. The density of conduction electrons could be significantly increased

when an external excitation source (e.g. optical or electrical source) is applied, causing many changes in the physical properties of the semiconductor.

2.1.2 Temperature dependence of band gap

As temperature increases the lattice spacing of semiconductor material expands, resulting in reduced binding energy of the electrons. This means that the required energy to excite the electrons from valence band to conduction band decreases with increasing temperature, i.e. decrease in the energy band gap. The temperature dependence of the energy gap ($E_g(T)$) can be described using the Varshni equation [52]:

$$E_g(T) = E_g(0) - \frac{\alpha T^2}{\beta + T} \quad (2.1)$$

where $E_g(0)$ is the energy gap at 0 K, and the coefficients α and β are fitting parameters which are related to the thermal expansion of the lattice and to the Debye temperature in the Debye theory, respectively.

2.1.3 III-V band gap alignment

Different types of band alignment occur when two semiconductor materials come into contact in a hetero-interface. The two materials are different in electron affinity (χ), which is defined as the separation between the vacuum level and the conduction band, and/or in band gap energy. Consequently, the conduction and valence band offsets, ΔE_c and ΔE_v , can be calculated using the formulas [53]:

$$\Delta E_c = \chi_2 - \chi_1 \quad (2.2)$$

$$\Delta E_v = (\chi_1 + E_{g1}) - (\chi_2 + E_{g2}) \quad (2.3)$$

Where E_g is the energy band gap of the semiconductor material.

2.1.3.1 Type I band alignment

In this band alignment, the valence band (E_v) of the material B is higher than that of the material A, and the conduction band (E_c) of the material B is lower than that of the material A, as illustrated in [Figure 2.2](#). In other words, the conduction band offset (ΔE_c) is negative and the

valence band offset (ΔE_V) is positive. Therefore, the electrons and holes are confined in the conduction and valence bands of the material A and their recombination occurs via direct transitions.

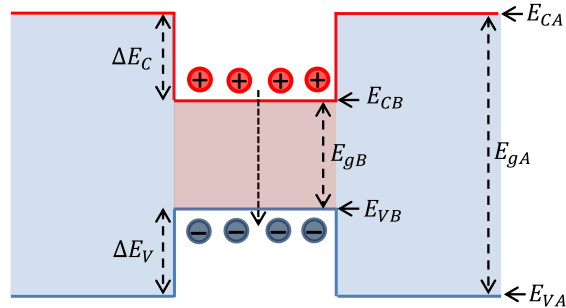


Figure 2.2: Schematic diagram of type I band alignment.

2.1.3.2 Type II band alignment

Type II band alignment occurs when the band offsets ΔE_C and ΔE_V are both negative, where the conduction band and valence band of the material B is lower than that of the material A as shown in Figure 2.3(a), or both positive, where the conduction band and valence band of the material B is higher than that of the material A as shown in Figure 2.3(b). Thus, the electrons and holes are confined in separate materials and the recombination occurs via spatially indirect transitions, but still direct in k-space.

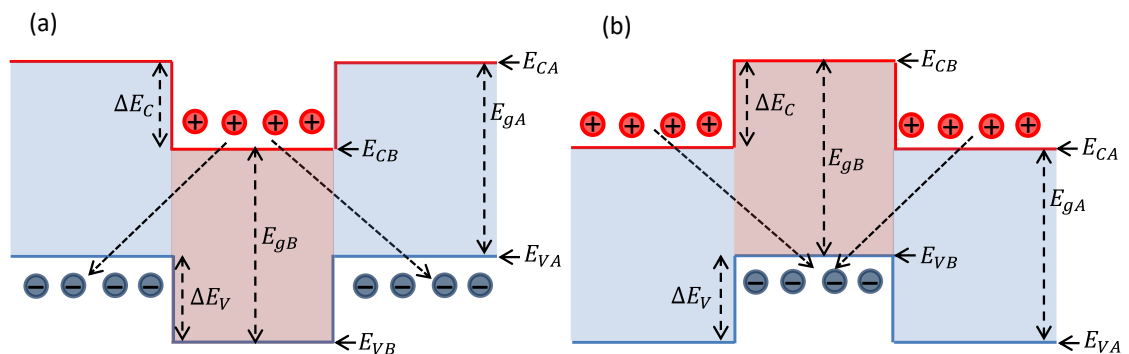


Figure 2.3: (a) and (b) Schematic diagrams illustrating the type II band alignments.

When the valence band of one material is higher than the conduction band of the other material (e.g. InSb/InAs and InAs/GaSb), a broken type II band alignment is formed, as illustrated in the schematic diagram in Figure 2.4.

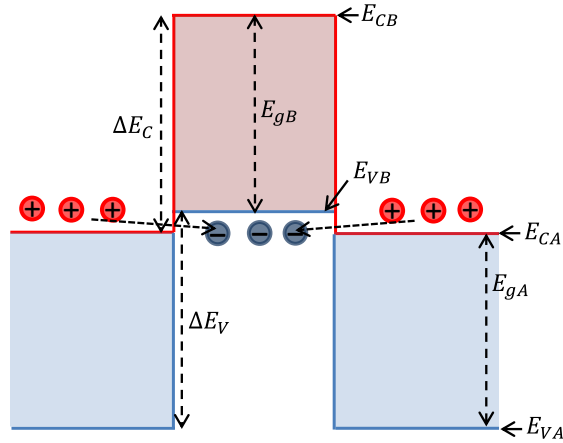


Figure 2.4: Schematic diagram of broken type II band alignment.

2.1.4 Band gap of III-V semiconductor materials

Most of the III-V semiconductor structures are zinc blende crystals and the room-temperature band gap energy of the zinc blende binary III-V semiconductors are plotted as a function of their lattice constant in Figure 2.5.

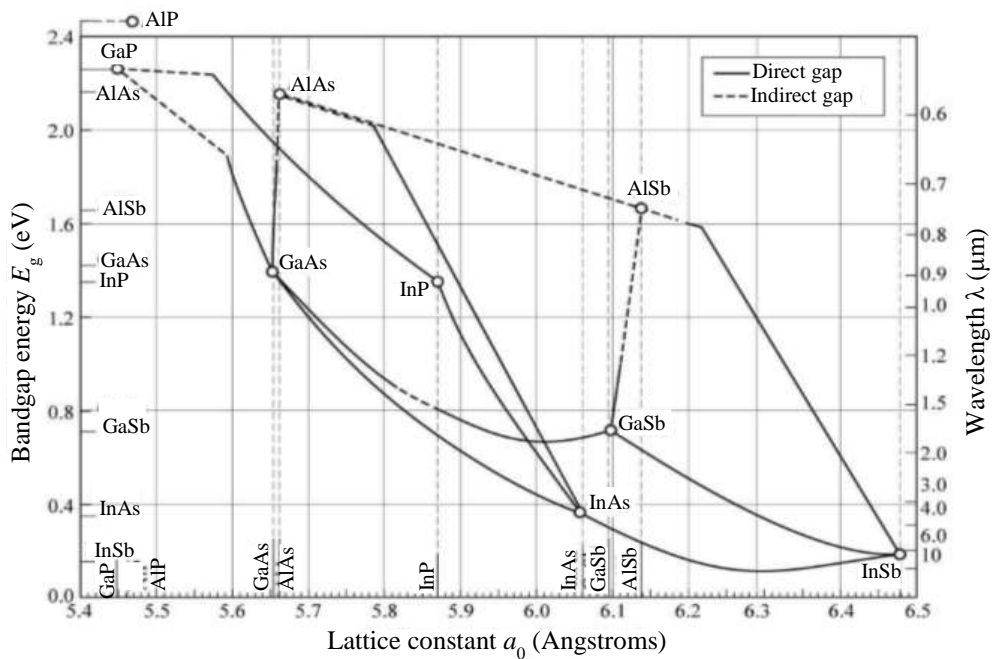


Figure 2.5: Direct Γ -valley energy gap as a function of lattice constant for the zinc blende form of 12 III-V binary compound semiconductors (points), and some of their ternary alloys (curves) at zero temperature [54].

In the case of the ternary and quaternary alloy semiconductor materials which are comprised of binary III-V semiconductors, the band gap energy of these alloys is varied by changing the composition of group-III or group-V elements and by changing the layer thickness. Using Vegard's law, the composition-dependent band gap energy of the ternary alloy E_g can be estimated as [55]:

$$E_g(A_{1-x}B_x) = (1 - x)E_g(A) + xE_g(B) - x(1 - x)C_p \quad (2.4)$$

where $E_g(A)$ and $E_g(B)$ are the band gap energies of the binary materials, x is the composition (percentage) of the element, and C_p is the bowing parameter.

2.1.5 Strained layers

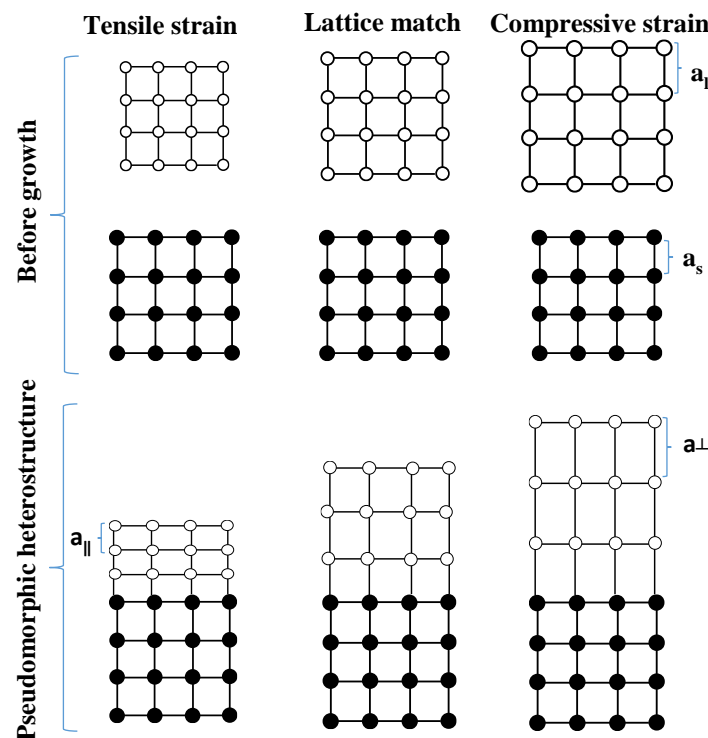


Figure 2.6: Schematic diagram of tensile strain, lattice matched, and compressive strain heteroepitaxial layers, where $a_{||}$ and a_{\perp} are the lattice constant of the grown material in the direction of growth for the tensile and compressive strain, respectively.

When a layer of semiconductor material with lattice constant a_1 is deposited on a substrate of different lattice constant a_s , the deposited layer is deformed to fit the underlying lattice structure as shown in Figure (2.6) and this deformation introduces strain into the epitaxial layer. If the

lattice constant of the deposited layer is greater than the substrate lattice constant ($a_1 > a_s$), then the layer must compress perpendicular to the growth direction and it increases in the direction of growth. In this case the layer is compressively strained. If ($a_1 < a_s$), then the converse occurs and it is denoted as tensile strain.

2.1.5.1 Critical thickness

When a thin strained layer of semiconductor material is grown heteroepitaxially on a substrate (which is not lattice matched), misfit dislocations are formed until the layer grows to a certain thickness (critical thickness). Increasing the thickness of this layer above the critical thickness leads to generation of dislocations. The value of the critical thickness depends on the lattice mismatch between the epitaxial layer and the substrate. Two main types of dislocations, the screw dislocation and edge dislocation, are illustrated in Figure 2.7. These defects negatively affect electronic, electrical and optical properties of the material by decreasing the carrier mobility due to increased scattering [56], and acting as non-radiative recombination centres, where undesirable energy levels are generated [57].

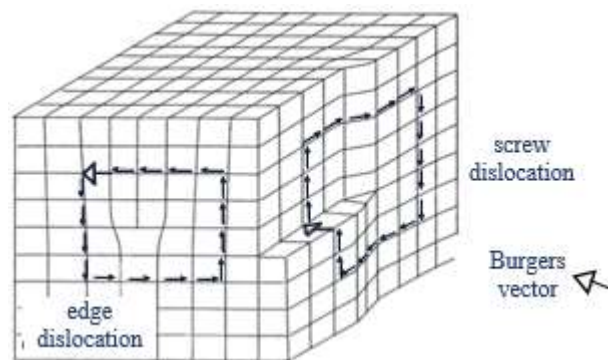


Figure 2.7: Example of the Burgers vector of edge and screw dislocations [26].

The model most used to calculate the critical thickness (h_c) has been developed by Mathews and Blakeslee [58]. In this model, the h_c value is reached if there is a mechanical balance between the two forces: the stress due to the film strain and the tension in dislocation. The Mathews and Blakeslee critical thickness (h_c) for zinc blende (001) substrate is given by:

$$h_c = \frac{a_o \left(1 - \frac{\nu}{4}\right) \left[\ln \left(\frac{\sqrt{2} h_c}{a_o} \right) + 1 \right]}{\sqrt{2} \pi f (1 + \nu)} \quad (2.5a)$$

$$f = \frac{a_o - a_l}{a_l} \quad (2.5b)$$

$$\nu = \frac{C_{12}}{C_{11} - C_{12}} \quad (2.5c)$$

where f is the layer strain when on the substrate, a_o is the substrate lattice constant, a_l is the layer lattice constant, ν is Poisson's ratio, C_{11} and C_{12} are the elastic constants of the layer.

In the case of a quantum well, Matthews and Blakeslee's expression could be approximated as: [59]

$$h_c = \frac{a_l}{f} \quad (2.6)$$

Another method for calculating the critical thickness for single layers on zinc blende (001) substrates is given by People & Bean using only energy considerations instead of mechanical forces, as: [60]

$$h_c = \frac{a_o^2 (1 - \nu) \ln \left(\frac{\sqrt{2} h_c}{a_o} \right)}{32 \sqrt{2} \pi f^2 a_l (1 + \nu)} \quad (2.7)$$

2.1.5.2 Effect of strain on the energy levels

The effect of the tensile and compressive strain on the energy levels of the epilayer is illustrated in Figure (2.8). The conduction band shifts up for layers under tensile strain and down for layers under compressive strain [61]. On the other hand, in the case of compressive strain, the heavy hole (hh) band moves up and the light hole (lh) moves down, while for tensile strain the opposite happens and thus the light hole band becomes the highest band.

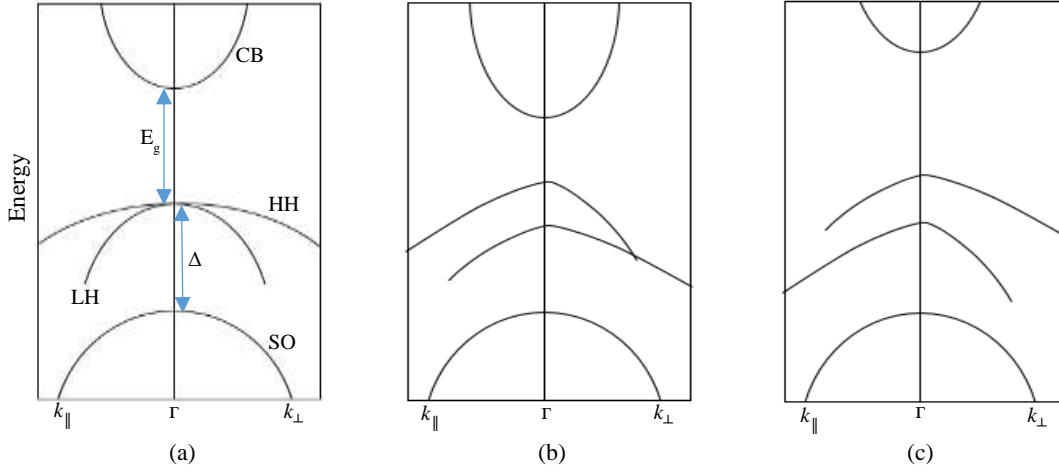


Figure 2.8: The effect of strain on the energy levels of a semiconductor. (a) Unstrained, (b) compressive strain, (c) tensile strain [61]. In the case of the biaxial tension, the band gap is reduced due to the hydrostatic component of strain. Whilst the axial component of strain splits the valence band, creating an anisotropic valence band structure where the light hole band (LH) becomes the highest band. In biaxial compression the opposite occurs where the band gap is increased and the heavy hole band (HH) becomes the highest band.

Let a_1 be the lattice constant of the epilayer in its unstrained state, and a_s be the lattice constant of the substrate. In a pseudomorphic epitaxial growth, the strained layer has two different lattice parameters: (i) the lattice parameter parallel to the growth surface, $a_{\parallel} = a_s = a_{Lx} = a_{Ly}$, which is the same in the x-direction (a_{Lx}) and the y-direction (a_{Ly}) and equal to the lattice parameter of the substrate (a_s), (ii) the lattice parameter perpendicular to the growth surface (in the z-direction), $a_{\perp} = a_{Lz}$, it is $< a_s$ or $> a_s$ depending on whether the strain is tensile or compressive. The parallel (biaxial) (ϵ_{\parallel}) and perpendicular (uniaxial) (ϵ_{\perp}) strains are related to the lattice mismatch (Δa_{\parallel} and Δa_{\perp}) by the relations [62]:

$$\epsilon_{\parallel} = \frac{\Delta a_{\parallel}}{a_1} = \frac{(a_{\parallel} - a_1)}{a_1} = -\frac{\Delta a_1}{a_1} = -\frac{(a_1 - a_s)}{a_1} \quad (2.8)$$

$$\epsilon_{\perp} = \frac{\Delta a_{\perp}}{a_1} = \frac{(a_{\perp} - a_1)}{a_1} \quad (2.9)$$

$$a_{\perp} = a_1(1 - D\epsilon_{\parallel}) \quad (2.10)$$

The constant D depends on elastic constants, C , of the epitaxial layer, and on the interface orientation, where:

$$D^{001} = 2 \frac{C_{12}}{C_{11}} \quad (2.11)$$

$$D^{111} = 2 \frac{C_{12} + 2C_{12} - 2C_{44}}{C_{11} + 2C_{12} + 4C_{44}} \quad (2.12)$$

For an unstrained layer, the valence band at Γ -point (E_V) is calculated from the vacuum valence band level of the valence band ($E_{V,\text{vac}}$) and the spin-orbit splitting (Δ_0):

$$E_V = E_{V,\text{vac}} + \frac{\Delta_0}{3} \quad (2.13)$$

The effect of strain on energy levels can be decomposed into two contributions, hydrostatic and shear components. The shift in the conduction band (ΔE_c^{hy}) is then given by:

$$\Delta E_c^{\text{hy}} = a_c(2\varepsilon_{\parallel} + \varepsilon_{\perp}) \quad (2.14)$$

where a_c is the conduction band hydrostatic deformation potential. The valence bands are shifted by both, a hydrostatic strain component:

$$\Delta E_{V,\text{av}}^{\text{hy}} = a_V(2\varepsilon_{\parallel} + \varepsilon_{\perp}) \quad (2.15)$$

where a_V is the valence band hydrostatic deformation potential, as well as a shear contribution which gives an additional splitting of the valence band energies: [63]

$$\Delta E_{V,\text{hh}}^{\text{sh}} = -\frac{1}{2}\delta E^{\text{sh}} \quad (2.16a)$$

$$\Delta E_{V,\text{lh}}^{\text{sh}} = -\frac{1}{2}\Delta_0 + \frac{1}{4}\delta E^{\text{sh}} + \frac{1}{2}\left(\Delta_0^2 + \Delta_0\delta E^{\text{sh}} + \frac{9}{4}(\delta E^{\text{sh}})^2\right)^{1/2} \quad (2.16b)$$

$$\Delta E_{V,\text{so}}^{\text{sh}} = -\frac{1}{2}\Delta_0 + \frac{1}{4}\delta E^{\text{sh}} - \frac{1}{2}\left(\Delta_0^2 + \Delta_0\delta E^{\text{sh}} + \frac{9}{4}(\delta E^{\text{sh}})^2\right)^{1/2} \quad (2.16c)$$

The strain-dependent shift (δE^{sh}) depends on the interface orientation (i.e. 001 and 111), where:

$$\delta E_{001}^{\text{sh}} = 2B(\varepsilon_{\perp} - \varepsilon_{\parallel}) \quad (2.17a)$$

$$\delta E_{111}^{\text{sh}} = \frac{2}{3}\sqrt{3}d(\varepsilon_{\perp} - \varepsilon_{\parallel}) \quad (2.17b)$$

The quantities B and d are the tetragonal and rhombohedra shear deformation potentials, respectively. Conduction bands at Γ point are not affected by the shear contribution to the strain.

Thus, the equations describing the total shifts in the valence band edges are given by:

$$\Delta E_{V,\text{hh}} = \Delta E_{V,\text{av}}^{\text{hy}} + \Delta E_{V,\text{hh}}^{\text{sh}} \quad (2.18a)$$

$$\Delta E_{V,\text{lh}} = \Delta E_{V,\text{av}}^{\text{hy}} + \Delta E_{V,\text{lh}}^{\text{sh}} \quad (2.18b)$$

$$\Delta E_{V,so} = \Delta E_{V,av}^{hy} + \Delta E_{V,so}^{sh} \quad (2.18c)$$

From equations (2.13), (2.14), (2.15), and (2.16a-c) the valence-band and conduction-band edge energies E_V and E_C of the strained layer can be written as:

$$E_{V,hh} = E_{V,av} + \frac{1}{3}\Delta_0 + \Delta E_{V,hh} \quad (2.19a)$$

$$E_{V,lh} = E_{V,av} + \frac{1}{3}\Delta_0 + \Delta E_{V,lh} \quad (2.19b)$$

$$E_{V,so} = E_{V,av} + \frac{1}{3}\Delta_0 + \Delta E_{V,so} \quad (2.19c)$$

$$E_C = E_{C,av} + \Delta E_{C,av} = E_{V,av} + \frac{1}{3}\Delta_0 + E_g + \Delta E_C^{hy} \quad (2.20)$$

2.1.6 Radiative and non-radiative recombination

In semiconductor materials and under non-equilibrium conditions, electrons in the conduction band and holes in the valence band recombine either radiatively or non-radiatively (see [Figure 2.9](#)). The former is the required recombination process for light-emitting devices, where photons are generated. There are a number of radiative and non-radiative mechanisms which can occur in semiconductors, which will be discussed in the next sections.

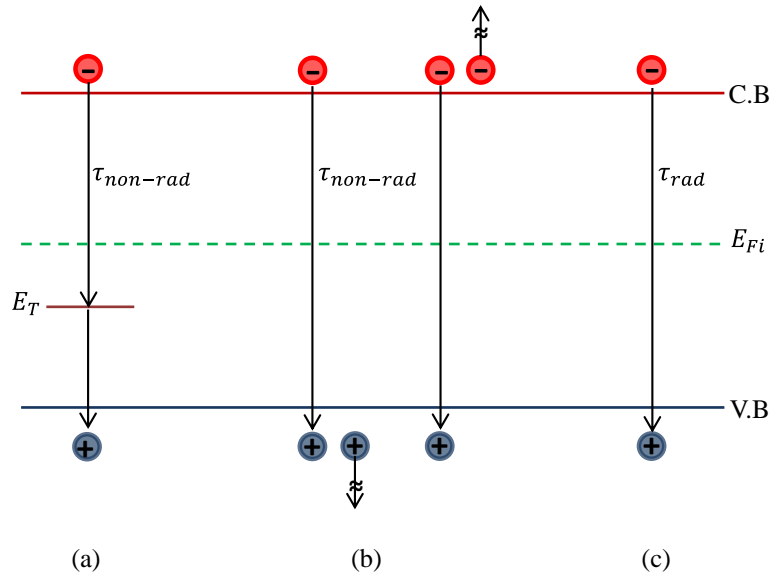


Figure 2.9: Schematic of the recombination processes (a) Shockley-Read-Hall (SRH) non-radiative recombination. (b) non-radiative Auger recombination. (c) radiative recombination. [26]

2.1.6.1 Radiative electron–hole recombination

Under equilibrium conditions, at a given temperature, the intrinsic carrier concentration n_i is a constant and is defined as the product of the free carriers, electrons (n_o) and holes (p_o), in doped or undoped semiconductor material, as:

$$n_o p_o = n_i^2 \quad (2.21)$$

Using external excitation sources, optical or electrical, excess holes and electrons in semiconductors can be generated. Thus, the total carrier concentration is given by:

$$n = n_o + \Delta n \quad \text{and} \quad p = p_o + \Delta p \quad (2.22)$$

where Δp and Δn are the excess hole and electron concentrations, respectively.

There are different mechanisms of radiative recombination which are, band to band recombination, donor to valence band recombination, conduction band to acceptor recombination, donor to acceptor recombination, and exciton recombination, as illustrated in

Figure 2.10.

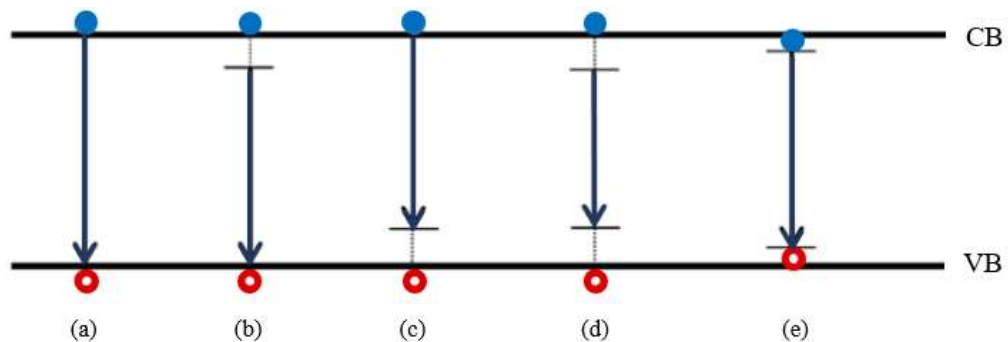


Figure 2.10: Schematic of the radiative recombination processes (a) band-to-band, (b) donor to valence band, (c) conduction band to acceptor, (d) donor to acceptor and (e) excitonic. The solid arrows and dashed lines indicate radiative processes and non-radiative processes, respectively.

In the case of the band to band recombination process, where the electron in the conduction band recombines with a hole in the valence band, the energy of the emitted photon is related to the band gap energy (E_g) by the relation:

$$h\nu = E_g(T) + k_B T/2 \quad (2.23)$$

where $h\nu$ is the photon energy. The rate of the band to band recombination (R) is proportional to the product of electron and hole concentrations, which can be written as:

$$R = -\frac{dn}{dt} = -\frac{dp}{dt} = Bnp \quad (2.24)$$

Where B is the bimolecular recombination coefficient, it typically has values of 10^{-11} – 10^{-9} cm³/s for direct band gap III–V semiconductors [64].

The donor to valence band recombination process occurs when the electron in the donor level recombines with a hole in the valence band, while the acceptor to the conduction band occurs when the electron in the conduction band recombines with hole in the acceptor level. This process can be obviously observed at low temperature [65]. If E_i is the donor or acceptor binding energy, then the photon energy is given by the formula:

$$h\nu = E_g(T) - E_i + k_B T/2 \quad (2.25)$$

When an electron from a donor level recombines with a hole in an acceptor level, the donor-acceptor recombination process can occur if there is a sufficiently high density of both acceptors and donors. The energy of the emitted photon in this process is related to the donor binding energy (E_{do}) and the acceptor binding energy (E_{ac}) by the relation:

$$h\nu = E_g(T) - (E_{do} + E_{ac}) + \frac{e^2}{4\pi\epsilon_0\epsilon_r r} \quad (2.26)$$

where e is electron charge, ϵ_0 is the static dielectric constants of the free space, ϵ_r is relative permeability of the semiconductor material, and r is the acceptor-donor separation. This recombination process is also obviously observed at low temperature [65].

In the exciton recombination process, which is formed due to Coulomb interactions, the emitted photon energy can be written as:

$$h\nu = E_g(T) - E_{exc} \quad (2.27)$$

where E_{exc} is the free binding energy of the e-h pair in the exciton which is typically in the range of only a few meV in narrow gap semiconductors.

2.1.6.2 Non-radiative recombination

In non-radiative recombination, the photon is not generated when the electron-hole pair recombines, but instead of that the electron energy is transferred to vibrational energy of the

lattice atoms, i.e. the energy is transferred to heat (phonons). Therefore, non-radiative recombination is an unwanted process in light emitting devices. Non-radiative recombination processes are usually formed due to defects in the crystal structure, such as dislocations, impurity atoms, and native lattice defects, where energy levels are generated within the forbidden gap of the semiconductor which work as deep traps (known as luminescence killers or recombination centres). In this section, the two most common non-radiative mechanisms - Shockley-Read-Hall (SRH) recombination and Auger recombination - are described.

2.1.6.2.1 Shockley-Read-Hall (SRH) recombination

Shockley-Read-Hall recombination occurs when the electron and hole recombine via deep energy levels within the band gap which are formed due to the defects or impurities in the crystal structure. If the semiconductor is p-type, then holes are in the majority and the minority carrier lifetime (τ_{n_0}) can be written as:

$$\frac{1}{\tau_{n_0}} = N_T u_n \sigma_n \quad (2.28)$$

where σ_n is capture cross section of the electron trap, u_n is the electron thermal velocity and N_T is the trap concentration. Similarly, when electrons are the majority carriers, the minority carrier lifetime τ_{p_0} can be given by:

$$\frac{1}{\tau_{p_0}} = N_T u_p \sigma_p \quad (2.29)$$

where σ_n is capture cross section of the hole traps, u_n is the thermal velocity of hole. When the conditions are close to equilibrium and holes are in majority, the lifetime of the SRH recombination (τ_{SR}) can be determined by assuming $u_n \sigma_n = u_p \sigma_p =$ and $\tau_{n_0} = \tau_{p_0}$:

$$\tau_{SR} = \tau_{n_0} \left(1 + \frac{p_0 + p_1}{p_0 + n_0} \right) \quad (2.30)$$

where p_1 is the hole concentration if the Fermi energy is positioned at the trap level. We can also estimate τ_{SR} when the electrons are the majority carrier. For the particular case of intrinsic material, i.e. $n_0 = p_0 = n_i$, equation (2.30) can be rewritten as:

$$\tau_{\text{SR}} = \tau_{n_0} \left[1 + \cosh \left(\frac{E_T - E_{F_i}}{k_B T} \right) \right] \quad (2.31)$$

Where E_T is the energy level of the trap, and E_{F_i} is the intrinsic Fermi level, which is typically close to the middle of the gap. If $E_T = E_{F_i}$, then the SRH lifetime is minimized ($\tau_{\text{SR}} = 2\tau_{n_0}$), i.e. the traps can act as effective SRH recombination centres when their energy levels are located at or close to the middle of the band gap. Equation (2.31) indicates that the SRH lifetime decreases as temperature increases. Consequently, the efficiency of the radiative band-to-band recombination decreases with increasing temperature [64].

2.1.6.2.2 Auger recombination

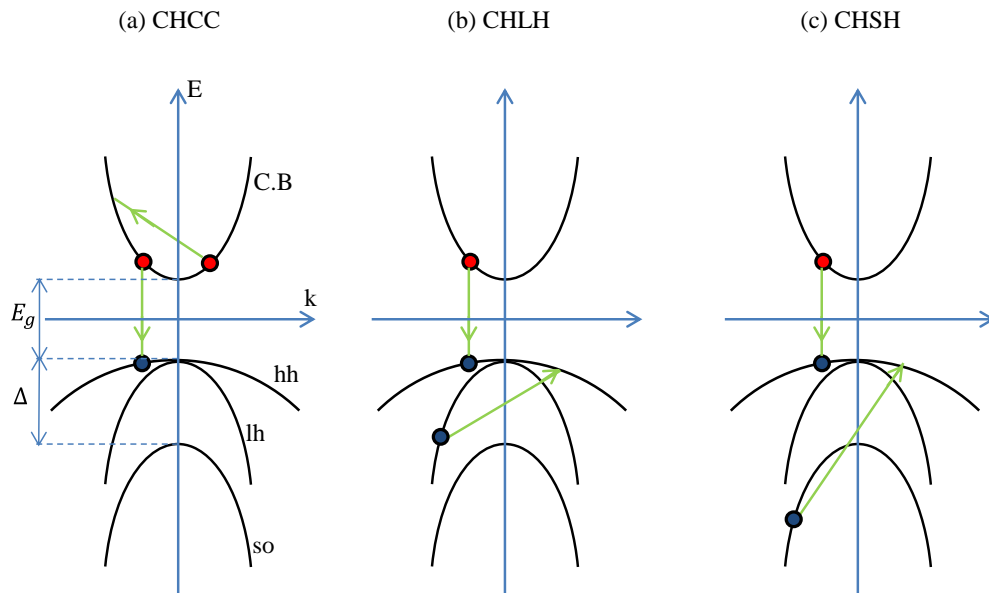


Figure 2.11: Schematic diagram of the three common non-radiative Auger recombination processes (a) CHCC, (b) CHLH, (c) CHSH. [66]

In Auger recombination processes, the energy released by the recombination of an electron and hole is not used to generate a photon but to excite another carrier. Depending upon the excited carriers, there are several mechanisms of Auger recombination. The three most common Auger recombination mechanisms are CHCC, CHSH and CHLH which are shown in the Figure (2.11). The CHCC process involves two electrons, one recombines with a hole and the energy of

recombination excites another electron up in the conduction band, thus it is most dominant in n-type semiconductor materials. In this process the activation energy E_a^{CHCC} is given by: [67]

$$E_a^{\text{CHCC}} = \left(\frac{m_e^*}{m_e^* + m_{hh}^*} \right) E_g \quad (2.32)$$

Where m_e^* and m_{hh}^* are the effective masses of the electron and hole in the heavy hole band, respectively. The CHLH process occurs when an electron recombines with a hole in the heavy hole band and the energy excites a hole from the light hole band to heavy hole band. Whilst in the CHSH process, the recombination of an electron with a heavy hole provides the energy to excite a hole from the split off band to the heavy hole band. The activation energy of the CHSH process is given by:

$$E_a^{\text{CHSH}} = \left(\frac{m_e^*}{m_e^* + 2m_{hh}^* + m_{so}^*} \right) (E_g - \Delta_{so}) \quad (2.33)$$

where Δ_{so} is the spin orbit splitting energy, and m_{so}^* is the holes effective mass in the split off band. If Δ_{so} is close to E_g , the CHSH process is dominant, whilst if Δ_{so} is much greater than the band gap energy E_g , the CHSH process can be negligibly small compared to CHLH transition [66]. It can be determined if CHSH is the dominant process by using the formula:

$$E_a^{\text{CHSH}} = \frac{(E_t - \Delta_{so})/E_t}{m_e^*/m_{so}^*} \quad (2.34)$$

where E_t is the transition energy (electron-hole recombination). If this condition in equation (2.34) is satisfied, then the CHCC process is dominant.

2.2 Light emitting diodes

In this section, the electrical and optical properties of light emitting diodes (LEDs) are described.

2.2.1 Electrical properties

The electrical characteristics of p-n junctions will be summarized, considering an abrupt p-n junction with a donor concentration of N_D and an acceptor concentration of N_A . It can be

assumed that all dopants are fully ionized therefore the free electron concentration is given by $n = N_D$ and the free hole concentration is given by $p = N_A$. It can be also assumed that no compensation of the dopants occurs by unintentional defects and impurities. In case of an unbiased p-n junction and due to the large difference in the carrier concentrations between n-type region and p-type region, electrons move from the n-type side to the p-type side, where the electron-hole recombination occurs. Additionally, a corresponding process occurs with holes that diffuse to the n-type region. Consequently, a region near the p-n junction interface is formed, which is known as a depletion region, W , and is depleted of free carriers.

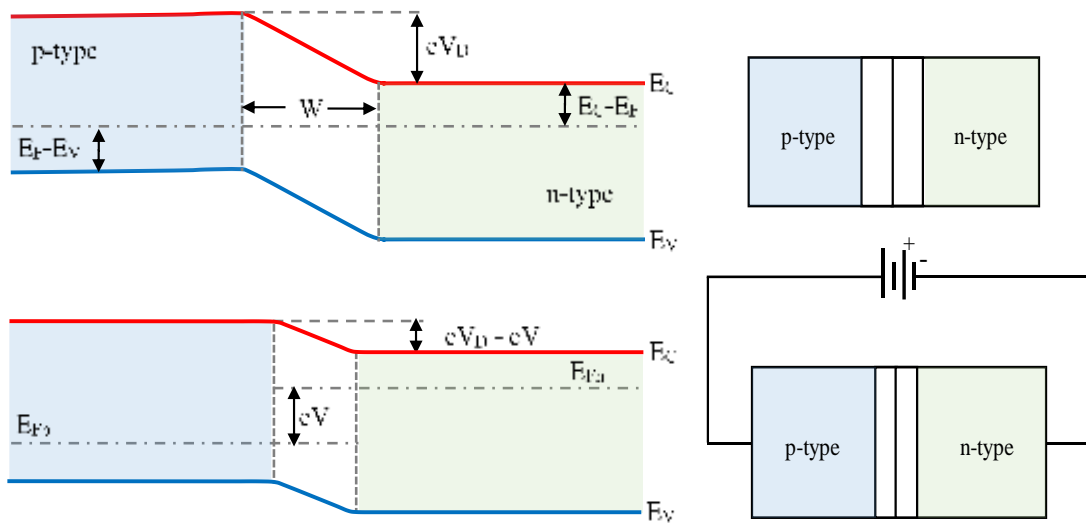


Figure 2.12: p-n junction under (a) zero bias and (b) forward bias. Under forward-bias conditions, minority carriers diffuse into the neutral regions where they recombine. [64]

The dopants, donors in the n-type region and acceptor in p-type region, form a space charge region which produces a potential known as the diffusion voltage. The diffusion voltage V_D , shown in the band diagram of Figure 2.12, can be calculated from the relation: [54]

$$V_D = \frac{k_B T}{e} \ln \frac{N_A N_D}{n_i^2} \quad (2.35)$$

where n_i is the intrinsic carrier concentration of the semiconductor. The diffusion voltage represents the required energy for free carriers to reach the oppositely charged region on the other side moving across the depletion region. The diffusion voltage and the width of depletion region (W_D) are related by the Poisson equation:

$$W_D = \sqrt{\frac{2\varepsilon}{e}(V_D - V) \left(\frac{1}{N_A} + \frac{1}{N_D} \right)} \quad (2.36)$$

where ε is the dielectric permittivity of the semiconductor material, and V is the bias voltage of the diode.

Under forward-bias conditions, an electrical current is applied and electrons and holes are injected in the n-type and p-type, respectively. The carriers move across the depletion region into the oppositely charged regions where they eventually recombine to produce photons. According to the Shockley diode equation (2.37), the electric current increases when the bias voltage increases, due to the exponential term shown in this equation [54]

$$I = eA \left(\sqrt{\frac{D_p}{\tau_p}} \frac{n_i^2}{N_D} + \sqrt{\frac{D_n}{\tau_n}} \frac{n_i^2}{N_A} \right) (e^{eV/kT} - 1) \quad (2.37)$$

where D_n and D_p are the electron and hole diffusion constants, respectively, and τ_n and τ_p are the electron and hole hole minority-carrier lifetimes, respectively, and A is the cross-sectional area. Equation (2.37) can be rewritten as: [54]

$$I = I_s (e^{eV/kT} - 1) \quad (2.38a)$$

$$\text{with } I_s = eA \left(\sqrt{\frac{D_p}{\tau_p}} \frac{n_i^2}{N_D} + \sqrt{\frac{D_n}{\tau_n}} \frac{n_i^2}{N_A} \right) \quad (2.38b)$$

where I_s is the reverse bias saturation current. Under typical forward bias conditions, the diode voltage is $V \gg kT/e$, and therefore $[e^{eV/kT} - 1] \approx e^{eV/kT}$. Based on this condition and from equations (2.35) and (2.37), the Shockley equation can be rewritten as:

$$I = eA \left(\sqrt{\frac{D_p}{\tau_p}} N_A + \sqrt{\frac{D_n}{\tau_n}} N_D \right) e^{e(V-V_D)/kT} \quad (2.39)$$

From equation (2.39) it can be found that when the diode voltage (V) approaches the diffusion voltage (V_D), the current strongly increases. The voltage at which $V_{th} \approx V_D$ is defined as threshold voltage (V_{th}).

Figure 2.12 also shows the separation of the band edges of the conduction band and valence band from the Fermi level. The energy difference between the Fermi level and the conduction band in the n-type region can be investigated from Boltzmann statistics and is determined using the formula [54],

$$E_C - E_F = -kT \ln\left(\frac{n}{N_C}\right) \quad (2.40)$$

and for the p-type region, the energy difference between the valence band and Fermi level can be calculated using the relation:

$$E_F - E_V = -kT \ln\left(\frac{p}{N_V}\right) \quad (2.41)$$

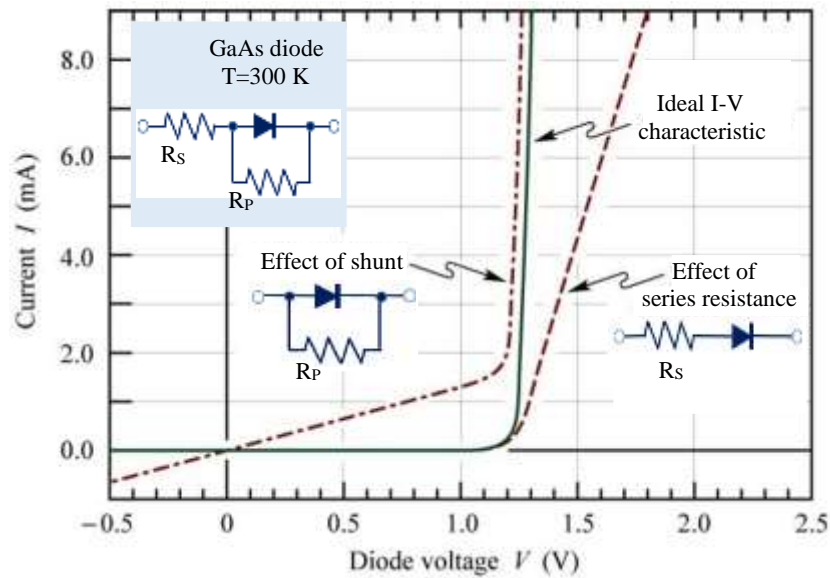


Figure 2.13: Effect of series and parallel (shunt) resistance on I-V characteristic. [54]

Equation (2.38), the Shockley equation, describes the expected theoretical I–V characteristic of the ideal diode. Experimentally, the formula given in Equation (2.42) can be used to describe the measured I-V characteristics: [54]

$$I = I_s e^{eV/(n_{ideal}kT)} \quad (2.42)$$

Assuming that the recombination process happens via band to band (low level injection) or via traps, diode ideality factor (n_{ideal}) has a value of unity ($n_{ideal} = 1.0$) and the ideal diode is dominated by diffusion current transport. The recombination process could also occur via other ways and other areas, giving ideality factor values of a real diode in the range from 1.1 to 2.0. However, ideality factor values as high as $n_{ideal} = 2.0$ are obtained, depending on the semiconductor material and the fabrication process.

Figure 2.13 presents the effect of a series resistance and a parallel resistance on the I-V characteristic of the real diode. These two unwanted resistances are not considered in the current equation of the ideal diode. A series resistance (R_s) can be created due to the excessive contact resistance or the neutral region's resistance. A parallel resistance (R_p) is created when the current bypasses the p-n junction caused by surface imperfections or damaged regions of the p-n junction. Taking into account the effect of these two resistance, the I-V characteristic of the ideal diode (Shockley equation) is modified, and thus the equation (2.42) can be rewritten as [54]:

$$I - \frac{(V - IR_s)}{R_p} = I_s e^{(V - IR_s)/(n_{ideal}/kT)} \quad (2.43)$$

when $R_p \rightarrow \infty$ and $R_s \rightarrow 0$, equation (2.43) reduces to the Shockley equation of the ideal diode.

2.2.2 Optical properties

2.2.2.1 Efficiency

In the ideal LED, the active region emits one photon for every electron and thus the LED has an internal quantum efficiency of unity. However, not all electron-hole recombinations produce photons and not all generated photons are emitted from the LED into free space. The reason that some photons cannot escape from the LED is attributed partly to reabsorption within the device or by the metallic contact surface. Therefore the internal and extraction efficiency of the real LED are not the same. The internal efficiency η_{int} of the LED can be determined using the relation: [54]

$$\eta_{int} = \frac{n_{ph(in)}}{n_{e(inj)}} = \frac{P_{int}/(h\nu)}{I/e} \quad (2.44)$$

where $n_{ph(in)}$ is the number of photons emitted from active region per second, $n_{e(inj)}$ is the number of electrons injected into LED per second, P_{int} is the optical power emitted from the active region, and I is the injection current. The light extraction efficiency $\eta_{extraction}$ is defined as [54]:

$$\eta_{\text{extraction}} = \frac{n_{\text{ph(ex)}}}{n_{\text{ph(in)}}} = \frac{P/(h\nu)}{P_{\text{int}}/(h\nu)} \quad (2.45)$$

where $n_{\text{ph(ex)}}$ is the number of photons emitted into free space per second, and P is the optical power emitted into free space. The extraction efficiency is also limited by total internal reflection which decreases the ability of the generated photons to escape into free space, where the photons emit in different angles. The external quantum efficiency (η_{ext}) gives the ratio of the number of emitted photons into free space to the number of injected electrons into LED, which can be calculated from the equation: [54]

$$\eta_{\text{ext}} = \frac{n_{\text{ph(ex)}}}{n_{\text{e(inj)}}} = \frac{P/(h\nu)}{I/e} \quad (2.46a)$$

$$\eta_{\text{ext}} = \eta_{\text{int}} \eta_{\text{extraction}} \quad (2.46b)$$

The power efficiency η_{power} , which is also called wallplug efficiency, is given by:

$$\eta_{\text{power}} = \frac{P}{IV} \quad (2.47)$$

where IV is the electrical power supplied to the LED.

2.2.2.2 Emission spectrum

The mechanism of the light emission in LEDs is electron–hole spontaneous recombination and simultaneous emission of photons, while in lasers and super-luminescent LED, the devices emit light by stimulated emission. The optical properties of LEDs are determined by the spontaneous recombination process. Assuming that the electrons in conduction band and holes in the valence band have a parabolic dispersion relation (see the schematic electron-hole recombination process shown in Figure 2.14), then: [54]

$$E = E_C + \frac{\hbar^2 k^2}{2m_e^*} \quad (2.48a)$$

$$E = E_V - \frac{\hbar^2 k^2}{2m_h^*} \quad (2.48b)$$

where \hbar is Planck's constant divided by 2π , and k is the carrier wave number.

The emission intensity of the bulk LEDs as a function of energy can be defined as:

$$I(E) \propto \sqrt{E - E_g} e^{-E/(k_B T)} \quad (2.49)$$

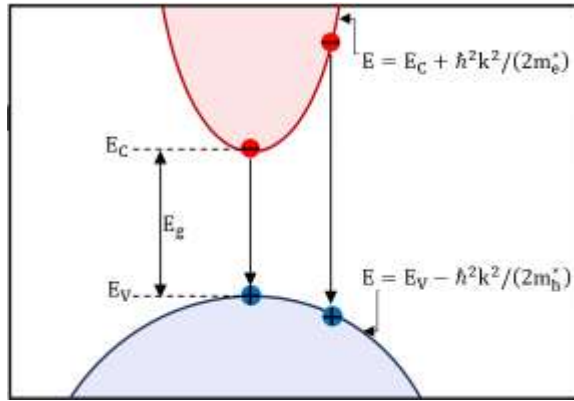


Figure 2.14: Parabolic dispersion relations of electrons and holes, showing electron-hole recombination and the resulting photon emission. [54]

From equation (2.49) the lineshape of the LED emission is illustrated in Figure 2.15, where the maximum intensity occurs at $E = E_g + k_B T / 2$.

The full-width at half-maximum (the spectral linewidth $\Delta\lambda$) of the LED emission is given by:

$$\Delta E = 1.8k_B T \quad \text{or} \quad \Delta\lambda = \frac{1.8k_B T \lambda^2}{hc} \quad (2.50)$$

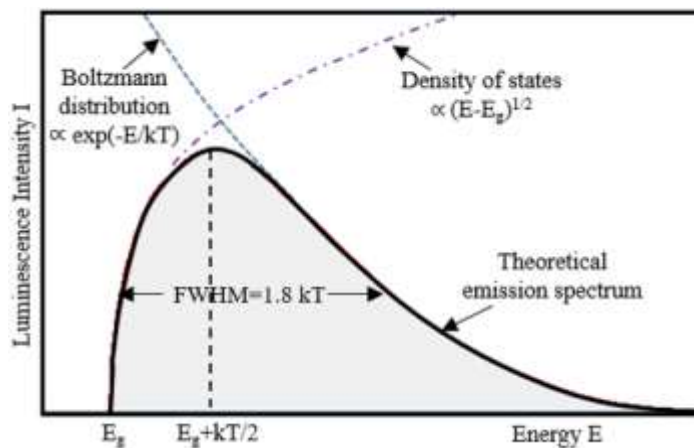


Figure 2.15: Theoretical emission spectrum of an LED. [54]

2.3 Resonant cavity light emitting diodes (RCLEDs)

2.3.2 Spontaneous emission

The transitions of electrons from an initial quantum state to a final quantum state (radiative transition) followed by the simultaneous emission of a light quanta, are one of the most

fundamental processes in optoelectronic devices. The emission of a photon can occur via two physical processes, known by spontaneous and stimulated emission. These two processes were first investigated by Einstein in 1917. Stimulated emission is employed in super-luminescent LEDs and semiconductor lasers [68,69]. The first experimental realisation was in the 1960s where the stimulated emission mode was used in semiconductors to drastically change their radiative emission characteristics. In spontaneous emission the recombination process occurs spontaneously, that is without a means to affect this process. In fact, spontaneous emission has long been believed to be uncontrollable. However, the studies in microscopic optical resonators, where optical modes are confined to the order of the light wavelength, exhibited the possibility of controlling the physical properties of the spontaneous emission of a light-emitting material. The changes of the spontaneous emission properties include the emission pattern, spontaneous emission rate, and spectral purity. These changes can be used to achieve brighter, faster, and more efficient optoelectronic semiconductor devices.

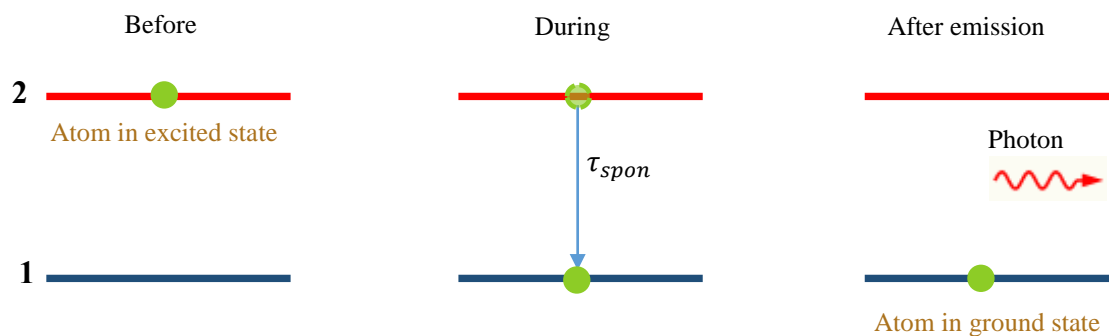


Figure 2.16: Schematic illustration of a spontaneous emission process.

Figure 2.16 shows the spontaneous emission process, where the number of light sources in the excited energy level at time t is given by $N(t)$, the rate at which N decays is: [70]

$$\frac{\partial N(t)}{\partial t} = -A_{21}N(t) \quad (2.52)$$

$$N(t) = N(0)e^{-A_{21}t} = N(0)e^{-\Gamma_{\text{spont}}t} \quad (2.53)$$

where $N(0)$ is the initial number of light sources in the excited energy level. The rate of the spontaneous emission (A_{21}) is inversely proportional to the lifetime τ_{spont} by the relation:

$$A_{21} = \Gamma_{\text{spon}} = \frac{1}{\tau_{\text{spon}}} \quad (2.54)$$

The spontaneous emission rate (Γ_{spon}) depends on two factors, the first is the atomic part which describes the matrix elements of the initial and final electron state, while the second is the field part which describes the density of electromagnetic modes of the medium.

2.3.2 Fabry-Perot resonator

The simplest design of optical cavity consists of two coplanar mirrors separated by a distance L_{cav} . The first optical cavities with coplanar reflectors were investigated by Fabry and Perot in 1899, having a large separation between the two reflectors ($L_{\text{cav}} \gg \lambda$). However, new physical phenomena occur when the distance between the two reflectors is of the order of the emission wavelength, including the enhancement in the emission of the active region (material) which is located inside the cavity. These resonators which have very small cavities are known as microcavities. In general, the structure of coplanar microcavities are simpler than that of optical microcavities.

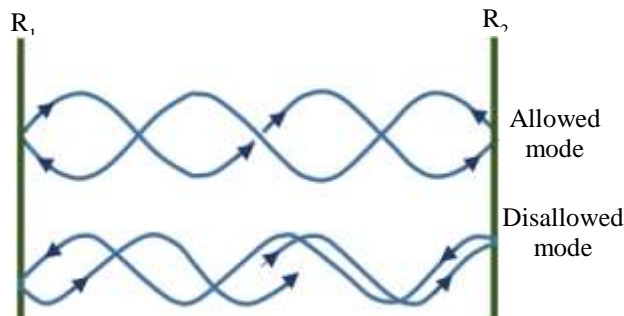


Figure 2.17: Schematic of a Fabry-Perot cavity consisting of two reflectors. Allowed mode and disallowed mode is also illustrated. [54]

Figure 2.17 presents a Fabry-Perot cavity which consists of two reflectors with reflectivities R_1 and R_2 . Stable (allowed) optical modes and attenuated (disallowed) optical modes are formed when the plane waves propagating inside the cavity interfere constructively and destructively, respectively. For non-absorbing reflectors, the transmittance through the two reflectors can be determined by $T_1 = 1 - R_1$ and $T_2 = 1 - R_2$. Considering the multiple

reflections within the cavity, the transmittance through the cavity can be written in terms of a geometric series. The transmittance of the Fabry-Perot cavity is then given by the formula: [54]

$$T = \frac{T_1 T_2}{1 + R_1 R_2 - 2\sqrt{R_1 R_2} \cos(2\Phi)} \quad (2.55)$$

where Φ is the phase change of the optical wave for a single pass between the two reflectors which is given by:

$$\Phi = 2\pi \frac{\bar{n}L_{\text{cav}}}{\lambda} = 2\pi \frac{\bar{n}L_{\text{cav}}\nu}{c} \quad (2.56)$$

where \bar{n} is the refractive index of the cavity materials, L_{cav} is the cavity thickness, λ is the wavelength of light in vacuum, ν is the frequency of light, and c is the speed of light in vacuum. The maximum value of the transmittance takes place if the condition of constructive interference is fulfilled, which means that $2\Phi = 0, 2\pi, \dots$ ($2\Phi = 2m\pi$, with m a positive integer).

The cavity finesse (F) is defined to be the ratio of the transmittance peak separation (λ_{FSR}) to the transmittance full-width at half-maximum ($\Delta\lambda$), which is written as: [54]

$$F = \frac{\text{peak separation}}{\text{peak width}} = \frac{\lambda_{\text{FSR}}}{\Delta\lambda} = \frac{\pi^4 \sqrt{R_1 R_2}}{1 - \sqrt{R_1 R_2}} \quad (2.57)$$

It is often that the cavity quality factor (Q) is used rather than the cavity finesse. The quality factor (Q) is defined as the ratio of the transmittance peak frequency (ν_{peak}) to the peak width ($\Delta\nu$). Using this definition and equation (2.57), one obtains [54]

$$Q = \frac{\text{peak frequency}}{\text{peak width}} = \frac{\nu_{\text{peak}}}{\Delta\nu} = \frac{2\bar{n}L_{\text{cav}}}{\lambda_0} \frac{\pi^4 \sqrt{R_1 R_2}}{1 - \sqrt{R_1 R_2}} \quad (2.58)$$

In addition, the cavity finesse and the cavity number (m_c) are related to the internal angle (on axis lobe), θ_{FWHM} , and internal solid angle ($\Delta\Omega$) by the formulas [71]:

$$\theta_{\text{FWHM}} = \sqrt{1/Fm_c} \quad (2.59)$$

$$\Delta\Omega = \pi/Fm_c \quad (2.60)$$

2.3.3 Optical mode density in a one-dimensional resonator

In this section and based on the changes of optical mode density in a one-dimensional (1D) resonator (coplanar Fabry-Perot microcavity), the theory of the enhancement of spontaneous

emission will be presented. We initially demonstrate the basic physics resulting in the changes of the spontaneous emission of the active region (material) placed inside a microcavity and present analytical relations for the spectral intensity and integrated emission enhancement. The rate of spontaneous radiative transition in an active homogeneous region is defined by: [70]

$$W_{\text{spont}} = \tau_{\text{spont}}^{-1} = \int_0^\infty W_{\text{spont}}^{(l)} \rho(v_l) dv_l \quad (2.61)$$

where $W_{\text{spont}}^{(l)}$ is identified as the rate of spontaneous transition into the optical mode l , and $\rho(v_l)$ is the optical mode density. The lifetime of spontaneous emission (τ_{spont}) is the inverse of the spontaneous emission rate, assuming that the optical medium is homogeneous. In the case of a cavity structure, where the density of the optical mode depends on the spatial direction, the emission rate which is given in equation (2.61) depends on the direction.

The rate of the spontaneous emission $W_{\text{spont}}^{(l)}$ is not changed by locating the active region inside the cavity. This is because the emission rate into the optical mode, l , contains the dipole matrix element of the two electronic states involved in the transition [70]. However, the optical mode density, $\rho(v_l)$, can be strongly modified by the presence of the cavity.

In the case of a 1D homogeneous medium, the density of optical modes per unit length per unit frequency ($\rho^{1D}(v)$) is defined as:

$$\rho^{1D}(v) = \frac{2\bar{n}}{c} \quad (2.62)$$

Using a similar formalism commonly used to derive the density of the optical mode in free space, Equation (2.62) can be derived. The optical mode density of a 1D planar microcavity and of homogeneous 1D free space is illustrated in [Figure 2.18](#).

In planar microcavities, the optical cavity modes are discrete and the frequencies of these modes are integer multiples of the frequency of the fundamental optical mode. The fundamental mode and first excited mode are positioned at frequencies v_o and $2v_o$, respectively. A cavity with two metallic reflectors (typically the reflector is made from a thin-layer of gold material), and a π phase shift of the optical wave upon reflection, the fundamental frequency is defined by $v_o = c/(2\bar{n}L_{\text{cav}})$.

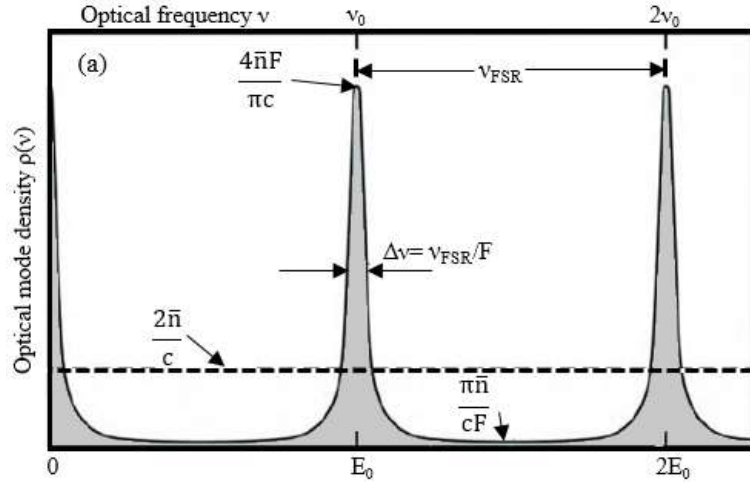


Figure 2.18: A one-dimensional optical mode density of a planar microcavity (solid line). [54]

For a resonant microcavity, the emission frequency of an active region placed inside the cavity equals the frequency of one of the optical cavity modes. The density of optical cavity modes along the axis of the cavity can be derived using the relation between the optical mode density in the cavity and the optical transmittance of the cavity ($T(\nu)$):

$$\rho(\nu) = K_d T(\nu) \quad (2.63)$$

where K_d is a constant. The value of this constant can be calculated by a normalization condition (single optical mode). From equation (2.55) and (2.56), the cavity transmittance has a maximum value at the frequencies $\nu = 0, \nu_0, 2\nu_0 \dots$, and a minimum value at frequencies $\nu = \nu_0/2, 3\nu_0/2, 5\nu_0/2 \dots$. By expanding the cosine term in equation (2.56) using $[\cos(x) = 1 - (x^2/2)]$, the Lorentzian approximation of a transmittance at $\nu = 0$ is obtained. Thus, $T(\nu)$ can be written as:

$$T(\nu) = \frac{T_1 T_2 (\sqrt{R_1 R_2})^{-1} (4\pi\bar{n}L_{\text{cav}}\nu/c)^{-2}}{\frac{(1-\sqrt{R_1 R_2})^2}{(\sqrt{R_1 R_2})^{-1} (4\pi\bar{n}L_{\text{cav}}\nu/c)^2} + \nu^2} \quad (2.64)$$

Integrating $\rho(\nu)$ over all frequencies and the cavity length yields a single optical mode, i.e.

$$K_d \int_0^{L_{\text{cav}}} \int_{-\infty}^{\infty} \rho(\nu) d\nu dL = 1 \quad (2.65)$$

From Equations (2.63) and (2.64), and using the integration formula $\int_{-\infty}^{\infty} (a^2 + x^2)^{-1} dx = \pi/a$, the constant K_d can be calculated from the relation:

$$K_d = \frac{(R_1 R_2)^{3/4} 4\bar{n}}{T_1 T_2 c} 1 - \sqrt{R_1 R_2} \quad (2.66)$$

By substituting equations (2.66) in equation (2.63), the density of optical cavity modes of a one-dimensional cavity for emission along the cavity axis can be rewritten as:

$$\rho(\nu) = \frac{(R_1 R_2)^{3/4} 4\bar{n}}{T_1 T_2 c} 1 - \sqrt{R_1 R_2} T(\nu) \quad (2.67)$$

The maximum and minimum values of the optical mode density can be calculated using equation (2.67). At the maxima, the mode density is defined as:

$$\rho_{\max} = \frac{(R_1 R_2)^{3/4} 4\bar{n}}{1 - \sqrt{R_1 R_2} c} \quad (2.68)$$

Using $(R_1 R_2)^{3/4} \approx 1$ and the expression derived for the cavity finesse (F), it can be obtained an approximate expression for the density of the optical cavity modes at the maximum value

$$\rho_{\max} \approx \frac{4\bar{n}F}{\pi c} \quad (2.69)$$

At the minima, the density of optical modes is defined as:

$$\rho_{\min} = \frac{(R_1 R_2)^{3/4} (1 - \sqrt{R_1 R_2}) 4\bar{n}}{(1 + \sqrt{R_1 R_2})^2 c} \quad (2.70)$$

Using $(R_1 R_2)^{3/4} \approx 1$ and the expression derived for the cavity finesse (F), it can be obtained an approximate expression for the density of the optical cavity modes at the minimum value

$$\rho_{\min} \approx \pi \frac{\bar{n}}{cF} \quad (2.71)$$

2.3.4 Spectral emission enhancement

The emission rate enhancement spectrum is defined by the ratio of the 1D optical mode density to the 1D free space mode density because the emission rate at a given wavelength is directly proportional to the density of optical cavity modes. As mentioned earlier, the lineshape of the cavity enhancement spectrum is a Lorentzian, therefore the enhancement factor at the resonance wavelength can be defined by the ratio of the optical mode densities with and without a cavity [54], i.e.

$$G_e = \frac{\rho_{\max}}{\rho^{1D}} \approx \frac{2}{\pi} F \approx \frac{2}{\pi} \frac{\pi (R_1 R_2)^{1/4}}{1 - \sqrt{R_1 R_2}} \quad (2.72)$$

Equation (2.72) represents the average emission rate enhancement out of the two reflectors. Thus, and in order to calculate the enhancement for a single direction, the enhancement factor given in equation (2.72) must be multiplied by the fraction of the transmitted light leaving the mirror with reflectivity R_1 , i.e. $1 - R_1$, divided by the average loss of the both reflectors for one round trip inside the cavity, i.e. $(1/2)[(1 - R_1) + (1 - R_2)]$. For large R_1 and R_2 , the spectral intensity enhancement factor can be rewritten as:

$$G_e = \frac{2(1-R_1)}{2-R_1-R_2} \frac{2F}{\pi} \approx \frac{(1-R_1)}{1-\sqrt{R_1R_2}} \frac{2F}{\pi} \approx \frac{2}{\pi} \frac{\pi(R_1R_2)^{1/4}(1-R_1)}{(1-\sqrt{R_1R_2})^2} \quad (2.73)$$

where the approximation $1 - \sqrt{R_1R_2} \approx (1/2)(2 - R_1 - R_2)$ is used in equation (2.73).

The standing wave effect must be also considered, i.e. the active region relative to the nodes and antinodes of the distribution of the electromagnetic field (the optical wave) inside the cavity. If the active region is positioned exactly at the antinode, then the antinode enhancement factor (ξ) has a value of 2. The value of ξ is zero if the active region is positioned at the node. Therefore, the spectral intensity enhancement factor is given by

$$G_e = \frac{\xi}{2} \frac{2}{\pi} \frac{\pi(R_1R_2)^{1/4}(1-R_1)}{(1-\sqrt{R_1R_2})^2} \frac{\tau_{cav}}{\tau} \quad (2.74)$$

where R_1 is the reflectivity of the light exiting the mirror and thus $R_1 < R_2$. In addition, equation (2.74) considers the changes in the lifetime of the spontaneous emission (τ), the lifetime without cavity, and the lifetime with cavity τ_{cav} . If the value of the cavity lifetime is larger than that of the lifetime without cavity, then the enhancement factor increases due to the factor τ_{cav}/τ .

2.3.5 Integrated emission enhancement

The total enhancement factor obtained by integrating over the wavelength spectrum, instead of the emission enhancement at the resonance wavelength, is relevant for many practical devices. On resonance, the emission is enhanced along the axis of the cavity, while at wavelengths sufficiently far off resonance, the emission is suppressed. Because the emission spectrum of the active region without a cavity is typically much broader than the resonant cavity, it is not

obvious whether the integrated emission is enhanced at all. In order to calculate the integrated emission enhancement, the spectral linewidth of the resonant cavity and the spectral linewidth of the emission spectrum of the active region must be taken in to account. The resonance spectral linewidth can be determined from the cavity finesse or the cavity quality factor. By assuming a Gaussian natural emission spectrum, the integrated emission enhancement ratio can be calculated analytically. For semiconductors at 300 K, in the case of high-quality cavities, the linewidth of the natural emission spectrum of the active region ($\Delta\lambda_n$) is larger than the linewidth of the resonant cavity ($\Delta\lambda_{cav}$). The linewidth of a Gaussian emission spectrum can be defined as $\Delta\lambda_n = 2\sigma(2\ln 2)^{1/2}$. In addition, the Gaussian emission spectrum has a peak value of $(\sigma(2\pi)^{1/2})^{-1}$, where σ is the standard deviation of the Gaussian function, then the integrated emission enhancement factor can be given by [72]:

$$G_{int} = \frac{\pi}{2} G_e \Delta\lambda \frac{1}{\sigma\sqrt{2\pi}} = G_e \sqrt{\pi \ln 2} \frac{\Delta\lambda_{cav}}{\Delta\lambda_n} \quad (2.75)$$

2.3.6 Distributed Bragg Reflector (DBR)

A distributed Bragg reflector (DBR) is a multi-layer reflector consisting of typically 5–50 pairs of two materials. Because the refractive indices of these two materials are different, Fresnel reflection occurs at each of the interfaces. The magnitude of the Fresnel reflection is very small owing to the small difference between the refractive index of the two materials. However, DBRs consist of many interfaces stacked next to each other. It is important to determine the thickness of the two materials of the DBR in such a way that the reflected waves are in constructive interference. For normal incidence, this condition can be achieved when both materials have a thickness of a quarter wavelength of the light [54], i.e.

$$d_L = \lambda_L/4 = \lambda_0/4n_L \quad (2.76a)$$

$$d_H = \lambda_H/4 = \lambda_0/4n_H \quad (2.76b)$$

where λ_0 is the vacuum Bragg wavelength of the light, d_L and d_H are the thicknesses of the materials with low-index (n_L) and of the material with high-index (n_H). For an oblique angle

of incidence, $\theta_{L,H}$, the optimum thicknesses for high reflectivity can be calculated from the relations:

$$d_L = \lambda_L / (4 \cos \theta_L) = \lambda_0 / (4n_L \cos \theta_L) \quad (2.77a)$$

$$d_H = \lambda_H / (4 \cos \theta_H) = \lambda_0 / (4n_H \cos \theta_H) \quad (2.77b)$$

The DBR stop band depends on the difference in refractive index of the two constituent materials, $n_H - n_L = \Delta n$. The spectral width of the stop band is given by [73]:

$$\Delta\lambda_{\text{stopband}} = \frac{2\lambda_0\Delta n}{2\left(\frac{1}{n_L} + \frac{1}{n_H}\right)^{-1}} \quad (2.78)$$

The reflectance of the DBR can be calculated using a transfer matrix method [74] which is a standard technique used to analyse light propagation in the material layers, based on the continuity of the electric field across the interfaces between different materials. The propagation of light of a given wavelength (λ) through a single layer of thickness (d) can be written in a matrix form, which represents the electric field exiting the layer as a function of the incident one:

$$MM = \begin{bmatrix} \cos \beta_j & -\frac{i}{p_j} \sin \beta_j \\ -ip_j \sin \beta_j & \cos \beta_j \end{bmatrix} \quad (2.79)$$

where

$$\beta_j = \frac{2\pi}{\lambda_0} n_j d_j \cos \theta_j, \quad p_j = n_j \cos \theta_j \quad (2.80)$$

$$j = L, H$$

For normal incidence $\theta_j = 0$, then

$$\beta_j = \frac{2\pi}{\lambda_0} n_j d_j, \quad p_j = n_j \quad (2.81)$$

A multilayer usually consist of a succession of homogeneous layers of alternately low and high refractive indices n_L and n_H and of thickness d_L and d_H , placed between two homogenous media with refractive indices n_1 and n_l as illustrated in [Figure 2.19](#). Assuming that the media is non-magnetic, the propagation through a layer stack is defined by the product of the individual layer matrices:

$$M = \prod_{j=1}^{2N} MM_j = \begin{bmatrix} m_{11} & m_{12} \\ m_{21} & m_{22} \end{bmatrix} \quad (2.82)$$

$$m_{11} = \left(\cos \beta_L \cos \beta_H - \frac{p_H}{p_L} \sin \beta_L \sin \beta_H \right) U_{2N-1}(a) - U_{2N-2}(a)$$

$$m_{12} = -i \left(\frac{1}{p_H} \cos \beta_L \sin \beta_H - \frac{1}{p_L} \sin \beta_L \cos \beta_H \right) U_{2N-1}(a)$$

$$m_{21} = -i(p_L \sin \beta_L \cos \beta_H + p_H \cos \beta_L \sin \beta_H) U_{2N-1}(a)$$

$$m_{22} = \left(\cos \beta_L \cos \beta_H - \frac{p_L}{p_H} \sin \beta_L \sin \beta_H \right) U_{2N-1}(a) - U_{2N-2}(a)$$

where $U_{2N}(a)$ are the Chebyshev polynomials of the second kind, which is defined as:

$$U_{2N}(a) = \frac{\sin[(2N+1) \cos^{-1} a]}{\sqrt{1-x^2}} \quad (2.83)$$

$$a = \frac{1}{2}(m_{11} + m_{22}) = \cos \beta_L \cos \beta_H - \frac{1}{2} \left(\frac{p_L}{p_H} + \frac{p_H}{p_L} \right) \sin \beta_L \sin \beta_H$$

The reflection coefficient of the DBR is then given by the formula:

$$r = \frac{(m_{11} + m_{12} p_1) p_1 - (m_{21} + m_{22} p_1)}{(m_{11} + m_{12} p_1) p_1 + (m_{21} + m_{22} p_1)} \quad (2.84)$$

In terms of r , the reflectivity is

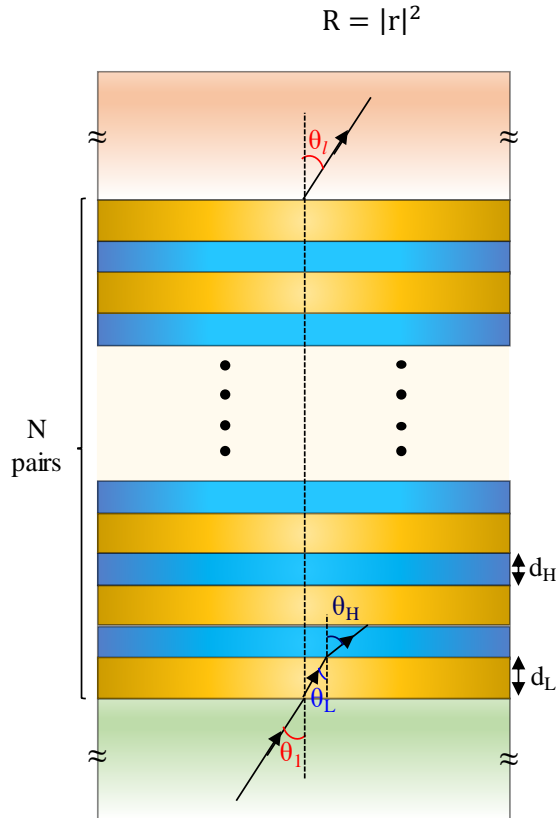


Figure 2.19 Schematic of a distributed Bragg reflector (DBR) consisting of a periodic multilayer.

2.3.7 RCLED design rules

The basic structure of an RCLED consists of a microcavity sandwiched between two DBR mirrors with reflectivity R_1 and R_2 , as shown in Figure 2.20. The two mirrors are designed so that their reflectivities are unequal, therefore the light exits the cavity through only one of the mirrors which is called the light-exit mirror (designated here with reflectivity R_1). An active region is placed inside the cavity between the mirrors, preferably at the antinode position of the standing optical wave of the cavity.

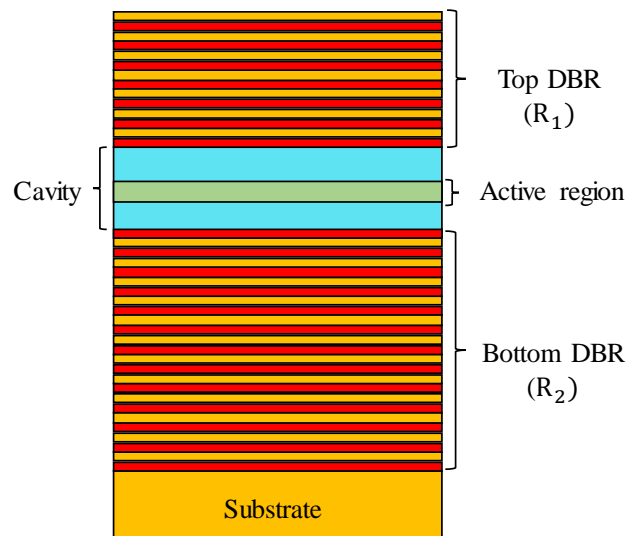


Figure 2.20: Schematic illustration of a resonant cavity structure consisting of two DBR mirrors with reflectivity R_1 and R_2 .

There are several design rules that can be used to maximize the spontaneous emission enhancement in resonant-cavity structures [75,76]. These rules will provide further insight into the fundamental operating principles of RCLEDs and the differences of these devices with respect to VCSELs.

The first criteria for the design of RCLEDs is that the reflectivity of the light-exit mirror (R_1), should be much lower than that of the back mirror, i.e.

$$R_1 \ll R_2 \quad (2.85)$$

This condition ensures that light exits the device mainly through the reflector with reflectivity R_1 .

The second criteria for the design of RCLEDs requires that the cavity length L_{cav} is reduced to a minimum. To derive this criterion, the integrated emission enhancement, discussed in the previous section, can be rewritten using the expressions for the cavity finesse (F) and cavity quality factor (Q). One obtains

$$G_{int} = \frac{\xi}{2} \frac{2}{\pi} \frac{(1-R_1)}{1-\sqrt{R_1 R_2}} \sqrt{\pi \ln 2} \frac{\lambda_0}{\Delta \lambda_n} \frac{\lambda_{cav}}{L_{cav}} \frac{\tau_{cav}}{\tau} \quad (2.86)$$

where λ_0 and λ_{cav} are the active region emission wavelengths in vacuum and inside the cavity, respectively. Since the emission wavelength (λ_0) and the natural linewidth of the active region ($\Delta \lambda_n$) are given quantities, equation (2.86) shows that the integrated emission maximizes when the cavity length (L_{cav}) is reduced to a minimum.

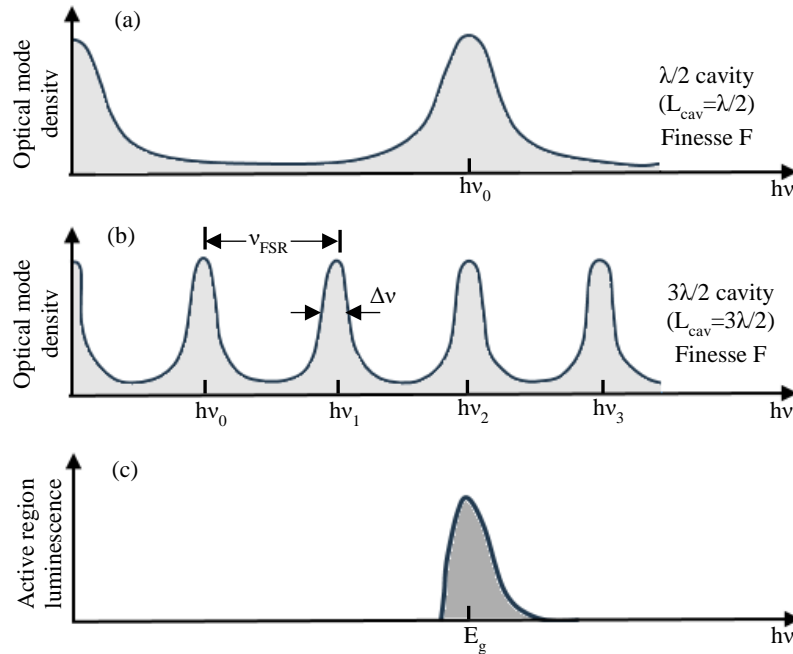


Figure 2.21: Density of optical cavity modes for (a) short cavity and (b) long cavity with same cavity finesse (F). (c) Spontaneous emission spectrum (natural emission) of the active region. [54]

The reason for the importance of a short cavity length is illustrated by Figure 2.21. The optical mode densities of a short and a long cavity, are shown in Figures 2.21(a) and 2.21(b), respectively. Both cavities have the same mirror reflectivities and cavity finesse. The spontaneous emission spectrum of the active region is shown in Figure 2.21 (c). The best overlap between the emission of the active region and the resonant optical mode is observed for the shortest cavity length.

The maximum enhancements can be achieved with the shortest cavities, which are obtained when the fundamental cavity mode is in resonance with the emission spectrum of the active region. In addition, using a high contrast refractive index DBR layers leads to reduce the cavity length.

The third criteria for the design of an RCLED cavity is the requirement for the minimization of self-absorption in the active region. This criterion can be stated as follows: the probability for photons emitted from the active region into the cavity mode to be reabsorbed should be much smaller than the probability of photons to escape through one of the reflectors. Assuming $R_2 \approx 1$, this criterion can be defined as

$$2\xi\alpha L_{\text{active}} < (1 - R_1) \quad (2.87)$$

where α and L_{active} are the absorption coefficient and the thickness of the active region, respectively. In the case where the criterion of equation (2.87) is not fulfilled, photons would probably be reabsorbed by the active region. Subsequently, re-emission will, with a certain probability, occur along the lateral direction (waveguide modes), i.e. not into the cavity mode. A second possibility is that the electron–hole pairs generated by reabsorption may recombine non-radiatively. In either case, reabsorption processes occurring in high-finesse cavities can reduce the emission of the cavity mode out of the cavity. Therefore, when the condition of equation (2.87) is not fulfilled, the emission intensity of resonant cavities is reduced rather than enhanced.

Chapter 3

Literature review

3.1 Introduction

In this chapter, the review of different types of electrically pumped light emitting devices such as light emitting diodes (LEDs), interband cascade light emitting diodes (ICLEDs), resonant cavity light emitting diodes (RCLEDs) and vertical cavity surface emitting lasers (VCSELs) in the mid-infrared range will be presented.

3.2 Mid infrared light emitting diodes (MIR LEDs)

Various Mid-infrared LED structures have been investigated for gas monitoring such as, methane (CH_4) at 3.3 μm [2,3,77,78-80], propane (C_3H_8) at 3.4 μm [81], hydrogen sulphide (H_2S) at 3.7 μm [24,77], sulphur dioxide (SO_2) at 3.9 μm [82], carbon dioxide (CO_2) at 4.2 μm [2,78,4-14], (N_2O) at 4.5 μm , carbon monoxide (CO) at 4.6 μm [2,9,11,15,16], and nitric oxide (NO) at 5.3 μm [21,78,83].

3.2.1 Bulk MIR LEDs

In 1966, the first bulk LED was investigated by Melangailis et al. [84]. The device structure included bulk InAs used as an emitter material, producing emission around 3.7 μm at room temperature. Similarly, Dobbelaere et al. (1993) demonstrated the electroluminescence of bulk InAsSb (Sb=15%) LEDs grown on GaAs substrate using Molecular beam epitaxy (MBE) [85].

The emission spectra exhibited a dip at 4.25 μm corresponding to the CO_2 absorption in the atmosphere (see Figure 3.1(a)). In 1998, Popov et. al. [10] investigated and studied the characteristics of the bulk InAsSbP/InAsSb/InAsSbP heterostructure LEDs grown on InAs substrate using liquid phase epitaxy (LPE). The room temperature electroluminescence spectrum of the LED emission exhibited a peak wavelength of 4.3 μm and a broadband linewidth of 800 nm (see Figure 3.1(b)). An optical power of 850 μW was measured under pulsed operation (1.2 A, 1 kHz in 5 μs).

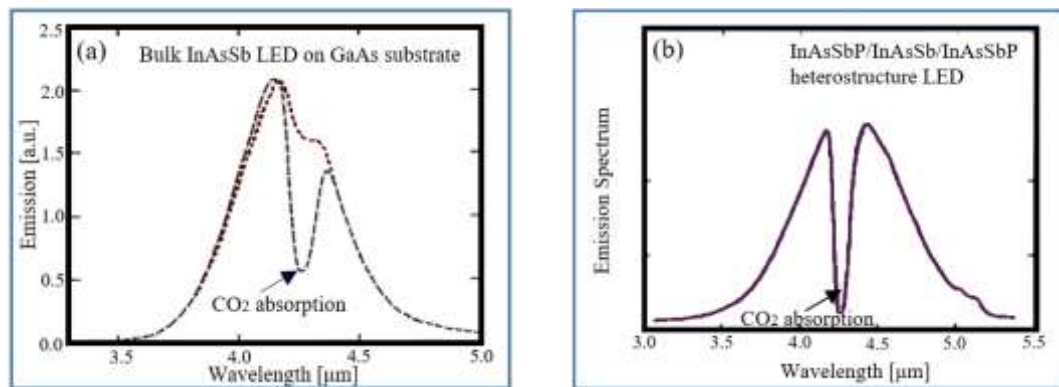


Figure 3.1: (a) Demonstration of the application of an InAsSb light emitting diode as a CO_2 sensor [85]. The emission spectrum of the LED contained a single emission band with a peak at 4.3 μm at room temperature [10].

One year later, InAsSbP/InAsSb (Sb =11% in InAsSb layer) double heterostructure LEDs grown on InAs substrate were also reported by H. Gao et. al. [9]. At room temperature, the linewidth of the emission spectrum was measured to be 507 nm with a peak wavelength of 4.6 μm (see Figure 3.2(a)). The device exhibited room-temperature output power of 50 μW under pulsed operation (1 A, 1% duty cycle at 1 kHz). Using rare-earth ion gettering, the active region (InAsSb layer) was purified, leading to improved performance of the device [16]. Based on that, an output power of about 1 mW under pulsed operation (2 A, 1 kHz in 2 μs) was achieved. Temperature dependence of the electroluminescence spectra from bulk InAsSb (Sb=9%) LED grown on GaSb substrate using LPE were presented by Krier et al. (2007) [19]. Broadband room temperature emission spectra were observed with a dip at 4.25 μm corresponding to the CO_2 absorption, suggesting using this device for CO_2 gas sensing (see Figure 3.2(b)).

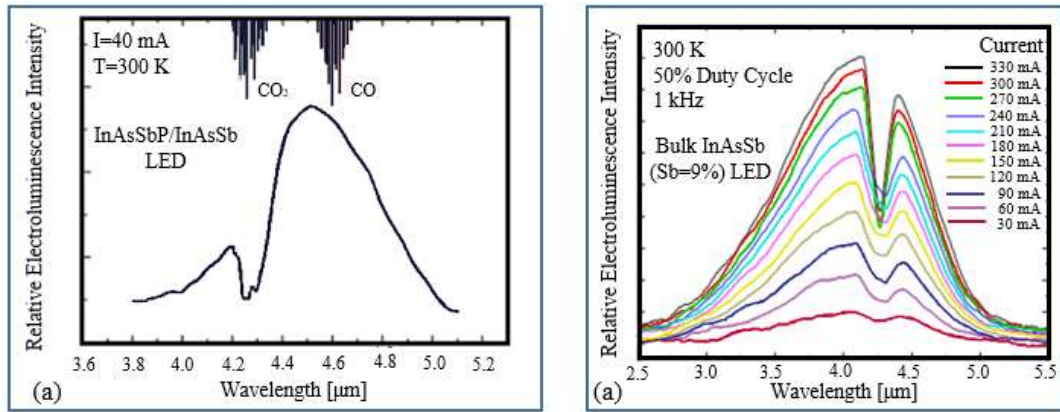


Figure 3.2: (a) 300 K electroluminescence spectrum measured from one of the InAsSbP/InAsSb LEDs [9]. (b) Room temperature electroluminescence spectra of the LED measured at different currents [19].

In QinetiQ Malvern technology centre, the emission characteristics of the bulk AlInSb LEDs were demonstrated as a function of Sb composition between 0% and 8.8% (see Figure 3.3(a)) [21]. The structures were grown on GaAs substrate by MBE. Five devices show room temperature emission centred at 3.4 μm (Sb=0%), 4.2 μm (Sb=2.5%), 4.6 μm (Sb=5.2%), 5.3 μm (6.1%), and 5.7 (8.8%) and produced emittance of approximately 7.5 mW/cm^2 , 27 mW/cm^2 , 15 mW/cm^2 , 12.5 mW/cm^2 , and 3.4 mW/cm^2 , respectively. Recently, in 2019, bulk InAsSb LEDs grown on Si substrate using MBE were investigated by Delli et al. [86] (see the structure in Figure 3.3(b)). Over the temperature range of 6-295 K, the electroluminescence spectra of the LEDs were measured (see Fig. 3.3c), showing a broadband emission peaking at 4.5 μm at room temperature with output power of 6 μW ($\sim 1.2 \text{ mW}/\text{cm}^2$).

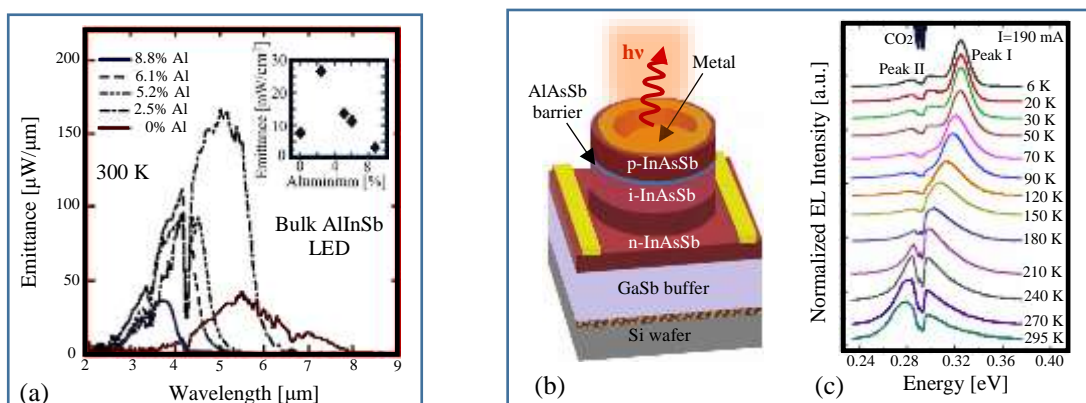


Figure 3.3: (a) The room temperature electroluminescence emission of the QinetiQ LEDs measured at various Sb composition [21]. (b) Schematic diagram of the InAsSb LED structure grown on Si, and (c) Temperature dependent normalized EL emission spectra obtained using 190 mA, 1 kHz and 50% duty cycle. [86]

3.2.2 Single quantum well (SQW), multi quantum well (MQWs), and super lattice (SL)

MIR LEDs

Mid infrared LEDs based on InAs/InAsSb single quantum wells (SQW) containing two different Sb composition (16.6% and 26%) were reported by Tang et al. and Hardaway et al. (1998 and 1999) [13,87]. The two structures were singly grown on InAs substrate by MBE. The 16.6% Sb LED show room temperature emission peaked at $\sim 5 \mu\text{m}$ with quasi-CW output power of $50 \mu\text{W}$, while the peak wavelength of the emission and the quasi-CW output power of the 26% Sb LED were measured to be $8 \mu\text{m}$ and $24 \mu\text{W}$, respectively. Two years later, InAs/InAsSb SQW LEDs exhibiting room temperature broadband emission (about 40 meV ($\sim 640\text{nm}$)) centred at around $4.2 \mu\text{m}$ with pulsed output power of more than $110 \mu\text{W/A}$ were reported by Heber et al. [88]. The structure was grown on *p*-InAs substrate using MBE and included an InAlAs barrier to improve the electron confinement in the active region. In comparison with LEDs grown without the barrier, the efficiency was enhanced by a factor of more than 6x.

Light emitting diodes based on multi quantum wells (MQWs) and strained layer superlattices (SLS) were extensively studied for mid infrared applications [12,14,24-26,89-92]. InAs/InAs_{1-x}Sb_x SLS LEDs grown on GaAs substrate using MBE were reported in 1995 by Tang et. al. [12]. The devices exhibited emission within the range of $4 \mu\text{m}$ to $11 \mu\text{m}$ corresponding to the Sb composition in the InAsSb layer. For the structure with Sb=9.5%, the temperature dependence of electroluminescence spectra of the device were measured (see Figure 3.4(a)), showing room temperature emission extended beyond $5 \mu\text{m}$ with output power of 200 nW at 100 mA injection current. In 1998, Allerman et. al. [89] reported multistage InAsP/InAsSb SLS LEDs grown on InAs substrate. At room temperature, the electroluminescence spectrum of 10 stage-5 period SLS LEDs show a broadband emission with a peak wavelength at $4.2 \mu\text{m}$ and a total output power of $100 \mu\text{W}$ (see Figure 3.4(b)).

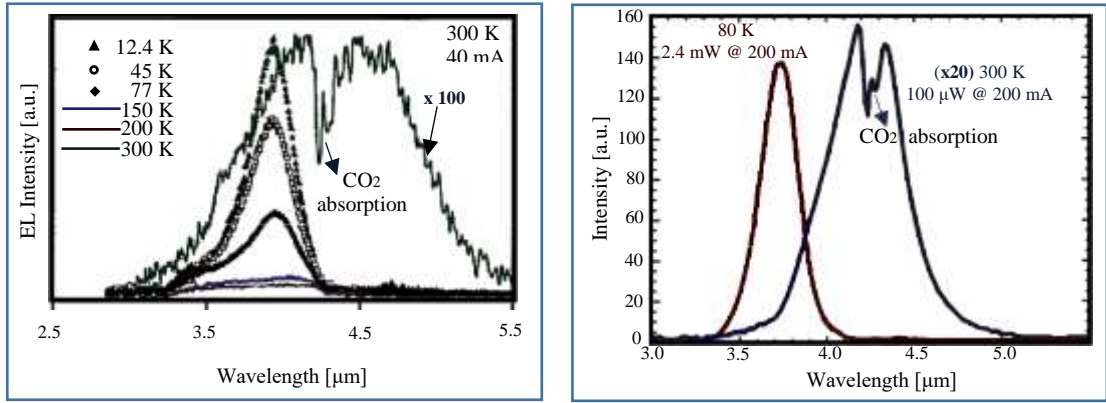


Figure 3.4: (a) Temperature-dependent EL spectra at $I = 40$ mA reported in [12]. (b) LED emission at 80K and 300K from a 10 stage -5 period SLS-LED reported in [89].

One year later, Imperial college London research group investigated InAs/InAsSb (Sb~8%) SLS LED grown on p -InAs substrate using MBE [14]. Two structures were grown, one included a strained AlSb barrier to improve electron confinement in the SLS active region (see Figure 3.5(a)) and the other was grown without barrier. The device with AlSb barrier showed an improvement in the emission spectrum at room temperature (see Figure 3.5(b)), producing an output power of more than $100 \mu\text{W}$ using a pulsed injection current of 2 A. In addition, Krier et. al. (in 2006) [25] also reported InAs/InAsSb (Sb=13%) MQWs LEDs grown on p -InAs substrate using MBE. In this study, temperature dependence of the electroluminescence spectra of the device were measured, observing a broadband emission centred at $\sim 4.0 \mu\text{m}$ with output power of $1.4 \mu\text{W}$ at room temperature. In that year, type II InAs/InGaSb/InAs/AlGaAsSb ‘W’ QWs based on LEDs grown singly on InAs substrate and GaSb substrate using MBE were investigated by Kuznetsov et al. [90]. Room temperature emission spectra of the device grown on InAs show a broadband emission with a peak wavelength of $4.4 \mu\text{m}$ with output power of $\sim 5 \mu\text{W}$, exhibiting better performance compared to that of the device grown on GaSb (which emitted output power of $\sim 2 \mu\text{W}$).

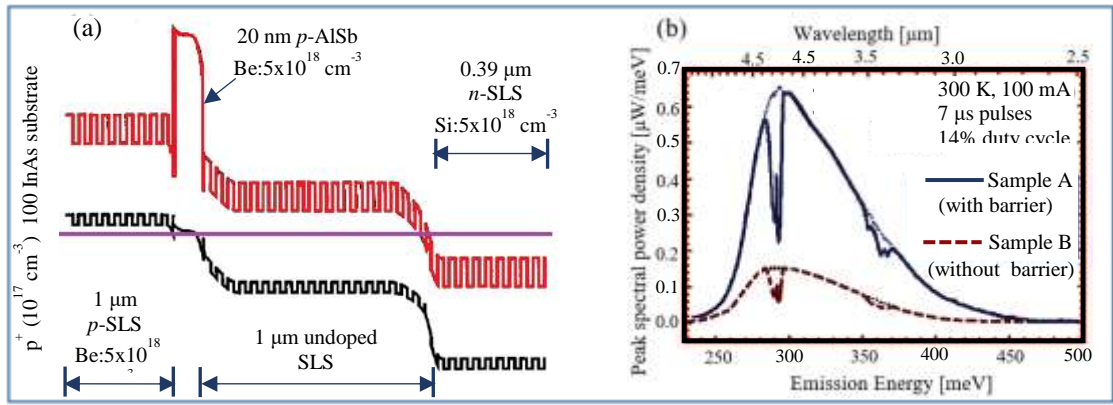


Figure 3.5: (a) Schematic diagram of SLS LED, and (b) Room-temperature electroluminescence spectra of samples A (with a barrier) and B (without a barrier) showing atmospheric CO₂ ~4.2 μm and C-H ~3.5 μm absorption features caused by a 1.1 m unevacuated beam path reported in [14].

Temperature dependence of electroluminescence spectra of InAs/InAsSb (Sb=8%) MQW LEDs were presented by Carrington et. al. (2009) [24]. The structure was grown on *n*-InAs substrate using MBE (see the inset of Figure 3.6(a)). The device exhibited room temperature electroluminescence peaking at 3.7 μm (0.33 eV) as seen in Figure 3.6(a) with an optical output power of 12 μW under quasi-CW operation (100 mA and 50% duty cycle at 1 kHz).

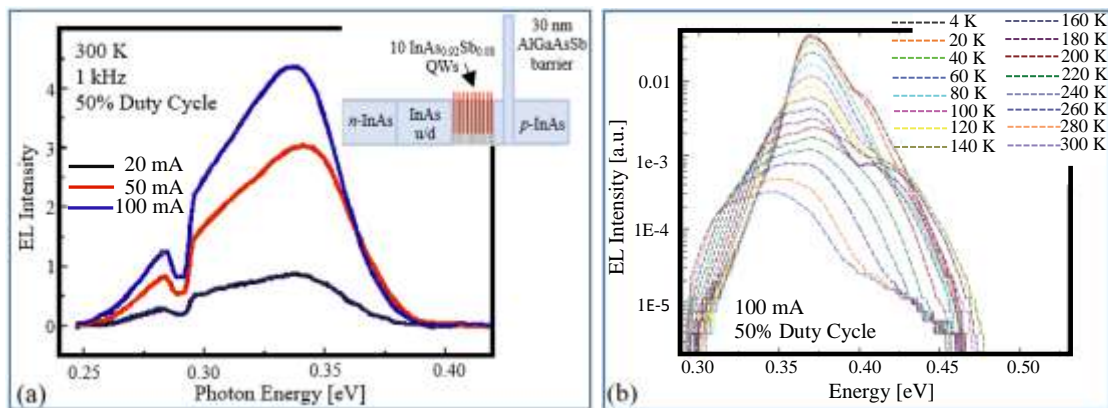


Figure 3.6: (a) Room temperature emission spectra at various injection currents from the InAsSb/InAs LED. The inset is the schematic diagram of the InAsSb/InAs MQW LED. [24] (b) The temperature-dependent electroluminescence emission spectra measured using 100mA and 1 kHz, 50% duty cycle. [91]

Furthermore, two years later, Carrington et al. [91] demonstrated the electroluminescence spectra of the type I InAsSbN/InAs (Sb=5%, N=0.8%) MQWs LEDs grown on InAs substrate

by MBE as a function of temperature over the range from 4 K to 300 K (see Figure 3.6(b)). At 300 K, the emission spectrum has a linewidth of about 600 nm (58 meV) and a peak wavelength at 3.59 μm (0.345 eV), producing output power of 6 μW under quasi-CW operation (100 mA, 50% duty cycle, 1 kHz).

Recently, in 2017, multispectral LEDs grown on GaAs substrate by MBE were designed and investigated by Aziz et. al. [92]. The structure consisted of four active regions including bulk AlInSb and three AlInSb/InSb/AlInSb QWs with different well width. Electroluminescence of the LED measured at room temperature, exhibited four emission spectra corresponding to the active region emission. The peak wavelengths of 3.40 μm , 3.50 μm , 3.95 μm , and 4.18 μm were observed in the bulk, 2 nm, 4 nm, and 6 nm quantum well LEDs, respectively. More recently, Electroluminescence spectra of type II InAs/InAsSb SLSs LEDs with two different Sb compositions of 4% and 6% (see the structure and the spectra in Figures 3.7(a) and 3.7(b)), were demonstrated as a function of temperature from 7 K to 300 K by Keen et al. [26]. At room temperature and under 100 mA quasi-CW injection current, the results show the broadband emission spectra peaked at 4.1 μm with output power of 8.2 μW for InAs/InAsSb (Sb=4%) LED, and at 4.7 μm with output power of 3.3 μW for InAs/InAsSb (Sb=6%) LED.

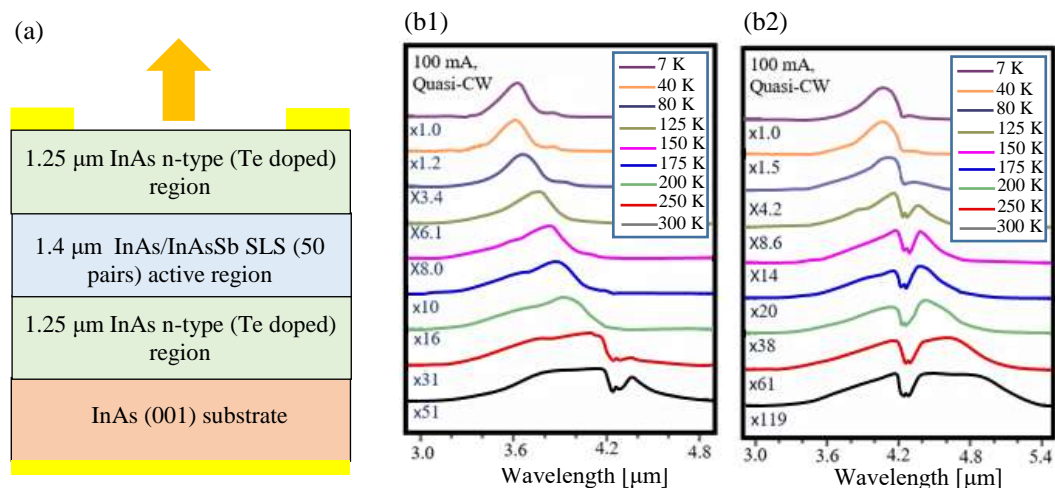


Figure 3.7: (a) Schematic of the LED structure containing the InAs/InAsSb SLS active region, and (b1) and (b2) normalised (7–300 K) electroluminescence spectra of the InAs/InAsSb SLS LEDs with Sb composition of 4% and 6%, respectively.[26]

3.3 Inter-band cascade mid infrared light emitting diodes (MIR ICLEDs)

Recently, research groups extensively developed cascade mid infrared light emitting diodes [36, 93-97]. In 2015, InAs/GaSb SLS based cascade LEDs grown on GaAs and GaSb substrates using MBE were reported by Provence et al. [93]. The schematic diagram of the structures are illustrated in Figures 3.8(a) and 3.8(b). The both devices show 77 K emission spectra with a peak wavelength at 4.7 μm , producing peak radiances of 0.69 $\text{W}/\text{cm}^2\text{-sr}$ for the device grown on GaSb and 1.06 $\text{W}/\text{cm}^2\text{-sr}$ for the device grown on GaAs (see Figure 3.8(c)).

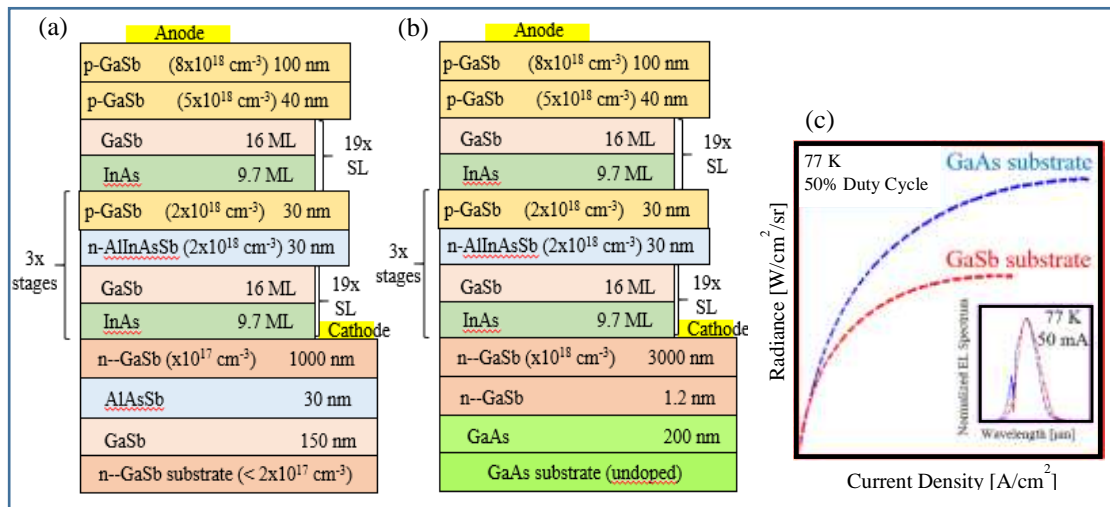


Figure 3.8: Stack diagrams of SLED devices developed on (a) an n-doped (100) GaSb substrate, and (b) on a semi-insulating (100) GaAs substrate, (c) Radiance vs. current density for SLED devices grown on GaAs and GaSb substrates collected at 77 K and a 50% duty cycle. The 77 K electroluminescence spectrum of the devices measured at 50 mA is in the inset. [93]

Two years later, Ricker et al. [94] demonstrated an InAs/GaSb SL cascade LED grown on GaSb substrate. The active region consisted of 20 periods of InAs/GaSb SLs each separated by *n*-AlInAsSb/*p*-GaSb tunnel junction. The device presented 77 K emission peaked at 3.68 μm and exhibited spectral radiances of up to 1.04 $\text{W}/\text{cm}^2\text{-sr}$. In this type of cascade LED, Muhowski et al. [95] reported 77 K emission spectra with peak wavelength of 4.6 μm and obtained a room temperature spectral radiance of 0.5 $\text{W}/\text{cm}^2\text{-sr}$ under pulsed operation (0.1% duty cycle). Type I GaInAsSb/AlGaInAsSb QWs cascade LEDs emitting at $\sim 3.1 \mu\text{m}$ grown on GaSb substrate were investigated by Ermolaev et al. in 2018 [96]. Output powers of more than 6 mW and 2 mW were measured at 77 K and 290 K, respectively. In addition, interband cascade LEDs

based on ‘W’ QWs active region were designed and fabricated by Kim et al. [97]. At room temperature, the device emitted emission showing peak wavelength at $\sim 3.1 \mu\text{m}$ and produced an output power of 2.9 mW ($0.73 \text{ W/cm}^2\text{-sr}$). More recently, in 2019, Zhou et al. [36] demonstrated the temperature dependence of 2-stage and 5-stage inter-band cascade LEDs grown on InAs substrate using MBE. The structure consisted of InAs/GaAsSb SLs active region (for generating photons), GaAsSb/AlAsSb tunnelling regions and InAs/AlAsSb injection regions which are designed to efficiently transfer the electrons and holes into active region, respectively (see Figure 3.9(a)). Room temperature electroluminescence spectra of the devices show a broadband linewidth of about 600 nm peaked at $4.47 \mu\text{m}$ and $4.39 \mu\text{m}$ for 2-stage and 5-stage ICLEDs, respectively. 5-stage ICLEDs exhibited output power of approximately 300 μW corresponding to wallpulg efficiency of $\sim 0.05\%$ using pulsed operation (400 mA, 1% duty cycle at 1 kHz) (see Figure 3.9(b)).

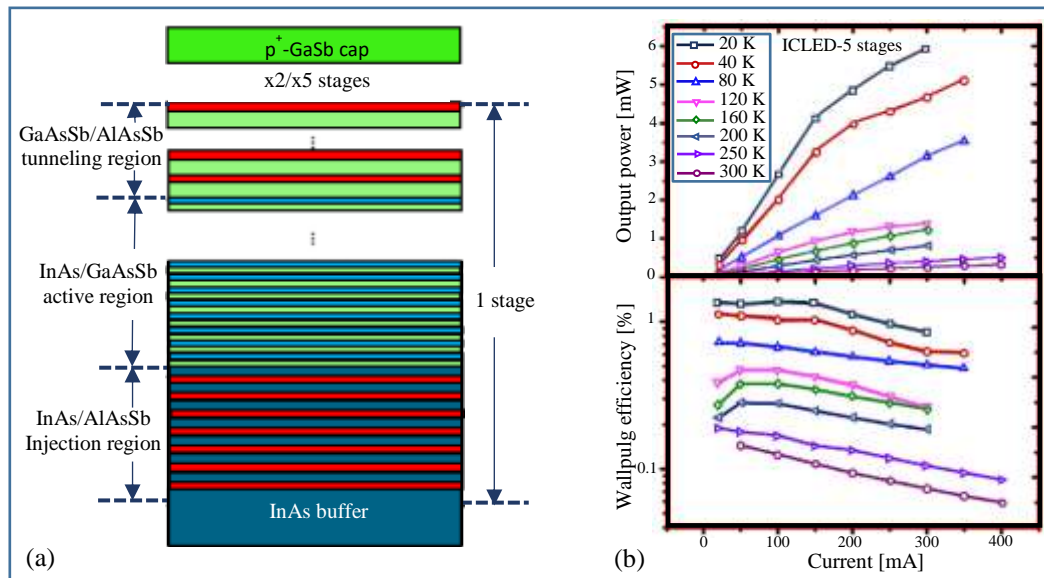


Figure 3.9: (a) Schematic illustration of the ICLED structure, and (b) output power and WPE dependence on current injection at 20–300 K for the 5-stage ICLED with a mesa size of $400 \times 400 \mu\text{m}$. [36]

3.4 Infrared-resonant cavity light emitting diode (I-RCLED)

3.4.1 Near-Infrared 850-980 nm RCLEDs

The first near-infrared resonant cavity light emitting diode (RCLED) was reported by Schubert et al. in 1991 [41]. It was grown on (001) n-type GaAs substrate using MBE. The structure consists of a thin GaAs active region placed inside the cavity at antinode position of the electric field. The cavity sandwiched between a high reflectivity ($R \approx 99\%$) quarter-wave AlAs/ $\text{Al}_{0.14}\text{Ga}_{0.86}\text{As}$ distributed Bragg reflector (DBR) used as a substrate-sided (bottom) mirror and a low reflectivity Ag and Ag/ CdSnO_x used as a top mirror (see Figure 3.10(a)). At room temperature, the results exhibited that the emission intensity of the RCLED was enhanced by a factor of 1.7 compared to a reference LED, producing an optical output power of $\sim 220 \mu\text{W}$ at 20°C as shown in Figure 3.10(b). Furthermore, the experimental emission linewidth was narrower than that of the reference LED which was found to be 17 meV .

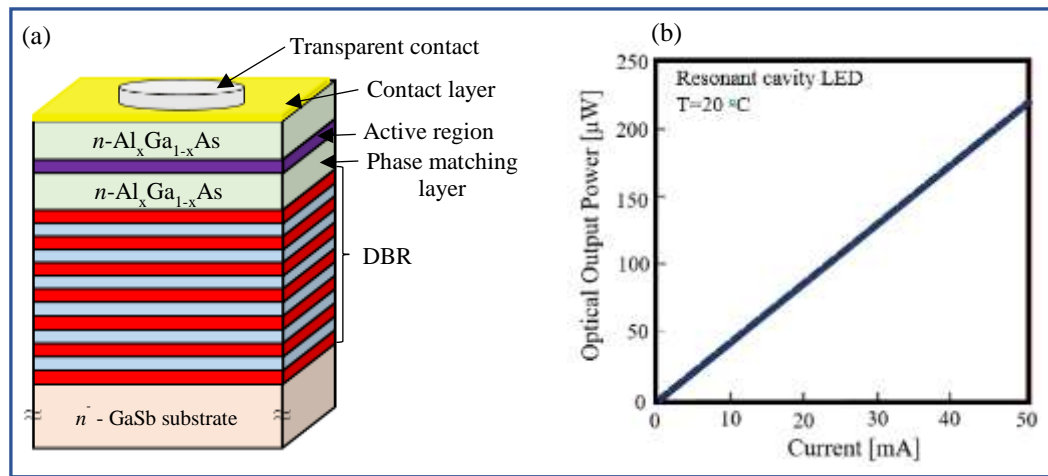


Figure 3.10: (a) Schematic layer sequence of the resonant cavity light-emitting diode (RCLED). (b) Optical output power vs injection current of a resonant cavity light-emitting diode at room temperature. [41]

Top emitting RCLEDs, exhibiting emission peaked at around 850 nm , were investigated with and without selectively oxidised current [98]. The device consisted of three $\text{Al}_{0.2}\text{Ga}_{0.8}\text{As}/\text{GaAs}$ QWs placed in the antinode of the cavity which is sandwiched between two $\text{Al}_{0.15}\text{Ga}_{0.85}\text{As}/\text{AlAs}$ DBRs. The oxidised devices show an optical power of $\sim 750 \mu\text{W}$ and overall quantum efficiency of about 14%. Dumitrescu et al. [99] used the transfer matrix based modelling with self-

consistent model to optimize the performance of two RCLEDs structures operating at 660 nm and 880 nm. The structure of the near-infrared (880 nm) QWs RCLED consisted of 1λ-thick cavity placed between a 20 pairs $\text{Al}_{0.2}\text{Ga}_{0.8}\text{As}/\text{Al}_{0.9}\text{Ga}_{0.1}\text{As}$ bottom DBR mirror and a 5 to 7 pairs $\text{Al}_{0.9}\text{Ga}_{0.1}\text{As}/\text{Al}_{0.2}\text{Ga}_{0.8}\text{As}$ top DBR mirror. Three $\text{Ga}_{0.96}\text{In}_{0.04}\text{As}$ QWs separated by $\text{Al}_{0.2}\text{Ga}_{0.8}\text{As}$ barriers were used in the active region and positioned inside the cavity. The device had a significant performance showing narrow linewidth below 15 nm and wall-plug efficiency of 14.1% corresponding to output power of 22.5 mW (see Figure 3.11(a)). One year later, Kato et al. [100] used two single quantum wells of different well width as active region to improve the performance of RCLED operating at 850 nm (see the structure in Figures 3.11(b)). Two structures were demonstrated, one contained two single GaAs QWs positioned in the cavity A with thickness 10 and 7 nm, while the thickness of the two single QWs placed in the cavity B were 10 nm for each. The wells were separated by $\text{Al}_{0.3}\text{Ga}_{0.7}\text{As}$ barriers and positioned at separate antinodes of the electric field. Both cavities were surrounded by a 30 pairs $\text{Al}_{0.2}\text{Ga}_{0.8}\text{As}/\text{GaAs}$ bottom DBR mirror with reflectivity 98% and 10 pairs $\text{Al}_{0.2}\text{Ga}_{0.8}\text{As}/\text{GaAs}$ top DBR mirror with reflectivity 89%. At low injection current ($I=50$ mA), the results presented that the measured output power of the structure with cavity A increased by 24% to be 2.2 mW and by 46% to be 2.7 mW at high injection current ($I=100$ mA).

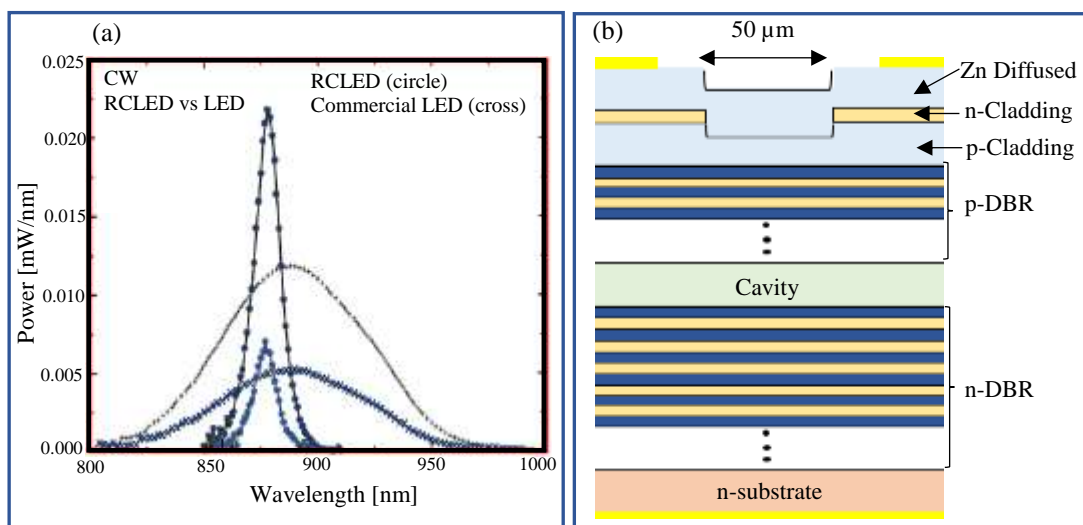


Figure 3.11: (a) Comparison between the emission spectrum of a 880 nm range RCLED and a commercial LED in the same wavelength range for two bias currents. [99] (b) Schematic illustrations of the fabricated resonant cavity light emitting diodes. [100]

An 980-nm top emitting RCLED, consisting of a 1λ -thickness cavity sandwiched between two high contrast DBRs, was demonstrated and the device show a narrow linewidth emission of 5 nm with an external differential quantum efficiency as high as 27% [101]. In this study, the structure of the top DBR was 1-2 period of SiO₂/ZnSe layers and of a bottom DBR was 6.5 period of AlO/GaAs layers.

Additionally, several near-infrared RCLED structures operating at wavelength of 1300 nm and 1550 nm were reported in [102-108]. Some of these structures were designed to emit the light from the substrate using top gold mirror with reflectivity of ~95% and low reflectivity bottom DBR mirror [102,103]. Top emitting RCLEDs are also investigated by placing the cavity between high reflectivity bottom DBR mirror and low reflectivity top DBR mirror [104-108].

3.4.2 Mid-infrared 2.5-4.3 μm RCLEDs

Hadji et al. (1995) [43] demonstrated mid-infrared RCLED emitting at 3.2 μm using Cd_{0.51}Hg_{0.49}Te/HgTe pseudo alloy as the active region. The structure consisted of a half-wavelength cavity sandwiched between a bottom Cd_{0.51}Hg_{0.49}Te/Cd_{0.75}Hg_{0.25}Te DBR with reflectivity of 86% and a top gold mirror with reflectivity of 95% (see Figure 3.12). At room temperature, the full width at half-maximum (FWHM) of the electroluminescence (EL) spectrum of the RCLED was found to be 8 meV at 300 K, less than that of the reference structure (without cavity) by a factor of 6. In addition, the results exhibited that the external quantum efficiency of the RCLED was 0.2×10^{-3} and the directivity of the emission spectrum was improved to be 55°.

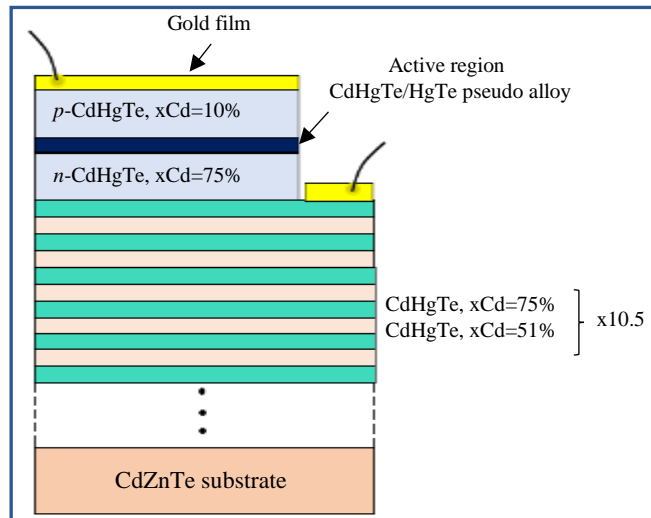


Figure 3.12: Schematic diagram of the $\text{Cd}_{0.51}\text{Hg}_{0.49}\text{Te}/\text{HgTe}$ RCLED device reported in [43].

A $4.0\ \mu\text{m}$ bottom emitting InAs/InAsSb SLs RCLED grown on GaAs substrate was demonstrated by Green et al. (2004) [44]. The 1λ -thick cavity included an InAs/InAsSb SL active region sandwiched between top CrAu mirror with $\sim 95\%$ reflectance and low reflectance bottom GaAs/AlGaAs DBR (see Figure 3.13(a)). Temperature dependence of the electroluminescence spectra of the device were measured as seen in Figure 3.13(b). The output power of the RCLED was enhanced by a factor of 2.2 compared to that of the reference LED, which is lower than the theoretical measurements due to the phase change from CrAu mirror and the uncertainty in the growth rate of InAs/InAsSb SLs.

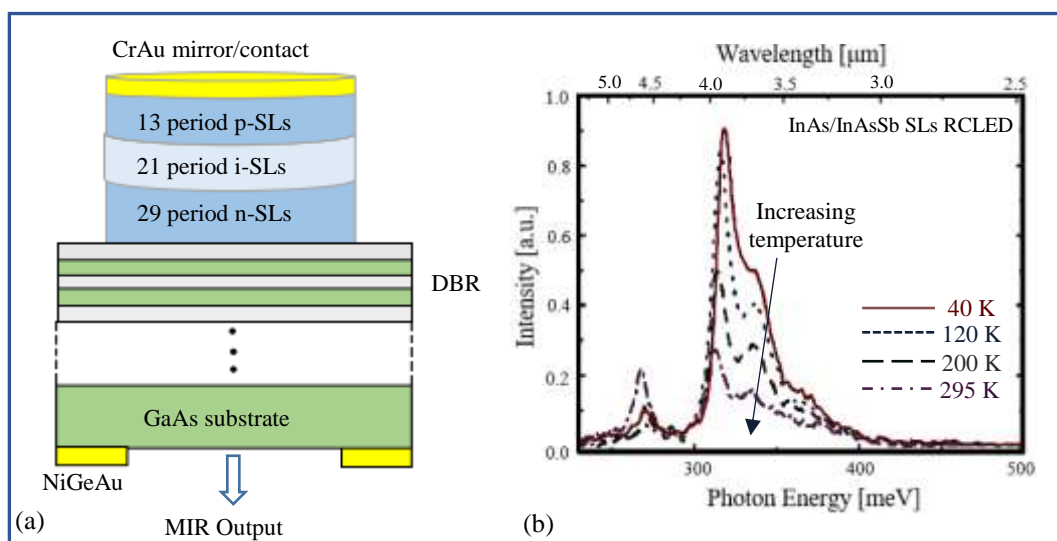


Figure 3.13: (a) Schematic of the $\text{InAs}/\text{InAs}_{0.91}\text{Sb}_{0.09}$ SLS RCLED, and (b) Measured electroluminescence spectra from the device, at various temperatures. [44]

GaSb-based RCLEDs operating near 2.3 μm were investigated with and without n^{++} -InAsSb/ p^{++} -GaSb tunnel junction [45]. Two series of 4 compressively strained GaInAsSb QWs separated by AlGaAsSb barriers were used as active region which are placed inside the 1.5 λ -thick cavity at two different antinodes of the electric field (see Figure 3.14). The active region was sandwiched between two AlAsSb/GaSb DBRs. The devices with tunnel junction show an optical output power of 0.4 mW operating under CW (800 mA) and for similar device without tunnel junction, the optical output power is limited to 0.15 mW.

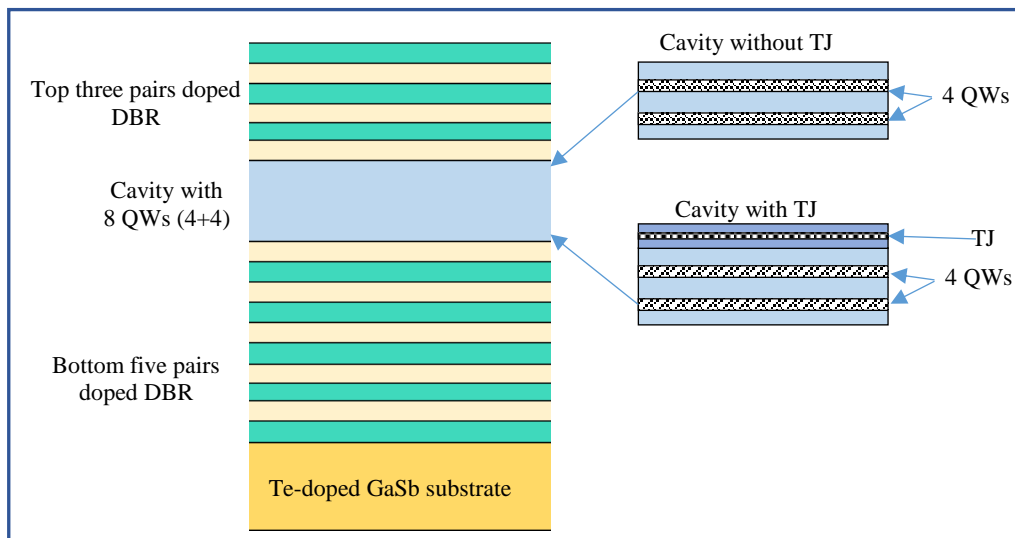


Figure 3.14: Schematic of the AlGaAsSb/GaInAsSb RCLED structure with and without tunnel junction reported in [45]

Grasse et al. [46] designed and fabricated mid infrared RCLEDs, the structure shown in Figure 3.15(a), emitting at 2.8 μm , 3.3 μm , and 3.5 μm grown on InP substrate using metalorganic vapour phase epitaxy (MOVPE). Two different active regions were used, GaInAs/GaAsSb type II ‘W’-shaped QWs and SLs. At 20 °C, the optical output power was measured under CW operation ($J=500 \text{ A/cm}^2$) and found to be 125 μW for 3.3 μm SLs RCLED and 86 μW for 3.5 μm ‘W’ QWs RCLED. Bulk AlInSb based on RCLED emitting at $\sim 4.2 \mu\text{m}$ grown on GaAs substrate was reported in [49]. The cavity surrounded by the bottom 5 pairs AlSb/GaSb DBR and top air-semiconductor interface reflector. Room temperature emission of the RCLED was enhanced by a factor of ~ 3 compared to that of the reference LED (see Figure 3.15(b)).

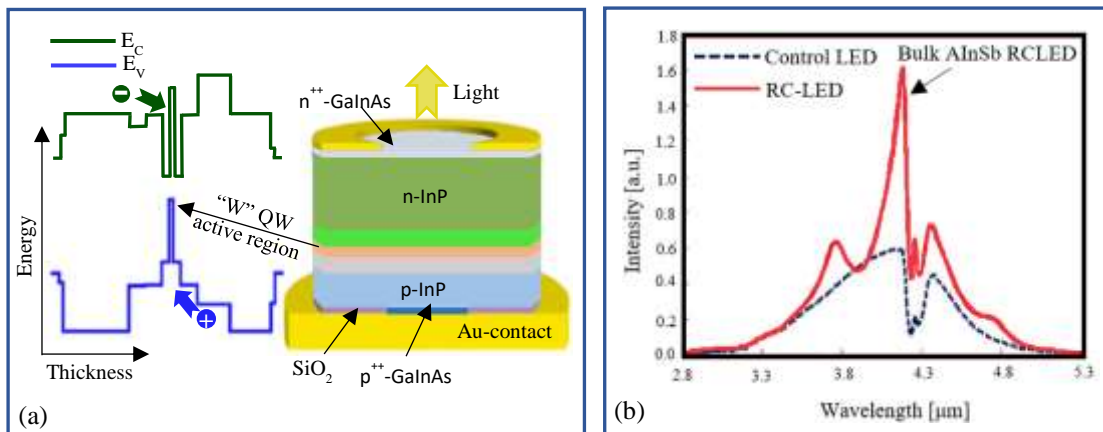


Figure 3.15: (a) Sketch of conduction and valence band alignment and the layer structure of the 3.5 μm InP-based RCLED device. The bottom Au contact serves also as heat sink and pseudo substrate.[46] (b) Measured spectral emission from a bulk AlInSb RCLED, showing a 3-fold enhancement compared to a reference non-resonant device. [49]

3.5 Mid-Infrared vertical-cavity surface-emitting lasers (MIR-VCSELs)

Several research groups have investigated mid-infrared III-V semiconductor VCSELs operating in the range from 2 μm to 4 μm [47,48,50,109-123]. Mid-infrared VCSELs emitting at 2.3 μm , 2.4 μm , 2.5 μm , and 2.6 μm were demonstrated [47,109-119]. The active regions of these structures are located between two high reflectivity DBR mirrors. Many of these devices exhibit room temperature output power under CW conditions. The VCSELs operating at the wavelength $\geq 3 \mu\text{m}$ are described in more detail in the next sub-section.

3.5.1 Mid-Infrared VCSELs emitting at 3 μm , 3.4 μm , and 4 μm

Type I GaInAsSb QWs VCSEL, consisting of AlAsSb/GaSb DBR used as bottom mirror and Ge/ZnS dielectric DBR used as a top mirror, have recently achieved lasing to 3 μm [48] (see the structure in Figure 3.16(a)). The device emitted up to 5 $^\circ\text{C}$ under CW operation and up to 50 $^\circ\text{C}$ under pulsed mode. Optical output powers under CW operation were measured to be 70 μW at -40 $^\circ\text{C}$ and $\sim 10 \mu\text{W}$ at 5 $^\circ\text{C}$ (see Figure 3.16(b)). However, when the emission wavelength is extended further, the performance of the type I GaInAsSb QWs tends to fall off dramatically. Therefore, Bewley et al. [120] investigated interband cascade VCSELs to achieve emission wavelength at 3.4 μm . The structure included three groups of five stages similar to those which

are used previously for edge-emitting interband cascade lasers (ICLs) [121] (the structure of 3.4 μm ICVCSEL shown in Figure 3.16(c)). Under pulsed operation and at room temperature, the device with a large aperture diameter of 40 μm produced an optical output power of ~ 500 μW (see Figure 3.16(d)).

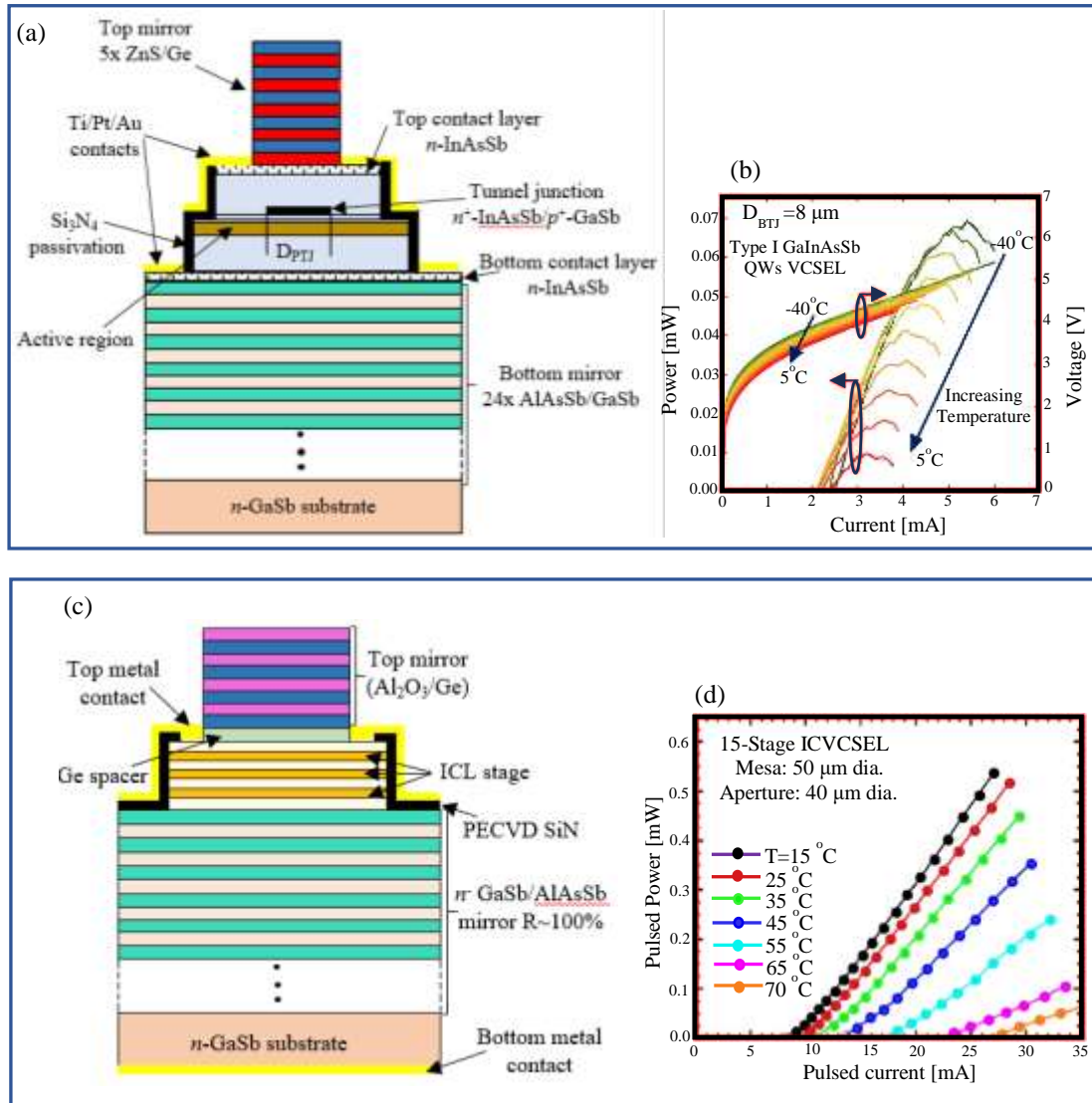


Figure 3.16: (a) Schematic structure of the GaSb-based VCSEL with undoped bottom DBR and intracavity contact, and (b) Power-current-voltage characteristic of a VCSEL at different temperatures in CW reported in [48]. (c) Schematic of the interband cascade VCSEL structure, and (d) Pulsed output power at various temperature reported in [120].

Although there are some mid-infrared lead-salt QWs VCSELs emitting at 4 μm and 4.4 μm , these devices are only optically pumped [122,123]. In 2017, Veerabathran et al. [50] reported electrically pumped type II W-shape QWs VCSEL emitting at 4 μm . the device with an aperture

diameter of $7\ \mu\text{m}$ exhibited optical output power up to $-7\ ^\circ\text{C}$ under CW operation, and up to $45\ ^\circ\text{C}$ under pulsed mode (see Figures 3.17(a) and 3.17(b)). The maximum pulsed output power was measured to be $750\ \mu\text{W}$ at $-40\ ^\circ\text{C}$, higher than that of CW operation by a factor of ~ 4 . At room temperature, the device show pulsed output power of $\sim 120\ \mu\text{W}$.

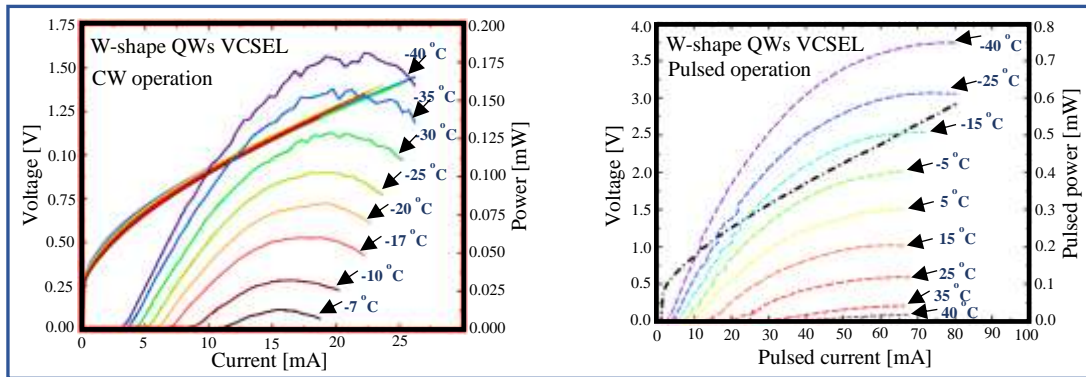


Figure 3.17: (a) Power-current-voltage characteristics of a $4\ \mu\text{m}$ VCSEL in (a) CW operation, and (b) pulsed operation reported in [50].

3.6 Summary

Mid-infrared LEDs operating at wavelengths $> 3\ \mu\text{m}$ have received significant attention by many research groups to develop the structures and optimize the active region. This is attributed to the many mid-infrared applications especially, gas sensing. Different III-V semiconductor materials such as bulk semiconductor, quantum dots (QDs), quantum wells (QWs) and superlattices (SLs) were used as active regions in these LEDs. However, most of these devices exhibit room-temperature broadband spectral linewidths with optical output power of few μW under quasi-CW conditions, giving low spectral brightness in the target wavelength. Mid-infrared ICLEDs were investigated and developed to optimize the optical output power and external efficiency. High output power ICLEDs were reported at $77\ \text{K}$, exhibiting spectral radiances of up to $1\ \text{W}/\text{cm}^2\text{-sr}$ under pulsed condition. Recently, room-temperature output power was also investigated in the ICLED with $300\ \mu\text{W}$ under pulsed operation. The spectral linewidth of the mid-infrared ICLEDs is still broadband, showing no improving emission linewidth compared to that of the LED.

Several research groups have investigated RCLEDs in the infrared region to improve the output power and the external efficiency as well as the spectral linewidth. Most of these devices are designed to emit at wavelengths in the near-infrared and mid-infrared ($\lambda < 3 \mu\text{m}$) spectrum. The results exhibit high brightness peak emission, high efficiency and narrower linewidth compared to that of the reference LEDs. Few RCLEDs were investigated at wavelength $\lambda \geq 4 \mu\text{m}$, where the structures were designed to emit light through the substrate, showing relatively low enhancement factors (< 5) due to the limitation in the reflectivity of the top gold mirror.

In addition, electrical pumped mid-infrared VCSEL are also reported. To date, these devices were designed to emit at wavelengths up to $4 \mu\text{m}$. The VCSELs operating at wavelengths $< 3 \mu\text{m}$ exhibit room-temperature output power of hundreds μW under CW conditions. However, when the wavelength emission is extended further, the output power of the devices tend to decrease and the CW operation is not achieved at room-temperature. Recently, $4.0 \mu\text{m}$ VCSEL exhibit output power up to 45°C under pulsed operation and up to -7°C under CW operation. At room temperature and under pulsed conditions, the devices exhibit output power of $120 \mu\text{W}$. Table 3.1 shows the summary of the literature review on the mid-infrared LEDs, RCLEDs and VCSELs.

Table 3.1: Summary of the literature review on LEDs, RCLEDs and VCSEL.

| Author(s) | Date | Structure | λ [μm] | $\Delta\lambda$ (nm) | Power / Emittance |
|--------------------------|------|--|------------------------------|----------------------|---|
| Mid-Infrared LEDs | | | | | |
| Melangailis et al. | 1966 | Bulk InAs LEDs | ~ 3.7 (300 K) | | |
| Dobbelaere et al. | 1993 | Bulk InAsSb (Sb=15%) LEDs | ~ 4.25 | | |
| Popov et. al. | 1998 | Bulk InAsSbP/InAsSb/InAsSbP heterostructure LEDs | 4.3 (300 K) | 800 | $850 \mu\text{W}$ (I=1.2 A) |
| Gao et. al. | 1999 | InAsSbP/InAsSb (Sb =11% in InAsSb layer) double heterostructure LEDs | 4.6 (300 K) | 507 | $50 \mu\text{W}$ (I=1 A) |
| Krier et al. | 2007 | Bulk InAsSb (Sb=9%) | ~ 4.25 (300 K) | | 1 mW (I=2 A) |
| Haigh et al. | 2007 | Bulk AlInSb LEDs Sb=0% Sb=2.5% Sb=5.2% | (300 K) 3.4 4.2 4.6 | | 7.5 mW/cm^2 27 mW/cm^2 |

| | | | | | |
|--|------|--|------------------------------|-----|--|
| | | Sb=6.1% Sb=8.8% | 5.3 5.7 | | 15 mW/cm ² 12.5 mW/cm ² 3.4 mW/cm ² |
| Delli et al. | 2019 | Bulk InAsSb LEDs on Si | 4.5 (295 K) | | 6 μW (I=0.1 A) |
| Tang et al. | 1998 | InAs/InAsSb single quantum wells (SQW) (Sb=16.6%) | 5 (300 K) | | 50 μW |
| Hardaway et al. | 1999 | InAs/InAsSb single quantum wells (SQW) (Sb=26%) | 8 (300 K) | | 24 μW |
| Heber et al. | 2001 | InAs/InAsSb SQW LEDs included an InAlAs barrier | 4.2 (300 K) | 640 | 110 μW/A |
| Tang et al. | 1995 | InAs/InAs _{1-x} Sb _x SLS LEDs (Sb=9.5%) | 5 (300 K) | | 0.2 μW (I=0.1 A) |
| Allerman et al. | 1998 | 10 stage-5 period InAsP/InAsSb SLS LEDs | 4.2 (300 K) | | 100 μW |
| Pullin et al. | 1999 | InAs/InAsSb (Sb~8%) SLS LED included a strained AlSb barrier | 4.2 (300 K) | | 100 μW (I=2 A) |
| Krier et al. | 2006 | InAs/InAsSb (Sb=13%) MQWs LEDs | 4.0 (300 K) | | 1.4 μW |
| Kuznetsov et al. | 2006 | InAs/InGaSb/InAs/AlGaAsSb 'W' QWs based on LEDs grown on InAs substrate | 4.4 (300 K) | | ~5 μW |
| Carrington et al. | 2009 | InAs/InAsSb (Sb=8%) MQW LEDs | 3.7 (300 K) | | 12 μW (I=0.1 A) |
| Carrington et al. | 2011 | InAsSbN/InAs (Sb=5%, N=0.8%) MQWs LEDs | 3.59 | 600 | 6 μW (I=0.1 A) |
| Aziz et al. | 2017 | Four active regions including bulk AlInSb and three AlInSb/InSb/AlInSb QWs with different well width | 3.40 3.50 3.95 4.18 | | |
| Keen et al. | 2018 | InAs/InAsSb MQWs LEDs Sb=4% Sb=6% | (300 K) 4.1 4.7 | | (I=0.1 A) 8.2 μW 3.3 μW |
| Mid-Infrared Interband cascade LEDs | | | | | |
| Provence et al. | 2015 | InAs/GaSb SLS based cascade LEDs grown on GaAs substrate GaSb substrate | (77 K) 4.7 4.7 | | ~3.33 W/cm ² ~2.16 W/cm ² |
| Ricker et al. | 2017 | InAs/GaSb SL cascade LED | 3.68 (77 K) | | ~3.27 W/cm ² |
| Muhowski et al. | 2017 | InAs/GaSb SL cascade LED | | | ~1.57 W/cm ² (pulsed) |
| Ermolaev et al. | 2018 | GaInAsSb/AlGaInAsSb QWs cascade LEDs | 3.1 | | 6 mW (77 K) 2 mW (290 K) |
| Kim et al. | 2018 | Interband cascade LEDs based on 'W' QWs | 3.1 (300 K) | | 2.9 mW |
| Zhou et al. | 2019 | Inter-band cascade LEDs based on InAs/GaSb SLs 2-stages 5-stages | (300 K) 4.47 4.39 | 600 | Pulsed (I=0.4 A) 300 μW |
| Mid-Infrared RCLEDs | | | | | |
| Hadji et al. | 1995 | Cd _{0.51} Hg _{0.49} Te/HgTe RCLED | 3.2 (300 K) | ~67 | |

| | | | | | |
|----------------------------|------|--|--------------------|-----|---|
| Green et al. | 2004 | InAs/InAsSb SLs RCLED | 4.0 (300 K) | | |
| Grasse et al. | 2012 | GaInAs/GaAsSb type II 'W'-shaped QWs and SLs RCLED | 3.3 SLs 3.5 QWs | | 125 μ W 86 μ W |
| Meriggi et al. | 2015 | Bulk AlInSb based on RCLED | | | |
| Al-Saymari et al. [124] | 2019 | Bulk InAsSb RCLED | 4.3 (300 K) | ~88 | 5.5 μ W (quasi-CW) |
| Al-Saymari et al. [125] | 2020 | AlInAs/InAsSb QWs RCLED | 4.5 (300 K) | ~70 | 140 mW/cm ² (pulsed) 10 mW/cm ² (quasi-CW) |
| Mid-Infrared VCSELS | | | | | |
| Andrejew et al | 2016 | Type I GaInAsSb QWs VCSEL | 3.0 | | ~10 μ W at 5 °C |
| Bewley et al. | 2016 | Interband cascade VCSELS | 3.4 (300 K) | | 500 μ W (pulsed) |
| Veerabathran et al. | 2017 | Type II W-shape QWs VCSEL | ~4.0 (300 K) | | 120 μ W (pulsed) |

Chapter 4

Experimental procedures

The experimental methods that were used to grow, fabricate and measure the semiconductor materials and the devices are discussed in this chapter.

4.1 Molecular beam epitaxy (MBE)

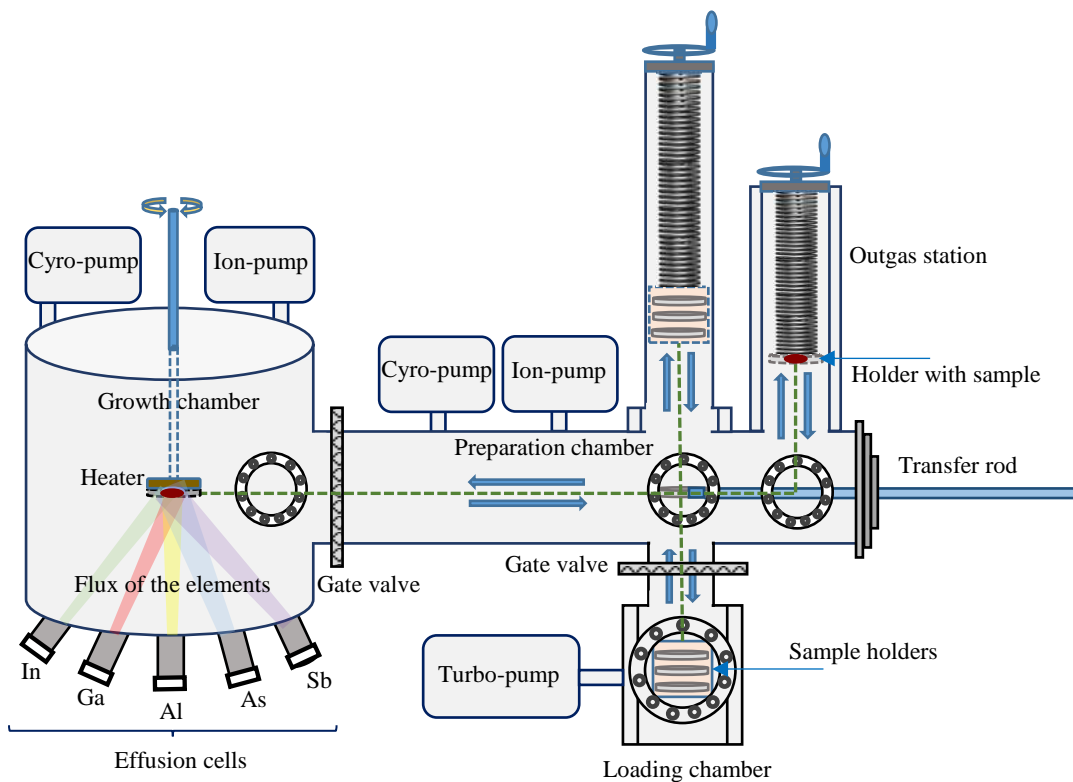


Figure 4.1: Simplified schematic diagram of the MBE system used in this work.

Molecular beam epitaxy is an epitaxial technique used to grow semiconductor materials on a crystalline substrate under ultra-high vacuum (typically $\sim 10^{-10}$ mbar). Using this technique, high quality structures can be produced with good control over doping concentration, thickness, and composition. The MBE system, which was used to grow the structures in this work, is a Veeco Explor MBE system and the simplified schematic diagram of this system is shown in

Figure 4.1. The system consists of three chambers, the loading chamber, preparation (outgas) chamber, and growth chamber. A cyro-pump together with ion pump are used to pump each of the preparation and growth chambers. The substrate was first placed into the loading chamber, which is evacuated using a turbo-pump, and then transferred into the preparation chamber where the substrate is baked inside the outgassing station to remove surface contamination. After that, the sample is moved into the growth chamber which contains the effusion cells. The thermal effusion k-cells are used to provide the flux of the group III elements (indium (In), gallium (Ga), aluminium (Al)) and the elements for doping (beryllium (*p*-type) and GaTe (*n*-type)). Whilst, the cracker cells are used to provide the flux of the group V elements, arsenic (As) and antimony (Sb). During growth, the sample is rotated to improve the uniformity in the epitaxial layers.

In-situ reflection high energy electron diffraction (RHEED) is a technique used for monitoring the surface construction of the sample during growth. In this technique, a beam of high energy electrons produced from electron gun is incident on the sample surface at a grazing angle of $< 2^\circ$. The electrons are diffracted from the surface and then hit a fluorescent screen forming a diffraction pattern. Therefore, the surface morphology of the sample can be identified from these patterns. A smooth surface is represented by observing a streaky pattern on the screen, whilst a spotty pattern indicates a rough surface [126,127]. No pattern is observed if the material is contaminated or if an oxide is present. During the deposition of a monolayer and in addition to the change in the pattern, the intensity of the pattern is also varied. Initially, the RHEED pattern is bright if the surface is smooth. As more material is deposited, the surface becomes rough and the intensity of the pattern reduces, (spotty pattern). After further material deposition, the surface becomes smooth again and the pattern transforms from spotty to streaky, indicating that the monolayer is deposited.

4.2 X-ray diffraction

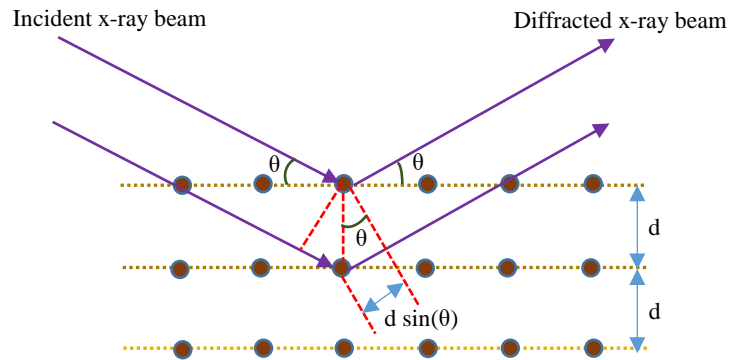


Figure 4.2: Schematic diagram showing the representation of Bragg's Law.

The characterization of the resulting MBE grown semiconductor structure can be determined by x-ray diffraction, which provides information about the crystalline structure, material compositions, strain, and the layer thickness. These characterizations can be investigated from the diffraction patterns of the monochromatic x-ray beam, provided the wavelength is on the order of the atomic spacing of the semiconductor. According to Bragg's law, the lattice plane spacing (d) is related to the wavelength of x-ray (λ) by the formula:

$$n\lambda = 2d \sin(\theta) \quad (4.1)$$

where n is an integer (the order of reflection), θ is the Bragg angle (the angle between the incident x-ray and the normal to the reflecting lattice plane). The schematic representation of Bragg's law is illustrated in [Figure 4.2](#).

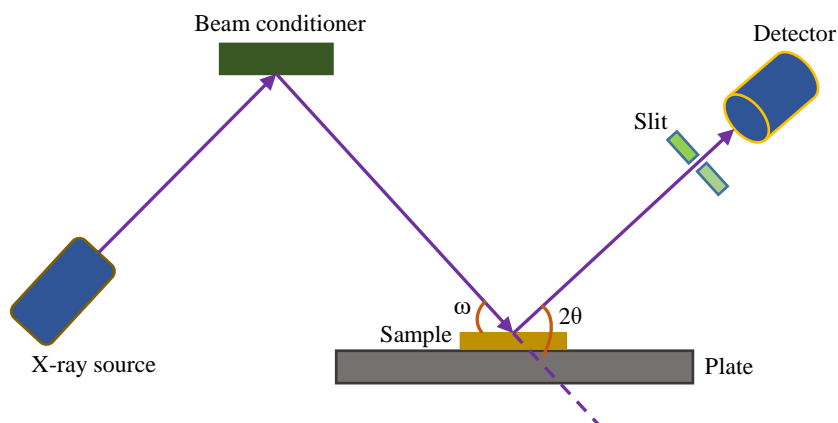


Figure 4.3: Schematic diagram of X-ray diffraction system.

In this work, A Bede QC200 x-ray diffraction system is used to investigate the characterizations of the semiconductor structure for the samples. The schematic diagram of the x-ray diffraction system is shown in Figure 4.3. The sample is positioned on the plate which can be rotated at various angles of ω . A beam of high energy electrons, created by a hot filament source and accelerated by high-voltage, are emitted towards a copper target, producing an x-ray beam with a wavelength of 1.54 \AA . The incident x-ray beam hits the sample at angles of ω , and the beam is then scattered from the sample and detected by a detector. When the sample is rotated through angle ω , the detector is moved through an angle 2θ at the same time, providing an ω - 2θ scan. The resulting diffraction spectra were analyzed using RADS Mercury software.

4.3 Photoluminescence experimental setup

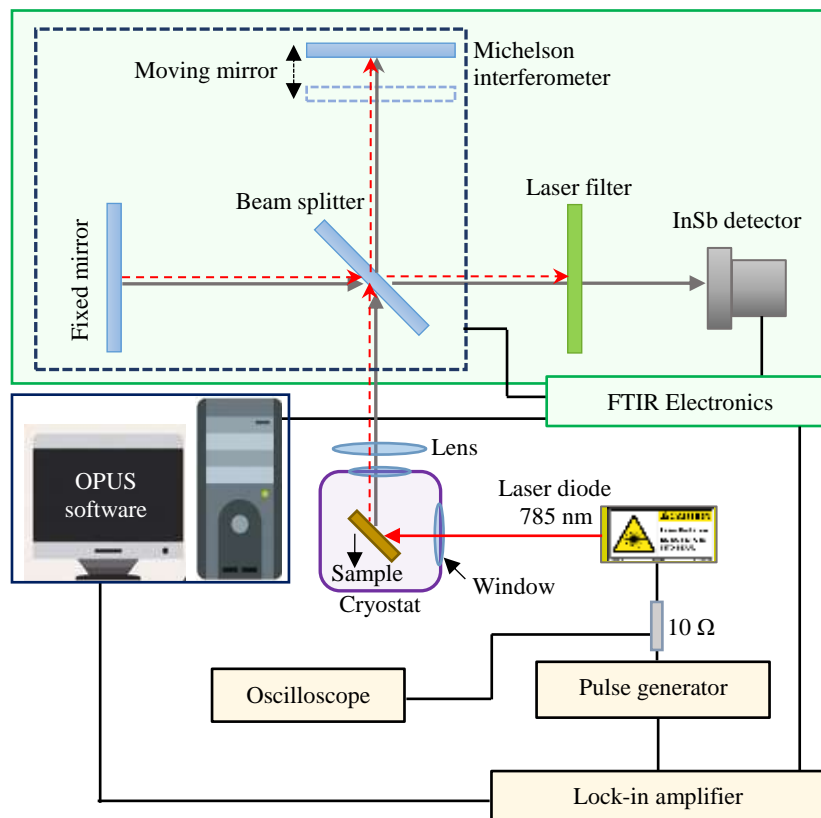


Figure 4.4: Schematic diagram of the FTIR photoluminescence system, the red dashed line is the laser beam and grey line is the photoluminescence emission from the sample.

[Figure 4.4](#) shows a schematic diagram of the photoluminescence spectroscopy measurement. A 785 nm laser diode with a drive current of 100 mA at 50% duty cycle was used to excite the samples, at an angle of 45 degrees to the laser beam. The sample was placed inside the inner chamber of a cryostat (Oxford Instruments) which can be cooled down to 4 K using a continuous flow of liquid helium. The temperature of the sample chamber can be chosen in the range from 4 K to 300 K using a temperature controller. The laser beam was focussed onto the sample surface with a spot size diameter of about 1 mm, resulting in an excitation power of about 2.5 W/cm². When the laser beam hit the sample, the photoluminescence emitted from the sample together with the laser beam reflected from the sample surface and they are focused using a concave lens which is positioned between the cryostat and the FTIR spectrometer. The laser diode and lens could be moved in x, y, z directions to align the laser beam and the sample emission, giving a maximum signal that is received into the FTIR system. The photoluminescence emission of the sample was analysed using a Bruker Vertex 70 Fourier Transform Infrared (FTIR) spectrometer with a resolution of 0.5 cm⁻¹ and the laser beam was blocked out using an optical edge filter. The resultant photoluminescence emission was detected by a liquid nitrogen cooled 77 K InSb photodetector. The signal is sent to the computer by the Stanford SR830 DSP lock-in amplifier, and it is analysed using OPUS software to convert the received signal to the spectrum of emission intensity as a function of wavenumber corresponding to the photoluminescence emission of the sample.

4.4 Transmission setup

The transmission spectra of the samples were measured using a Bruker Vertex 70 Fourier Transform Infrared (FTIR) spectrometer and the setup of this system is shown in [Figure 4.5](#). The sample was placed inside the sample chamber of a liquid nitrogen cooled 77 K cryostat. Using a temperature controller, the temperature of the sample chamber can be chosen in the range from 77 K to 300 K. The cryostat was positioned in the path of the light beam between the (FTIR) Michelson interferometer and the InSb detector. Using a beam splitter (half-silvered mirror), the broadband infrared light is split into two beams, one reflected back towards the

beam splitter by a fixed mirror and one reflected back by a moveable mirror. The two light beams recombine on the other side of the beam splitter and then the recombined beam hits the sample. The transmitted light from the sample is detected by a 77 K InSb detector. In the step scan mode of the FTIR system, the detected signal (transmitted light from the sample) is recorded as a function of the wavelength, corresponding to the change in the optical path difference caused by the change in the position of the moving mirror.

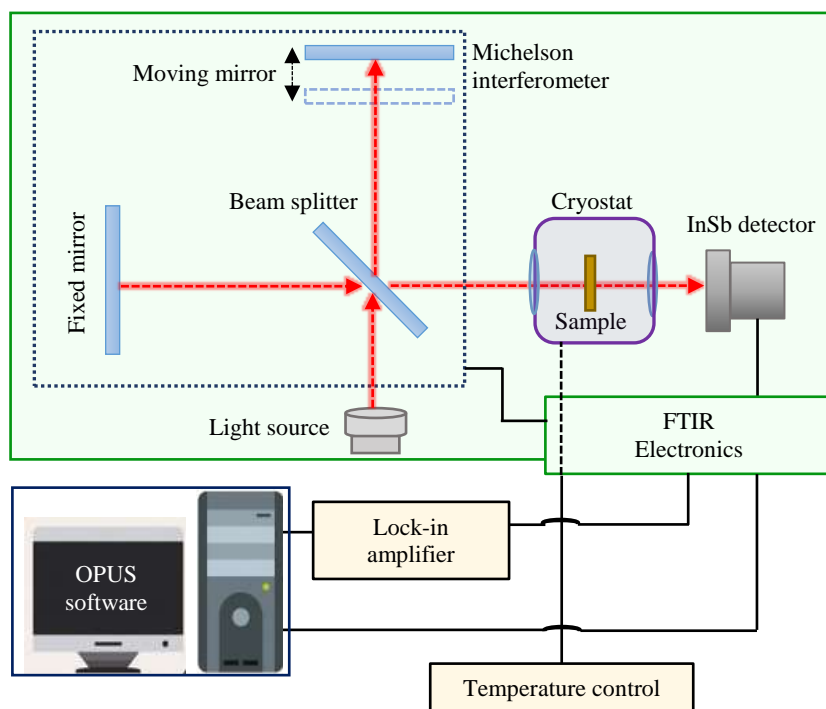


Figure 4.5: Schematic diagram of the FTIR system configured to measure the transmission of the samples.

4.5 Scanning electron microscopy (SEM)

Scanning electron microscopy (SEM) is a powerful-magnification tool, which is used to produce high resolution images from the sample by scanning the surface with a beam of focused electrons in high-vacuum. These electrons are emitted using typically either a thermionic source or field emission source. The electron beam is then focused using electromagnetic lenses. The interaction between the electron beam and the atoms of the sample produces various signals recorded by different detectors, showing information about the sample composition and the surface topography. Resolution better than 1 nm and magnification more than 1,000,000x can

be achieved using the SEM instrument. In our work, an ultrahigh-resolution JEOL JSM-7800F Field Emission SEM (see [Figure 4.6](#)) was used to produce the cross-section and the surface images of the samples. It has accelerating voltage in the range of 10 V to 30 kV, a magnification range of 25× to 1,000,000×, a resolution of 0.8 nm at 15 kV, and probe current range of a few pA to 200 nA.

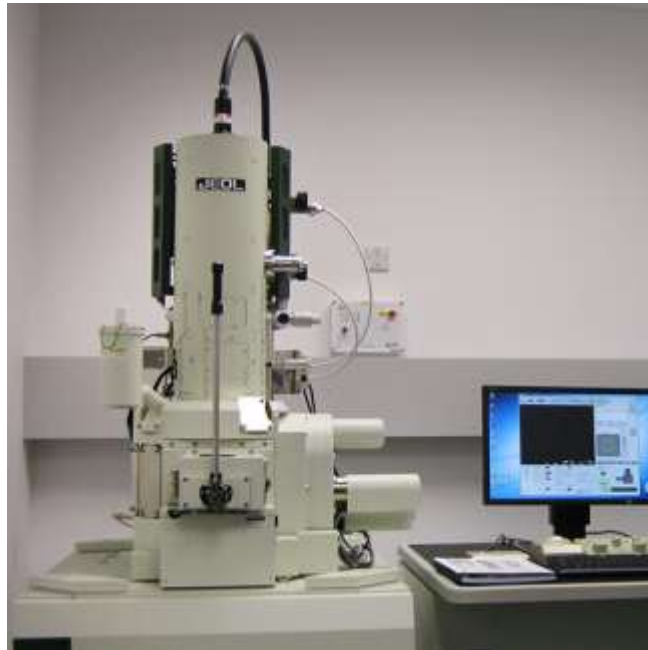


Figure 4.6: Scanning electron microscope (SEM) tool.

4.6 Device Fabrication

After MBE growth the devices that are presented in this work were processed in the class 1000 and 100 cleanrooms at the Quantum Technology Centre of Lancaster University Physics Department. All the devices were fabricated using the mask No.1 (see [Figure 4.7\(a\)](#)), except one used the mask No.2 (see [Figure 4.7\(b\)](#)). Both masks contain different mesa sizes, for mask No.1, the circle mesas have the diameters, 800 μm , 400 μm , and 200 μm . The square mesas of the mask No2 have the dimensions, 600 μm , 400 μm , and 200 μm .

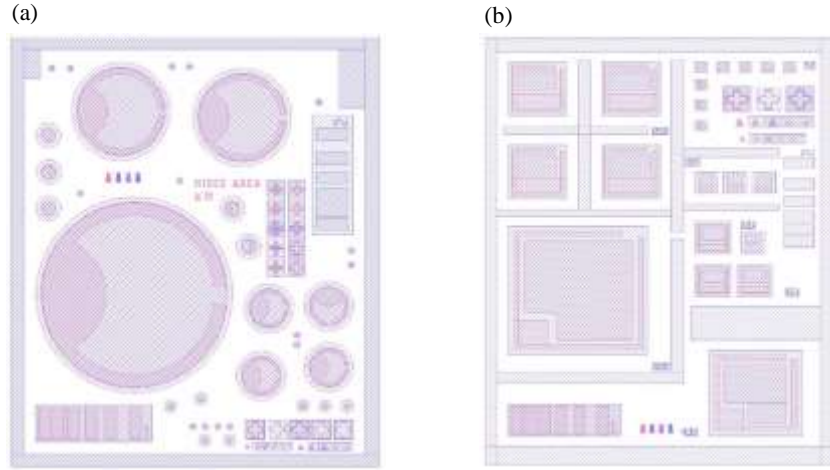


Figure 4.7: Device patterns of varying mesa dimension of (a) mask No.1 and (b) Mask No.2.

The fabrication steps of the device processing using mask No.1 are illustrated in Figure 4.8. Typically, the processing was carried out using standard photolithography and wet chemical etchants followed by Ti/Au metallization for the Ohmic contacts. The steps of the device processing are discussed in detail as follows:

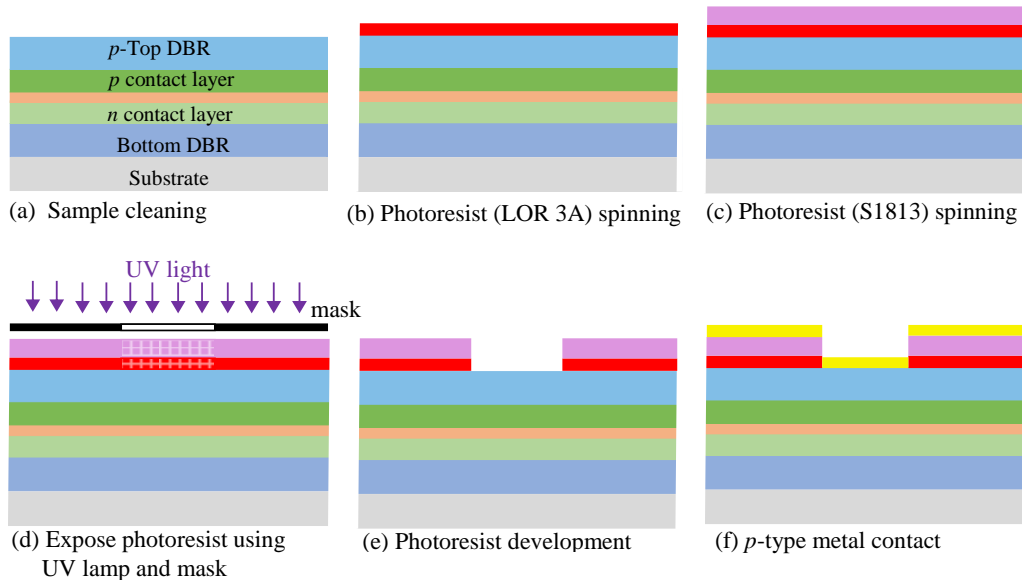


Figure 4.8: Schematic illustration of the fabrication steps for the definition of RCLEDs (using mask No.1). (a) Cleaning sample using acetone and IPA. (b-d) First photolithograph process, applied photoresist LOR 3A and S1813 on the sample surface and then the sample with photoresist layers was exposed using UV light and the mask. (e) Photoresist development using MF-SD-26 developer. (f) Au/Ti metal *p*-type contact deposited on the surface of the sample using thermal evaporator.

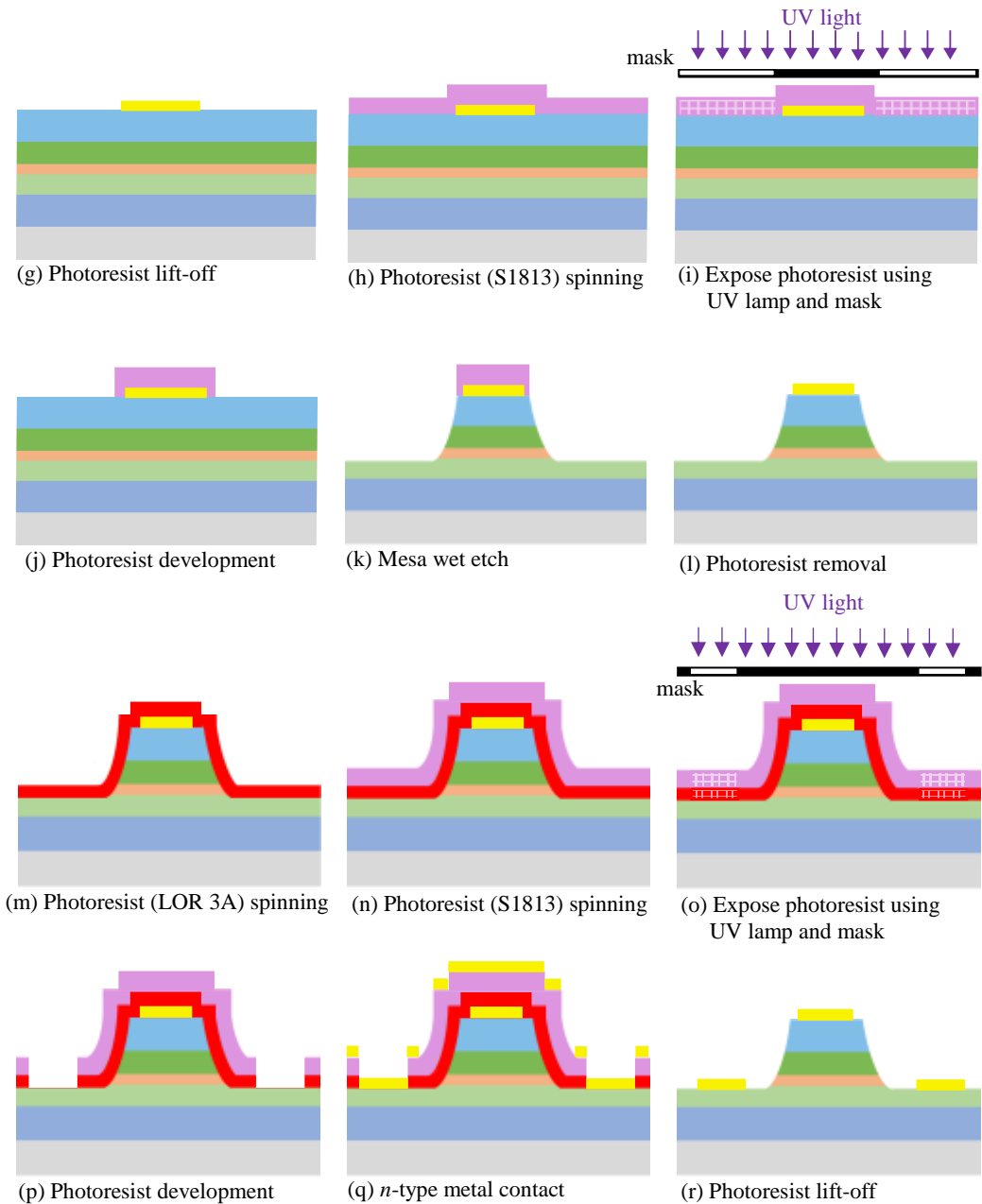


Figure 4.8: (Continue) Schematic illustration of the fabrication steps for the definition of RCLEDs. (g) Photoresist lift-off using acetone. (h-i) second photolithography process, applied photoresist (S1813) on the sample surface and then the sample with photoresist was exposed. (j) Photoresist development using MF-SD-26 developer. (k) Mesa etching, etch the top layers and stopping within *n*-type layer using. (l) Photoresist removal using Microposit 1165 remover. (m-o) third photolithograph process, applied photoresist LOR 3A and S1813 on the sample surface and then the sample with photoresist layers was exposed using UV light and mask. (p) Photoresist development using MF-SD-26 developer. (q) Au/Ti metal *n*-type contact deposited on the surface of the *n*-type layer. (r) Photoresist lift-off using acetone.

Sample preparation: In this step, the sample surface is cleaned of any undesirable particles by immersing the samples in the acetone and isopropyl alcohol (IPA) for 4 minutes each. After that, the samples are dried from the remaining liquid using compressed nitrogen gas.

Photolithography 1: In this step, using a spin coating method, a thin uniform thickness of an optically sensitive polymer (photoresist) is applied on the sample surface. Using a clean pipette, a few drops of LOR 3B photoresist is distributed on the sample surface, and spun at 3000 rpm for 30 seconds. Then the sample was baked at 180 °C using a hotplate for 5 minutes, providing a thickness of about 350 nm of LOR 3A. Typically, the thickness of the photoresist is determined by the parameters: time, speed and acceleration. After that, S1813 photoresist was applied on the sample surface and spun at 4000 rpm for 60 seconds. Then the sample was baked at 120 °C for 2 minutes, resulting in a thickness of about 1µm of S1813 photoresist layer. After that, the mesa patterns of the mask (given in the figure) were developed on the photoresist layers using a Suss Microtec MJB4 mask aligner with a 260 W ultraviolet (UV) lamp. The mask was aligned with the sample, where the top contact features are clear and the background is solid chrome. The sample surface were exposed to UV light (365 nm) for 2.5 seconds, causing a photochemical reaction between incident light and photoresist layers. The area of the photoresist layers that has been exposed by UV light is removed by rinsing the sample in Microposit MF-SD-26 developer for about 90 seconds. The sample is then rinsed in deionized water and dried using compressed nitrogen gas.

Metallization and lift-off (*p*-type contact): In this step, the metal top contact (*p*-contact) is applied using a Moorfield thermal evaporator. The samples with photoresist patterns are fixed on an aluminium plate using Kapton tape and then the plate with samples is put into the evaporator chamber by inserting it on its holder at the top of the evaporator. This means that the sample surface is facing the Au and Ti coils. The metals, Au wire and Ti pellets, are cleaned using acetone and IPA and then are placed into their respective coils. The pressure inside the chamber was pumped down to the order of 10^{-6} mbar to prevent oxidation. The shutter of the samples is closed before the Ti coil is heated by gradually increasing the current to about 70 A,

then the shutter could be opened to start the deposition of Ti on the sample surface. The deposition rate was approximately 2 °A/s, resulting in a thickness of about 20 nm of Ti layer. The shutter is closed and the current is gradually decreased to 0 and then the Au coil was heated by gradually increasing the current through the coil to 27 A followed by opening the shutter to start the deposition of Au on the sample surface. The shutter is closed again and the current is gradually decreased to 0. About 150 nm Au-thick was deposited on top of Ti at a rate of 3 °A/s. The metal is deposited on the samples surface, covering all the area that is with or without photoresist. After metal deposition, the sample was rinsed in acetone to dissolve the photoresist mask and lift-off the metal that was deposited on top of the photoresist, leaving only the metal contact the samples surface. Then the samples rinsed in IPA and dried using compressed nitrogen gas.

Photolithography 2: In this step, after the top contact deposition, S1813 photoresist was applied on the sample and spun using the same parameters of speed, acceleration and time that were used before in photolithography 1, followed by baking the sample at 120 °C for 2 minutes. Using the mask aligner, the sample is first aligned with the mask, where the background is clear and the top mesa features are solid chrome. The sample surface was then exposed to UV light using the same parameters of the power and exposure time that were used before. After that, the sample with photoresist was immersed in the developer to remove the photoresist that is exposed by the UV light, following by rinsing the sample in deionized water and then dried using nitrogen gas gun. The Photoresist patterns were viewed using the optical microscope to ensure that the top contact features on the sample surface were covered by the photoresist and the sample is ready for the wet etching process.

Mesa etching: In order to produce the individual devices, the upper part p-type cladding layers and the un-doped active region layer which are not covered by photoresist should be etched down to stop within the n-type cladding layer. GaSb and AlAsSb DBR layers were etched using a dilute ammonia based etchant at a rate of 300 nm/min. For etching the InAsSb layer, 20 g of citric acid (C₆H₈O₇) was dissolved in 20 ml deionized water and then the solution mixed with

hydrogen peroxide (H_2O_2) in ratio (2:1). The etch rate of the InAsSb layer was about 100 nm/min. Sulphuric acid/hydrogen peroxide/deionized water ($\text{H}_2\text{SO}_4:\text{H}_2\text{O}_2:\text{H}_2\text{O}$) (1:8:80) solution was used for etching the AlInAs/InAsSb QWs at a rate of about 500 nm/min. After each etch step, the sample was directly rinsed in deionized water and then dried using compressed nitrogen gas. In order to measure the thickness of the etched layer, a profile meter was used after each etching step. All the etch process is performed at room temperature.

Photoresist removal: after mesa etching, the sample with photoresist was immersed in Microposit 1165 remover for 5 minutes to dissolve the photoresist followed by rinsing the sample in the deionized water and then dried using compressed nitrogen gas.

Photolithography 3: In this process, after applying the photoresists (S1813 and LOR 3A) on the sample surface, the mask patterns of the n-type contact were developed on the photoresist layers. The mask was aligned with the sample, where the contact patterns is clear and all other features and background is solid chrome. In this process, the same steps as in photolithography 1 were performed, where the same parameters of the photoresist spinning and baking were used to apply the S1813 and LOR 3A on the sample surface. In addition, the same parameters of the UV power and the exposure time were used to expose the photoresist layers. The sample with photoresist is then rinsed in the developer to remove the exposed photoresist layers.

Metallization and lift-off (n-type contact): Au/Ti metal contact is deposited on the sample using the thermal evaporation and performing the same procedure used to deposit the p-type contact. The sample is then immersed in acetone to dissolve the photoresist layer and lift-off the metal which is deposited on top of the photoresist, leaving the metal contact on the n-type layer. After that, the fabricated samples were rinsed in IPA and dried using nitrogen gas gun.

The fabrication steps of the device processing using mask No.2 are shown in [Figure 4.9](#). The processing was also carried out using standard photolithography and wet chemical etchants followed by Ti/Au metallization for the Ohmic contacts using the same parameters of the fabrication steps, which are used in the previous fabricated device.

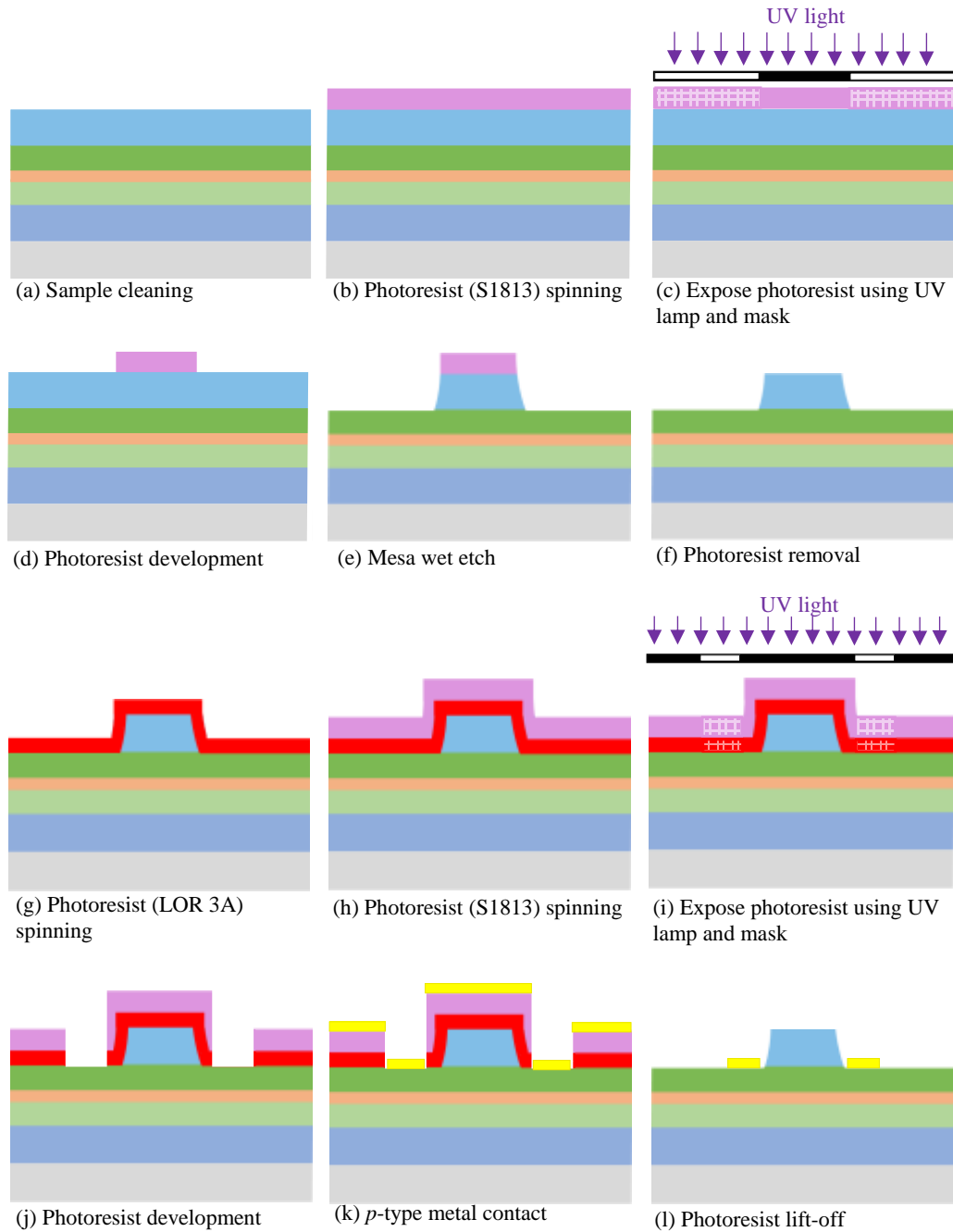


Figure 4.9: Schematic illustration of the fabrication steps for the definition of RCLEDs. (a) Cleaning sample using acetone and IPA. (b-c) First photolithograph process, applied photoresist S1813 on the sample surface and then the sample with photoresist layers was exposed using UV light and the mask that is given in Figure 4.8 (b) using the same parameters which are used in the previous fabricated device. (d) Photoresist development using MF-SD-26 developer. (e) Mesa etching, etch the top DBR layers and stopping within *p*-type cavity layer. (f) Photoresist removal using Microposit 1165 remover. (g-i) Second photolithograph process, applied photoresist LOR 3A and S1813 on the sample surface and then the sample with photoresist layers was exposed. (j) Photoresist development using MF-SD-26 developer. (K) Au/Ti metal *p*-type contact deposited on the surface of the sample using thermal evaporator. (l) Photoresist lift-off using acetone.

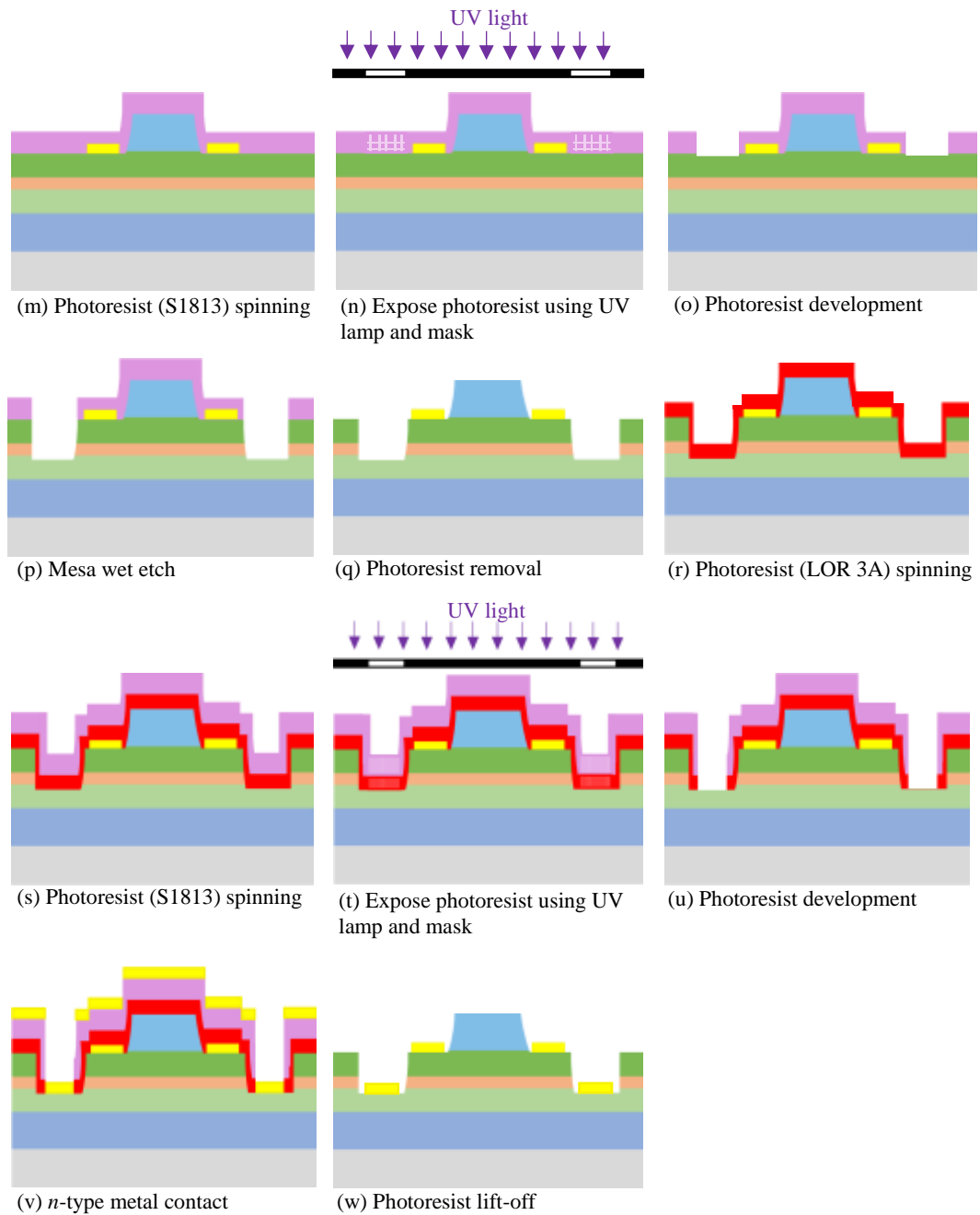


Figure 4.9: (Continued) Schematic illustration of the fabrication steps for the definition of RCLEDs. (m-n) Third photolithography process, applied photoresist S1813 on the sample surface and then the sample with photoresist layers was exposed (o) Photoresist development using MF-SD-26 developer. (p) Mesa etching, etch the *p*-type cavity and un-doped active region layers and stopping within *n*-type cavity layer. (q) Photoresist removal using Microposit 1165 remover. (r-t) Forth photolithograph process, applied photoresist LOR 3A and S1813 on the sample surface and then the sample with photoresist layers was exposed. (u) Photoresist development using MF-SD-26 developer. (v) Au/Ti metal *n*-type contact deposited on the surface of the *n*-layer using thermal evaporator. (w) Photoresist lift-off using acetone.

Wire bonding: Using a diamond scribe, the wafer of the fabricated sample is divided into individual chips and then the chip was attached to the header using Ag conducting paste. An Accelonix TPT HB05 manual wire bonder was used to bond the contact pad to the header pins with 25 μm thick gold wires. One side of wire is connected to the header pin and the other side is connected to the contact pad of the device where a ball bond is formed between them.

4.7 Electroluminescence setup

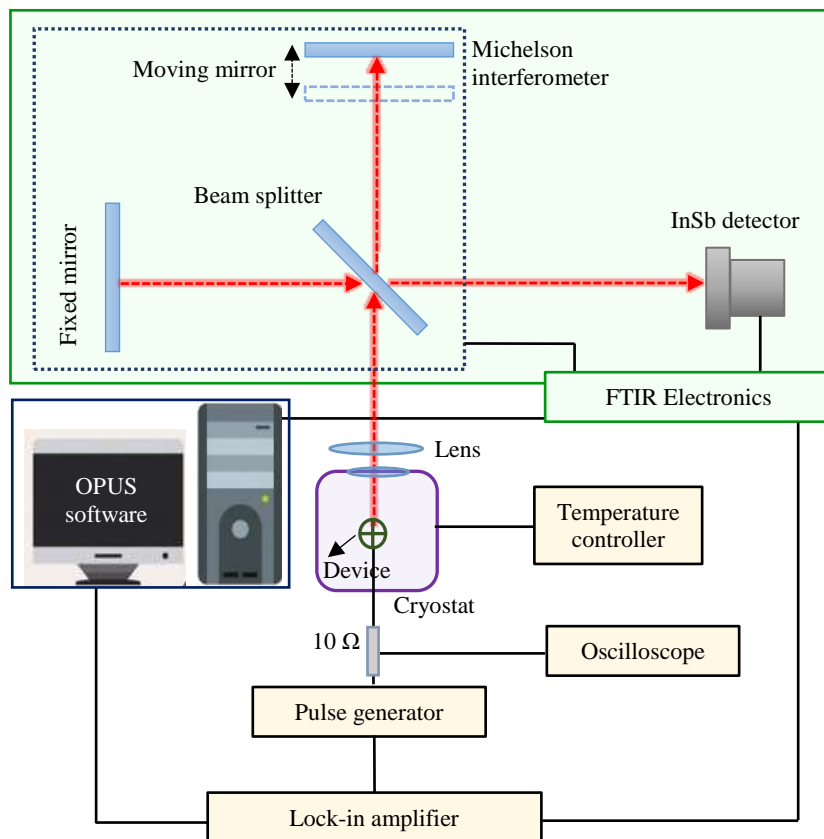


Figure 4.10: Schematic diagram of FTIR electroluminescence system. The red dashed arrow represent the electroluminescence emission of the device.

The schematic diagram setup of the Electroluminescence spectroscopy measurement is shown in Figure 4.10. The current setup is similar to that which is used for measuring the photoluminescence, except the laser source is replaced by pulse generator (Agilent B114A) and the laser filter was removed from the FTIR system. The pulse generator is connected to 10 Ω resistor, and also the reference signal of the pulse generator is sent to the lock-in amplifier. The device and the oscilloscope is connected to the pulse generator through the 10 Ω resistor. In this

setup, the oscilloscope is used to measure the exact current. The electroluminescence emission spectra of the sample were measured over the temperature range from 20 K to 300 K, and at various currents and duty cycle.

4.8 Photo-response experimental setup

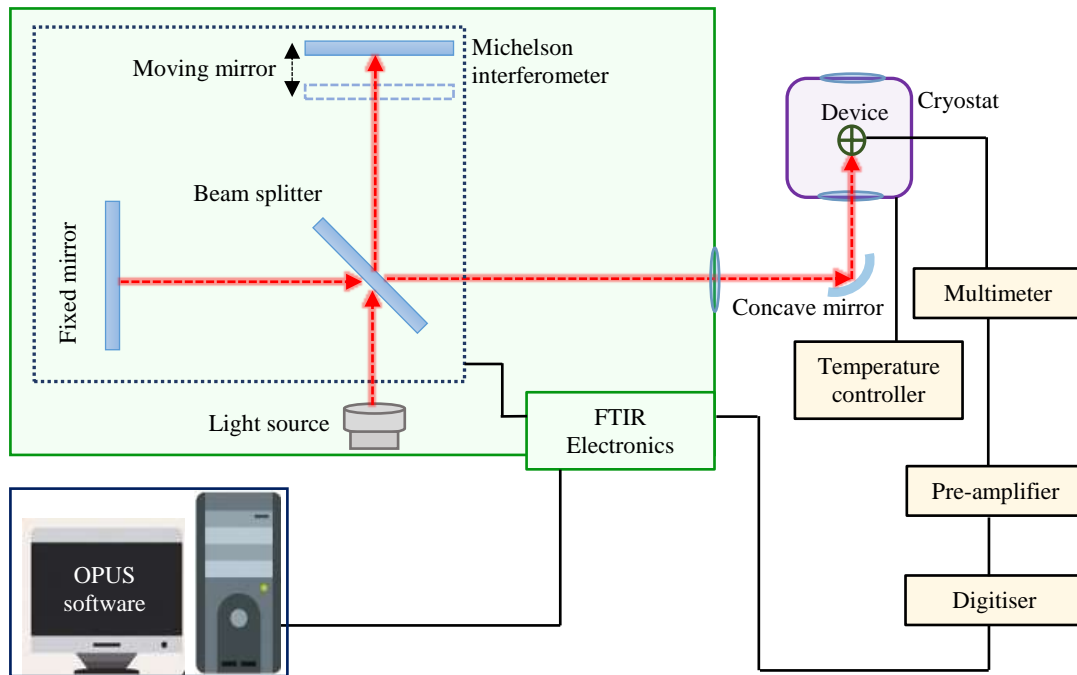


Figure 4.11: Schematic diagram of FTIR photo-response system.

Figure 4.11 shows the schematic diagram of the FTIR photo-response system used to measure the spectral photo-response of the device at different temperatures. The device was placed inside the chamber of the OptistatDN-V2 cryostat (Oxford Instruments) which can be cooled down to 77 K using liquid nitrogen. In this setup, the broadband infrared light beam that is transmitted from the FTIR is used as a light source. A concave mirror is carefully aligned with the light beam of the FTIR to hit the device. A Stanford Research System SR570 pre-amplifier is connected to the device, providing a bias of -0.1 V to measure the spectral response of the device. The photo-response signal is sent from the device to the computer by a Bruker digitiser, and it is analysed using OPUS software to convert the received signal to the spectrum of photo-

response (in A/V) as a function of wavenumber. The results is obtained over the temperature range from 77 K to 300 K, where the temperature is controlled using a temperature controller.

4.9 Current-voltage (I-V) experimental setup

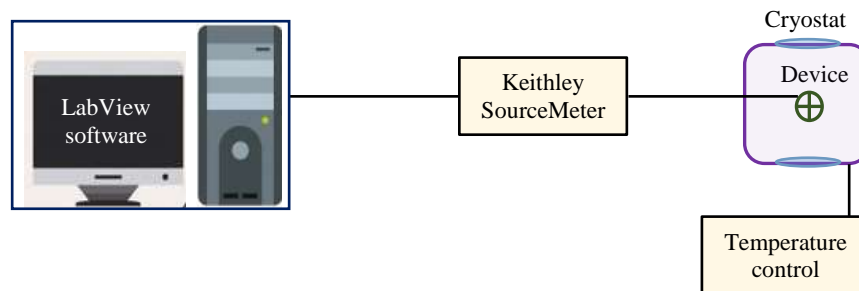


Figure 4.12: Experimental setup of the I-V measurements.

The experimental setup of the current-voltage measurements at different temperature is illustrated in [Figure 4.12](#). The device is placed inside the inner chamber of the liquid helium cooled 4 K cryostat. The temperature of the inner chamber (the device temperature) is controlled over the temperature range from the 4 K to 300 K using the temperature controller. Using a Keithley 2400-LV SourceMeter, which is controlled by LabView software, the applied voltage through the device can be controlled and recorded in small increasing steps. The current is measured corresponding to the voltage recorded, setting to an upper limit value of 200 mA to avoid damaging the device. I-V characteristics are measured over the temperature range from 20 K to 300 K.

Chapter 5

Resonant cavity structures for mid infrared applications: theoretical and experimental study

5.1 Introduction

In this chapter, the optical characteristics of the resonant cavity (RC), including the distribution of the electric field inside the cavity, cavity quality factor (Q), the linewidth of the optical cavity mode ($\Delta\lambda_{\text{cav}}$), and the resonance emission and the integrated emission enhancement factors, were investigated theoretically. The results were simulated over the temperature range from 77 K to 300 K. Also studied was the reflectivity of the DBR mirrors using a transfer matrix method and the number of periods of the DBR layers to achieve high enhancement factors was evaluated. Based on that, four samples were successfully designed and grown on GaSb and InAs substrates using MBE. The structures consist of 1λ -thick cavity sandwiched between 13.5 periods bottom-DBR mirror and 5 periods top-DBR mirror. Different active regions such as bulk InAsSb, AlInAs/InAsSb MQWs and InAs/GaAsSb SLSs were used in these RC structures, positioned at the antinode of the electric field inside the cavity (typically, in the center of the symmetric cavity). The temperature dependence of the transmission of the RC samples was measured experimentally over the temperature range from 77 K to 300 K. The DBR stopband center, the optical mode position, the linewidth of the optical mode and the quality factor of the resonance cavity are evaluated for all samples. At room temperature, the transmission spectra of the RC samples show an optical cavity mode positioned at 4.0 μm , 4.3 μm , 4.5 μm , and 4.6 μm . The results exhibit narrow linewidth (<100 nm), a superior temperature stability (<0.4 nm/K), and a high quality factor, suggesting that these results are attractive characteristics for LEDs suitable for the development of next generation SO_2 , CO_2 , N_2O , and CO gas sensor instrumentation.

5.2 Theoretical analysis

5.2.1 Fabry-Perot transmission

The transmission spectra of the Fabry-Perot cavity were calculated according to equation (2.55). At various reflectivity values (R_1 and R_2), the transmission spectra of the cavity with thickness of 1λ are plotted as a function of wavelength in Figure 5.1(a). It can be seen that when the reflectivity of the mirrors increases, the linewidth of the optical modes and the transmission intensity decrease.

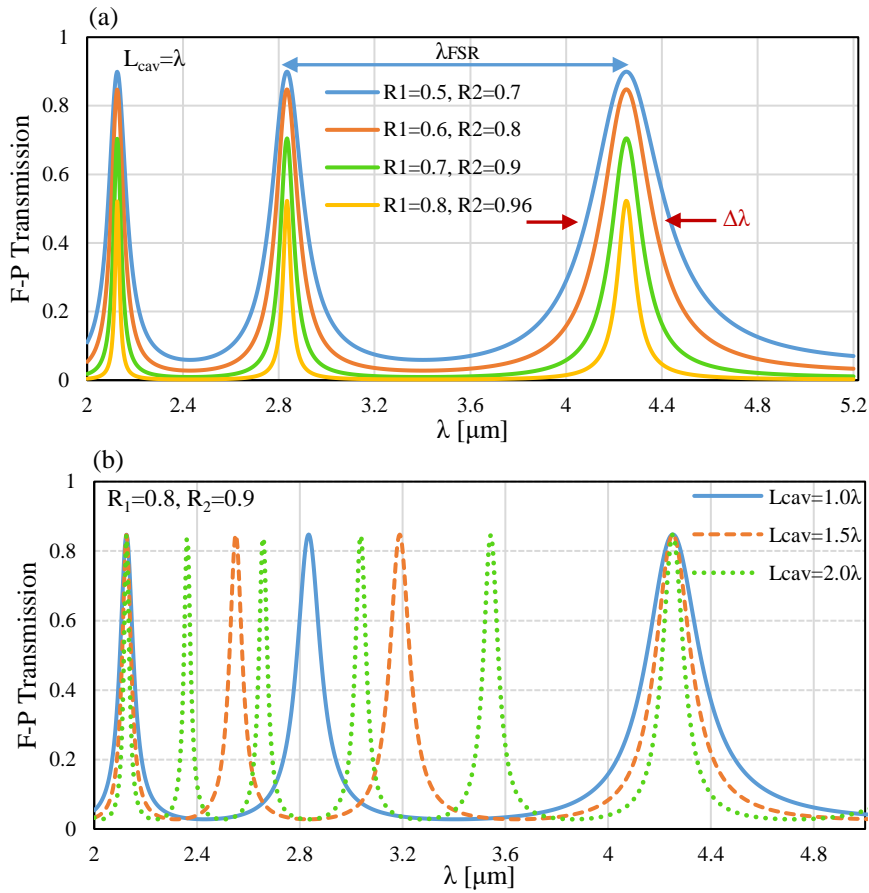


Figure 5.1: Transmission spectrum of Fabry-Perot cavity, (a) at different reflectivities of R_1 and R_2 (for cavity thickness = 1λ), and (b) at different cavity thickness. The cavity refractive index $\bar{n} = 3.8$.

On the other hand, the Fabry-Perot cavities at different thickness were also investigated and the results are plotted in Figure 5.1(b). The linewidth of the optical modes decreased as the cavity thickness increases, while the number of optical modes increased with increasing thickness. There is no noticeable change observed in the peak transmission intensity.

5.2.2 Optical parameters of the Fabry-Perot cavity

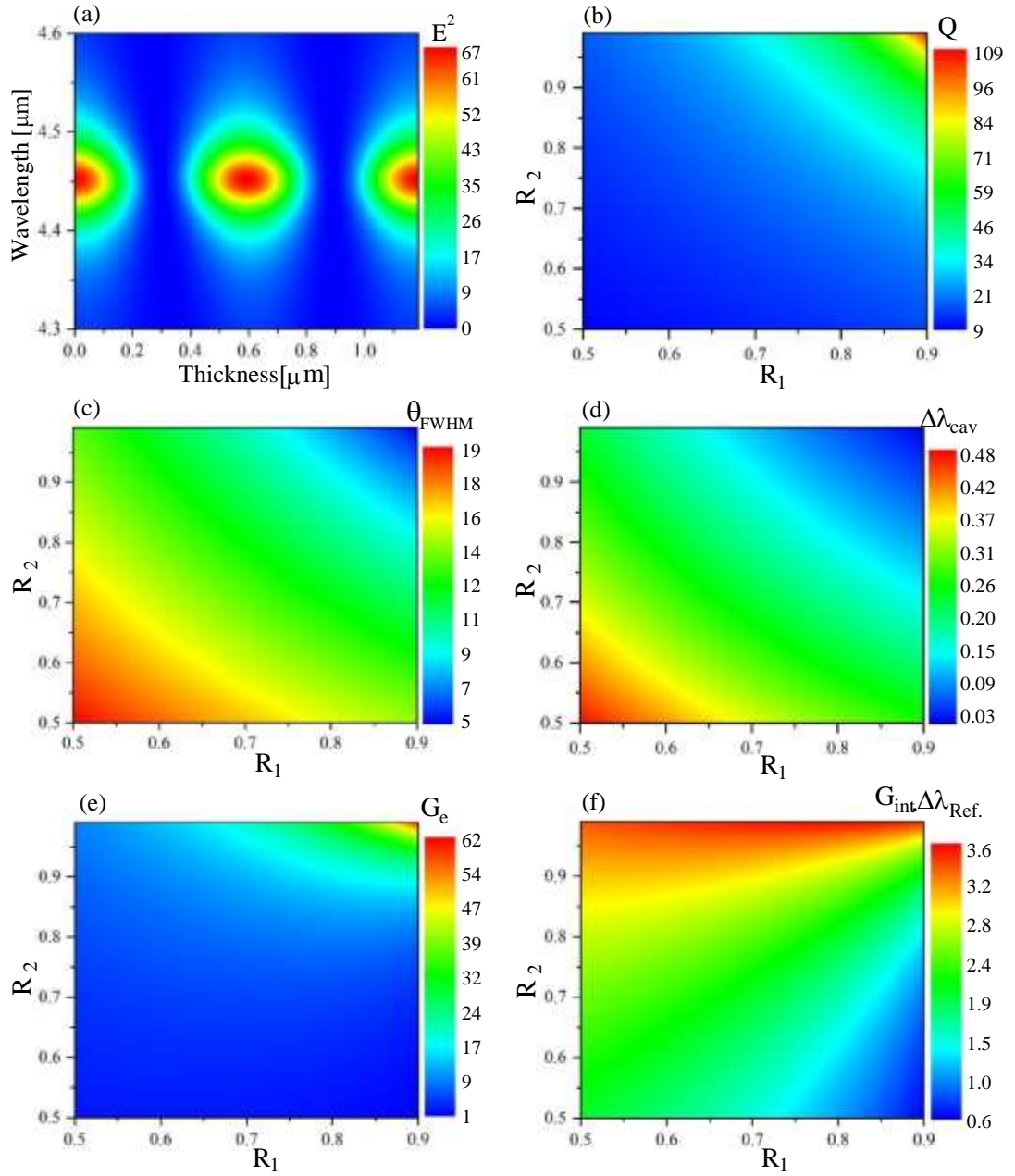


Figure 5.2: Room temperature simulation results of the Fabry-Perot cavity parameters, (a) the distribution of the electric field inside the cavity. (b) Quality factor, Q , (c) the internal angle (on axis lobe), θ_{FWHM} , (d) Linewidth of the optical mode emission, (e) and (d) The resonant emission (G_e) enhancement factor, and the integrated emission (G_{int}) enhancement factor as a function of the top and bottom DBR mirror reflectivity, R_1 and R_2 , respectively. The refractive index of the cavity is $\bar{n} = 3.8$ and the cavity thickness = 1λ . The parameters in this work were simulated using *MATLAB* software.

The Fabry-Perot cavity parameters such as, the electric field distribution (E), the quality factor (Q), the internal angle (on axis lobe) (θ_{FWHM}), the linewidth of the optical mode emission

($\Delta\lambda_{\text{cav}}$), the intensity emission enhancement (G_e), and the integrated emission enhancement (G_{int}) were investigated using the equations (2.59), (2.60), (2.58), (2.72), and (2.73), respectively. Results were obtained for the 1λ -thick cavity and are plotted as a two-dimensional plane (contour plot) in Figures 5.2(a-f). As expected, the distribution of the electric field inside the cavity shows an antinode located in the center of the cavity (see Figure 5.2(a)), suggesting that the active region (emitter material) should be placed in the center of the cavity.

As seen in Figures 5.2(b-d), it was found that the cavity quality factor (Q) increases as the reflectivity of the mirrors R_1 (top mirror) and R_2 (bottom mirror) increases, while the linewidth of the optical mode emission and the internal angle decreased with increasing reflectivity of the mirrors. Figures 5.2(e) and 5.2(f) show the emission rate enhancement at the resonance wavelength and the integrated emission enhancement as a function of the DBR mirror reflectivity. The highest integrated emission enhancement (G_{int}) is achieved when $R_2 > 95\%$, and $50\% < R_1 < R_2$. Furthermore, in order to obtain a high emission enhancement factor (G_e) of more than say 30 times, R_2 and R_1 should be greater than 96% and 82%, respectively.

In order to design successful resonant cavity structures, the cavities in our samples were surrounded by two DBR mirrors, a bottom DBR with reflectivity of R_2 and a top DBR with reflectivity of R_1 . The reflectivity of these mirrors was modelled using a transfer matrix method [74], with the refractive indices of $n_L \approx 3.16$ for AlAsSb and $n_H \approx 3.76$ for GaSb. The main advantage of this layer combination is the large refractive index contrast ($\Delta n \sim 0.6$), which requires fabricating only a few quarter- λ -thick layer pairs to achieve high reflectivity. The simulation results indicate that 13.5 periods of the bottom DBR and 5 periods of the top DBR are sufficient to achieve high reflectivity, $R_2 > 97\%$ and $R_1 > 83\%$, as shown in Figure 5.3(a). (The half period is necessary for phase matching). The stopband center of the DBR (λ_{DBR}) and the optical mode position of the micro-cavity (λ_{cav}) are related to the period layer thickness of the DBR mirror ($d_L + d_H$) and the cavity thickness (d_{cav}), respectively, via the relations: [128]

$$\lambda_{\text{DBR}} = 2(n_L d_L + n_H d_H) \quad (5.1)$$

$$\lambda_{\text{cav}} = n_{\text{cav}} d_{\text{cav}} \quad (5.2)$$

Where, d_L and d_H are the thickness of the alternating DBR layers of the AlAsSb and GaSb, respectively. Ideally, (i) the optical mode wavelength (λ_{cav}) and the emission in the active region (λ_{source}) should be in resonance, (ii) the MQW in the active region should be located at an antinode of the electric field inside the cavity, (iii) there should be resonance between λ_{DBR} and λ_{cav} .

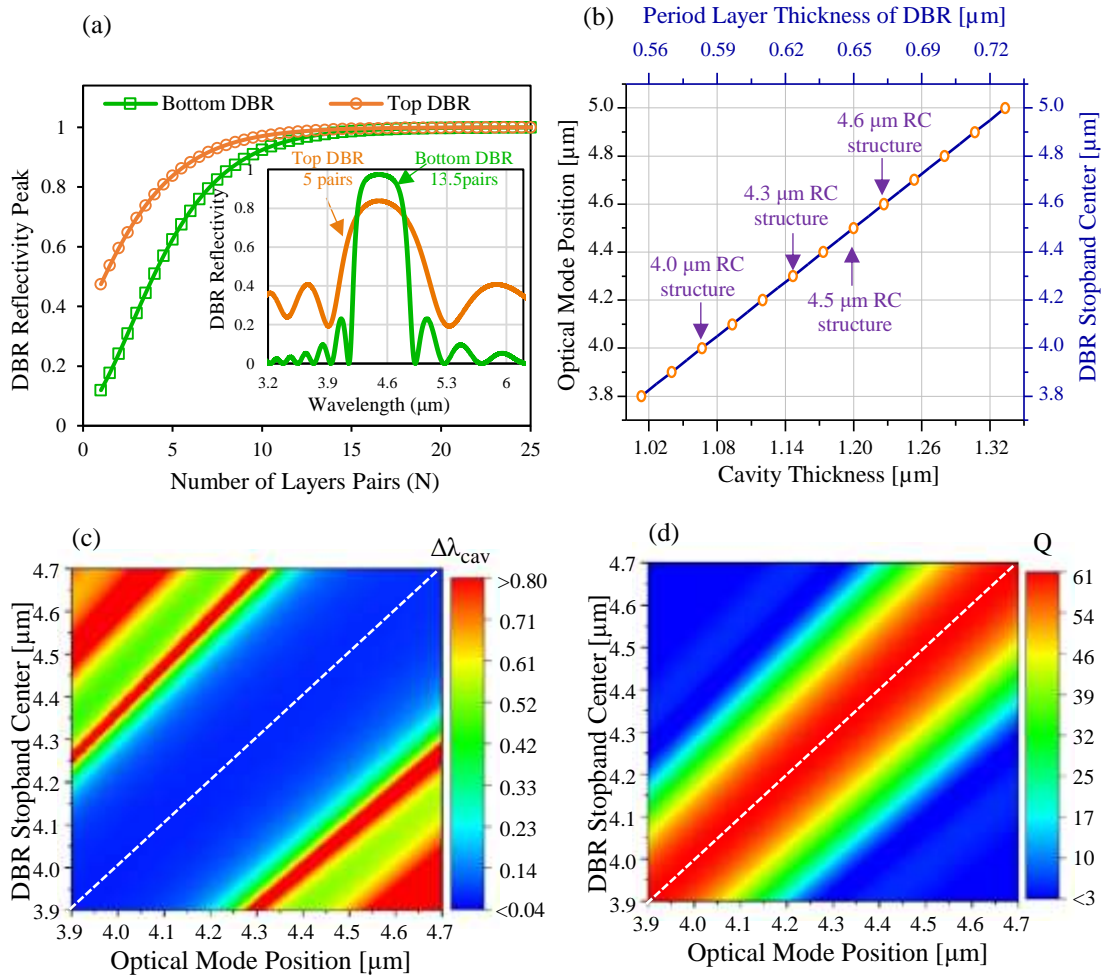


Figure 5.3: (a) The reflectivity peak of the DBR as a function of the number of layer pairs (N). The inset shows simulations of the DBR reflectivity as a function of the wavelength for 13.5 pairs (bottom DBR) and 5 pairs (top DBR). (b) The resonance condition between the optical mode and the DBR stopband center as a function of the cavity thickness and the DBR period layer thickness, respectively. (c) and (d) Room temperature simulations of the optical mode linewidth ($\Delta\lambda_{\text{cav}}$) and the quality factor (Q) as a function of the DBR stopband center and the peak emission of the cavity mode, respectively. The white dashed-dotted line represents the resonance case between the optical cavity mode and the DBR stopband center.

We calculated the values of the λ_{DBR} and λ_{cav} at resonance as a function of the DBR period thickness ($d_L + d_H$) and the cavity thickness (d_{cav}), respectively. The results are plotted in [Figure 5.3\(b\)](#). A small change in the thickness of d_{cav} and/or $d_L + d_H$ leads to a change in λ_{cav} and λ_{DBR} , respectively, causing detuning between λ_{cav} and λ_{DBR} . This detuning is considered theoretically in [Figure 5.3\(e\) and 5.3\(f\)](#) which map the effect of detuning on linewidth of the optical cavity mode ($\Delta\lambda_{cav}$) and the quality factor (Q), respectively. The dashed-dotted line represents the resonance case between λ_{cav} and λ_{DBR} , where maximum quality factor is achieved. Our results show that even if there is some detuning, the Q factor still maintains high values over a wide wavelength range, and $\Delta\lambda_{cav}$ is still narrow (<100 nm), predicting that the enhancement factors are also achieved.

5.2.3 Temperature-dependent transmission of the DBR mirror

The experimental and theoretical results of the transmission spectra of the DBR mirror, consisting of 13.5 pairs of AlAsSb/GaSb layers, were demonstrated as a function of the temperature over the range from 77 K to 300 K in [Figures 5.4\(a-f\)](#). The sample was grown on GaSb substrate using MBE. The experimental measurements of the reflectivity spectra of the DBR mirror are presented in [Figure 5.4\(a\)](#) at 77 K and 300 K, showing a centre wavelength of the DBR at 3.205 μm and 3.252 μm , respectively. In order to investigate the temperature-dependent transmission of the DBR mirror theoretically, it is necessary to evaluate the thickness and the reflective index of the DBR layers as a function of temperature. The lattice constant (a) of the DBR layers can be determined using the formulas: [\[129\]](#)

$$a_{\text{GaSb}} = 6.0959 + 4.72 \times 10^{-5}(T - 300) \quad (5.3a)$$

$$a_{\text{AlAs}} = 5.6611 + 2.90 \times 10^{-5}(T - 300), \quad (5.3b)$$

$$a_{\text{AlSb}} = 6.1355 + 2.60 \times 10^{-5}(T - 300), \quad (5.3c)$$

Based on equations (5.3a) and (5.43), the lattice constant of the InAsSb layer can be calculated by interpolation from the formula:

$$a_{\text{AlAs}_x\text{Sb}_{1-x}} = x \cdot a_{\text{AlAs}} + (1 - x) \cdot a_{\text{AlSb}} \quad (5.5)$$

where, a_{GaSb} and $a_{\text{AlAs}_x\text{Sb}_{1-x}}$ are the lattice constant of GaSb and AlAs_xSb_{1-x} layers, respectively. The theoretical results of the temperature dependence of the layers lattice constant are shown in [Figure 5.4\(b\)](#). According to these equations, the thickness of the DBR layers were calculated and plotted as a function of temperature in [Figure 5.4\(c\)](#). It can be seen that the thickness of the GaSb layer and the AlAs_{0.08}Sb_{0.92} increase with increasing temperature by a factor of $1.65 \times 10^{-3} \text{ nm.K}^{-1}$ and $1.10 \times 10^{-3} \text{ nm.K}^{-1}$, respectively. This change in the thickness of the DBR layers leads to a shift in the DBR stopband center by approximately 7% of the total wavelength shift. Therefore, the major contribution originates from the change in the variation in the refractive index of the DBR layers as a function of temperature. [Figure 5.4\(d\)](#) shows the temperature dependence of the refractive index of the GaSb and AlAsSb DBR layers which are measured to be $3.09 \times 10^{-4} \text{ K}^{-1}$ and $4.61 \times 10^{-5} \text{ K}^{-1}$, respectively, using the following formula:[\[130\]](#)

$$\frac{1}{n} \frac{dn}{dT} (\text{GaSb}) = 8.2 \times 10^{-5} \text{ K}^{-1} \quad (5.5)$$

$$\frac{1}{n} \frac{dn}{dT} (\text{AlAs}_x\text{Sb}_{1-x}) = [4.6 \times 10^{-5}x + 1.19 \times 10^{-5}(1-x)] \text{ K}^{-1} \quad (5.6)$$

Based on that, the transmission spectra of the DBR mirror were investigated theoretically and are plotted in [Figure 5.4\(e\)](#). It was found that the spectra shift towards longer wavelength when the temperature increases, showing a stopband center of the DBR at $3.210 \text{ } \mu\text{m}$ (77 K) and at $3.251 \text{ } \mu\text{m}$ (300 K) which were calculated using equation (5.1). The thickness and the refractive index in this equation are functions of temperature.

The shift in the spectrum is attributed to changes in the thickness and the refractive indices of the DBR layer as temperature increases as illustrated in [Figures 5.4\(c\) and 5.4\(d\)](#). Over the temperature range from 77 K to 300 K, the experimental results of the stopband center wavelength of the DBR were plotted together with corresponding numerical results in [Figure 5.4\(f\)](#), exhibiting variation at a rate of $\sim 0.184 \text{ nm/K}$ (numerical) and $\sim 0.22 \text{ nm/K}$ (experimental). Furthermore, and as temperature increases, the experimental transmission spectra of the DBR mirror show that the side peaks, on the right side of the stopband DBR, shift towards the longer wavelength at a higher rate compared to that of the side peaks on the left side.

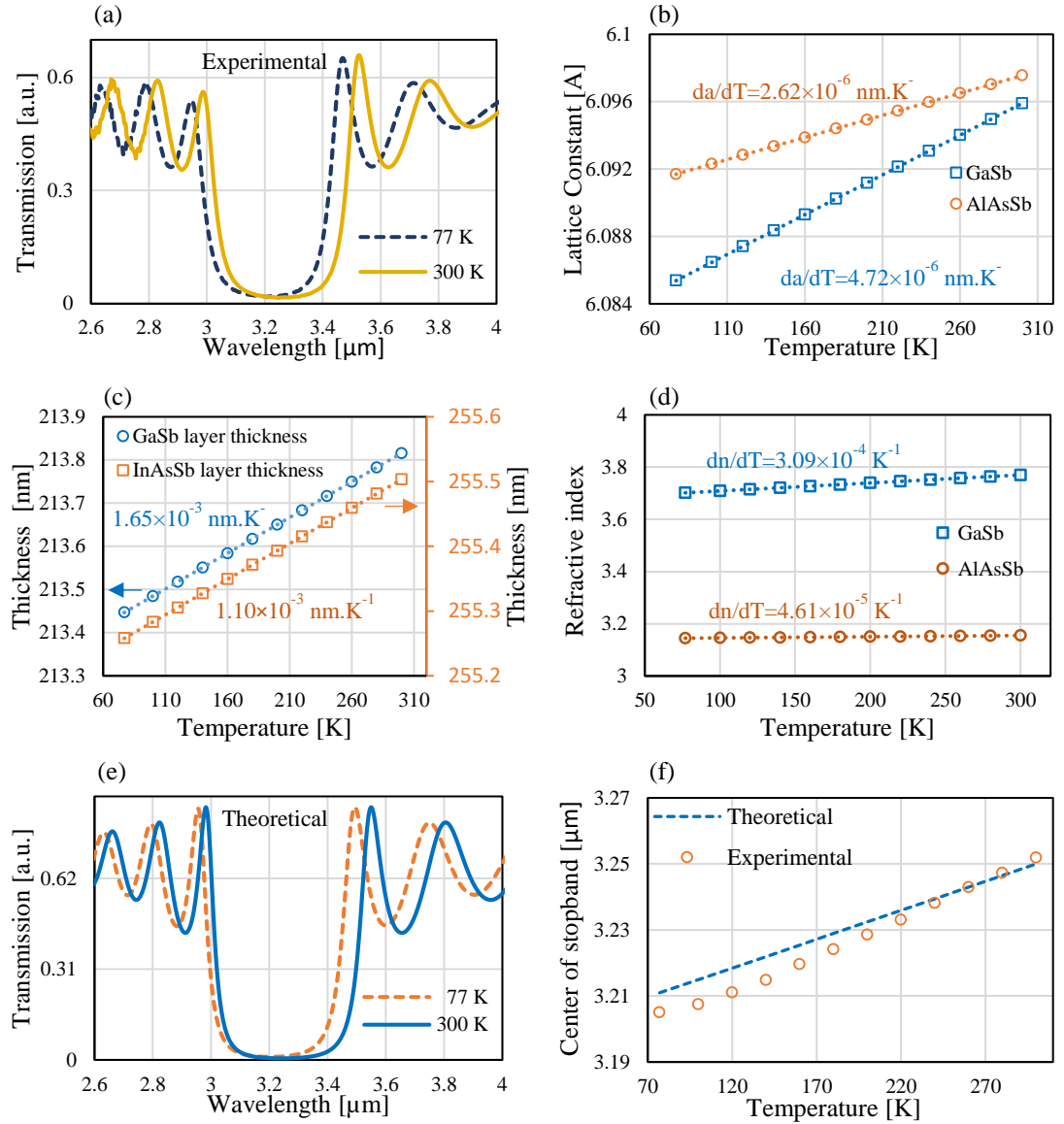


Figure 5.4: (a) Experimental transmission spectra of the 13 pairs DBR mirrors at 77 K and 300 K. (b) Temperature coefficient of the lattice constants for the DBR layers. (c) Temperature dependence of the InAsSb and GaSb DBR layers. (d) Temperature coefficient of the refractive index of the InAsSb and GaSb layers. (e) Simulated transmission spectra of the 13 pairs DBR mirrors at 77 K and 300 K. (f) Our experimental results of the DBR stopband center compared to the fitted results calculated from the values of da/dT and dn/dT reported in [127,128], which seems to have a slightly different slope due to the refractive index values that used to calculated the fit values.

5.3 Mid-infrared resonant cavity (RC) structures: Design and growth

Four mid-infrared resonant cavity (RC) structures, consisting of 13.5 pairs of AlAsSb/Ga(As)Sb DBR used as a bottom mirror and a 5 pairs of AlAsSb/Ga(As)Sb DBR used as a top mirror, were designed based on the theoretical results demonstrated in section 5.2.2.

Using molecular beam epitaxy (MBE), three RC samples were singly grown on n -GaSb substrates and another one was grown on an n -InAs substrate. Two samples of the GaSb-based resonant cavity structures used InAsSb for the cavity and another one used GaSb as a cavity, while InAs was used as a cavity material in the InAs-based RC structure. The thickness of the cavities were 1λ corresponding to cavity order $m_c=2$. The energy band diagrams of the cavity layers of the RC structures were simulated using *nextnano*. The growth steps of the RC structures are discussed in detail in the following sections.

5.3.1 Growth of GaSb-based 4.3 μm bulk RC structure with InAsSb cavity

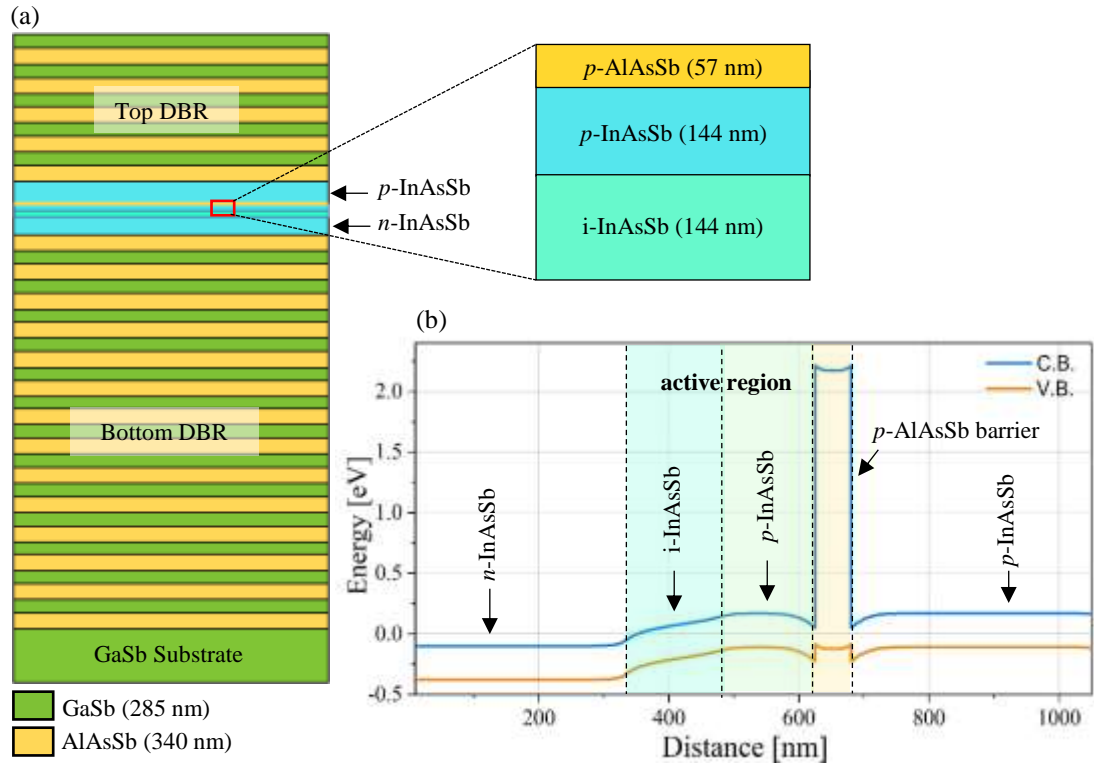


Figure 5.5: (a) A schematic diagram of the GaSb-based 4.3 μm bulk InAsSb RC structure showing the details of the i -InAsSb/ p -InAsSb in the active region of the p - i - n diode within the AlAsSb/GaSb DBRs, which form the microcavity, (b) The energy band diagram of the cavity layers calculated using *nextnano*, showing the electron-blocking barrier.

The InAsSb bulk RC sample, with its structure as illustrated in Figure 5.5(a), was grown as follows: an n -type ($4 \times 10^{17} \text{ cm}^{-3}$) GaSb buffer layer was grown on (001) n -doped GaSb substrate, followed by a 13.5 pairs lattice-matched undoped $\text{AlAs}_{0.08}\text{Sb}_{0.92}$ /GaSb bottom-DBR

mirror. The growth temperature of the DBR layers was 505 °C and the growth rate was 0.7 ML/s and 0.75 ML/s for GaSb and AlAsSb layers, respectively. After that, the first grown layer of 1λ -thick micro-cavity was an n -doped InAs_{0.90}Sb_{0.10} layer followed by i -InAs_{0.90}Sb_{0.10} and p -InAs_{0.90}Sb_{0.10} (used as active region), a 56 nm-thick p -doped AlAs_{0.08}Sb_{0.92} barrier layer to block the flow of majority carriers in the active region, and then a p -doped InAs_{0.90}Sb_{0.10} layer to complete the micro-cavity structure. The growth rate of the cavity layers (included the active region layers) was ~ 0.4 ML/s, except the barrier layer which was ~ 0.74 ML/s. The growth temperature of the cavity layers was fixed at 450 °C, except for the barrier layer which was grown at 530 °C. Finally, the top-DBR mirror comprising 5 pairs of p -doped AlAs_{0.08}Sb_{0.92}/GaSb grown under the same conditions used for the bottom DBR layers. The n -type and p -type dopants were Te and Be, respectively.

Figure 5.5(b) shows the energy band diagram of the cavity structure. As seen from this figure, we designed the cavity considering that the interface between i -InAsSb and p -InAsSb should be located at the center of the cavity where the antinode of the electric field distribution is positioned. This is attributed to the fact that the emission and the recombination process could occur in the p -type layer more than that in the i -layer [6].

5.3.2 Growth of GaSb-based 4.5 μm MQW RC structure with InAsSb cavity

The schematic structure of the MQW resonant cavity is illustrated in Figure 5.6(a). It consists of a single wavelength, 1λ -thick, cavity which is sandwiched between two distributed Bragg reflectors (DBRs). The active region contains 4.5 pairs of Al_{0.12}In_{0.88}As/InAs_{0.85}Sb_{0.15} strained-layer QWs, placed at the center of the cavity corresponding to the antinode position of the electric field intensity in order to obtain maximum enhancement. The energy band diagram of the MQWs structure shows that the band alignment is type I, as depicted in the inset of Figure 5.6(b), where the (e1-hh1) ground state transition occurs in the InAsSb layer. The energy transition and the conduction band offset were calculated to be ~ 268 meV and ~ 30 meV, respectively. Type I band alignment and compressive strain ($\sim 1\%$) are employed to maximize e-h overlap and reduce non-radiative Auger recombination respectively. The thickness of the

$\text{Al}_{0.12}\text{In}_{0.88}\text{As}$ barrier and $\text{InAs}_{0.85}\text{Sb}_{0.15}$ quantum well layers were approximately 6 nm and 17 nm, accordingly.

After growing the bottom-DBR layers on n -GaSb substrate, a 1λ -thick micro-cavity was grown as follows: an n -doped $\text{InAs}_{0.90}\text{Sb}_{0.10}$ layer; i - $\text{AlInAs}/\text{InAsSb}$ QWs; a 10 nm-thick p -doped AlSb barrier layer; and a p -doped $\text{InAs}_{0.90}\text{Sb}_{0.10}$ layer. The AlSb barrier layer provides a strong electron confinement inside the $\text{AlInAs}/\text{InAsSb}$ MQWs region because of the high conduction band offset at the heterointerface of the active region as shown in Figure 5.6(b). After that, the top-DBR mirror comprising 5 pairs of p -doped $\text{AlAs}_{0.08}\text{Sb}_{0.92}/\text{GaSb}$ was grown to finalize the resonant cavity structure. The growth temperatures were 425 °C for the QW layers and 445 °C for the InAsSb cavity layers. All growth rates were < 1 ML/s, with 0.75 ML/s for AlAsSb , 0.95 ML/s for GaSb, 0.25 ML/s for InAsSb and 0.75 ML/s for AlInAs .

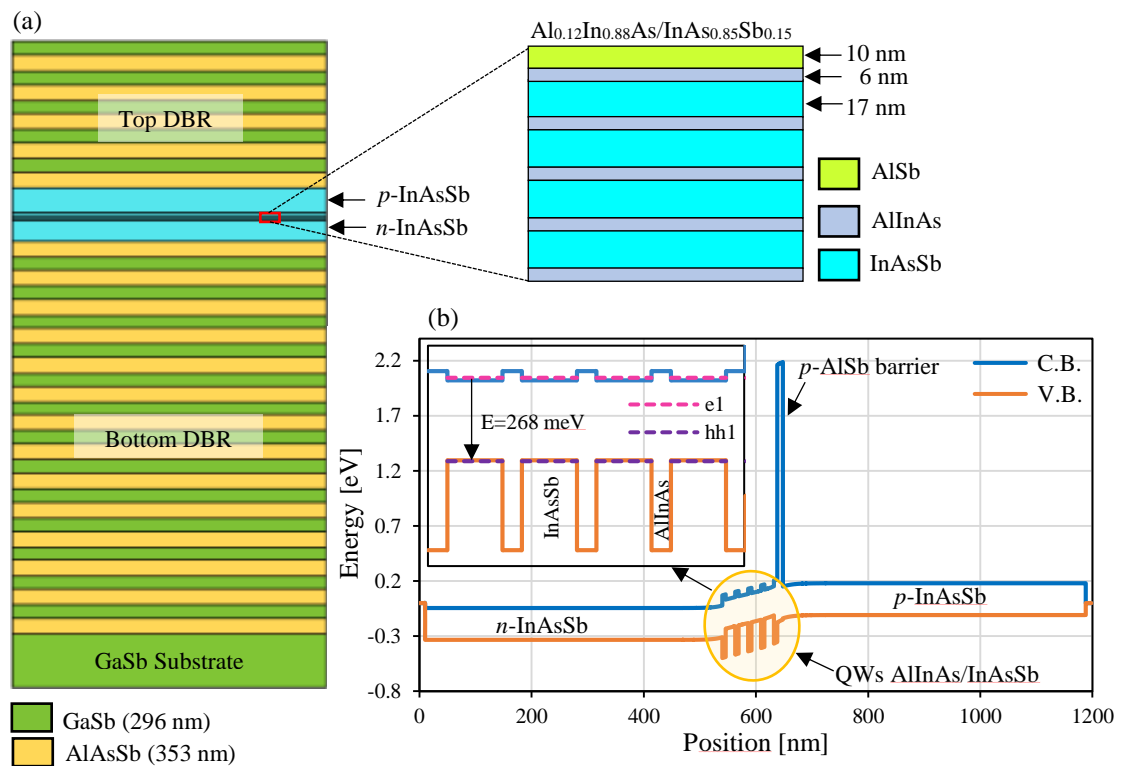


Figure 5.6: (a) A schematic diagram of the GaSb-based 4.5 μm MQWs RC structure showing the details of the $\text{AlInAs}/\text{InAsSb}$ MQW in the active region of the p - i - n diode within the $\text{AlAsSb}/\text{GaSb}$ DBRs, which form the microcavity, (b) The energy band diagram of the cavity layers calculated using *nextnano*, showing the electron-blocking barrier. Details of the type I band alignment in the MQW are highlighted in the inset.

5.3.3 Growth of GaSb-based 4.0 μm MQWs RC structure with GaSb cavity

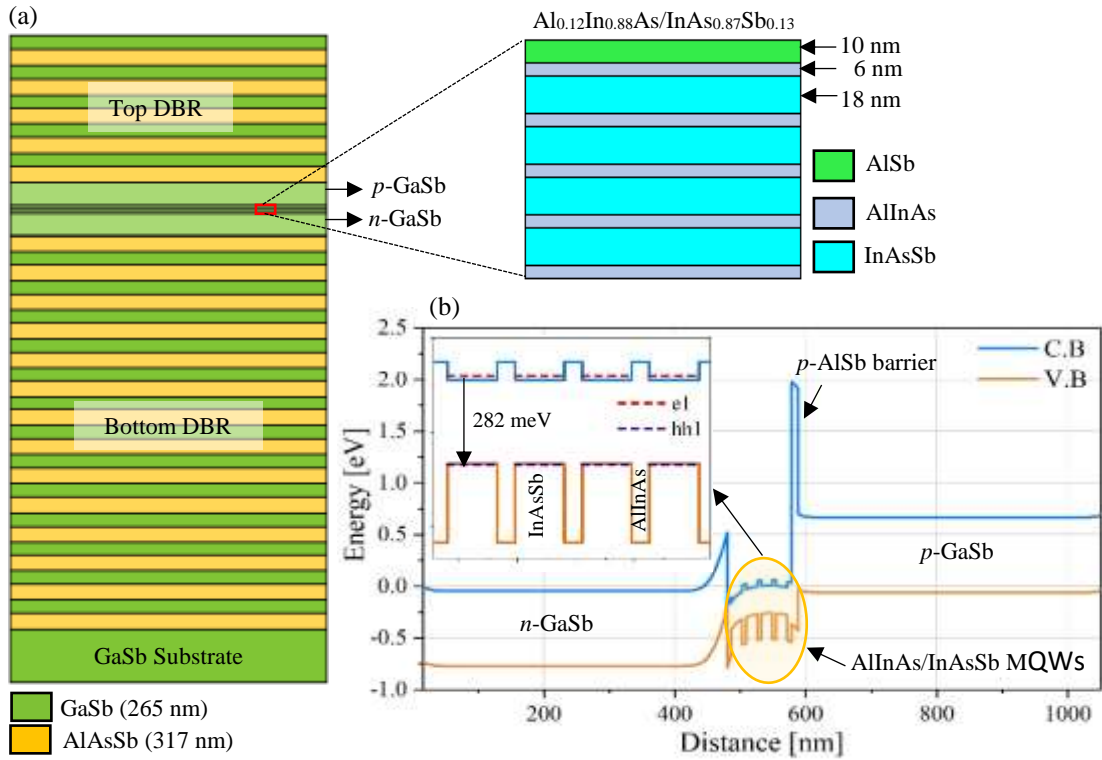


Figure 5.7: (a) A schematic diagram of the GaSb-based 4.0 μm MQWs RC structure showing the details of the AlInAs/InAsSb MQW in the active region of the p-i-n diode within the AlAsSb/GaSb DBRs, which form the microcavity, (b) The energy band diagram of the cavity layers calculated using *nextnano*, showing the electron-blocking barrier. Details of the type I band alignment in the MQW are highlighted in the inset.

The structure of AlInAs/InAsSb MQWs resonant cavity designed for emitting light at $\sim 4.0 \mu\text{m}$ is demonstrated in Figure 5.7(a), consisting of a 1λ -thick GaSb micro-cavity surrounded between two AlAsSb/GaSb DBRs used as top and bottom mirrors. Under the same growth conditions that are used in the last two structures, the layers of the DBR mirrors were grown on n-GaSb substrate. The cavity layers, included the MQWs active region, were grown as follows: an n-GaSb layer grown on the bottom DBR mirror; followed by 4.5 pairs of Al_{0.12}In_{0.88}As/InAs_{0.85}Sb_{0.13} strained-layer QWs (used as active region); a 10 nm-thick p-type AlSb layer used as barrier to confined the electrons in the active region; a p-GaSb to finalize the micro-cavity structure. The growth temperature of the active region layers was 425 °C and the growth rates were 1.4 ML/s for AlInAs layer and 1.3 ML/s for InAsSb layer.

The energy band diagram of the micro-cavity structure was evaluated and depicted in [Figure 5.7\(b\)](#), showing also type I band alignment with energy transition of ~ 282 meV and conduction band offset of ~ 56 nm. The thickness of the active region layers were ~ 6 nm and ~ 18 nm for $\text{Al}_{0.12}\text{In}_{0.88}\text{As}$ barrier and $\text{InAs}_{0.87}\text{Sb}_{0.13}$ quantum well layers, respectively.

5.3.4 Growth of InAs-based 4.6 μm InAs/GaAsSb SLs RC structure

In this section, a lattice matched AlAsSb/GaAsSb DBR mirror with high refractive index contrast ($\Delta n \approx 0.6$) was designed to investigate RC structures including active regions grown on InAs substrate instead of the GaSb substrate.

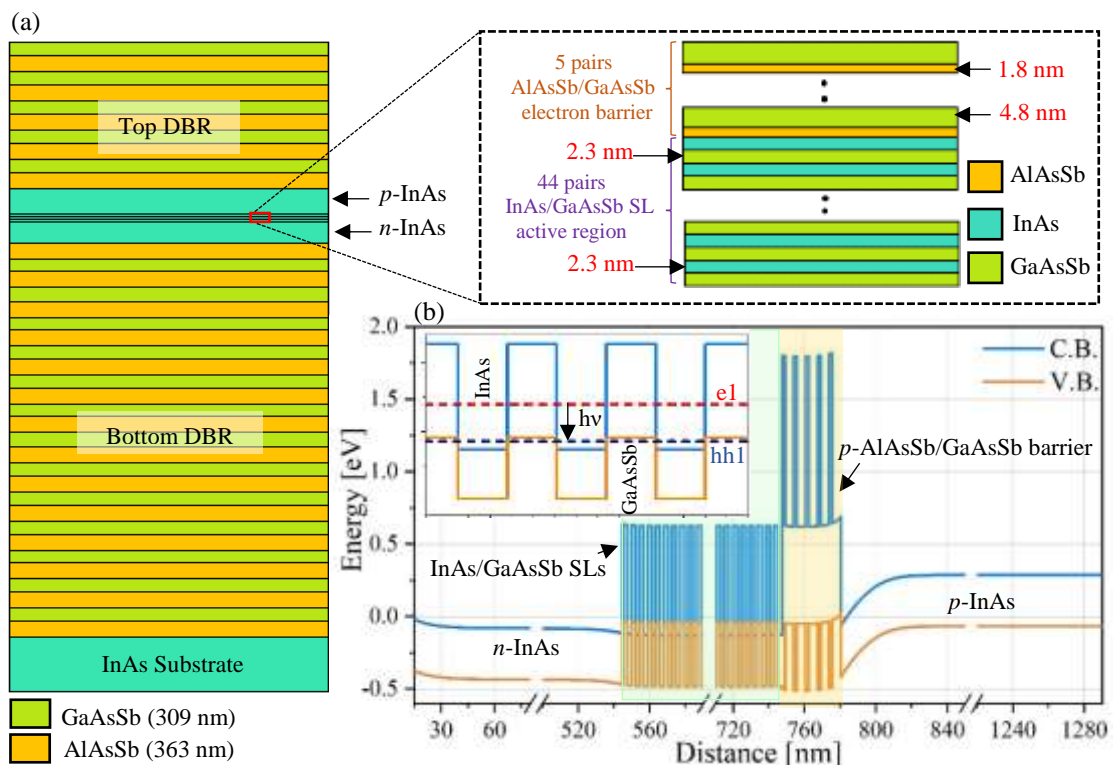


Figure 5.8: (a) A schematic diagram of the InAs-based 4.6 μm SLS RC structure showing the details of the InAs/GaAsSb SLs in the active region of the p-i-n diode within the AlAsSb/GaAsSb DBRs, which form the microcavity, (b) The energy band diagram of the cavity layers calculated using *nextnano*, showing the electron-blocking barrier. Details of the broken type II band alignment in the MQW are highlighted in the inset.

An InAs-based resonant cavity, designed for mid-infrared emitters operating at 4.6 μm , grown on n -InAs substrate was also investigated and is presented in [Figure 5.8\(a\)](#). The structure used a type II InAs/GaAsSb strained layer superlattice (SLS) as the active region placed in the center

of the InAs cavity where the antinode of the electric field distribution is positioned. The λ -thick cavity is sandwiched between 13.5 pairs un-doped lattice-matched AlAs_{0.16}Sb_{0.84}/GaAs_{0.08}Sb_{0.92} bottom-DBR mirror and 5 pairs of lattice-matched *p*-type AlAs_{0.16}Sb_{0.84}/GaAs_{0.08}Sb_{0.92} top-DBR mirror. The growth temperature of the DBR layers was 500 °C and the growth rates were 0.5 ML/s and 0.8 ML/s for AlAsSb and GaAsSb layers, respectively. The micro-cavity layers were grown as follows: firstly an *n*-InAs layer was grown on the bottom DBR mirror, followed by the active region layers (44 pairs InAs/GaAsSb SLS); *p*-type 5 pairs of AlSb/GaSb SLS used as blocking electron layers; and finally the cavity was completed by growing a *p*-InAs layer. The growth temperature of the cavity layers was 465 °C for InAs and the active region layers, and 500 °C for the electron blocking layers. The growth rates were 0.5 ML/s for all cavity layers except the GaSb in the electron blocking layers, which was 0.8 ML/s. The thickness of the InAs and GaAsSb layers in the SLS were approximately 2.30 nm and 2.25 nm, respectively. After that, the *p*-type top-DBR mirror was grown to complete the resonant cavity structure. The energy band diagram of the micro-cavity as shown in [Figure 5.8\(b\)](#) was obtained using *nextnano* simulation, showing that the band alignment is broken gap type II.

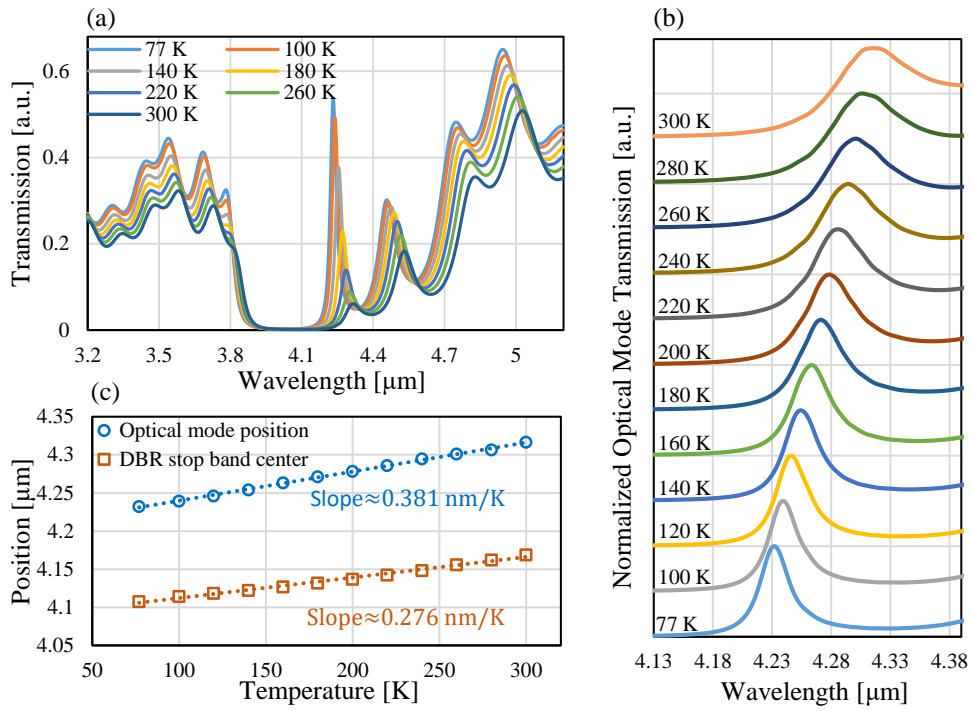
5.4 Optical characteristics of the resonant cavity (RC) structures

In this section, temperature dependence of the transmission spectra of the resonant cavity structures were carried out using the FTIR system described in section (4.4). For all samples, the position of the optical cavity mode, DBR stopband centre, linewidth of the optical mode, and the cavity quality factor were evaluated.

5.4.1 GaSb-based RC structures with InAsSb active region

Because both the 4.3 μm bulk InAsSb and 4.5 μm MQWs RCs, have the same DBR structure and the same InAsSb cavity, the transmission results of the two structures were demonstrated together in this section. Over the temperature range from 77 K to 300 K, the transmission spectra were measured and plotted in [Figures 5.9\(a\) and 5.9\(d\)](#).

Bulk RC



MQWs RC

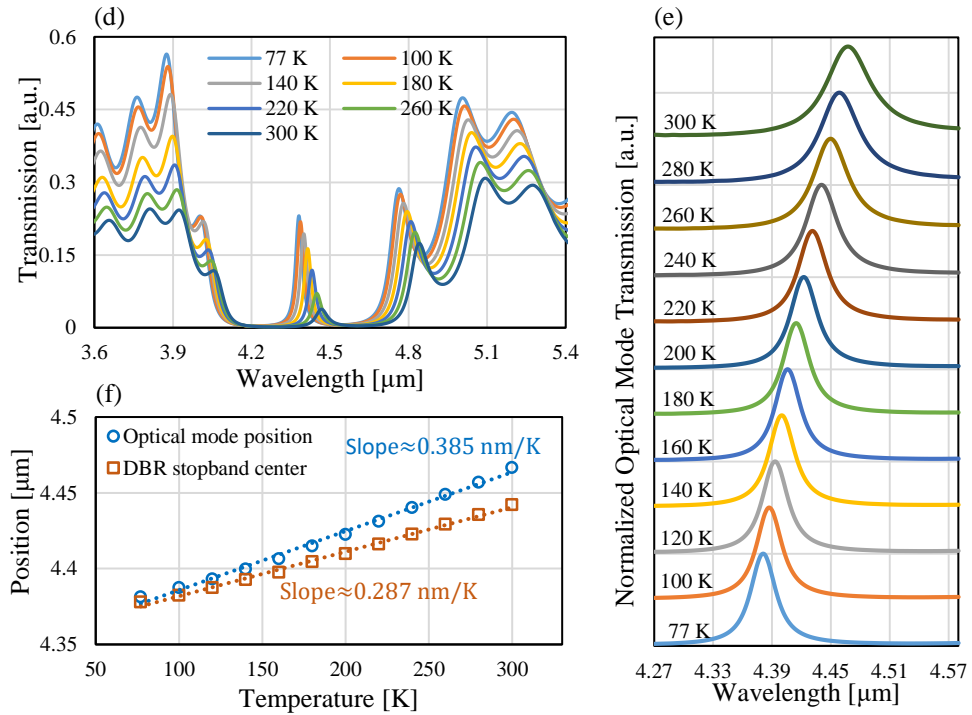


Figure 5.9: (a) Temperature dependence of the transmission spectra of the GaSb-based 4.3 μm bulk InAsSb RC sample. (b) Temperature dependence of the optical mode transmission. (c) The position of the optical cavity mode and the DBR stopband center of the sample as a function of temperature. (d) Temperature dependence of the transmission spectra of the GaSb-based 4.5 μm MQWs RC sample. (e) Temperature dependence of the optical mode transmission. (f) The position of the optical cavity mode and the DBR stopband center of the sample as a function of temperature.

The position of the optical cavity mode of the bulk RC and MQW RC samples is shown in [Figure 5.9\(b\)](#). There is a shift to longer wavelength (red-shift) when the temperature increases from 77 K to 300 K at a rate of ~ 0.381 nm/K and ~ 0.385 nm/K for bulk and MQWs RC samples (see [Figure 5.9\(c\)](#)), respectively. The cavity mode of the bulk RC has a peak at $4.232 \mu\text{m}$ (77 K) and $4.317 \mu\text{m}$ (300 K), while the QWs RC has a cavity mode centred at $4.381 \mu\text{m}$ (77 K) and $4.467 \mu\text{m}$ (300 K).

The DBR stopband centre is also shifted towards longer wavelength at a rate of 0.276 nm/K and 0.287 nm/K for bulk and MQWs RC samples, respectively (see [Figure 5.9\(f\)](#)). The shift in the resonant optical mode position is attributed to the variation in thickness and refractive index of the micro-cavity active region layers as a function of temperature, whereas the shift in the DBR stopband centre is due to the temperature dependence of the refractive index and the thickness of the AlAsSb/GaSb DBR layers. Furthermore, the room temperature quality factor (Q) of the bulk and MQWs RC structure were determined to be approximately 60 and 79, respectively, increasing with decreasing temperature to be ~ 132 and ~ 129 at 20 K, respectively.

5.4.2 GaSb-based RC structure with GaSb material cavity

The transmission spectra of the GaSb cavity-based MQWs RC sample were measured as a function of temperature over the temperature from 77 K to 300 K and are plotted in [Figure 5.10\(a\)](#). The spectra of the optical cavity mode, shown in [Figure 5.10\(b\)](#), shift to longer wavelength from $3.940 \mu\text{m}$ at 77 K to $4.0 \mu\text{m}$ at 300 K. In addition, the linewidth of the cavity mode was determined to be 31 nm and 37 nm at 77 K and 300 K, respectively. Based on the results of the position and the linewidth of the cavity mode, and according to the equation (2.59), the quality factor was evaluated and found to be 127 at 77 K and 108 at 300 K. The position of the optical mode and the DBR stopband centres were calculated and plotted as a function of temperature in [Figure 5.10\(c\)](#), showing a shift at a rate of 0.268 nm/K and 0.276 nm/K, respectively.

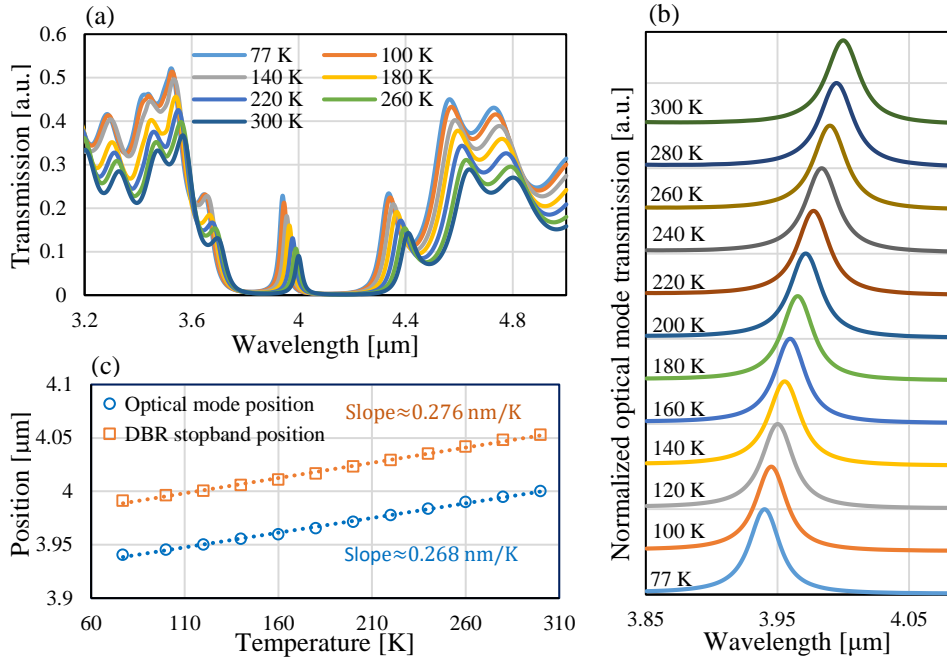


Figure 5.10: (a) Temperature dependence of the transmission spectra of the GaSb-based 4.0 μm MQWs RC sample. (b) Temperature dependence of the optical mode transmission. (c) The position of the optical cavity mode and the DBR stopband center of the sample as a function of temperature.

5.4.3 InAs-based RC structure with InAs active region

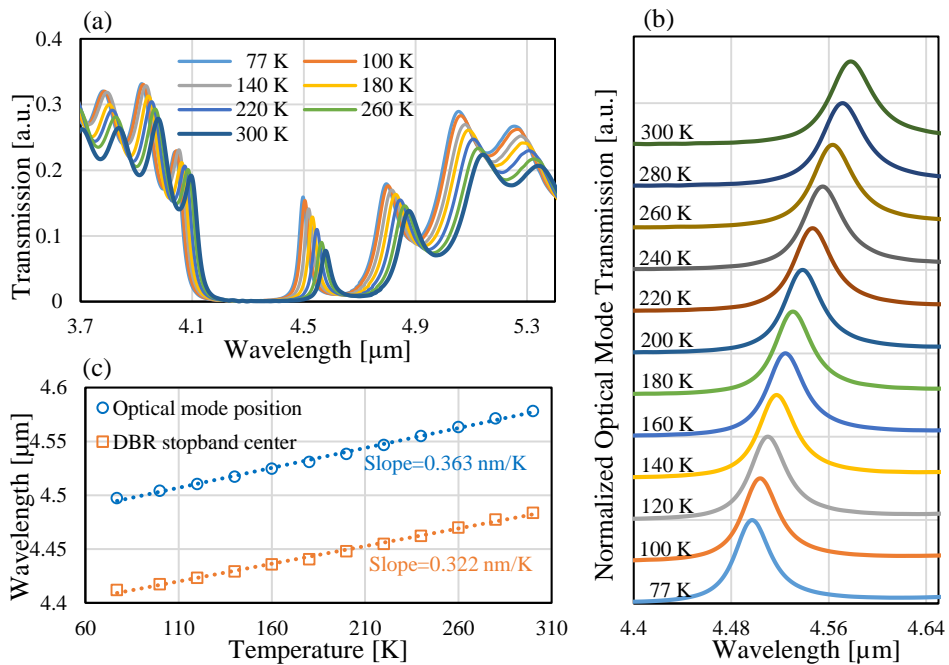


Figure 5.11: (a) Temperature dependence of the transmission spectra of the InAs-based SLs RC sample. (b) Temperature dependence of the optical mode transmission. (c) The position of the optical cavity mode and the DBR stopband center of the sample as a function of temperature.

Figure 5.11(a) presents the temperature-dependent transmission spectra of the InAs-based RC sample illustrated in Figure 5.8(a). A red-shift in the cavity mode was observed from 4.497 μm at 77 k to 4.578 μm at 300 K as shown in Figure 5.11(b) and the corresponding linewidth was found to be 34 nm and 45 nm respectively. Based on these results, the quality factors of the cavity were obtained as 132 at 77 K and 101 at 300 K. In addition, the temperature dependence of the DBR stopband centre and the position of the cavity mode are plotted together in Figure 11(c), changing at a rate of 0.322 nm/K and 0.363 nm/K, respectively.

5.5 Comparison between the experimental and simulated results

In order to evaluate the agreement between the experimental and the numerical results of the optical mode positions for all samples, the refractive index and the thickness of the cavity layers including the active region layers should be determined as a function of temperature. The temperature coefficient of the refractive index formula for the ternary cavity layers, $\text{InAs}_x\text{Sb}_{1-x}$, $\text{Al}_x\text{In}_{1-x}\text{As}$, and $\text{GaAs}_x\text{Sb}_{1-x}$ are given by: [131,132]

$$\frac{1}{n} \left(\frac{dn}{dT} \right) (\text{InAs}_x\text{Sb}_{1-x}) = [1.2 \times 10^{-4}x + 6.90 \times 10^{-5}(1-x)]K^{-1} \quad (5.7)$$

$$\frac{1}{n} \left(\frac{dn}{dT} \right) (\text{Al}_x\text{In}_{1-x}\text{As}) = [1.2 \times 10^{-4}x + 4.6 \times 10^{-5}(1-x)]K^{-1} \quad (5.8)$$

$$\frac{1}{n} \left(\frac{dn}{dT} \right) (\text{GaAs}_x\text{Sb}_{1-x}) = [4.5 \times 10^{-5}x + 8.2 \times 10^{-5}(1-x)]K^{-1} \quad (5.9)$$

The temperature coefficient of the refractive index for GaSb was given in equation (5.5), and for InAs is given according to the following relation: [132]

$$2n \frac{dn}{dT} (\text{InAs}) = 2.18 \times 10^{-3}K^{-1} \quad (5.10)$$

To investigate the variation of the thickness as a function of temperature, the temperature coefficient of the lattice constant of the ternary cavity layers were determined from the following equations:

$$a_{\text{InAs}_x\text{Sb}_{1-x}} = x \cdot a_{\text{InAs}} + (1-x) \cdot a_{\text{InSb}} \quad (5.11)$$

$$a_{\text{Al}_x\text{In}_{1-x}\text{As}} = x \cdot a_{\text{AlAs}} + (1-x) \cdot a_{\text{InAs}} \quad (5.12)$$

$$a_{\text{GaAs}_x\text{Sb}_{1-x}} = x \cdot a_{\text{GaAs}} + (1-x) \cdot a_{\text{GaSb}} \quad (5.13)$$

The formulas for the temperature-dependent lattice constant of the binary materials are given by: [129]

$$a_{\text{GaAs}} = 5.65325 + 3.88 \times 10^{-5}(T - 300) \quad (5.14)$$

$$a_{\text{InAs}} = 6.0583 + 2.74 \times 10^{-5}(T - 300) \quad (5.15)$$

$$a_{\text{InSb}} = 6.4794 + 3.48 \times 10^{-5}(T - 300) \quad (5.16)$$

The temperature coefficient of the lattice constants for the GaSb, AlAs, and AlSb were listed in equations (5.3a), (5.3b), and (5.3c). The results exhibit an excellent agreement between the experimental (points) and the numerical results (dotted lines) as illustrated in Figure 5.12.

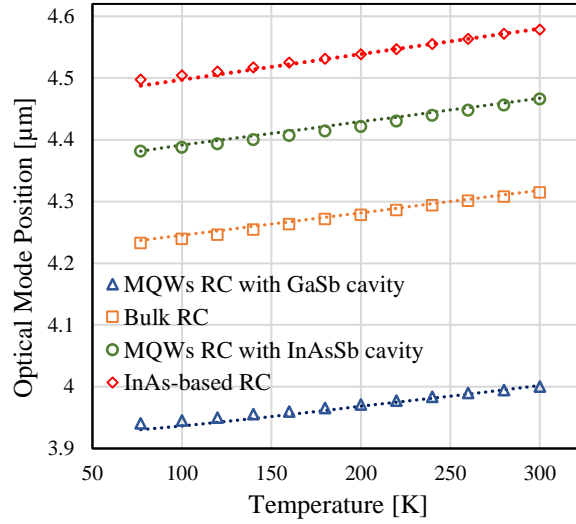


Figure 5.12: The position of the optical cavity mode for all RC samples as a function of temperature.

5.6 Discussion

Because of the different temperature dependence of the refractive index (n) and the thickness (d) of the DBR layers (see Figures 5.4 (b) and (c)), it is difficult to maintain a typical DBR design at all measured temperatures. As seen before, the wavelength of the DBR stopband centre was typically determined at 300 K, where the quantity ($\lambda=4dn$) of the Ga(As)Sb layer should be equal to that of the AlAsSb layer. When the temperature decreases/increases, the two quantities become unequal.

$$d_{\text{GaSb}}n_{\text{GaSb}} \neq d_{\text{AlAsSb}}n_{\text{AlAsSb}} \quad (5.17)$$

To design our RC structures (as mentioned in section 5.3), we select the cavity thickness of 1λ corresponding to cavity order $m_c=2$, because for low values of m_c , high extraction efficiency should be achieved owing to the greater overlap between the cavity response and the underlying emission spectrum [44,71].

Due to the change in the band gap of the semiconductor layers of the micro-cavity and the DBR mirror with temperature, the refractive index of these layers increases as temperature increases [133], causing a red-shift in the position of the optical cavity mode and the DBR stopband centre. Furthermore, the transmission spectra of the RC samples show that the transmission of the optical cavity mode decreases as temperature increases. This is attributed to an increase in the absorption coefficient of the active region material as the temperature increases [134].

Based on the results of the position of the optical cavity mode and the DBR stopband centre, the detuning, which is defined as a difference between λ_{cav} and λ_{DBR} , was evaluated and plotted in Figures 5.14. The results indicate that all the samples exhibit detuning and the bulk RC sample (4.3 μm GaSb-based RC) shows the highest relative detuning compared to other samples, while the MQWs RC with InAsSb cavity shows the lowest detuning. The detuning values of the GaSb-based 4.3 μm bulk RC sample were calculated to be ~ 130 nm at 77 K and ~ 155 nm at 300 K, while the detuning of the GaSb-based 4.5 μm MQWs RC sample were determined to be 3 nm at 77 K and ~ 24 nm at 300 K. At 300 K, the InAs-based 4.6 μm SLS RC sample and GaSb-based 4.0 μm MQWs RC sample show detuning values of 95 nm and 53 nm, respectively, decreasing to 86 nm and 51 nm at 77 K, respectively. In general, even if we designed perfect matching at temperature T_{tuning} , increase/decrease in the temperature leads to some detuning. This is because the shift in the position of the optical cavity mode and the DBR stopband centre do not occur at the same rate, i.e. $d\lambda_{cav}/dT \neq d\lambda_{DBR}/dT$.

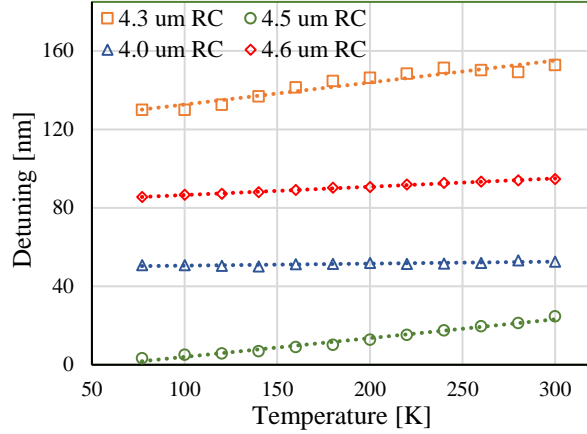


Figure 5.14: Temperature dependence of the detuning values for all RC samples.

However, our simulated results presented in Figure 5.15(a) and 5.15(b), show that even if there is some detuning, G_{int} and G_e still maintain high values over a wide wavelength range, depending on the bandwidth of the DBR stopband. The GaSb-based 4.0 μm bulk RC shows relatively the lowest values of the enhancement factors compared to other RC structures. The dashed line represents the resonance case between λ_{cav} and λ_{DBR} , where maximum emission enhancement is achieved.

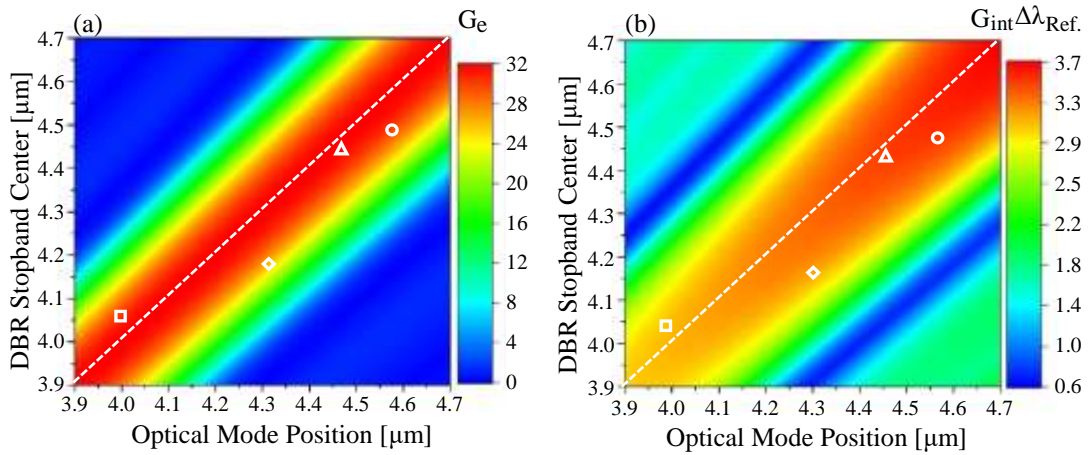


Figure 5.15: Room temperature simulations of (a) the resonance emission (G_e) and (b) the integrated emission (G_{int}) enhancement factor, as a function of the DBR stopband center and the peak emission of the cavity mode, respectively. The white dashed line represents the resonance case between the optical cavity mode and the DBR stopband center. Square (GaSb-based 4.0 μm MQWs RC), Diamond (GaSb-based 4.3 μm bulk RC), triangle (GaSb-based 4.5 μm MQWs RC), circle (InAs-based 4.6 μm SLs RC).

The transmission spectra of the RC structures exhibit optical cavity modes with narrow linewidth (<100 nm) and high quality factor (> 60), to achieve strong enhancement factors in the fabricated RCLED structures. This originates from the high reflectivity of the DBR mirrors and high antinode enhancement - the position of the active region at the antinode of the electric field. The structures were grown successfully with good quality as seen in the SEM cross-section of the bulk RCLED and MQWs RCLED which are shown in Figures 5.16(a) and 5.16(b), respectively. The optical properties of the RC structures are summarized in Table 5.1.

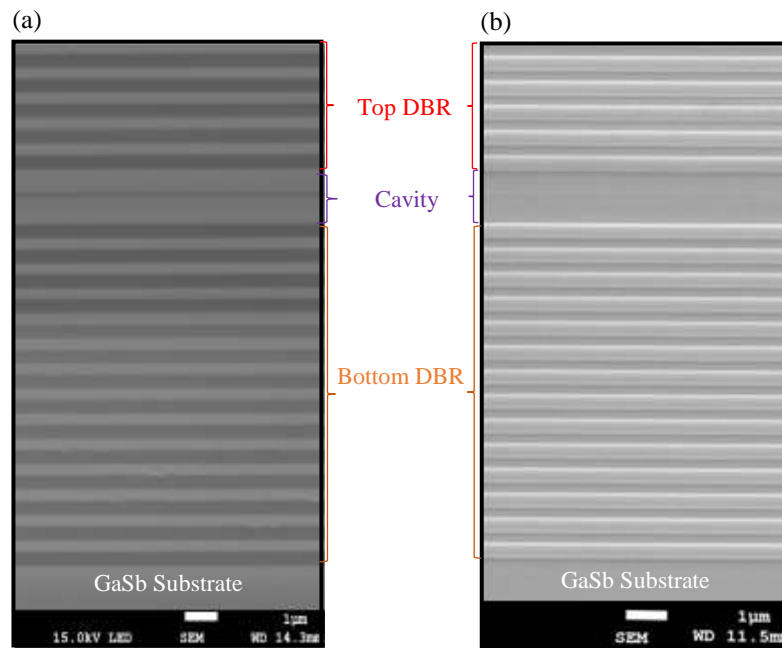


Figure 5.16: SEM cross-section of the (a) bulk RCLED and (b) MQWs RCLED.

Table 5.1: Room temperature optical properties of the RC samples.

| Sample | Cavity mode | | | | DBR stopband centre | | Detuning Nm |
|-------------------------------|---------------------------|-----------------|-----------------------|------------------------------------|---------------------|------------------------------------|----------------|
| | Position μm | Linewidth Nm | Quality factor [Q] | $d\lambda_{\text{cav}}/dT$ nm/K | Position Nm | $d\lambda_{\text{DBR}}/dT$ nm/K | |
| Bulk InAsSb RC | 4.317 | 72 | 79 | 0.381 | 4.163 | 0.276 | ~ 154 |
| MQWs RC with InAsSb cavity | 4.467 | 56 | 60 | 0.385 | 4.443 | 0.287 | ~ 24 |
| MQWs RC with GaSb cavity | 4.0 | 37 | 108 | 0.268 | 4.053 | 0.276 | ~ 53 |
| SLs RC with InAs cavity | 4.578 | 45 | 101 | 0.363 | 4.483 | 0.322 | ~ 95 |

Chapter 6

Bulk InAsSb resonant cavity light emitting diode for mid-infrared applications

6.1 Introduction

In this chapter, we demonstrate a mid-infrared resonant cavity light emitting diode (RCLED) operating near 4.25 μm at room temperature, grown lattice-matched on a GaSb substrate by molecular beam epitaxy, suitable for CO₂ gas detection. The device consists of a 1λ -thick micro-cavity containing a bulk InAs_{0.90}Sb_{0.10} active region sandwiched between two high contrast, lattice-matched AlAs_{0.08}Sb_{0.92}/GaSb distributed Bragg reflector (DBR) mirrors. Two resonant cavities (RC) with different detuning (the difference between the position of the DBR stopband center and the optical cavity mode) were investigated.

The electroluminescence emission spectra of the high detuning RCLED were measured over the temperature range from 20 to 300 K, exhibiting significant side mode peaks. These results were compared to that of the RCLED without top DBR mirror. The emission spectra of the low detuning RCLED were also measured as a function of temperature, showing a strong emission enhancement in comparison with the conventional LED due to the resonant cavity effects. At room temperature the peak emission and the integrated emission of the RCLED were found to be enhanced by a factor of ~ 70 and ~ 11 , respectively, while the total integrated emission enhancement was $\sim \times 33$. Furthermore, the RCLED also exhibits significantly (10x) narrower spectral linewidth (88 nm) and superior temperature stability ~ 0.35 nm/K, which is 6x less than that of the reference LED.

Our results indicate that the RCLED's emission has attractive characteristics which would enable such devices to be developed for the detection of CO₂.

6.2 Fabrication of the GaSb-based bulk InAsSb RCLED

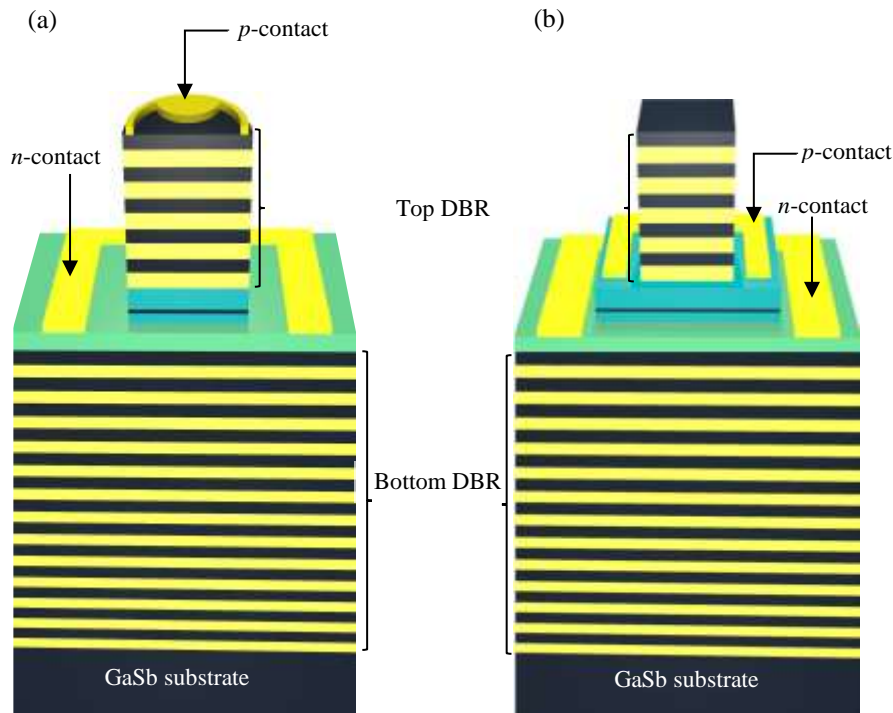


Figure 6.1: Schematic structure of the (a) bulk RCLED-M1 (b) bulk RCLED-M2. The two devices were fabricated using two different masks (different mesa) to test the improvement in the optical and electrical properties.

Processing was carried out using standard photolithography and wet chemical etchants followed by Ti/Au metallization for the ohmic contacts as illustrated in [section 4.6](#). In particular, InAsSb layers were etched using citric acid: H_2O_2 (2: 1). GaSb and AlAsSb were etched using a dilute ammonia based etchant. Two devices were fabricated using two different masks. For the device (RCLED-M1), which has the schematic structure shown in [Figure 6.1\(a\)](#), the first photolithography step was carried out to deposit a 250 nm thick *p*-type top metal contact of Ti/Au on the top-DBR mirror. A second photolithography step was carried out to pattern the sample for subsequent wet etching of the mesa, by etching through the structure and stopping within the *n*-InAsSb layer. Finally, a Ti/Au metal contact was then deposited on the *n*-InAsSb layer to provide an ohmic contact for the *n*-side. For the device RCLED-M2, which is shown in [Figure 6.1\(b\)](#), the first lithography step was carried out for etching the top-DBR mirrors and stopping at the top of the *p*-InAsSb layer. Then, a *p*-type Ti/Au metal contact was deposited on

the p -InAsSb layer. The next lithography step was carried out for etching the cavity layers and stopping within the n -InAsSb layer followed by depositing the n -type Ti/Au metal contact.

6.3 Optical Characterisation

After fabrication, temperature dependence of the optical transmission of the RC sample and the electroluminescence (EL) measurements of the RCLEDs were obtained using the systems illustrated in [sections 4.4 and 4.7](#), respectively.

6.3.1 Electroluminescence emission of the high detuning RCLED device with and without top DBR

In this section, we have demonstrated the temperature dependence of the electroluminescence spectra of the RCLED with and without top DBR mirror, which was described in [section 5.3.1](#). As we mentioned in that section, the structure has a high detuning between the optical cavity mode and the DBR stopband centre (~ 155 nm). Consequently, several side peaks could be observed, appearing on both sides of the DBR stopband. The electroluminescence spectra of the RCLED with top DBR mirror were measured and plotted in [Figures 6.2\(a\)](#) as a function of temperature over the range from 20 K to 300 K. From this figure, at low temperature ($T < 120$ K), it is significantly found that the side peak emission located at ~ 3.8 μm has a high intensity compared to that of the main resonant peak which is positioned at ~ 4.3 μm . This is because the side peak emission has a low detuning between its optical mode emission and the active region emission, compared to that of the main resonant peak. As temperature increases over 120 K, the relative intensity increases to be more than 1 (see [Figure 6.2\(b\)](#)), as the intensity of the main resonant peak (4.3 μm) becomes higher than that of the side peak (3.8 μm). This is due to a decrease in detuning between the emission of the active region and the main optical cavity mode. In addition, other side peaks located at longer wavelengths were significantly enhanced with increasing the temperature.

The electroluminescence spectra of the RCLED show that all the resonant peaks (the main peak emission and the side peaks emission) shift towards longer wavelength when the temperature increases, showing that the temperature coefficient of the wavelength shift of the resonance peaks are less than that of the active region emission. For the main resonance peak, the peak shifts at a rate of 0.375 nm/K. Whilst and as presented in Figure 6.1(c), the side peaks located at $\sim 3.8 \mu\text{m}$ and $\sim 4.5 \mu\text{m}$ shift by the rate of 0.195 nm/K and 0.369 nm/K, respectively.

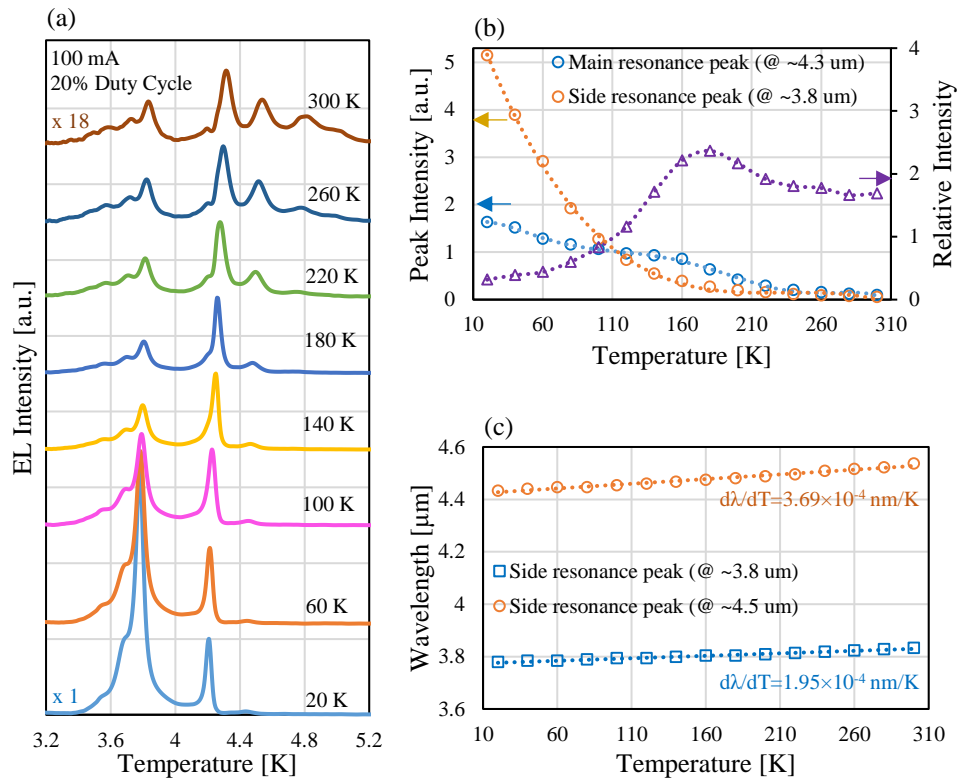


Figure 6.2: (a) Temperature dependence of the EL spectra of the high detuning RCLED, (b) The peak intensity of the main resonance mode and the side mode as a function of temperature. The open triangles represent the relative intensity, (c) Temperature dependence of the peak position of the side modes (at $3.8 \mu\text{m}$ and $4.5 \mu\text{m}$).

The temperature dependence of the electroluminescence spectra of the high detuning RCLED without top DBR mirror were demonstrated in Figure 6.3(a). As can be seen from this figure, and compared to the emission of the RCLED with top mirror, removal of the top DBR mirror from the RCLED structure leads to an increase in the emission linewidth of the main resonance mode and a decrease of the enhancement factor. This is attributed to the lower reflectivity of the semiconductor/air interface which acts as a top mirror. In fact, the reflectivity at the interface

between the surface of the top InAsSb layer of the device and air could be determined according to Fresnel's equation, which is given by [74]:

$$R = (n - 1)^2 / (n + 1)^2 \quad (6.1)$$

The value of R, which represents the reflectivity of the InAsSb/air top mirror, was calculated to be 33% corresponding to the refractive index of InAsSb ($n \approx 3.71$).

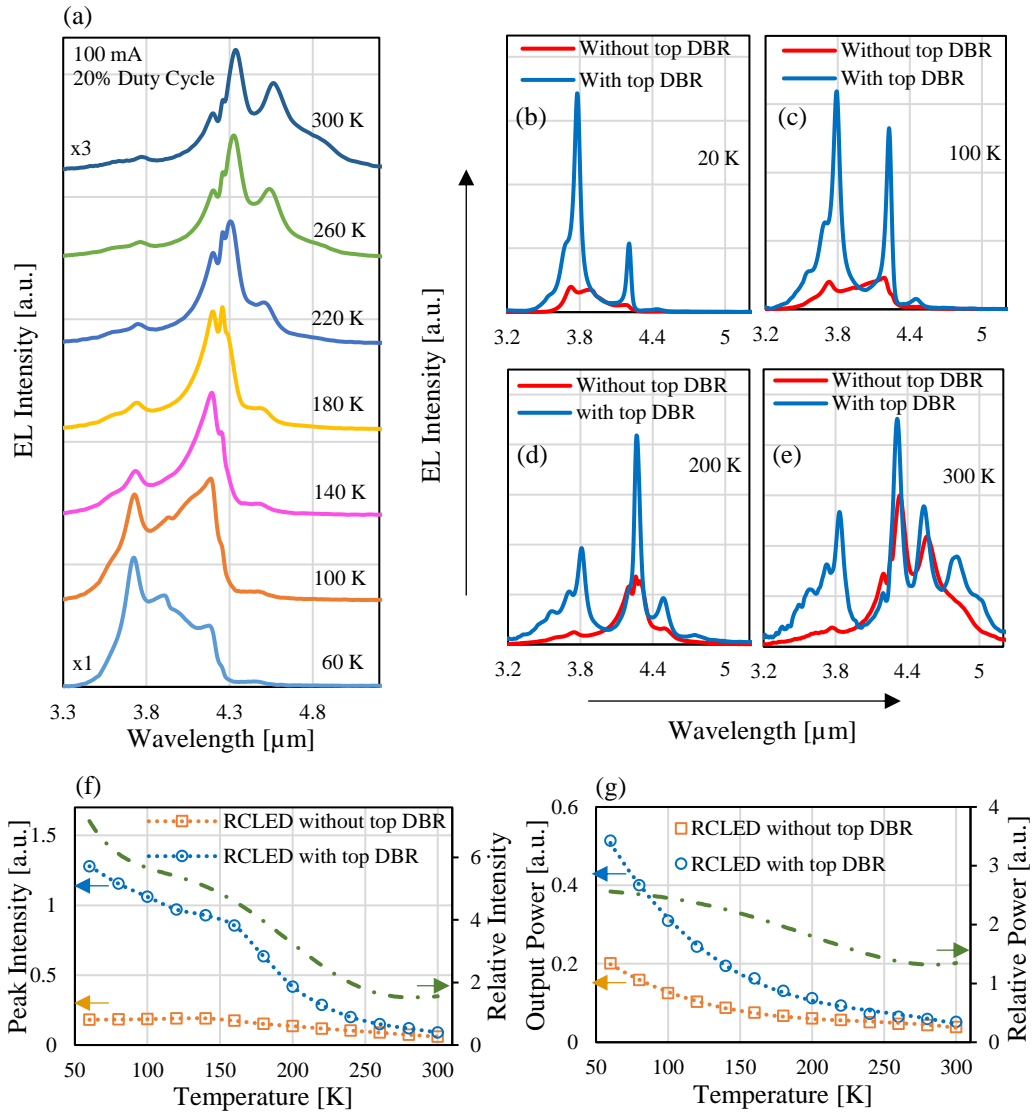


Figure 6.3: (a) Temperature dependence of the EL spectra of the high detuning RCLED without top DBR mirror, (b-e) The electroluminescence spectra of the RCLED with top DBR compared to that of the RCLED without top DBR at various temperature, (f) Peak intensity of the emission of the RCLED with top DBR compared to that of the RCLED without top DBR. Dash-dot line represents the relative intensity, (g) Optical output power of the emission of the RCLED with top DBR compared to that of the RCLED without top DBR. Dash-dot line represents the relative output power.

The comparison between the emission spectra of the RCLEDs with top DBR and without top DBR mirror were plotted together at various temperature as illustrated in [Figures 6.2\(b-e\)](#). It can be seen that the peak emission intensity of the RCLED with top DBR is higher than that of the RCLED without top DBR. The peak intensity and the total output power of the two devices were plotted as a function of temperature from 60 K to 300 K in [Figures 6.3\(f\) and 6.3\(g\)](#), respectively. As can be noticed from these figures, the relative intensity of the resonance peaks and the relative total output power of the emission spectra are higher than 1 over all the temperature range, indicating that the emission intensity and the total output power of the RCLED with top DBR mirror are higher than that of the RCLED without top DBR. It was also found that the relative intensity and the relative output power decrease with increasing temperature. At $T=60$ K, the emission spectra of the RCLED with top DBR has a peak intensity higher than that of the RCLED without top DBR by a factor of more than ~ 7 , decreasing with increasing the temperature to be ~ 1.7 at 300 K (see [Figure 6.2\(f\)](#)). Whilst the relative output power decreases from 2.5 to 1.35 when the temperature increases from 60 K to 300 K.

6.3.2 Optical characterization of the low detuning resonance cavity structure

In this section, we demonstrated the optical properties of the low detuning InAsSb bulk resonance cavity (RC) structure grown under the same growth condition which is used to grow the high detuning RC structure. We redesigned the structure to decrease the detuning between the main resonance optical cavity mode and the DBR stopband centre by decreasing the cavity thickness. The optical transmittance spectrum of the full resonance cavity (RC) structure was measured at room temperature and plotted in [Figure 6.4\(a\)](#). The peak of the main resonant optical cavity mode observed at $4.295 \mu\text{m}$ is slightly detuned from the centre of the DBR stopband at $4.180 \mu\text{m}$. According to the detuning results which are considered in [Figures 5.15\(a\) and \(b\)](#), it was found that the values of G_{int} and G_e fall within the high range—i.e., no less than 6% and 15% of the maximum value compared to the resonance case, respectively.

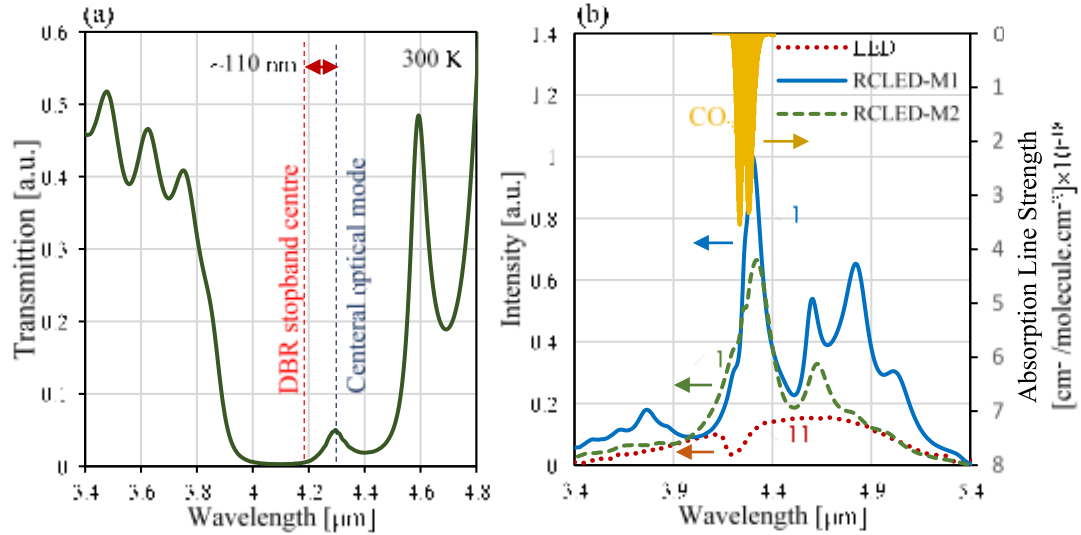


Figure 6.4: (a) Experimentally measured transmittance spectrum of the RC structure at room temperature, showing that the optical cavity mode occurs at $4.295 \mu\text{m}$, and the DBR stopband is centred at $4.180 \mu\text{m}$. (b) Comparison of the RCLED-M1 (solid line), RCLED-M2 (dashed line), and the reference LED (dotted line) electroluminescence emission spectra at 300 K using the same injection current (100 mA at 1 kHz with 20% duty cycle). The dip in the reference LED spectrum originates from atmospheric CO_2 absorption in the optical path. Also shown are the fundamental fingerprint absorptions of CO_2 gas.

From the same RC sample, two different RCLEDs (RCLED-M1 and RCLED-M2) were fabricated using the processing illustrated in section 6.2. Figure 6.4(b) presents the electroluminescence emission spectra of the RCLED-M1, RCLED-M2, and reference LED measured at 300 K under quasi-continuous operation using an injection current of 100 mA at 1 kHz with 20% duty cycle. As can be seen in this figure, both RCLEDs emission exhibit peak intensity centred at $4.295 \mu\text{m}$, matching to the position of the optical cavity mode and overlapping nicely with the fundamental CO_2 fingerprint absorption. Furthermore, the electroluminescence spectra of the RCLED-M1 show two significant side peaks, particularly in the longer wavelength, centred at $\sim 4.6 \mu\text{m}$ and $\sim 4.82 \mu\text{m}$, and the RCLED-M2 emission shows one side peak centred at $\sim 4.62 \mu\text{m}$. This is attributed to enhancement of other optical modes located in the sides of the DBR stopband, which are overlapping with the broadband emission of the active region.

The linewidth at full width at half maximum (FWHM) of the RCLED-M1 is 88 nm and of the RCLED-M2 is $\sim 200 \text{ nm}$, which are $\sim 10\times$ and $\sim 4.5\times$ narrower than the reference LED,

respectively, so that substantially more *useable* photons fall within the CO₂ absorption envelope. In addition to reducing the linewidth, the resonant cavity enhancement has the effect of significantly increasing the peak emission intensity of the RCLED-M1 and RCLED-M2 by ~70x and ~49x, respectively. The total integrated emission enhancement factor of the RCLED-M1 was calculated to be 33x, higher than that of the RCLED-M2 by a factor of ~1.6, which corresponds to an emittance of 2.2 mWcm⁻².

6.3.2.1 Current injection and duty cycle effects on the electroluminescence spectra of the low detuning RCLED

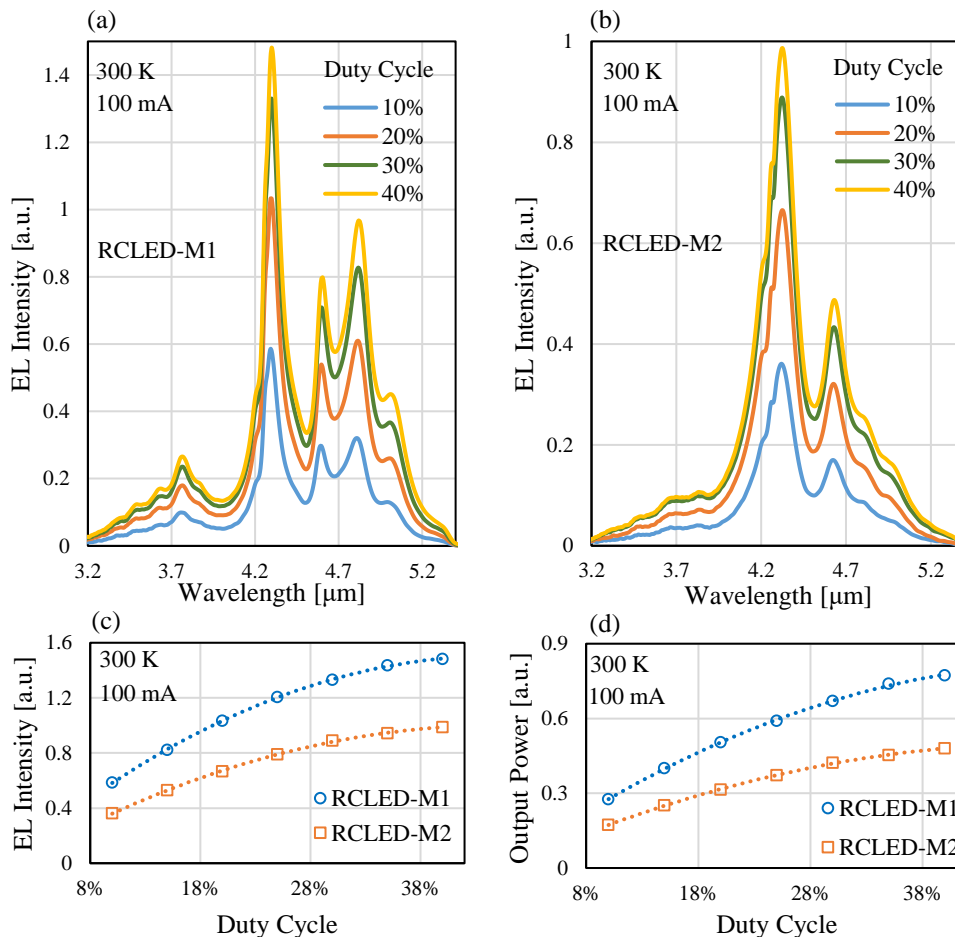


Figure 6.5: (a) and (b) Room temperature electroluminescence spectra of the RCLED-M1 and RCLED-M2 at various duty cycle using 100 mA injection current, respectively. (c) Peak intensity of the RCLED-M1 and RCLED-M2 emission as a function of duty cycle. (d) Total integrated emission of the RCLED-M1 and RCLED-M2 as a function of duty cycle.

Room temperature electroluminescence spectra of the RCLED-M1 and RCLED-M2 emission at various duty cycle using quasi CW operation (100 mA at 12 kHz) were demonstrated in [Figures 6.5\(a\) and 6.5\(b\)](#), respectively. The emission of the main resonance mode, centred at 4.295 μm , of the RCLED-M1 exhibits higher peak intensity compared to that of the RCLED-M2 emission by a factor of $\sim 1.55x$. Furthermore, when the duty cycle increase from 10% to 40%, the emission spectra of the RCLED-M1 show increase in the peak intensity by a factor of 2.5, and for RCLED-M2 by a factor of ~ 2.7 . On the other hand, it is found that the integrated emission of the both devices increases by a factor of ~ 2.8 with increasing duty cycle, showing that the total output power of the RCLED-M1 is higher than that of the RCLED-M2 by a factor of 1.6x. Under quasi-CW operation (100 mA, 40% duty cycle at 1 kHz), the total output power of the RCLED-M1 and RCLED-M2 were measured to be $\sim 8.3 \mu\text{W}$ and $\sim 5.2 \mu\text{W}$, respectively. However, and as seen in [Figure 6.6](#), the main resonance mode of the RCLED-M2 exhibits output power quite close to that of the RCLED-M1 over the duty cycle range from 10% to 40%, but with a lower intensity and a broader linewidth ($\sim 200 \text{ nm}$). Although we used a CO_2 filter, the absorption of this gas is still affecting the emission spectra, therefore it is difficult to evaluate accurately the shift in the position of the resonance peak and the change in the emission linewidth as the duty cycle increase.

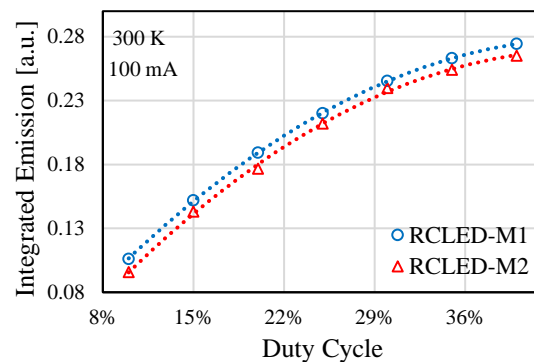


Figure 6.6: Integrated emission of the main resonance mode for RCLED-M1 compared to that of the RCLED-M2 as a function of duty cycle using 100 mA injection current.

Room-temperature current-dependent electroluminescence spectra of the RCLED-M1 emission were measured at various duty cycles; 20%, 30% and 40%. The peak intensity and the optical

output power were evaluated from these spectra and plotted in Figures 6.7(a) and 6.7(b), respectively. Over the injection current range from 10 mA to 100 mA, the emission spectra exhibit an increase in the peak intensity by a factor of ~ 6 as current increases. It was also found that the optical output power of the RCLED-M1 emission increases with increasing the injection current by a factor of 6.3 at 20% duty cycle and by a factor of 6.7 at 30% and 40% duty cycle. However, when the duty cycle increases from 20% to 30% the total output power as a function of injection current increases by 30%, more than that when the duty cycle increases from 30% to 40% by a factor of $\sim 2x$. This is could be attributed to increased Joule heating in the RCLED with increasing duty cycle.

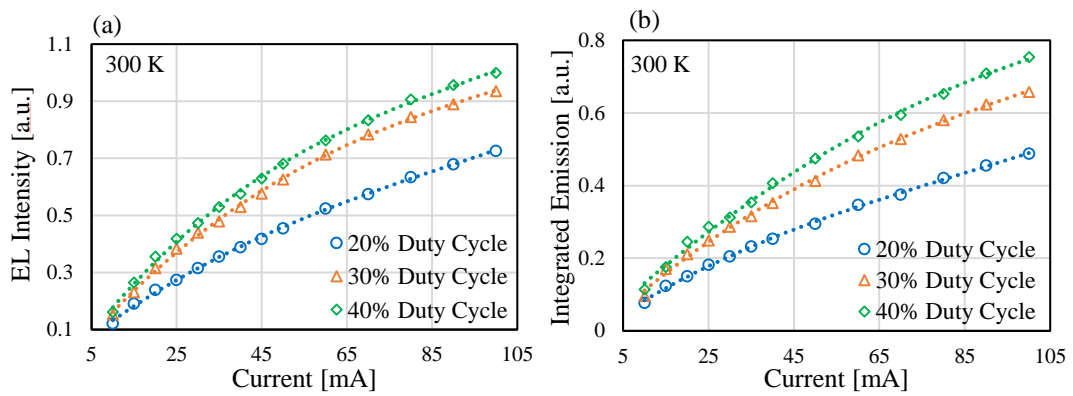


Figure 6.7: (a) Peak intensity of the RCLED-M1 emission as a function of injection current. (b) Optical output power of the RCLED-M1 emission as a function of injection current.

The far-field technique has been used to measure the angular emission profile of the RCLED, where the distance between the emitter and the detector was about 1 cm. In this technique, the emission intensity was measured from the top surface and the vertical facets. The far-field intensity profile of the RCLED-M1 at 300 K is shown in the Figure 6.8. A single lobe intensity distribution centred at 0° with a half angle of 60° was obtained, in good agreement with previous work on RCLEDs at shorter wavelengths [54,135].

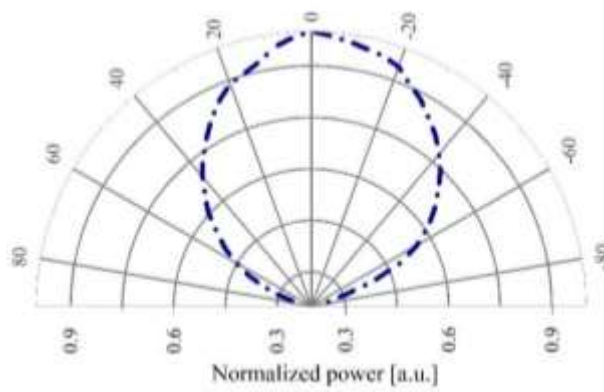


Figure 6.8: Far field angular profile of the RCLED emission, which shows a half power solid angle of 60° .

6.3.2.2 Temperature dependence of the electroluminescence spectra

Temperature dependence of the electroluminescence (EL) emission spectra of the InAsSb RCLED-M1 and the reference LED are shown in [Figures 6.9\(a\) and 6.9\(b\)](#), respectively. Over the measured temperature range (20–300 K), the main peak intensity of the RCLED and the EL emission peak of the reference LED decreased with increasing temperature by a factor of 68 and 32, respectively. In addition, the total optical output power of the RCLED-M1 and the reference LED were determined and plotted in [Figure 6.9\(c\)](#). As can be seen from this figure, the output power of the RCLED and the LED decreases with increasing temperature by a factor of 13 and 7.5, respectively. It was also found that the output power of the RCLED emission is higher than that of the reference LED by a factor of 57 at 20 K, and by a factor of 33 at 300 K. The EL emission peak of the RCLED also shifts to longer wavelengths with increasing temperature but much more slowly compared to the reference LED. In the conventional LED, the wavelength shift of the EL spectrum is due to the temperature dependence of the active region bandgap, whereas, for the RCLED, the EL peak depends on the wavelength of the resonant cavity optical mode which is determined by the thickness and the refractive index of the materials forming the cavity. With an increase in temperature, the thickness of the cavity increases according to the thermal expansion coefficients of the cavity materials. We calculated the variation of the cavity thickness as ~ 1.6 nm. This represents $<4\%$ of the total wavelength

shift and therefore the main contribution comes from the temperature variation of the refractive index [119,120]. Consequently, the main EL emission peak of the RCLED shifts only by 100 nm at a rate of ~ 0.35 nm/K, compared with 600 nm at a rate of ~ 2.15 nm/K in the reference LED [see Figure 6.9 (d)]. This represents more than a factor of 6 improvement in the emission wavelength stability with temperature, which is useful in applications such as gas detection where wavelength stability is required to ensure that the emission peak remains within the gas absorption envelope as the temperature varies.

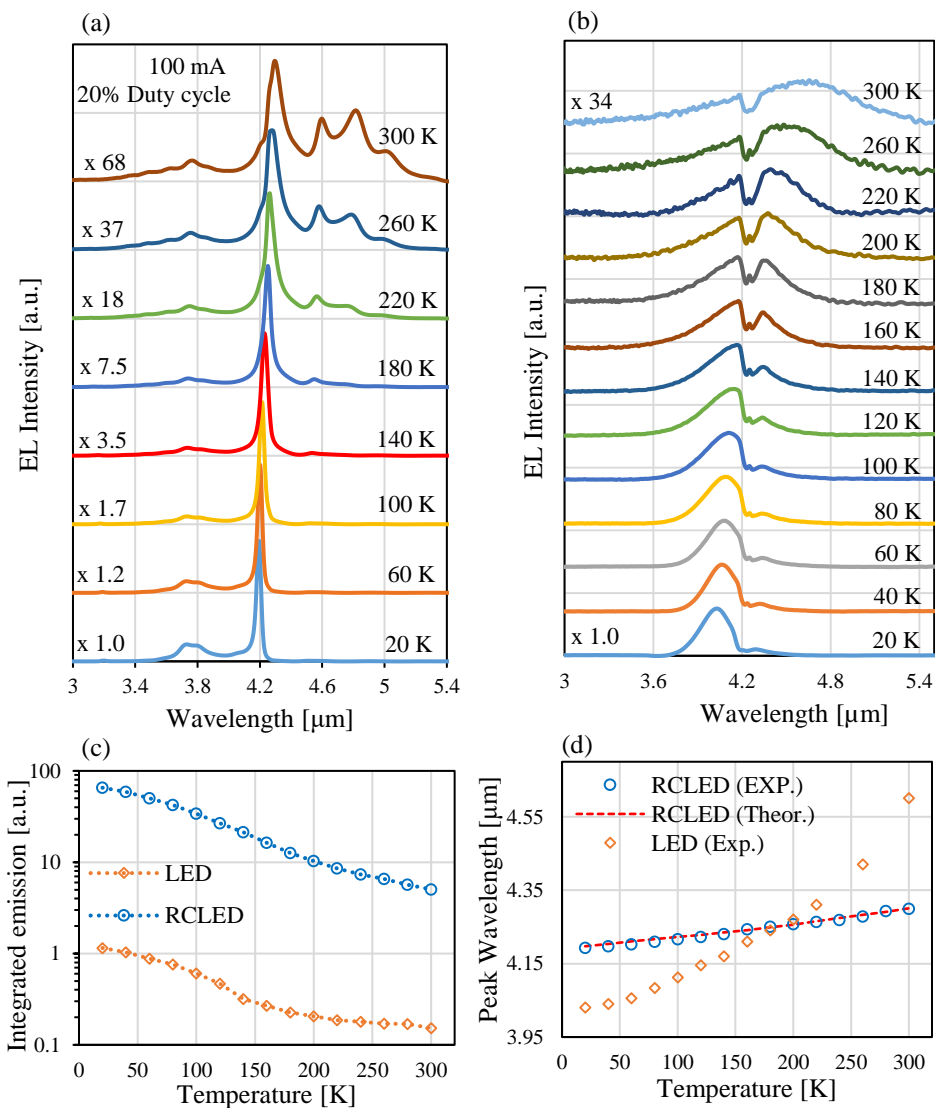


Figure 6.9: Temperature dependence of the EL spectra for (a) the RCLED-M1 and (b) the reference LED. (c) Intensity peak values of the EL spectra for the RCLED and reference LED. The dashed-dotted line represents the relative intensity. (d) The position of the EL peaks as a function of the temperature. The dashed line represents the theoretical results of the EL intensity peak of the RCLED.

The full width at half maximum (FWHM) of the RCLED emission spectra is clearly narrower than that of the conventional LED. For the RCLED-M1, the FWHM of the electroluminescence spectra increased from 35 nm at 20 K to 88 nm at 300 K, whereas the reference LED had a linewidth of 250 nm at 20 K and 900 nm at 300 K. The linewidth of the reference LED is determined by the joint density of states and the thermal energy of carriers—typically FWHM 1.8 kT [41]. In contrast, for the RCLED, the linewidth depends on the quality factor of the resonant cavity. At room temperature, the emission spectrum of the RCLED has a linewidth $\sim 10\times$ narrower than that of the conventional reference LED. Consequently, the RCLED can be designed and tailored to match the absorption wavelength of the target gas.

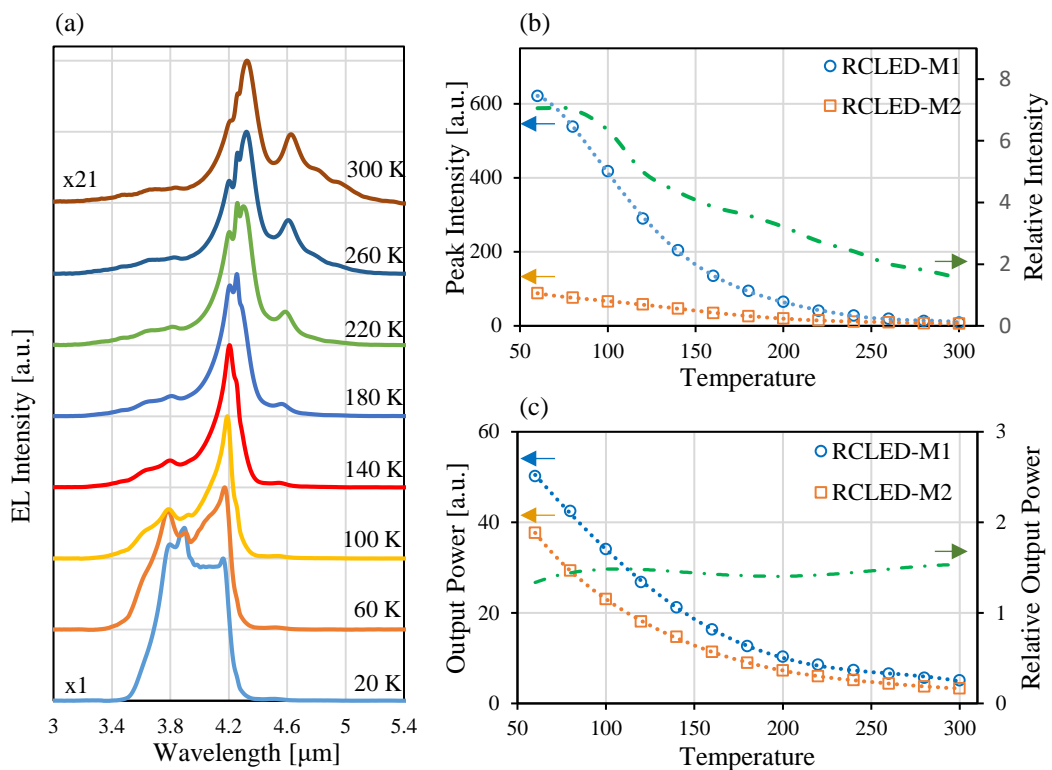


Figure 6.10: (a) Temperature dependence of the EL spectra for the RCLED-M2. (b) and (c) Peak emission intensity and the output power for the RCLED-M1 and RCLED-M2 as a function of temperature, respectively. The dashed-dotted line represents the relative values. Over the temperature range 20-300 K, the relative values are greater than 1, indicating that the peak intensity and the output power of the RCLED-M1 emission are higher than that of the RCLED-M2.

Temperature-dependent electroluminescence spectra of the RCLED-M2 were measured and plotted in Figure 6.10(a). As can be seen in this figure, the emission spectra of the mean resonant

cavity mode at low temperature ($T < 60$ K) does not have a significant peak intensity. As temperature increases, a significant peak intensity of the main emission mode was observed. This is because as the temperature increases the detuning between the emission of the optical cavity mode and the active region decreases. In comparison with results of the emission spectra of the RCLED-M2, the RCLED-M1 device has a significant peak intensity of the main resonance mode emission over all temperatures, showing that the peak intensity is higher than that of the RCLED-M2 emission. In [Figure 6.10\(b\)](#), we plotted the intensity of the mean resonant emission peak of the RCLED-M2 together with that of the RCLED-M1 over the temperature range from 60 K to 300 K. From this figure, it is noticed that the peak intensity of the RCLED-M1 and the RCLED-M2 emission decreases with increasing temperature by a factor of ~ 66 and ~ 15 , respectively. It was also found that the peak intensity of the RCLED-M1 emission is higher than that of the RCLED-M2 emission by a factor of ~ 7 at 60 K, decreasing with increasing temperature to be 1.55x at 300 K. Increase of the relative intensity with decreasing temperature indicates that the quality factor (Q) of the RCLED-M1 increases at a rate higher than that of the RCLED-M2. Furthermore, the total optical output power of the RCLED-M2 was evaluated as a function of temperature and plotted together with the output power of the RCLED-M1 emission as shown in [Figure 6.10\(c\)](#). As the temperature increases from 60 K to 300 K, the output power of both devices decrease by a factor of ~ 10 , with a small variation in the relative output powers which was determined to be around 1.45. The RCLED-M1 has an optical output power higher than that of the RCLED-M2 emission.

6.4 Electrical Characterisation of the low detuning InAsSb RCLED

Over the temperature range of 77-300 K, the current-voltage I-V characteristics of the RCLED-M1, RCLED-M2 and reference LED were measured and plotted in [Figures 6.11\(a\)](#), [6.11\(b\)](#) and [6.11\(c\)](#), respectively. For RCLED-M1 and RCLED-M2 devices, the voltage was applied in the range from -10 to $+10$ and from -2.5 to 2.5 V respectively, and over the range from -0.8 to 0.8 V for the reference LED, where a current compliance of 200 mA was used throughout. From

the data in Figure 6.11(c), the series resistance of the devices was evaluated. The reference LED has a series resistance of $\sim 2 \Omega$ at 77 K and 4Ω at 300 K, while the resistance of the RCLED-M1 decreases gradually from 33Ω to 25Ω when the temperature increases from 77 K to 300 K. In comparison with RCLED-M1, removal of the top DBR mirror leads to improvement in the I-V characteristics of the RCLED-M2, having a low series resistance and low reverse current. As temperature increases from the 77 K to 300 K, the resistance of the RCLED-M2 increases slightly from $\sim 9 \Omega$ to $\sim 12 \Omega$.

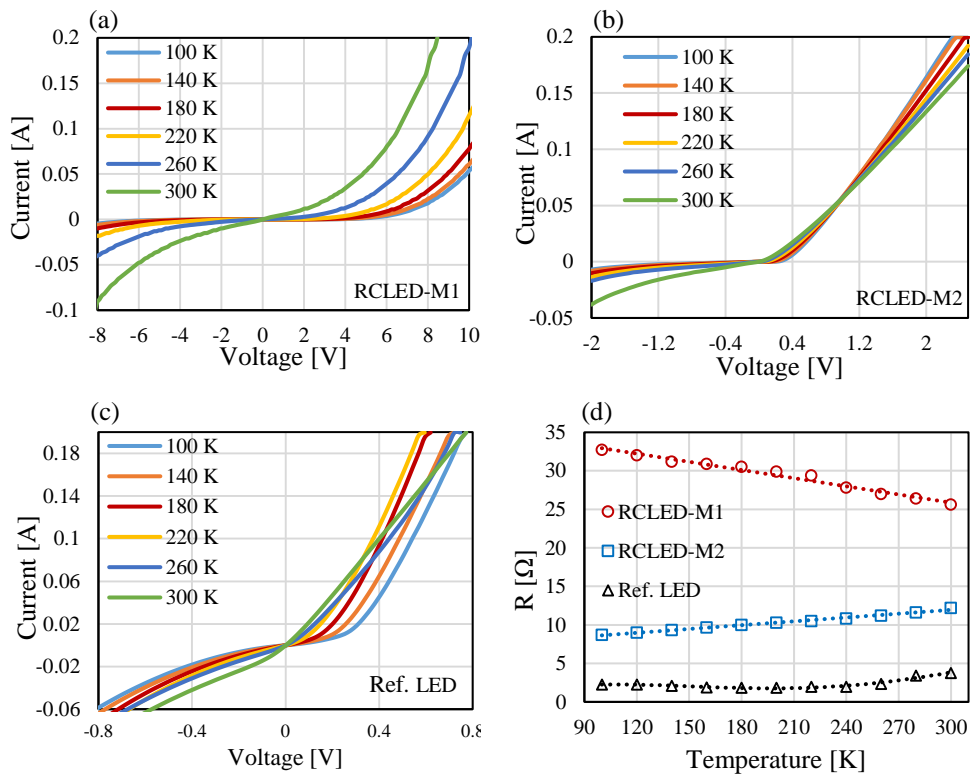


Figure 6.11: (a)-(c) Current-Voltage (I-V) characteristics of the RCLED-M1, RCLED-M2, and the reference LED measured as a function of temperature, respectively. (d) Temperature dependence of the series resistance of the RCLED-M1, RCLED-M2, and the reference LED.

From Figure 6.11 (a), the turn on voltage for RCLED-M1 is high and increased with decreasing temperature. In comparison with I-V characteristics shown in Figures 6.11 (b) and (c), the results show that the turn on voltage of the RCLED-M2 is lower than that of the RCLED-M1, and the reference LED has the lower turn on voltage among them. The high turn on voltage of the RCLED-M1 is because the current must pass through the AlAsSb and GaSb DBR layers, where there is a high conduction band offset between these layers and the cavity layers.

6.5 Photo-response of the low detuning InAsSb RCLED-M1

In this section we demonstrated the measurements of the spectral photo-response of the RCLED-M1 as a function of the temperature under various reverse bias voltage. The photo-response spectra were carried out using the system which is described in [section 4.8](#). At room temperature, and as shown in [Figure 6.12\(a\)](#), it was observed that the photo-response spectra have a resonant peak positioned at $\sim 4.275 \mu\text{m}$ and a linewidth of 88 nm. The peak intensity of the photo-response spectra was plotted as a function of the bias voltage in [Figure 6.12\(b\)](#). The peak intensity increases with increasing reverse bias until $V=-500 \text{ mV}$, then the intensity slightly decreases as reverse bias increases.

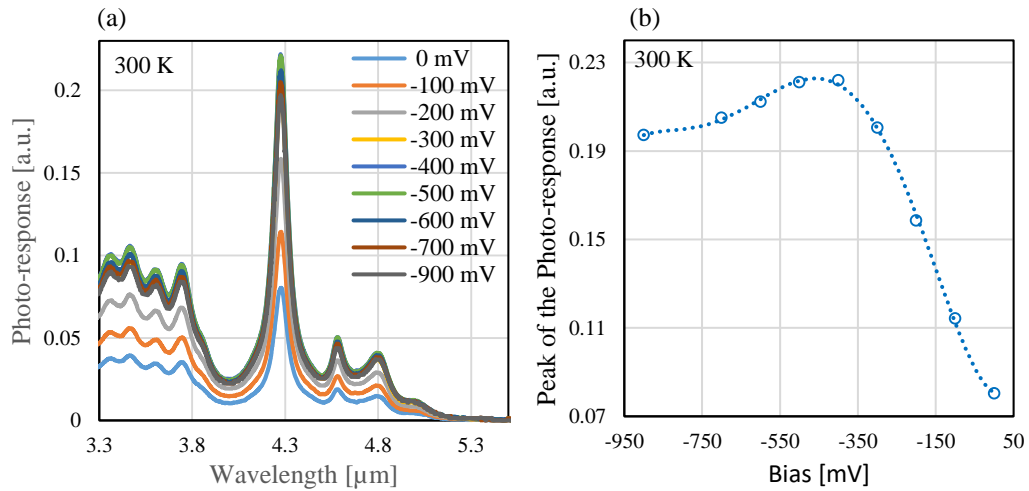


Figure 6.12: (a) Room temperature photo-response spectra of the RCLED-M1 at various bias voltage. (b) Peak intensity of the photo-response spectra as a function of the bias voltage measured at 300 K.

The photo-response of the RCLED-M1 as a function of temperature were also evaluated. For temperature $T < 200 \text{ K}$, it was found that there is no significant photo-response could be observed until $T = 200 \text{ K}$. [Figure 6.13\(a\)](#) presents the photo-response of the RCLED-M1 at $T = 200 \text{ K}$ at various bias voltage, showing the peak intensity decreases with increasing reverse bias voltage. In comparison between the spectral photo-response at 200 K and at 300 K (see [Figures 6.13 \(b\)](#) and [6.13\(c\)](#)), we found that the intensity of the spectra at 300 K is higher than at 200 K even if the reverse bias voltage increases.

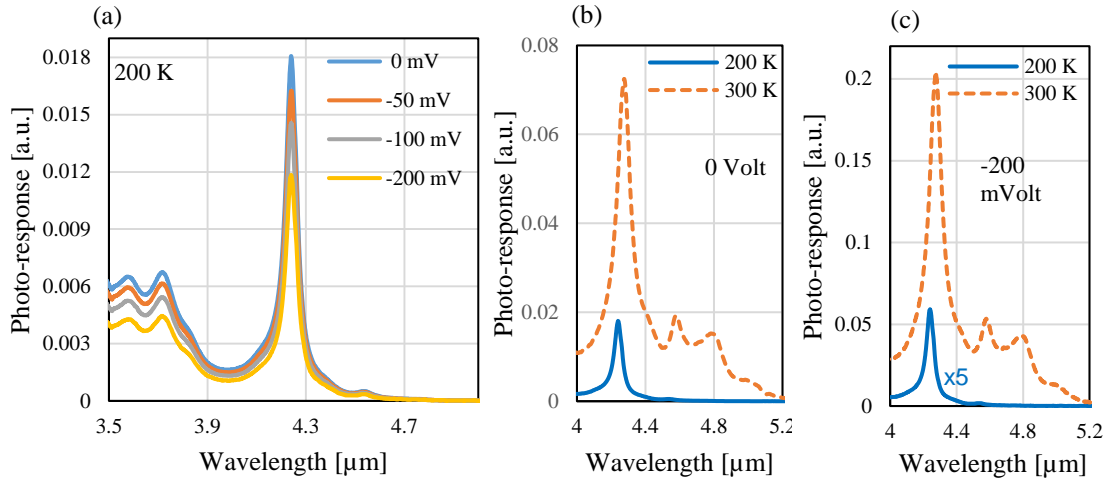


Figure 6.13: (a) Photo-response spectra of the RCLED-M1 measured at 200 K at various bias voltage. (b) and (c) Spectral photo-response at 300 K compared to that at 200 K at 0 bias and -200 mV, respectively.

As temperature increases, the wavelength of the peak intensity of the photo-response spectra shifts to longer wavelength and the linewidth becomes boarder. At 200 K, the photo-response has a peak intensity centered at 4.240 μm with linewidth of ~ 57 nm, shifting to be positioned at 4.262 μm with linewidth of 78 nm at 260 K. Furthermore, it was found that the intensity of the photo-response increases with increasing temperature. In Figure 6.14 we plotted the photo-response spectra measured at 260 K at various reverse bias. We found that the intensity is higher than that at 200 K and less than that at 300 K.

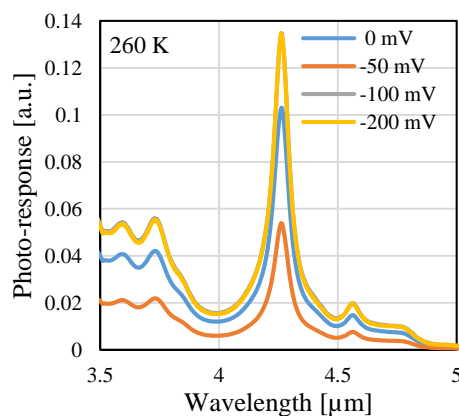


Figure 6.14: (a) Photo-response spectra of the RCLED-M1 measured at 260 K at various reverse bias voltage.

6.6 Discussion

The results of the electroluminescence spectra of the RCLED designed with high detuning between the resonant optical cavity mode and the DBR stopband center show that side peaks could be observed on both sides of the DBR stopband. It was noticed that the short wavelength side peaks shift towards longer wavelength with increasing temperature at a rate less than the longer wavelength side peaks. To explain this, note that as illustrated in Figure 6.15, the transmission spectra of this sample exhibited these side peaks which are also shifted towards longer wavelength as temperature increases. It was found that when the temperature increases from 77 K to 300 K, the shorter wavelength side peaks shift at a rate of 0.194 nm/K and the longer wavelength side peaks shift by a rate of 0.374 nm/K, which is in a very good agreement with results obtained from the side peaks observed in the electroluminescence spectra of the RCLED. Based on these results, the wavelength of the side peaks is determined by the temperature dependence of the refractive index and the thickness of the DBR layers compared to that of the resonant optical mode which is determined by the refractive index and the thickness of the cavity layers.

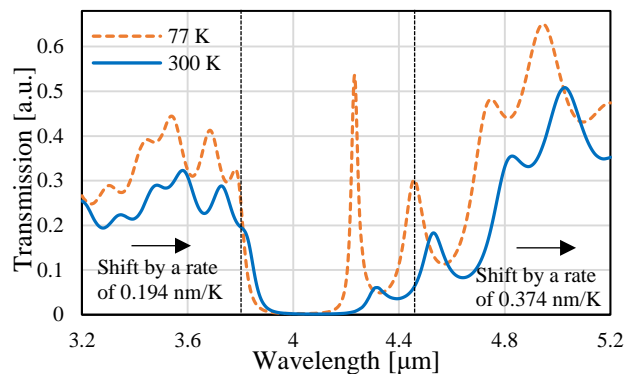


Figure 6.15: (a) Transmission spectra of the high detuning RC sample at 77 K and 300 K.

The emission of the RCLED without top DBR mirror shows that the emission intensity and the integrated emission are still enhanced, but less than that of the full RCLED structure. This is due to the low reflectivity of the semiconductor/air interface (~33%) which is working as a top mirror when the top DBR is removed from the RCLED structure.

The results from the emission spectra of the RCLED-M1 and RCLED-M2 show that the device configuration (and fabrication method) play a significant role in the resulting optical and electrical properties of the device. In the RCLED-M2 structure the p-type contact was deposited on top of the cavity and as a result, the current-voltage characteristics were improved compared to that of the RCLED-M1 (the p-contact deposited on the top DBR), whilst the enhancement factors of the emission were decreased. The results of the electroluminescence spectra of the RCLED-M2 were similar to that of the RCLED without top DBR, suggesting that the electroluminescence of the RCLED-M2 is emitted from the surface of the cavity instead of the surface of the top DBR mirror. Therefore, the emission intensity and the integrated emission enhancement factors of the RCLED-M2 were determined by the high reflectivity bottom DBR mirror (>98%) and the low reflectivity top InAsSb/air mirror (~33%), showing lower enhancement factors compared to that of the RCLED-M1 emission.

The electroluminescence spectra of the RCLED show that the wavelength of the resonant emission peak red shifts at a rate less than that of the reference LED and the emission linewidth is narrower than that of the LED. This is because the wavelength of the resonant emission peak and the emission linewidth of the RCLED depend primarily on the refractive index and the thickness of the cavity layers, and the reflectivity of the DBR mirrors (the quality factor Q), respectively. In addition and as shown in [Figure 6.4\(b\)](#), a strong emission enhancement at the resonant wavelength is obtained in close agreement with our resonant cavity design, and, in particular, due to the reflectivity of the DBR mirrors and the positioning of the active region at the electric field antinode within the cavity (the antinode enhancement $\xi=2$). The resonant peak emission, the integrated peak emission, and the total integrated emission are enhanced by a factor of ~70, ~11, and ~33, respectively. Due to the more reflective DBR mirrors and higher cavity Q-factor, our results show greater enhancement values (x10) compared with previous work [\[44,49\]](#). The output power of the RCLED was measured to be 5.5 μW (external efficiency ~0.024%) at 300K rising to 45 μW at 77 K. We note that the electroluminescence of our RCLED lies entirely within the CO₂ absorption band which coupled with the improved directionality

provides a higher level of useful emission intensity compared with previous works [7,14,21,22,24-26,136].

The photoresponse shows a partial resonance at 4.3 μm . However, the strength of the resonance does not resemble constructive interference as seen in resonant cavity enhanced detectors. This is because the cavity thickness was chosen to be 1x lambda, in order to maximize emission, rather than to maximize the optical field at the cavity centre. As a result the strength of the resonance is only around 2x the background signal away from the resonant wavelengths. The response increases with bias between 150 – 400 mV, due to improved collection of photogenerated carriers, but reduces again at larger bias conditions due increased recombination due to dark currents.

Chapter 7

AlInAs/InAsSb MQWs resonant cavity light emitting diode for N₂O Detection

7.1 Introduction

In this chapter, we demonstrate a mid-infrared resonant cavity light emitting diode (RCLED) operating near 4.5 μm at room temperature to detect N₂O gas, grown lattice-matched on a GaSb substrate by molecular beam epitaxy. The device consists of a 1λ -thick micro-cavity containing an Al_{0.12}In_{0.88}As/InAs_{0.85}Sb_{0.15} QWs active region sandwiched between two high contrast, lattice-matched AlAs_{0.08}Sb_{0.92}/GaSb distributed Bragg reflector (DBR) mirrors. Under similar conditions, the QWs RCLED and a conventional LED were grown and fabricated to demonstrate the enhancement achieved as a result of using a resonant cavity. The electroluminescence emission spectra of the RCLED and the reference LED were measured over the temperature range from 20 to 300 K. In comparison with reference LED, the RCLED exhibits a strong enhancement in the emission intensity and integrated emission enhancement due to the resonant cavity effects- constructive interference. At room temperature, the RCLED emission exhibits significantly (16x) narrower spectral linewidth (69.5 nm) and superior temperature stability ~ 0.36 nm/K, which is $\sim 7x$ less than that of the reference LED. Electroluminescence spectra of the RCLED at different injection current and duty cycle were measured at room temperature. As injection current increases, the emission intensity, the output power and the linewidth of the RCLED emission are increased, and the emission peak shifts to longer wavelengths. Similar behaviour was observed when the duty cycle was increased. Temperature dependent current-voltage characteristics revealed that both the series resistance and the turn on voltage decrease as temperature increases. It was also found that the emission peak shifts towards longer wavelength and the linewidth of the emission spectra become broader. Finally, the optical and electrical characteristics of the RCLED without top DBR mirror

were investigated. The results show that a strong enhancement in the emission intensity and integrated emission are still achieved. In comparison with reference LED, the intensity peak and the integrated emission of the RCLED without top DBR mirror were enhanced by a factor of 24x and 8x, respectively. It was also found that the emission spectrum shows a narrow linewidth (185 nm) which is less than that of the reference LED by a factor of 6x.

The high brightness, better spectral purity, narrow linewidth and superior temperature stability, are attractive features, which would enable these devices to be implemented in next generation N₂O gas sensor instrumentation.

7.2 AllInAs/InAsSb MQWs RCLED

7.2.1 Fabrication of the MQWs RCLED and the reference LED

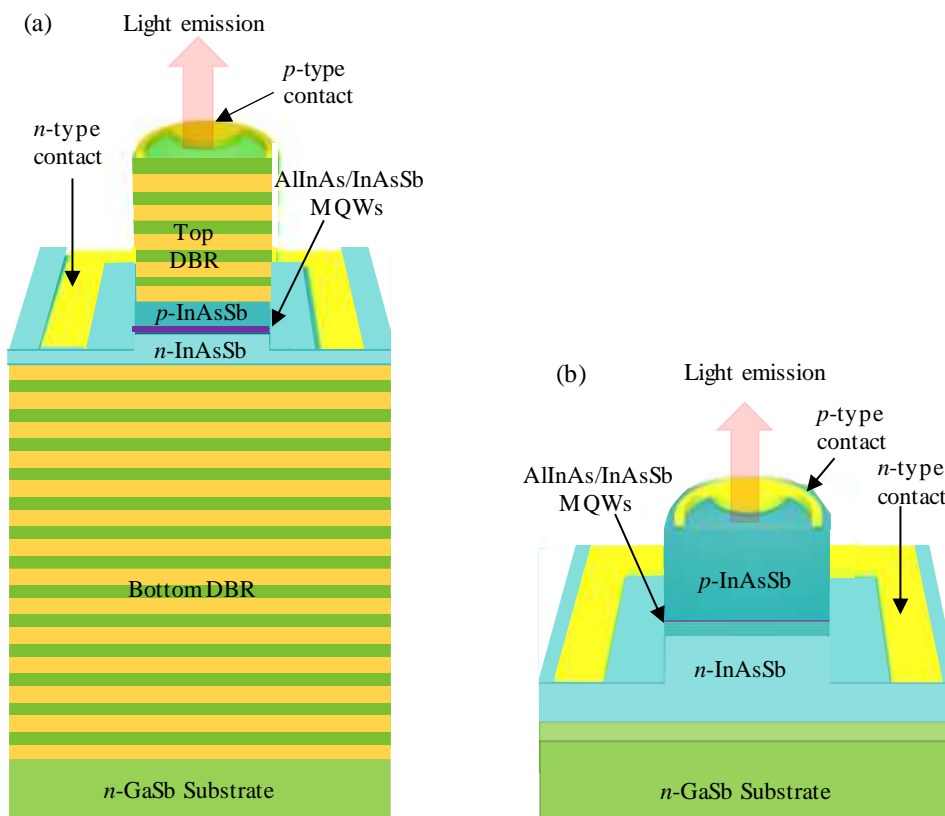


Figure 7.1: Schematic structure of the (a) AllInAs/InAsSb QWs RCLED. (b) reference LED.

Processing was carried out using standard photolithography and wet chemical etchants followed by Ti/Au metallization for the ohmic contacts as described in chapter 4. Ti/Au top contact for the p -side of the RCLED was deposited on the top p -type GaSb DBR layer by thermal evaporation and metal lift-off. A second photolithography step was carried out to pattern the sample for subsequent wet etching of the mesa, by etching through the structure and stopping within the n -InAsSb cavity layer. The first layers etched are the top DBR layers followed by etching the p -InAsSb cavity layer and then the active region layers. Finally, a Ti/Au metal contact was then deposited on the n -InAsSb layer to provide an Ohmic contact for the n -side. In the case of the LED, Ti/Au top contact for p -side was deposited on the top p -type InAsSb layer and the bottom contact was deposited on the cavity n -InAsSb layer following wet etching. The structure of the RCLED and reference LED are illustrated in [Figure 7.1\(a\)](#) and [7.1\(b\)](#), respectively.

7.2.2 Optical Characterisation

After fabrication, the optical transmission and the electroluminescence (EL) measurements of the samples were obtained using the two systems which are described in chapter 4, section 4.7 and 4.8, respectively.

7.2.2.1 Micro-cavity enhancement of mid-infrared electroluminescence

As reported in chapter 5, numerical modelling has been utilised to design and evaluate the emission enhancement of the full resonant-cavity structure and the reflectivity of the top and bottom DBR mirrors. The results of the modelling exhibits that 13.5 periods of the bottom DBR with reflectivity over 97.5% and 5 periods of the top DBR with reflectivity over 83% are sufficient to achieve a high emission enhancement. Furthermore, it was found that, in comparison with the resonance case, the enhancement values could be decreased due to detuning which is defined as a difference between the wavelength of the resonance cavity mode, λ_{cav} , and the wavelength of the DBR stop-band centre, λ_{DBR} .

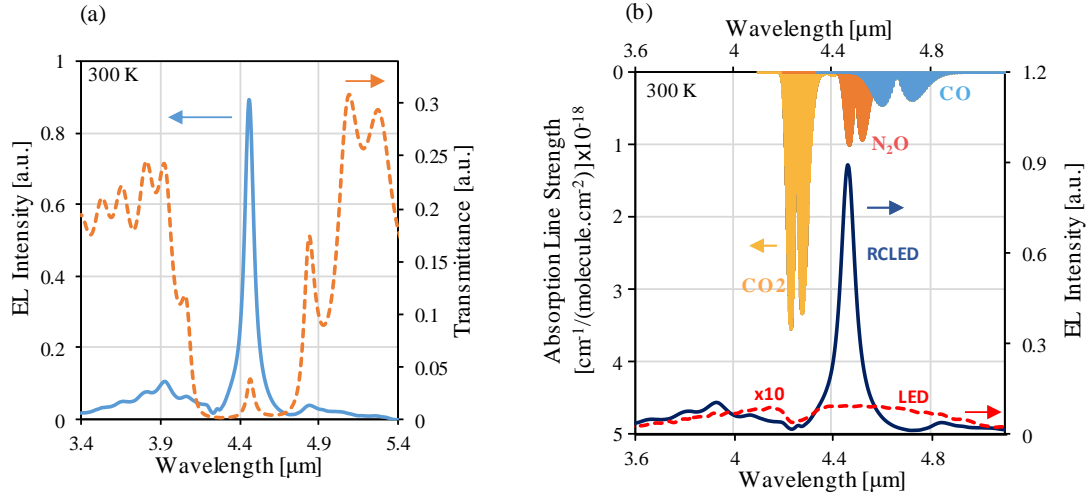


Figure 7.2: (a) Experimentally measured transmittance spectrum and EL emission spectrum of the RCLED structure, showing that the wavelength of the main EL emission peak at room temperature occurs at 4.462 μm , which corresponds to the cavity resonance wavelength. (b) Comparison of the RCLED (solid line) and the reference LED (dashed line) electroluminescence emission spectra at 300 K using the same injection current (100 mA at 1 kHz with 30% duty cycle). The dip in the reference LED spectrum originates from atmospheric CO_2 absorption in the optical path. Also shown are the fundamental fingerprint absorptions of greenhouse gases of interest in this spectral range.

Experimentally, the optical transmittance spectrum of the full RC structure is typically used to identify the value of the detuning. Figure 7.2(a) shows the transmittance spectrum of the QWs resonant-cavity structure measured using a Fourier-transform infrared (FTIR) spectrometer and the electroluminescence (EL) spectrum of the QWs RCLED at room temperature. It was found that the wavelength of the main EL emission peak occurs at 4.462 μm , corresponding to the wavelength of the resonant cavity mode observed in the transmittance spectrum. (The small emission peaks on either side of the main peak originate from fluctuations in cavity transmission). In addition, the transmittance spectrum exhibits a DBR stop-band (λ_{DBR}) centred at around 4.447 μm , exhibiting a low detuning (~ 15 nm) with emission of the resonant cavity mode (λ_{cav}). However, the magnitude of this detuning (the difference between λ_{cav} and λ_{DBR}) is less than that of the bulk InAsSb RCLED (see chapter 6). Based on the detuning result of the QWs RC, the theoretical measurements exhibit that the QWs RCLED has a higher enhancement factor compared to that of the bulk RCLED - especially the emission intensity enhancement. Figure 7.2(b) compares the electroluminescence emission spectra of the RCLED

and reference LED measured at 300 K using the same quasi-continuous injection current of 100 mA at 1 kHz with 30% duty cycle. As shown in this figure, at room temperature the RCLED peak emission at 4.462 μm overlaps nicely with the fundamental N_2O fingerprint absorption. The linewidth at full width at half maximum (FWHM) of the RCLED is 70 nm, which is 16x narrower than the MQW reference LED, so that substantially more *useable* photons fall within the N_2O absorption envelope. With minor adjustments to the micro-cavity dimensions, the peak position and spectral overlap can be optimised, or adjusted to detect other gases – CO_2 or CO , without changing the Sb content in the MQW (– see discussion). In addition to reducing the linewidth, the resonant cavity enhancement has the effect of significantly increasing the peak emission intensity by 85x, with an increase in the total integrated emission (average output power) of 13x, which corresponds to an emittance of 2.5 mWcm^{-2} (or radiance $\sim 1.6 \text{ mW/ cm}^2 \text{ sr}$) and a spectral intensity of 36 $\mu\text{Wcm}^{-2}\text{nm}^{-1}$.

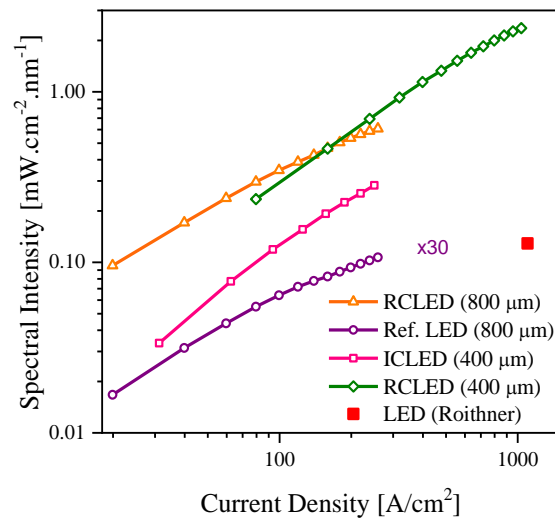


Figure 7.3: The spectral intensity of two RCLEDs of different diameter vs current density, measured at room temperature using a 1 kHz injection current with 1% duty cycle. The MQW reference LED is also shown (x30) together with other results from the literature measured under similar conditions. The ICLED made in our laboratory is 400 μm x 400 μm [36]. The conventional 4.6 μm LED spectral intensity was estimated from the peak power given in the Roithner Lasertechnik data sheet [137].

The spectral intensity compares favourably with that of commercial devices [137] and non-resonant structures [21,86]. Figure 7.3 shows the peak spectral intensity measured under high injection using a 1% duty cycle to reduce Joule heating effect. Conventional, non-resonant

LEDs can be series connected in a small array to increase the output power for gas sensing but much of this radiation lies outside the gas absorption band [28,138]. Interband cascade LEDs (ICLEDs) can exhibit higher output power at 300 K [36,95], but again spread over a much larger linewidth (FWHM \sim 500-1000 nm). Recent results from 5-stage ICLEDs made in our laboratory which exhibit high output power are also shown in Figure 7.3 for comparison, but the spectral intensity of the RCLED is much superior, reaching $> 2 \text{ mWcm}^{-2}\text{nm}^{-1}$. All the devices exhibit some rollover at high injection, due to the build-up of non-radiative Auger recombination. The 400 μm dia. RCLED exhibits more linear performance, which we attribute to increased ohmic loss due to the higher current drawn in larger area devices. This is also evident in the ICLED.

The far-field technique which is described in chapter 6 (section 6.3.2.1) has been used to measure the angular emission profile of the MQWs RCLED, where the distance between the emitter and the detector was also about 1 cm. At room temperature, the results exhibited a single-lobe emission profile with a half power solid angle of 45° as illustrated in Figure 7.4, showing a better directionality compared with that of the bulk InAsSb RCLED.

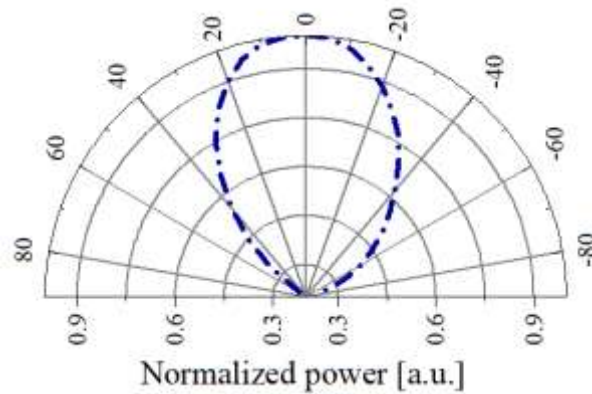


Figure 7.4: Far field angular profile of the RCLED emission, which shows a half power solid angle of 45° .

7.2.2.2 Temperature dependence of the electroluminescence spectra

The electroluminescence (EL) emission spectra of the QWs RCLED and reference LED devices measured at different temperatures in the range 20 – 300 K using 100 mA injection current at

30% duty cycle and 1 kHz are shown in [Figure 7.5\(a\)](#) and [7.5\(b\)](#), respectively. The results show that the intensity peaks of the emission spectra of the reference LED decrease gradually from its highest value at 20 K to the lowest value at 300 K by a factor of 501. While, for the RCLED, the highest value of the intensity peak was measured at 120 K and found to be higher than the lowest value measured at 300 K by a factor of ~ 4 . As seen in [Figure 7.5\(c\)](#), over the temperature range from 20 K to 200 K, the EL spectra of the RCLED have approximately similar intensity peak values. When the temperature increases from 200 K to 300 K, the intensity peak values decrease gradually. Consequently, the relative intensity which is defined as the ratio of the intensity peak value of the RCLED and reference LED increases with increasing the temperature until $T \approx 240$ K and then slightly decreases. This is attributed to the non-resonance between the emission spectra of the AlInAs/InAsSb QWs active region and the resonant cavity mode. When the temperature increases, the detuning decreases gradually resulting in increasing the intensity peak of the RCLED compared with those values of the reference LED.

In addition, the results show that the EL emission peak of the RCLED shifts to longer wavelengths with increasing temperature but much more slowly compared to the EL spectra of the reference LED. This behavior arises because in the conventional LED the wavelength shift of the EL spectrum is due to the temperature dependence of the active region bandgap. Whereas, for the RCLED, the EL peak depends on the wavelength of the resonant cavity optical mode which is determined by the thickness and the refractive index of the materials forming the cavity. Theoretically, as reported in the chapter 6, the thickness of the cavity has been calculated as a function of the temperature and it has been found that this variation represents less than 4% of the total wavelength shift. Therefore, the main contribution to the wavelength shift comes from the temperature variation of the refractive index [[119,120](#)]. Consequently, the main EL emission peak of the RCLED shifts only by ~ 102 nm at a rate of 0.362 nm/K, while the peak of the EL spectrum of the conventional reference LED shifts by ~ 600 nm at a rate of ~ 2.5 nm/K. This represents a factor of 7 improvement in the emission wavelength stability with temperature, which is useful in applications such as gas detection where wavelength stability is required to ensure the emission peak remains within the gas absorption envelope as the

temperature varies. Good agreement between the theoretically expected and experimentally observed wavelength shift was achieved as shown in Figure 7.5(d), based on the relation given in equations (2.57), (5.7), (5.8), (5.11) and (5.12). Typically, the parameters listed in equation (2.57), λ_{cav} , n_{cav} , and L_{cav} are functions of the temperature.

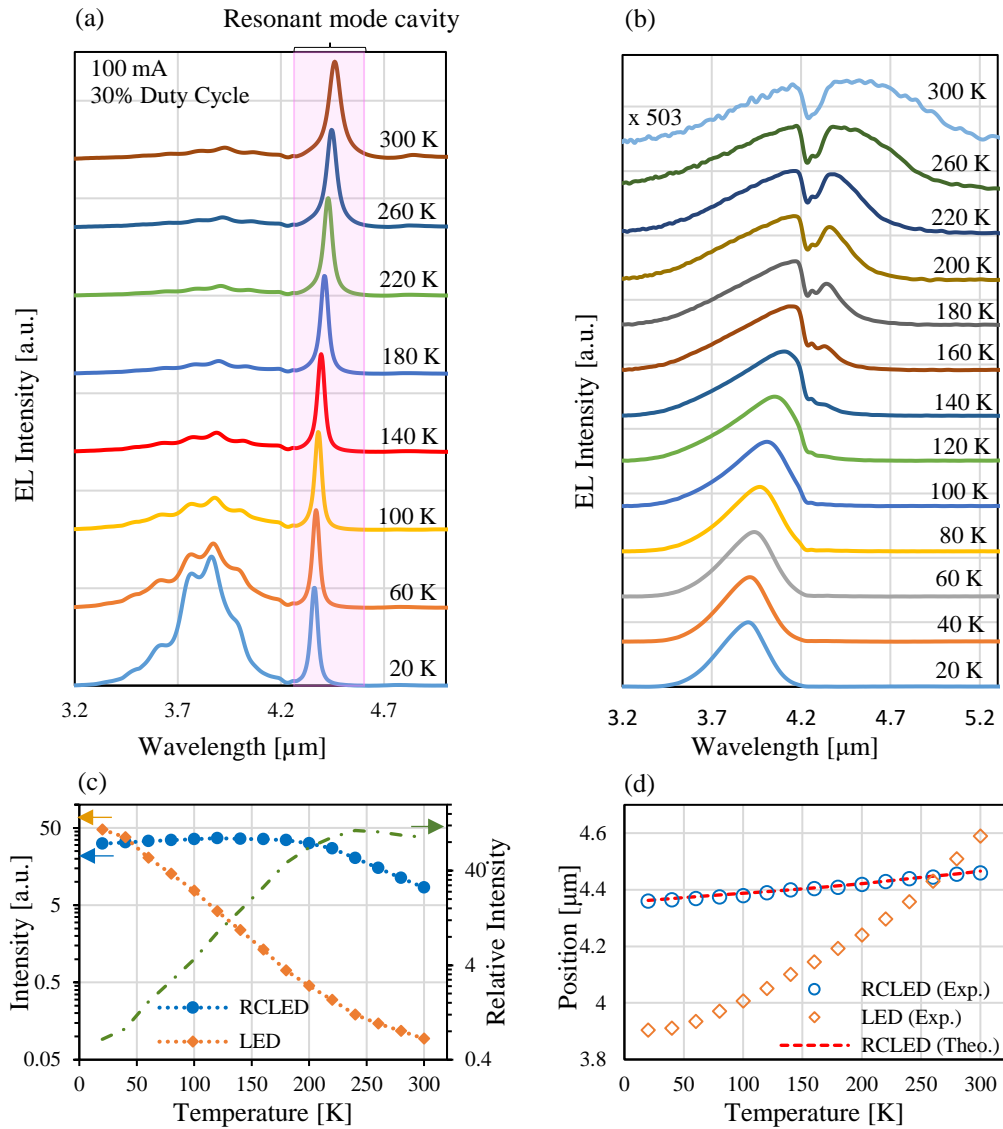


Figure 7.5: Temperature dependence of the EL spectra for (a) the RCLED and (b) the reference LED. (c) Intensity peak values of the EL spectra for the RCLED and reference LED. The dashed-dotted line represent the relative intensity. (d) The position of the EL peaks as a function of the temperature. The dashed line represent the theoretical results of the EL intensity peak of the RCLED.

From Figure 7.6(a), it is noticed that the full width at half maximum (FWHM) of the RCLED emission spectra are clearly narrower than those of the conventional LED. For the RCLED, over the temperature range from 20 K to 100 K, it was found that there is no noticeable change

in the linewidth, which is measured to be around 41 nm. As the temperature rises up ($T > 100$ K), the FWHM slightly increases to be 69.5 nm at 300 K. Whereas, the EL spectra of the reference LED become broaden rapidly with increasing temperature, with a linewidth of ~ 300 nm at 20 K and ~ 1140 nm at 300 K. This is attributed to the fact, as mentioned in chapter six, that the linewidth of the reference LED is determined by the joint density of states in the conduction and valance band and the thermal energy of carriers [41]. In contrast, for the RCLED, the linewidth depends on the quality factor of the resonant cavity. At room temperature, the emission spectrum of the RCLED has a linewidth ~ 16 x narrower than that of the reference LED. Consequently, the RCLED can be designed and tailored to match the absorption of the target gas. Over the measured temperature range from 20 K to 240 K, the relative linewidth ($\Delta\lambda_{\text{cavity}}/\Delta\lambda_{\text{reference}}$) decreases with increasing the temperature. It was also observed that the relative linewidth has approximately the similar value when the temperature increases above 240 K.

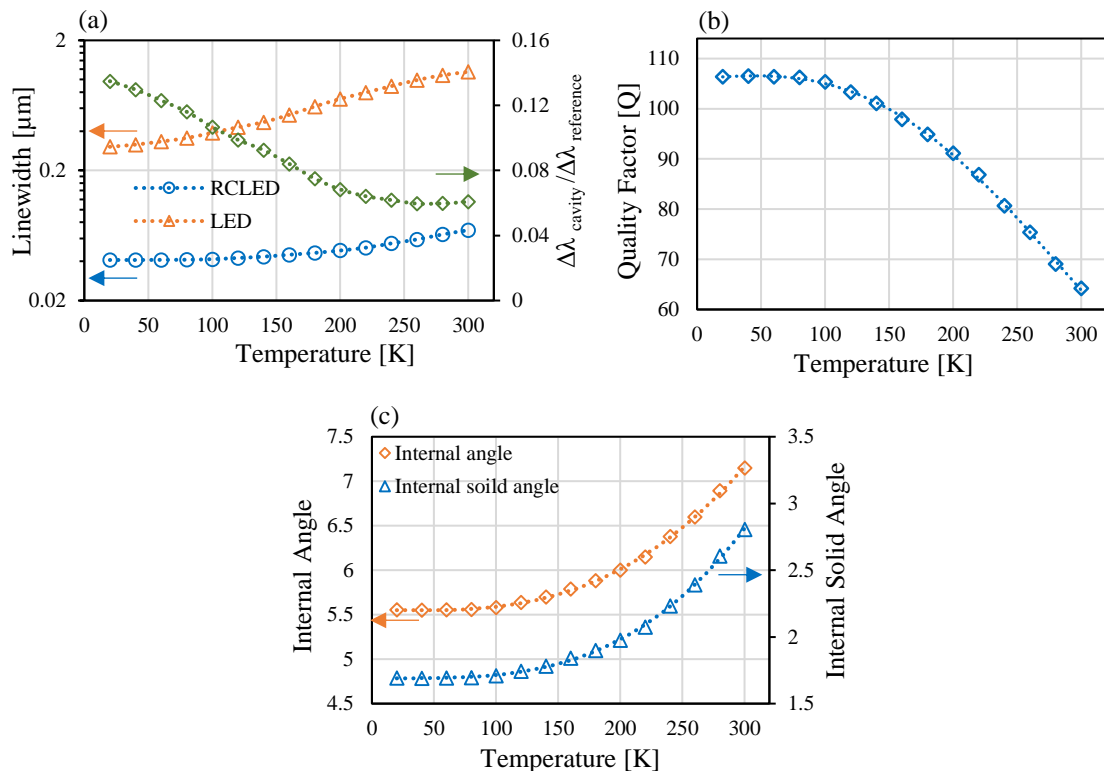


Figure 7.6: Temperature dependence of (a) The linewidth of the EL spectra for RCLED and reference LED, (b) the Quality factor (Q) of the RCLED, (c) The internal angle and solid angle of the RCLED which are determined according to the equations (2.60) and (2.61) and by using the experimental results of quality factor Q.

The measured experimental values of the FWHM and the position of the emission peak of the RCLED show that the quality factor of the resonant cavity decreases from $Q \approx 106$ to $Q \approx 64$ over the temperature range 20 – 300 K (see Figure 7.6(b)). The quality factor values were calculated according to the relation (2.59). The number of the resonant mode in the cavity (in the present work $m_c = 2$). Based on this relation, the cavity finesse has the same behavior as the quality factor as a function of the temperature. According to the relation (2.60) and (2.61), temperature dependence of the internal angle (on axis lobe), θ_{FWHM} , and internal solid angle, $\Delta\Omega$ have been investigated and plotted in Figure 7.6(c). The results indicate that the angle increases with increasing temperature, corresponding to a decrease the cavity finesse.

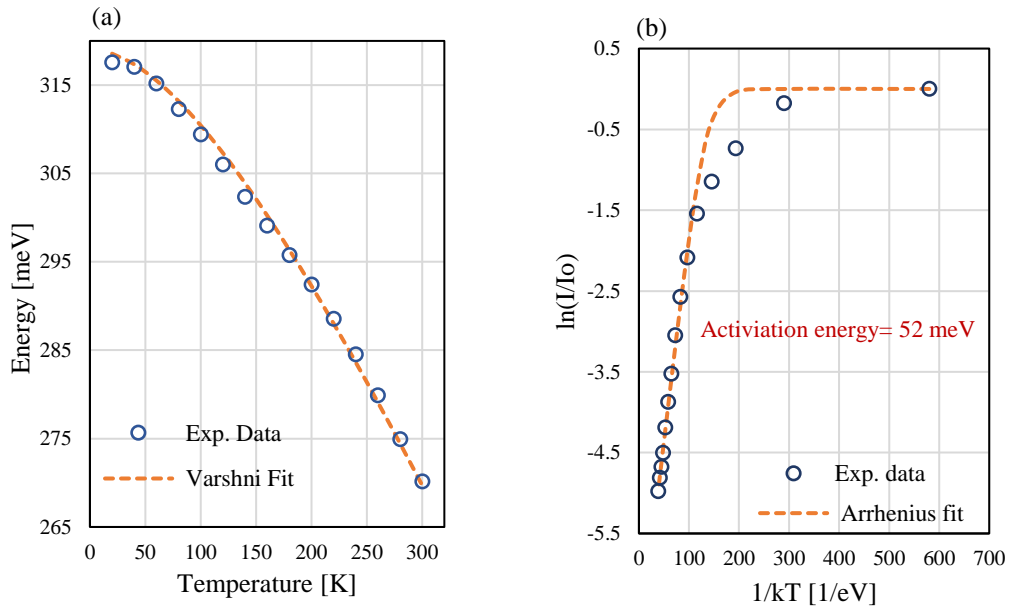


Figure 7.7: (a) Peak energy of the EL emission for the reference LED and the fitting using Varshni equation. (b) Arrhenius plot of the integrated EL intensity for the reference LED indicating an activation energy of 52 meV.

Figure 7.7(a) shows the temperature dependence of the EL peak energy of the reference LED. The measured data were fitted using the Varshni equation (2.1). The values obtained for the Varshni fitting parameters were $E_g(T = 5K) = 319$ meV, $\alpha = 0.305$ meV/K and $\beta = 255$ K which are in good agreement with the results previously reported for InAsSb lattice matched on a GaSb substrate [139]. As seen in Figure 7.7(b), the EL spectra of the reference LED show a

decrease of the integrated intensity as temperature increases. This behavior could be described by the Arrhenius equation [139]:

$$I = I_0/[1 + A_i \exp(-E_a/kT)] \quad (7.1)$$

where A_i is the non-radiative recombination process coefficient. E_a and k are the activation energy corresponding to the recombination process and the Boltzmann constant, respectively. The dashed line in Figure 7.7(b) represents the fitting of the experimental data using the Arrhenius equation indicating that the activation energy is about 52 meV. The decreasing of the EL intensity with increasing temperature is attributed to a progressively larger proportion of electron-hole recombination being non-radiative, as Auger processes are strongly temperature dependent and follow the general relation [140]:

$$R_{\text{Auger}} \propto \exp(-E_a/K_B T) T^3 \quad (7.2)$$

where E_a is the activation energy for the non-radiative Auger process and the exponential term dominates. The specific Auger processes, CHCC and CHSH, have their own activation energies defined by the equations (2.32) and (2.33). Furthermore, it is possible to determine the dominant Auger process occurring in a structure according to following equation:

$$\frac{(E_T - \Delta_{\text{so}})/E_T}{m_e^*/m_{\text{so}}^*} > 1 \quad (7.3)$$

The ground state transition energy ($E_T = e1 - hh1$) and the spin orbit splitting energy Δ_{so} have been calculated using *nextnano* simulation. The non-radiative CHCC process is the dominant Auger recombination process when the condition in equation (7.3) is satisfied. Using linear interpolation for the carrier effective masses, the activation energy of the CHCC and CHSH processes were calculated to be 13.4 meV and 37.2 meV, respectively. The value of the condition given by the equation (7.3) was calculated to be 4.54 (greater than 1), hence non-radiative CHCC recombination process is the dominant Auger recombination process.

7.2.2.3 Peak emission intensity and integrated emission enhancement

In order to evaluate the intensity enhancement factor, the peak intensity of the emission spectra of the RCLED and the EL intensity of the reference LED were measured corresponding to the peak position of the main EL emission spectra. The results were obtained over the temperature range from 140 K to 300 K and are plotted in Figure 7.8(a). The ratio of the EL intensity peak of the RCLED to the EL intensity peak of the reference LED represents the intensity enhancement factor. Over the measured temperature range, it was found that the intensity enhancement factor of the RCLED decreases with increasing temperature due to a decrease in the quality factor as temperature increases (see Figure 7.6(b)).

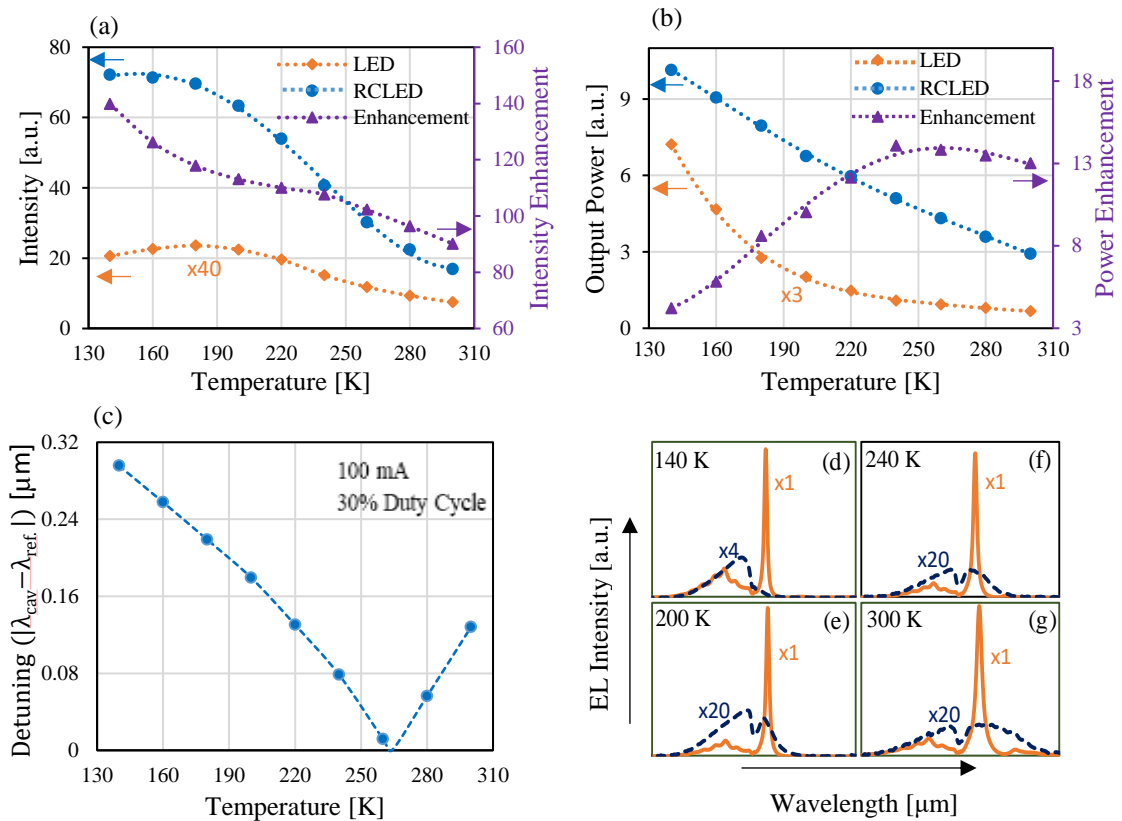


Figure 7.8: (a) Temperature dependence of the intensity peak for the resonance emission spectra of RCLED and the emission spectra of LED. (b) Temperature dependence of the output power for the emission spectra of the RCLED and LED. (c) The difference between the peak wavelengths (spectral detuning) as a function of temperature. (d)-(g) EL spectra of the RCLED and LED at different temperature, 140 K, 200 K, 240 and 300 K, respectively.

Figure 7.8(b) shows the output power of the emission spectra of the RCLED and reference LED as a function of the temperature. It was noticed that the output power of the EL emission spectra

of the RCLED and LED decreases with increasing temperature. As mentioned earlier, when $T < 260$ K, the quantity $\Delta\lambda_{cavity}/\Delta\lambda_{reference}$ and the intensity enhancement factor decrease as temperature increases. Consequently, the integrated enhancement factor should also decrease as the temperature increases. However, because the cavity resonance implicit in equation (2.73) is not satisfied at all temperatures (see the detuning values in [Figure 7.8\(c\)](#)), the integrated enhancement increases with temperature, as shown in [Figure 7.8\(b\)](#). The emission spectrum of the RCLED shifts to longer wavelengths more slowly compared to that of the reference LED – see [Figures 7.8\(d\) – 7.8\(g\)](#). Consequently, the difference between the peak wavelengths (spectral detuning) decreases gradually with increasing temperature and becomes zero at around $T = 260$ K, as shown in [Figure 7.8\(c\)](#). At room temperature, the resonance emission and integrated emission are enhanced by a factor of ~ 85 and ~ 13 , respectively. Hence, the influence of the microcavity on the electroluminescence spectrum of the RCLED is clearly evident. A strong emission enhancement is obtained due to, in particular, the reflectivity of the DBR mirrors and the positioning of the active region at the electric field antinode within the cavity. Due to the low detuning in the MQWs RCLED, the results show a greater intensity enhancement factor and narrower emission linewidth compared to that of the bulk RCLED.

7.2.2.4 Duty cycle effect on the electroluminescence emission

The electroluminescence emission spectra of the RCLED as a function of the duty cycle, measured at 300 K using 100 mA injection current at 1 kHz are shown in [Figure 7.9\(a\)](#), together with the peak intensity and the output power shown in [Figure 7.9\(b\)](#). As the duty cycle increases from 5% to 35%, the peak intensity increases by a factor of ~ 6 , whilst the output power increases by a factor of ~ 7 , ranging from ~ 1.4 μW at 5% to ~ 9.5 μW at 35%. As shown in [Figure 7.9\(c\) and \(d\)](#), the peak wavelength of the RCLED red shifts from 4.457 μm to 4.463 μm and the linewidth (FWHM) increases from 66.5 nm at duty cycle 5% to 70.5 nm at duty cycle 35%, respectively. The shift in the peak position and increase of the linewidth is consistent with the increase in temperature of the device, which was calculated to be approximately 16.5

K, corresponding to a 6.0 nm red shift in the emission spectrum. According to equation (2.59) and based on the results of the peak position and the linewidth of the electroluminescence spectra, the Q-factor were determined and plotted as a function of duty cycle in Figure 7.9(d). It was found that the Q-factor decreases slightly from 67 at duty cycle 5% to 63 at duty cycle 35%.

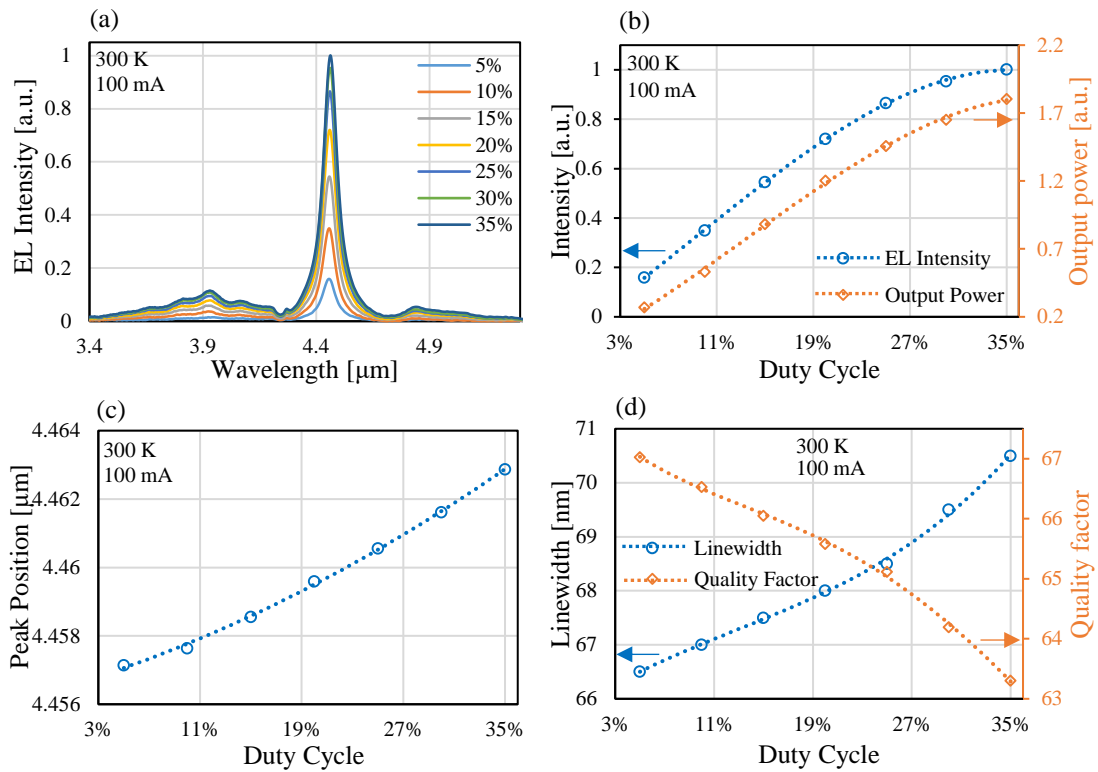


Figure 7.9: (a) Room temperature electroluminescence emission spectra of the RCLED as a function of the wavelength at different duty cycles using 100 mA injection current. (b) The peak intensity and the output power of the RCLED as a function of duty cycle. (c) The peak position of the electroluminescence emission vs the duty cycle. (d) The linewidth (FWHM) and the Q-factor of the electroluminescence spectra as a function of the duty cycle.

7.2.2.5 Injection current effect on the electroluminescence emission

The room-temperature power dependence of the electroluminescence spectra of the RCLED on injection current, using 30% duty cycle at 1 kHz, is shown in Figure 7.10(a). Over the range 20 mA-100 mA, the electroluminescence spectra are red-shifted to longer wavelength, where the emission peak shifts from 4.4555 μm at 20 mA to 4.4620 μm at 100 mA as shown in the inset Figure 7.10(a). The results also show that the spectrum has become broader with increasing

current, as the linewidth increases from 64.5 nm at 20 mA to 69.5 at 100 mA as illustrated in Figure 7.10(b). As expected, this behavior originates from the temperature increase of the RCLED. The redshift in the emission spectra was determined to be approximately 6.5 nm, corresponding to an increase in the temperature of the device by ~ 18 degrees. Similarly, the quality factor decreases from 69 to 64 when the injection current increases from 20 mA to 100 mA.

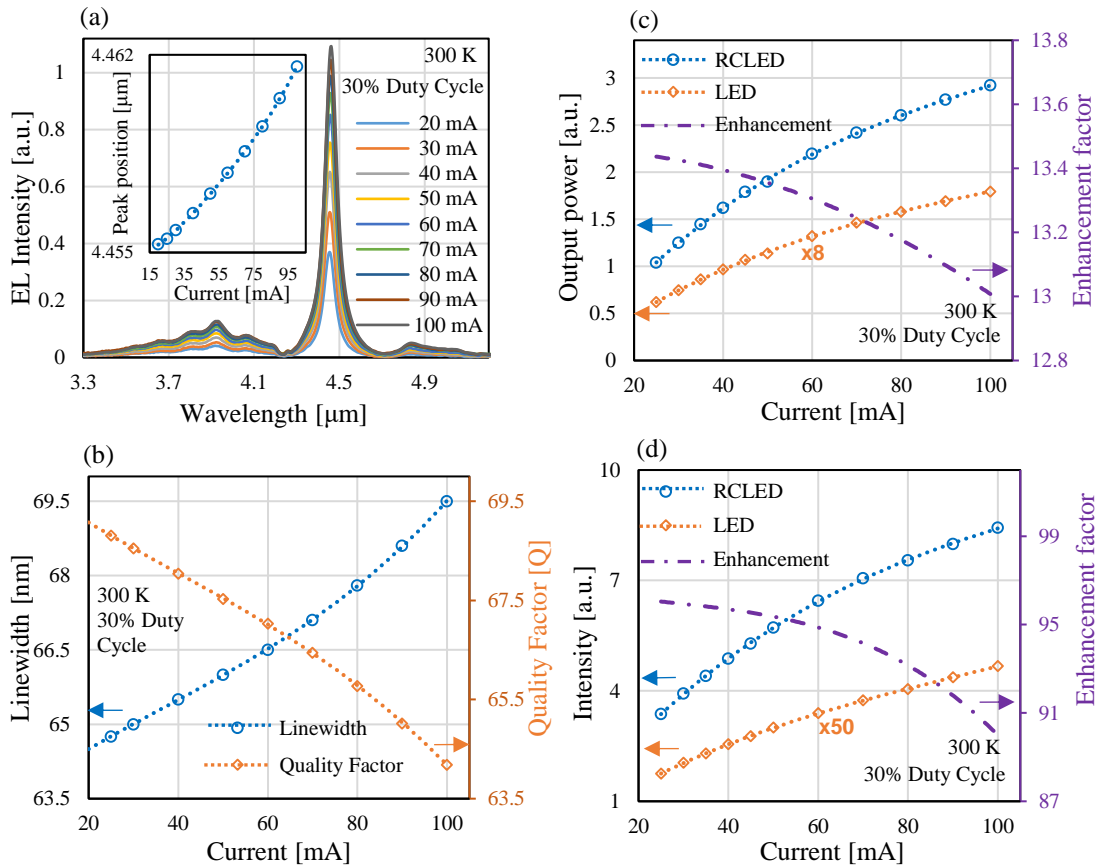


Figure 7.10: (a) Room-temperature power dependence of the electroluminescence emission spectra of the RCLED using different injection currents at 30% duty cycle. The inset is the peak position of the electroluminescence versus injection current. (b) The linewidth and the quality factor of the RCLED dependence on injection current. (c) Output power of the RCLED and reference LED as a function of injection current. The dashed-dotted line represents the power enhancement factor (the relative power). (d) Peak intensity of the RCLED and the reference LED as a function of injection current. The dashed-dotted line represents the intensity enhancement factor (the relative intensity).

Furthermore, the integrated enhancement factor and output power at 300 K are compared in Figure 7.10(c). The integrated emission (output power) enhancement factor decreases gradually as the current increases, indicating that Joule heating in the RCLED is more significant

compared to the reference LED, particularly for injection currents >50 mA. A similar behavior was observed in the peak intensity, where the emission (intensity) enhancement factor decreases gradually as the injection current increases, as shown in Figure 7.10(d). We estimated the output power of the RCLED to be ~ 3.0 μ W at 25 mA and ~ 8.5 μ W at 100 mA.

7.2.3 Temperature dependence of the current-voltage characteristics

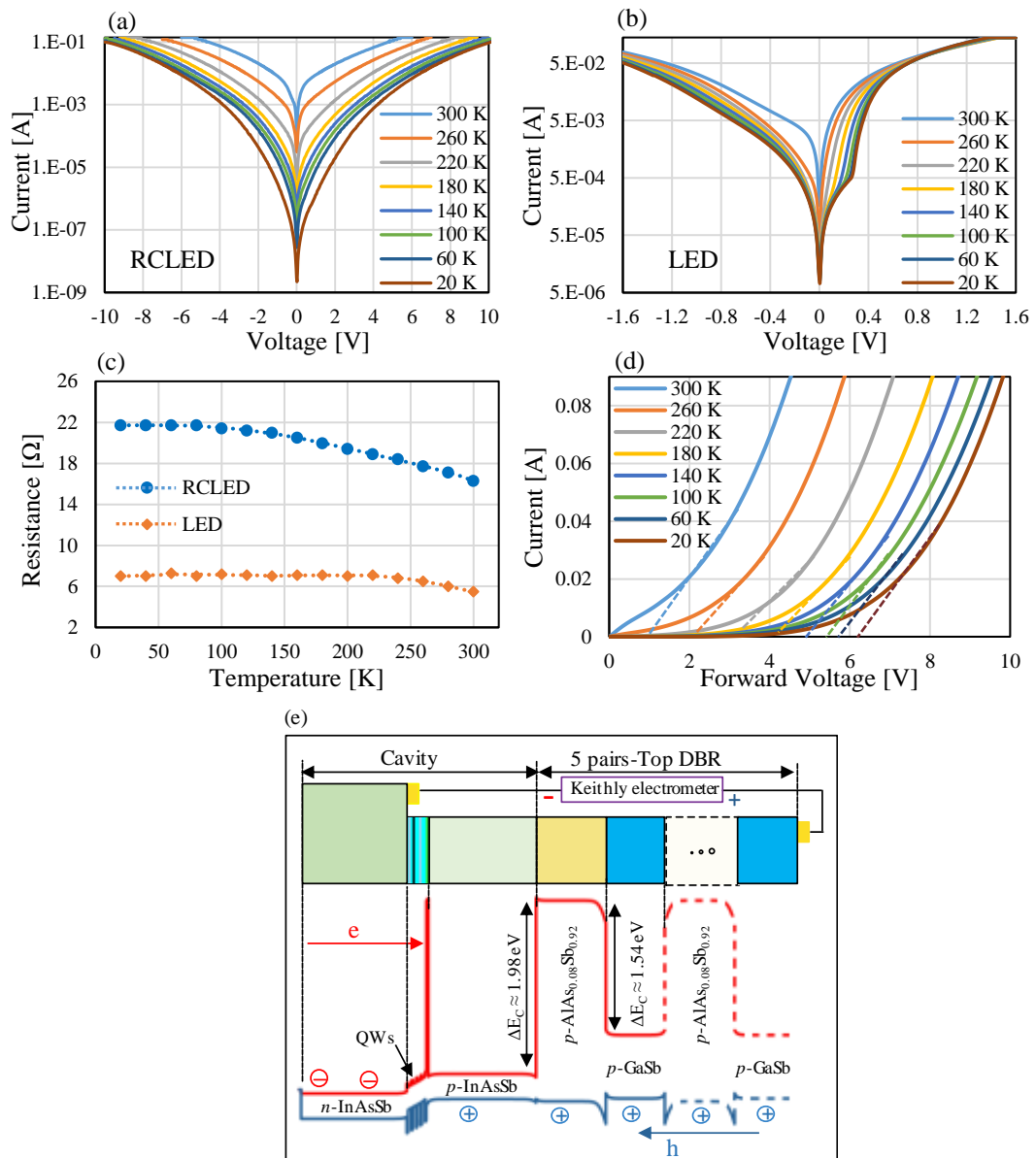


Figure 7.11: (a) and (b) The forward and reverse current-voltage characteristics of the RCLED and the reference LED over the temperature range 20 K-300 K. (c) The series resistance of the RCLED and reference LED as a function of temperature. (d) Forward current-voltage characteristic of the RCLED against the temperature. There is a clear trend of decreasing the turn on voltage with increasing the temperature. (e) Schematic diagram illustrates the path of the current through the DBR and cavity layers.

Measurements of the current-voltage I-V characteristics were carried out on RCLED and reference LED devices over a temperature range of 20-300 K in 20 K steps as seen in [Fig. 7.11\(a\)](#) and [7.11\(b\)](#), respectively. For the RCLED device, the voltage was applied in the range from -10 V to +10 V and over the range from -1.6 V to 1.6 V for the reference LED, where the current compliance of 100 mA was used throughout. From the data in [Figure 7.11\(c\)](#), it was found that the reference LED has a series resistance with value around 7.7 Ω at 20 K and slightly decreased with increasing temperature to be 5.5 Ω at 300 K. In comparison, the high applied voltage for the RCLED is accompanied by high differential resistances exceeding 21 Ω at 20 K, which gradually decreases to 16 Ω at 300 K, indicating that the turn on voltage of the device decreases with increasing the temperature as illustrated in [Figure 7.11\(d\)](#). This behaviour is attributed to the DBR layers placed in the current path, where the band structure, which is presented in [Figure 7.11\(e\)](#), clearly shows the high band offset energy between the conduction band of the cavity layers and the top DBR layers, corresponding to about 1.98 eV.

7.2.4 Mesa area effect

Room temperature electroluminescence spectra of RCLEDs with 800 μm , 400 μm , 200 μm mesa diameter were investigated and analyzed as demonstrated in [Figure 7.12\(a\)](#). All three devices were fabricated in the same manner from the same epiwafer. To evaluate the effect of the mesa area on the electroluminescence, the devices were driven with the same square-wave modulation, using 100 mA injection current (having a peak value of 1 volt) with 30% duty cycle at 1 kHz. From [Figure 7.12\(b\)](#), it is clearly observed that the 200 μm device had the lowest emission intensity which is less than that of the 800 μm device by $\sim 3x$, whereas the emission intensity of the 400 μm device exhibited a decrease in emission intensity of only 20% compared to that of the 800 μm device. On the other hand, the 800 μm and 400 μm devices exhibit approximately the same output power, while the output power of the 200 μm device is estimated to be less than that of the other two devices by $\sim 50\%$. The difference in the output power results of the three devices is less than the difference in the emission intensity. This is attributed to

increase in the linewidth of the emission spectra as mesa area decreases. The electroluminescence peaks of the 800 μm , 400 μm and 200 μm RCLEDs were identified at 4.462 μm , 4.466 μm and 4.478 μm , respectively, indicating that the emission spectra exhibit a redshift when the mesa area decreases as shown in Figure 7.12(c). Based on the redshift in the electroluminescence peak, there exists a significant Joule heating in the 200 μm RCLED, where the temperature increased by ~ 45 degrees compared to that of the 800 μm RCLED.

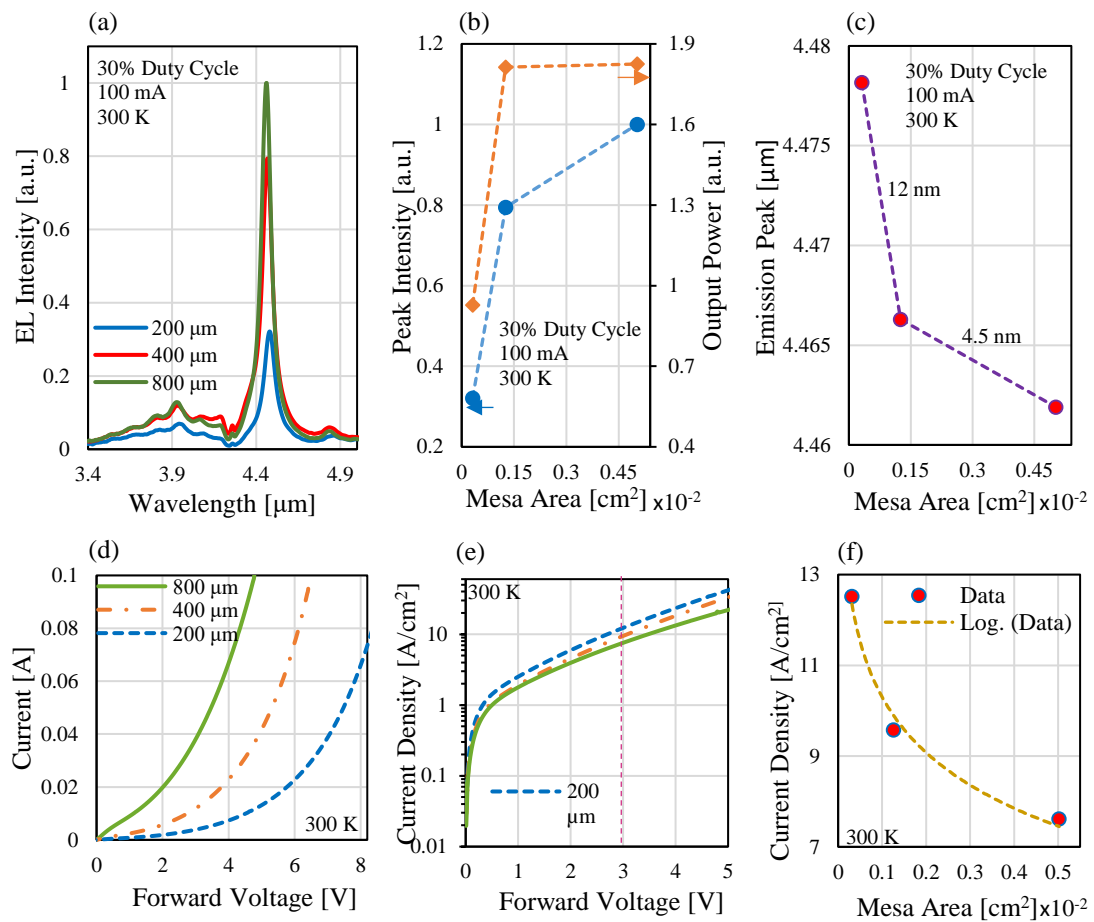


Figure 7.12: (a) Room temperature EL emission spectra of the RCLED as a function of the wavelength at different mesa size using 100 mA injection current. (b) The emission intensity of the RCLED as a function of mesa area. (c) The intensity peak position of the emission spectra of the RCLED as a function of mesa area. (d) Measured forward I-V characteristics of the RCLED at three different mesa size. (e) Measured forward J-V curves for devices with different mesa width. The current was normalized to the mesa area. (f) The current density values at $V_{\text{bias}} = 3$ V are extracted and plotted against the mesa area. A log dependence over the mesa area is shown for comparison.

On the other hand, the I-V characteristics of the devices with different mesa sizes are shown in Figure 7.12(d), where it is evident that as the mesa size decreases, the turn on voltage of the

RCLED increases. Typically, it is known that when the area of mesa contact decreases, using the same applied current (i.e. increase the current density), the current density increases with decreasing mesa area (seen [Figure 7.12\(e\)](#)), leading to increase the resistance of the devices. The current density values at $V_{\text{bias}} = 3 \text{ V}$ of the devices were extracted from the measured current density for the devices are shown in [Figure 7.12\(e\)](#) and plotted in [Figure 7.12\(f\)](#). The extracted values of current density exhibit a logarithmic dependence on the mesa diameter, where the current density in the $200 \mu\text{m}$ RCLED was ~ 1.7 times higher than in the $800 \mu\text{m}$ RCLED. This non-linear behavior could be attributed to the non-uniform current distribution within the mesa area, as area increases the current could be concentrated out of the center. Furthermore, increase the current density as mesa area decreases explains why the resistance of the devices decreases when the area increases and then decrease the Joule heating in the device.

7.3 AllnAs/InAsSb MQWs RCLED without top DBR mirror

In order to investigate the optical and electrical properties of the MQWs RCLED without top DBR mirror, wet chemical etching was used to remove the top DBR mirror from the same epiwafer of the full RCLED structure.

7.3.1 Device fabrication

After removal of the top DBR mirror, the device was photo-lithographically patterned and wet chemically etched for subsequent Ohmic metal contact deposition by thermal evaporation. The first lithography was carried out to deposit Ti/Au top contact for p-side on the top of the p-InAsSb layer using thermal evaporation and lift-off. After that, the p-InAsSb layer, AllnAs/InAsSb MQWs active region and a part of n-InAsSb layer were chemically etched. Citric acid: H_2O_2 (2: 1) and sulfonic acid: H_2O_2 : H_2O (1:8:80) were used for etching the InAsSb layers and MQWs active region, respectively. Finally, a Ti/Au bottom contact for the n-side was deposited on the n-InAsSb layer. The schematic diagram of the RCLED structure without top DBR mirror is presented in [Figure 7.13](#).

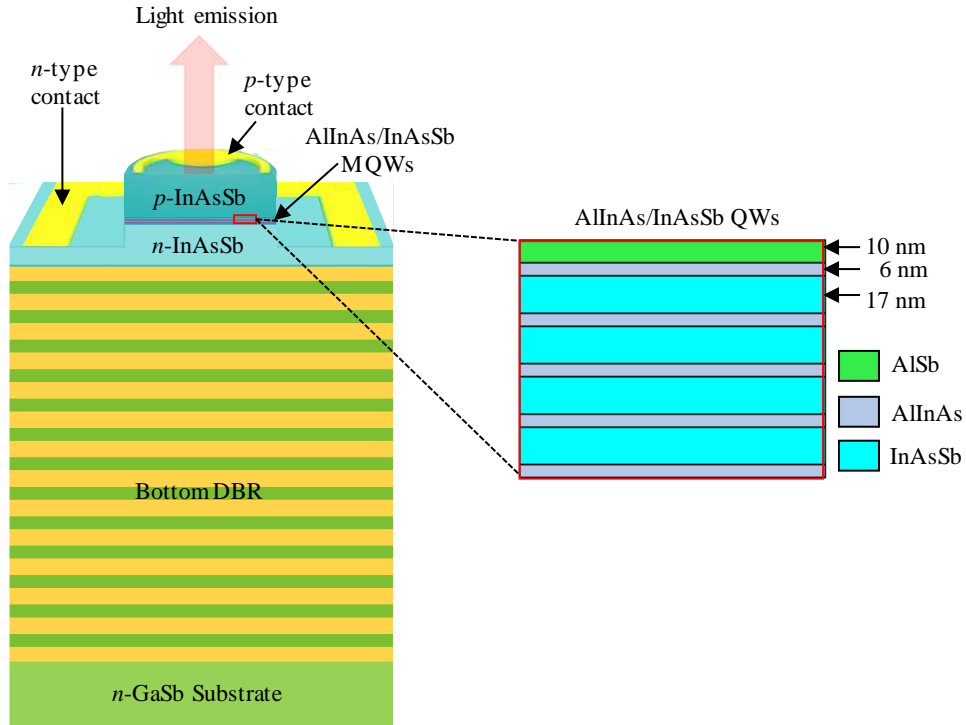


Figure 7.13: Schematic diagram of the RCLED device structure without top DBR mirror.

7.3.2 Electroluminescence measurements

Temperature-dependent electroluminescence spectra of the RCLED without top DBR mirror were measured using 100 mA injection current at 30% duty cycle and 1 kHz. The results are plotted in Figure 6.14(a) over the temperature range from 20 K to 300 K. As seen in this figure, the resonant optical mode is still observed in the emission spectra, indicating that the resonant cavity effect is still achieved. This is attributed to that, as we mentioned in chapter 6, the interface between the surface of the top InAsSb layer of the device and air acts as a top reflector, resulting in a micro-cavity structure sandwiched between the top mirror with reflectivity ($R_1 \approx 33\%$) and bottom DBR mirror with reflectivity ($R_2 > 98\%$). The room temperature electroluminescence spectra of the RCLED with top DBR mirror, the RCLED without top mirror, and the reference LED are shown in Figure 7.14(b). At the resonant wavelength, the ratio between the electroluminescence peak of the RCLED without top DBR mirror and the reference LED gives an enhancement in the emission intensity of a factor of 24, which is $\sim 3.5x$

less compared to that of the full RCLED structure. Whilst, the integrated emission of the RCLED without top DBR was enhanced by 8 times, - less than ~40% compared to that of the full RCLED structure.

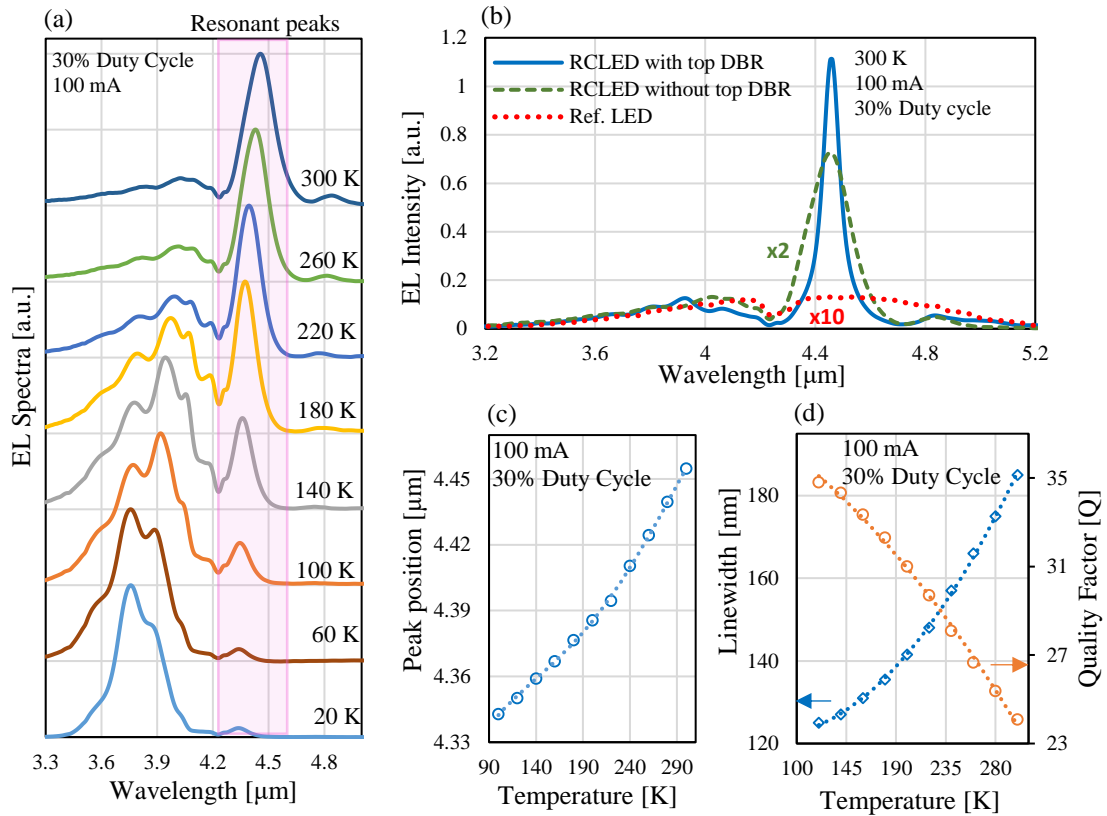


Figure 7.14: (a) Temperature dependence of the EL spectra for the RCLED without top DBR. (b) Room temperature electroluminescence emission of the RCLEDs with and without the top DBR mirror, and the reference LED. (c) Peak position of the EL emission spectra of the RCLED without top DBR versus temperature. (d) The linewidth and the quality factor of the EL spectra of the RCLED without top DBR as a function of temperature.

Based on the results of the temperature dependence of the electroluminescence emission, the wavelength of the resonant peak were evaluated and plotted as a function of the temperature in Figure 7.14(c). As can be seen in this figure, the resonant peak of electroluminescence spectra are red shifted towards longer wavelength, where the emission peak shifts by 112 nm, from 4.343 μm at 100 K to 4.455 μm at 300 K. Over the temperature range between 100 K to 220 K, the emission peak shifts at a rate of ~ 0.42 nm/K. As the temperature increases from 220 to 300 K, we note that the emission peak shifts at a rate of ~ 0.76 nm/K (2x greater than that of the full

RCLED). In comparison with reference LED emission, the RCLED without top DBR mirror exhibits better temperature stability by a factor of 6. Figure 7.14(d) shows the linewidth and the quality factor (Q) of the electroluminescence emission as a function of temperature. At low temperature (T=100 K), the emission linewidth was determined to be approximately 124 nm, increasing gradually to be ~185 nm at 300 K. At room temperature, the emission linewidth is ~2.7 times larger compared to that of the full RCLED structure, due to the smaller 33% reflectivity of the top InAsSb/air interface. However, the linewidth of the RCLED without top DBR mirror is still narrower than that of the reference LED - by a factor of ~6 at 300 K. Based on the experimental results of the emission peak and the linewidth, the quality factor was determined and calculated to be ~35 at 100 K and ~24 at 300 K. In this work, we did not consider the results below 100 K due to the lower accuracy in the measurement, where the emission was affected by the CO₂ absorption.

7.3.3 Current and duty cycle effect on the electroluminescence

The room temperature electroluminescence spectra of the RCLED without top DBR at various injection current using 30% duty cycle was presented in Figure 7.15(a). As injection current increases, the emission spectra are red-shifted from 4.449 μm at 25 mA to 4.455 μm at 100mA. This is attributed to an increase in the temperature of the device, which is calculated to be ~8 degrees. It was also found that the emission linewidth (FWHM) increases from 181 nm to 185 nm as injection current increases from 25 mA to 100 mA. The emission peak intensity and the integrated power of the RCLED without top DBR mirror and the full RCLED structure are plotted as a function of the injection current in Figure 7.15(b) and 7.15(c), respectively. Over the range from 25 mA to 100 mA, it was observed that the peak intensity and the integrated power of the RCLED without top DBR mirror increases by a factor of 2. At low injection current (25 mA), the output power was measured to be 2.5 μW less than that of the full RCLED by 17%. The ratio increases to 40% when the current increases to 100 mA, where the output power of the RCLED without top DBR mirror was measured to be 5.0 μW . As expected, the

full RCLED structure shows better performance at high injection currents (>50 mA) compared to the RCLED without top DBR.

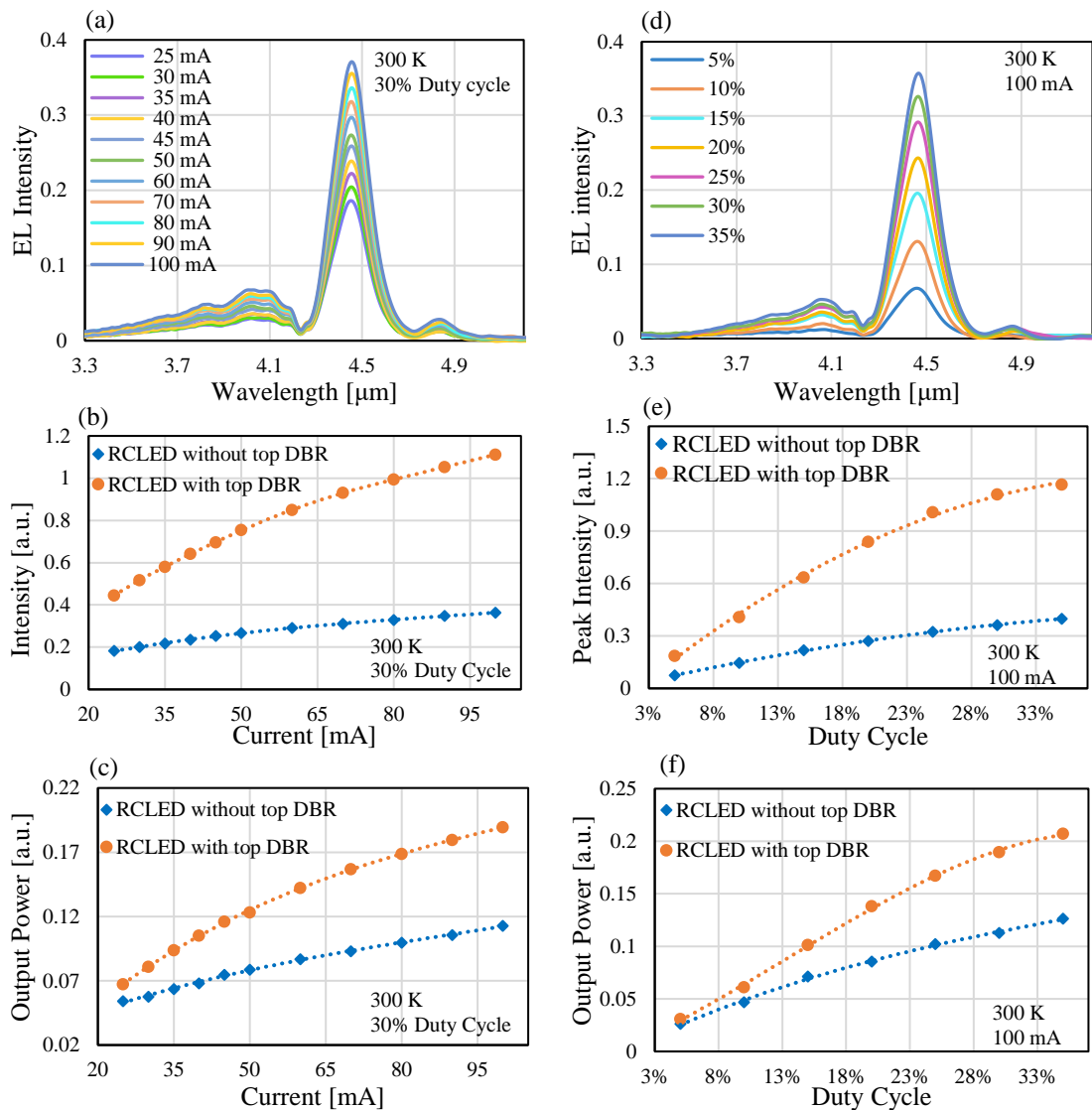


Figure 7.15: (a) and (d) Room temperature EL emission spectra of the RCLED without top DBR as a function of the wavelength at different injection current and at different duty cycle, respectively. (b) and (e) The emission intensity peak of the RCLED with and without top DBR as a function of the current and duty cycle, respectively. (c) and (f) The integrated emission of the RCLED with and without top DBR as a function of the current and duty cycle, respectively.

Figure 7.15(d) presents the room temperature electroluminescence emission of the RCLED at different duty cycle using 100 mA drive current. As seen in Figures 7.15(e) and 7.15(f), the emission peak intensity and the integrated power increase by a factor of 5 as the duty cycle increases from the 5% to 35%. We estimated the average output power to be $1.1 \mu\text{W}$ at 5% duty

cycle, increasing to $5.5 \mu\text{W}$ at 35% duty cycle. However, in comparison to the RCLED without top DBR, the full RCLED structure still exhibits higher power output and peak emission intensity becoming being better when the duty cycle increases.

7.3.4 Area mesa effect on the optical and electrical characteristics

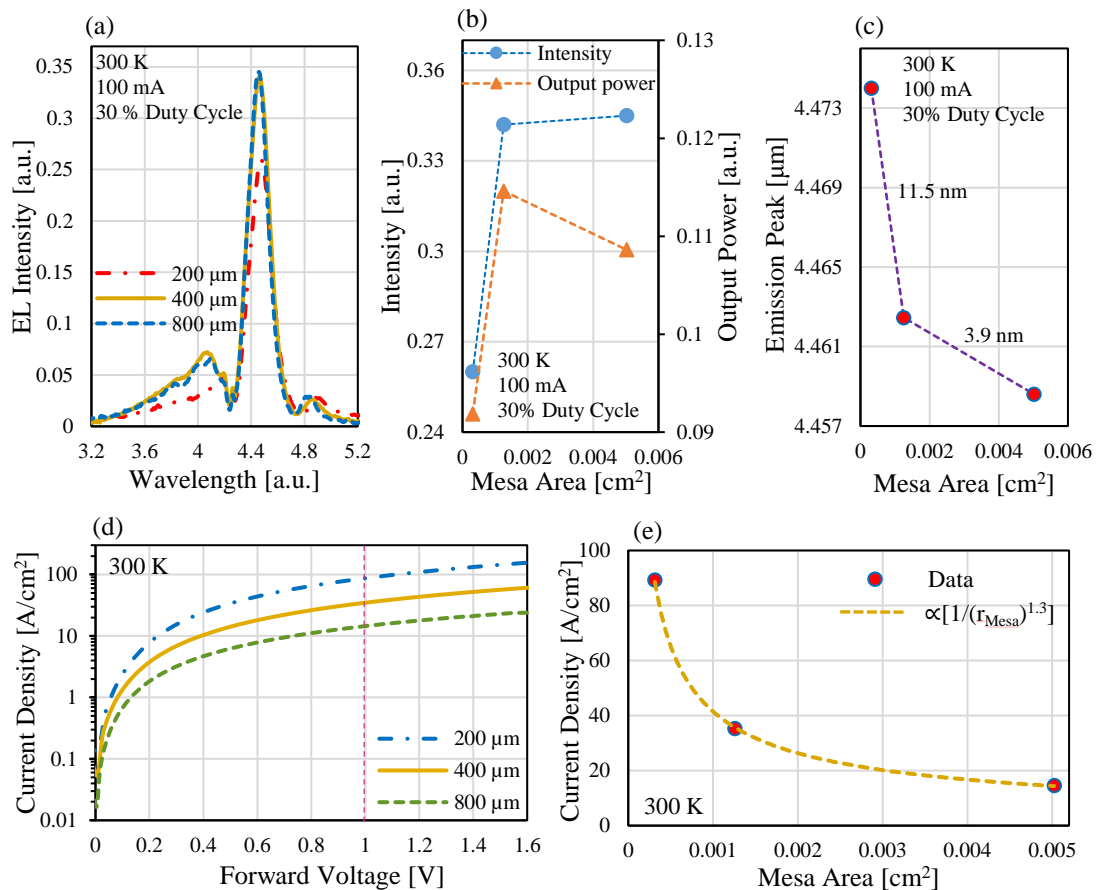


Figure 7.16: (a) Room temperature EL emission spectra of the RCLED without top DBR as a function of the wavelength at different mesa size using 100 mA injection current. (b) The emission peak intensity and the integrated emission of the EL spectra as a function of the mesa area. (c) The peak intensity position of the emission spectra as a function of mesa area. (d) Measured forward J-V curves for devices with different mesa width. (e) The current density values at $V_{\text{bias}} = 1 \text{ V}$ are extracted and plotted against the mesa area. A $1/r^{1.3}$ dependence over the mesa area is shown for comparison.

Room temperature electroluminescence and I-V characteristics of three devices with 800 μm, 400 μm, 200 μm mesa diameter were investigated and analysed as demonstrated in Figure 7.16. All the three devices were fabricated in the same manner, without top mirror and from the same

epiwafer. Figure 7.16(b) shows the peak intensity and the integrated power of the emission spectra plotted in Figure 7.16(a). It is obviously noticed that the 400 μm and 800 μm devices have approximately the same peak emission intensity, whereas the integrated power of the 400 μm device increases by 5%. It was also found that the 200 μm device exhibited a decrease in emission intensity of 25% compared to that of the 800 μm , whereas the integrated power decreases by only 15%. This is attributed to the increase the linewidth of the emission spectra as mesa area decreases, where it is measured to be 185 nm, 193 nm and 206 nm corresponds to 800 μm , 400 μm and 200 μm mesa diameter, respectively. In addition, the electroluminescence peaks of the 800 μm , 400 μm and 200 μm RCLEDs were identified at 4.4586 μm , 4.4625 μm and 4.4740 μm , respectively, indicating that the emission spectra exhibit a redshift when the mesa area decreases as shown in Figure 7.16(c). The increase in the linewidth emission and the red shift in the peak spectra are attributed to increase the temperature of the devices as the mesa diameter decreases, particularly, in the 200 μm RCLED, where the temperature increased by approximately 22.5 degrees compared to that of the 800 μm RCLED. This means that the increase in the temperature of the RCLED without top DBR is less than that of the RCLED with top DBR by 2x.

On the other hand, the J-V characteristics of the devices with different mesa area are shown in Figure 6.16(d). As seen in this figure, the current density increases when the mesa diameter decreases as a result of increase the resistance of the device. The current density values at $V_{\text{bias}} = 1 \text{ V}$ of the devices were extracted from the measured current density for the devices plotted in Figure 6.16(e). The extracted values exhibit that the current density in the 800 μm RCLED was ~6 times less than in the 200 μm RCLED and ~2 times less than in the 400 μm RCLED, showing a $1/r^{1.3}$ dependence on the mesa diameter. This behaviour is attributed to the non-uniform current distribution within the mesa area as mentioned in section 7.2.4. Additionally, this explains why the resistance of the devices increases when the mesa area decreases and then increase the Joule heating in the device. However, the effect of the mesa area on the performance of the RCLEDs without top DBR mirror is less than that of the full

RCLED structure, where better optical and electrical characteristics and less Joule heating effect were observed.

7.4 Discussion

Resonant cavity enhancements are due to constructive interference of light in the cavity, which increases the amount of light emitted towards the surface within the escape angle from the high-index semiconductor material into air. The cavity enhances the propagation of optical modes, which match the optical length of the cavity, whereas the other modes are suppressed [9] (i.e. the optical mode density is strongly enhanced for on-resonance wavelengths). We also note that the associated decrease in spontaneous lifetime makes non-radiative Shockley-Read processes less important. The main difference compared to a VCSEL is the criterion that $(1-R_{\text{out}}) \gg \alpha d_{\text{active}}$, where d_{active} is the thickness and α is the absorption coefficient of the active region and R_{out} is the reflectivity of the out-coupling mirror (see chapter 2, section 2.3). This ensures that more light escapes the cavity than gets re-absorbed in the active region because the device emits only spontaneous emission. By carefully combining InAsSb strained MQW with high contrast AlAsSb/GaSb DBR mirrors our design enables an RCLED with high spectral brightness within a narrow linewidth which is well suited to selective gas detection and optical spectroscopy. Where, as we mentioned before, the emission peak and the integrated emission of the MQWs RCLED were significantly enhanced, therefore the external efficiency of the RCLED was also improved compared to that of the reference LED as presented in Figure 7.17.

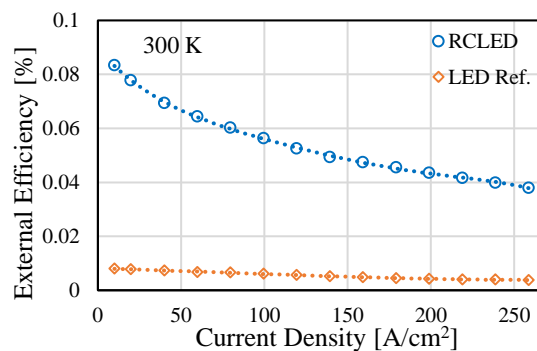


Figure 7.17: Room temperature external efficiency of the MQWs RCLED and reference LED as a function of current density.

The emission wavelength is determined by the Sb content in the MQW (see Figure 7.19) but also by the construction of the resonant cavity. The emission enhancement, linewidth and Q-factor are strongly dependent on the DBR mirror reflectivity. The high refractive index contrast ($\Delta n = 0.6$) between AlAsSb and GaSb means that relatively few pairs of layers are needed to achieve sufficiently high reflectivity.

Figure 7.18 shows the accessible spectral range for our RCLED extends from 3.9 μm to 4.9 μm – maintaining 70% of the peak emission intensity. We estimated the effect on the emission intensity keeping the same MQWs in the active region and changing the thickness of the cavity (red line) and the DBR layers (green line). The results show that if the thickness of the DBR layers and the cavity are both reduced by 4.5%, then the emission peak readily tunes down in wavelength to 4.25 μm , which is well matched to CO₂ detection. Meanwhile, the emission intensity is decreased by only 3% from that of our MQW RCLED at 4.5 μm . Similarly, for CO detection at 4.6 μm , the thickness of the DBR layers and the cavity simply needs to be increased by 3%, where the emission intensity is again reduced only slightly by 3%. This is possible because of the relatively broadband emission of the AlInAs/InAsSb MQWs in the active region. Consequently, our RCLED design is readily able to address three important greenhouse gases.

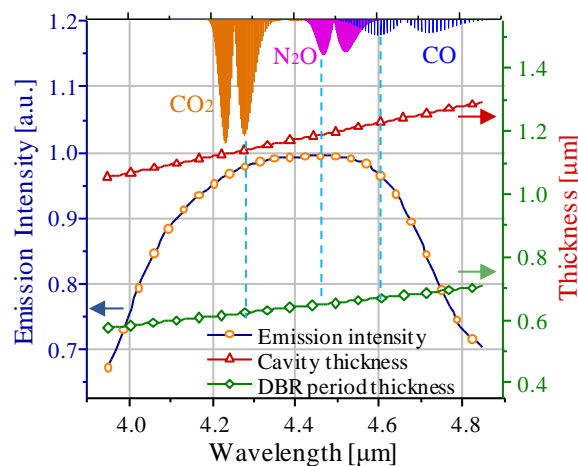


Figure 7.18: The calculated variation in RCLED wavelength and emission intensity dependence on cavity thickness or DBR period thickness. Also shown are the absorption spectra of key greenhouse gases to illustrate the accessible tuning range, which encompasses CO₂, N₂O and CO.

The emission wavelength of the RCLED can be tuned further out to longer wavelengths by adjusting the Sb content in the MQW as shown in Figure 7.19, although this requires a

corresponding redesign of the DBRs and cavity. However, due to lattice mismatch and strain considerations, with 15% Sb the QW are type I with a conduction band offset of 30 meV. This means that the emission wavelength cannot be significantly increased without the structure becoming type II, resulting in a likely reduction in output power.

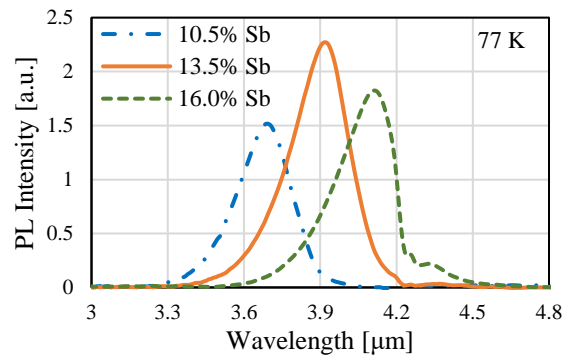


Figure 7.19: Photoluminescence spectra of the AlInAs/InAsSb MQWs at various Sb composition.

On the other hand reducing the Sb content would provide larger conduction band offset with deeper confinement and enable RCLED emission down to $\sim 4.0 \mu\text{m}$. However, compressive strain limitations on the critical thickness prevents the realization of RCLEDs at shorter wavelengths. Increasing the number of periods in the upper/lower DBR would have the effect of increasing the cavity finesse and Q-factor which would result in a narrower spectral linewidth and higher optical output at the resonance wavelength but could be lower overall output power. However, output power could be increased by using a number of RCLED chips in a small array - as implemented by GSS Ltd. in their COZIR sensor [28] which employs 9 LED elements. The resonant cavity concept can also be applied to enhance detector performance and recently, we demonstrated a resonant cavity detector operating at around $4.41 \mu\text{m}$ with peak responsivity of 3.0 AW^{-1} , corresponding to quantum efficiency of 84%. [141] Clearly, it is also possible to implement a resonant cavity LED - resonant detector pair to obtain even higher sensitivity although care is needed to maintain effective matching of the resonance peaks.

The optical properties of the full structure RCLED and the RCLED without top DBR mirror were listed in Table 7.1, compared to that of the reference LED. In addition, the area mesa effect on the optical properties of the both devices was summarized in Table 7.2.

Table 7.1: Room temperature optical properties of the RCLED full structure compared to that of the RCLED without top DBR (800 μm mesa diameter).

| Sample | Resonance peak emission | | | | Enhancement factor | |
|----------------------------|-------------------------|--------------|--------------------|--|--------------------|---------------------|
| | Position μm | Linewidth nm | Quality factor [Q] | $d\lambda_{\text{cav}}/dT$ nm/K | Intensity peak | Integrated emission |
| MQWs RCLED full structure | 4.462 | 69.5 | 64 | 0.36 | 85x | 13x |
| MQWs RCLED without top DBR | 4.455 | 185 | 24 | 0.42 ($T < 220\text{K}$) 0.76 ($T > 220\text{K}$) | 24x | 8x |

Table 7.2: Room temperature optical properties of the RCLED full structure compared to that of the RCLED without top DBR for different area mesa.

| Mesa diameter | Device | Peak position (μm) | Linewidth (nm) | Quality factor [Q] | Normalized Intensity | Output power μW |
|-------------------|-----------------------|---------------------------------|----------------|--------------------|----------------------|----------------------------|
| 800 μm | RCLED full structure | 4.462 | 69.5 | 64 | x1 | 8.5 (quasi-CW condition) |
| 400 μm | | 4.466 | 72 | 62 | Less by 20% | 8.5 (quasi-CW condition) |
| 200 μm | | 4.478 | 77.5 | 58 | Less by 3x | 4.3 (quasi-CW condition) |
| 800 μm | RCLED without top DBR | 4.458 | 185 | 24 | x1 | 5 (quasi-CW condition) |
| 400 μm | | 4.4625 | 193 | 23 | x1 | 5.2 (quasi-CW condition) |
| 200 μm | | 4.474 | 206 | 22 | Less by 25% | 4 (quasi-CW condition) |

Chapter 8

Conclusion and Future Work

8.1 Conclusion

Mid-infrared Resonant cavity (RC) structures. Simulated results of the resonant cavity (RC), including quality cavity factor (Q), the linewidth of the cavity mode ($\Delta\lambda_{\text{cav}}$), resonance emission (intensity) enhancement factor (G_e), and the integrated emission enhancement factor (G_{int}) were evaluated as a function of the reflectivity of the top and bottom mirrors. The distribution of the electric field inside the cavity was also investigated to identify the antinodes. All the results were obtained using the cavity thickness of a single wavelength (1λ -thick). It was found that the high quality factor and high enhancement factors were achieved using high reflectivity of mirrors under the condition $R_{\text{bottom}} \gg R_{\text{top}}$. The reflectivity of the DBR mirrors was modelled using a transfer matrix method and the results show that 13.5 pairs of bottom DBR mirror and 5 pairs of top DBR mirror are enough to achieve high enhancement factors. Therefore and in order to design successful resonant cavity structures, four samples with a 1λ -thick cavity sandwiched between two DBR mirrors (13.5 pairs bottom DBR and 5 pairs top DBR) were grown using MBE. Three of these samples grown on *n*-GaSb substrate and one grown on *n*-InAs substrate. The samples included the following structures: GaSb-based bulk InAsSb RC (S1), GaSb-based $\text{Al}_{0.12}\text{In}_{0.88}\text{As}/\text{InAs}_{0.855}\text{Sb}_{0.145}$ MQWs RC (S2), GaSb-based $\text{Al}_{0.12}\text{In}_{0.88}\text{As}/\text{InAs}_{0.87}\text{Sb}_{0.13}$ MQWs RC (S3), and InAs-based InAs/GaAsSb SLSs RC (S4).

The temperature dependence of transmission spectra of the all samples was experimentally measured over the temperature range from 77 K to 300 K. Based on that, the position of the cavity mode and the DBR stopband centre were determined. Corresponding to the thickness of the cavity, the cavity mode of the samples S1, S2, S3, and S4 exhibit room temperature wavelengths peaked at $\sim 4.3 \mu\text{m}$, $\sim 4.5 \mu\text{m}$, $4.0 \mu\text{m}$, and $4.6 \mu\text{m}$, respectively. It was also found that the optical cavity mode for all samples has a significant temperature stability ($< 0.4 \text{ nm/K}$),

narrow linewidth (<100 nm) and a high quality factor, confirming that high enhancement factors were achieved in practice. Based on the temperature coefficient of the refractive index and the lattice constants of the cavity material, the theoretical results of the wavelength shift of the optical mode were investigated, showing a good agreement with experimental results. Although all the samples exhibit detuning (the difference between the wavelength of the optical cavity mode and the DBR stopband center), our simulated results indicate that high enhancement factors for all samples are still maintained. The narrow linewidth and superior temperature stability, are attractive features, enabling these structures to be implemented in next generation optical gas sensor instrumentation for gases such as SO₂ (4.0 μm), CO₂ (4.25 μm), N₂O (4.5 μm), and CO (4.6 μm).

GaSb-based bulk InAsSb RCLED. We investigated the optical and electrical properties of the mid-infrared resonant cavity LEDs (RCLEDs) operating near 4.3 μm at room temperature. Two samples were grown on a GaSb substrate by molecular beam epitaxy under the same growth conditions, one with high detuning between the resonance optical cavity (~160 nm) and another with lower detuning (~110 nm). The RCLED structures are based on a design using high contrast DBR mirrors, a 13.5 lattice-matched AlAs_{0.08}Sb_{0.92}/GaSb ($\lambda/4$) pairs for the bottom DBR and 5 pairs for the top DBR, with a 1λ -thick microcavity which consists of a bulk InAsSb as the active region. Temperature dependence of the electroluminescence spectra of the RCLEDs shows that when the detuning increases, significant side peaks become enhanced at the two sides of the DBR stopband. It was also found that the side peaks positioned at the left side of the DBR stopband (short wavelength side) shift towards longer wavelength as temperature increases by a rate of 0.194 nm/K, less than that of the side peaks positioned at the right side of the DBR stopband (long wavelength side) which are shifted at a rate of 0.374 nm/K.

Two different fabrication methods were used to design these low detuning RCLEDs. For the RCLED-M1 structure, where the top *p*-type contact was deposited on the surface of the top DBR mirror, the following features of the emission spectra were observed:

- The main resonance emission peak (resonance optical cavity mode) of the RCLED has a significant temperature stability, showing a red-shift with a rate of ~ 0.36 nm/K which is less than that of the reference LED by a factor of 6x.
- The spectral linewidth of the main emission peak was calculated to be ~ 88 nm at 300 K which is narrower than that of the reference LED by a factor of ~ 10 x.
- At room temperature, the emission intensity and the total integrated emission of the electroluminescence spectrum of the RCLED were enhanced by a factor of ~ 70 x and 33x, respectively.

The RCLED-M2 emission at room temperature shows broader linewidth and smaller enhancement factors compared to that of the RCLED-M1 emission, but still has narrower linewidth, higher intensity, and higher integrated emission compared to that of the reference LED, where:

- The main emission peak of the RCLED has a spectral linewidth of ~ 200 nm at 300 K, narrower than that of the reference LED by a factor of 4.5x.
- The emission intensity and the total integrated emission of the RCLED were enhanced by a factor of 49x and 21x, respectively.

These results indicate that the emission spectra of the full structure RCLED-M2 seems to be similar to that of the RCLED without top DBR mirrors, suggesting that the EL spectrum of the RCLED-M2 originates from the surface of the cavity.

Temperature dependence of the current-voltage (I-V) characteristics of the RCLEDs show that the series resistance and the turn on voltage of the RCLED-M2 are less than that of the RCLED-M1.

GaSb-based AlInAs/InAsSb MQWs RCLED. We have also demonstrated the temperature dependence of the electroluminescence spectra of the AlInAs/InAsSb MQW LED, designed for mid-infrared applications near 4.5 μm at room temperature, grown lattice-matched on a GaSb substrate by molecular beam epitaxy using high contrast DBR mirrors. The RCLED structure is based on a design using 13.5 lattice-matched AlAs_{0.08}Sb_{0.92}/GaSb ($\lambda/4$) pairs for the bottom DBR and 5 pairs for the top DBR, with a 1λ -thick microcavity which consists of an AlInAs/InAsSb QWs as the active region. The EL emission spectra of the RCLED were measured over the temperature range from 20 to 300 K and compared with a reference LED without DBR mirrors. The EL spectra of the RCLED show higher intensity, higher output power (8.5 μW under quasi-CW condition, 120 μW under pulsed condition), better directionality, better spectral purity and superior temperature stability compared to the reference LED. These features are listed in detail below:

- Because the emission wavelength of the optical cavity mode is determined by the temperature coefficient of the refractive index of the cavity materials, the emission peak of the RCLED shifts toward longer wavelengths as temperature increases at a rate of only 0.362 nm/K, which is less than that of the reference LED by a factor of 7.
- The EL spectra of the RCLED have a linewidth narrower than that of the LED, where the linewidth of the RCLED emission spectrum was measured to be 42 nm at 20 K and 69.5 nm at 300 K, which is 7 and 16 times lower than that of the LED, respectively, because the linewidth depends on the Q-factor of the cavity.
- Due to the resonant cavity effects, the room temperature emission intensity and the integrated emission (output optical power) was found to be enhanced by a factor of ~ 85 and ~ 13 , respectively.

The effect of the injection current and the duty cycle on the EL spectra of the RCLED were investigated. It was observed that the emission peak was red-shifted and the emission spectrum became broader when the injection current increases. Similar behavior was observed with increasing duty cycle. This is attributed to increased temperature of the device due to Joule

heating effects. In addition, room temperature emission spectra of the RCLED with different mesa area exhibited higher intensity, higher output power, narrower linewidth and blue-shifted when the mesa area increases. This is attributed to the fact that the resistance of the device increases with decreasing mesa area, leading to an increase of the temperature in the device.

As temperature increases, the series resistance and the turn on voltage of the RCLED are decreased.

The results of the electroluminescence spectra of the AlInAs/InAsSb MQWs RCLED *without top DBR mirror* show that the resonant cavity effects on the emission are still achieved, where the following features were observed:

- The emission intensity and the integrated emission were enhanced by a factor of 24 and 8 respectively, compared to that of the reference LED.
- At high temperature ($T > 200$ K), the device exhibited narrower linewidth (x6) and better temperature stability by a factor of 6.
- At room temperature and as injection current increases, the peak intensity and the output power of the emission spectra increases by a factor of 2, less than that observed in the emission of the full RCLED structure (which increased by ~2.5x and ~2.8x, respectively). It was also found that the peak intensity and the output power increase with increasing the duty cycle by a factor of 5, less than that of the full RCLED structure which are estimated to be 6x and 7x, respectively.
- The effect of the mesa area on the optical and electrical characteristics of the RCLED without top DBR is less than that of the full RCLED structure, where less Joule heating was observed.

Room temperature electroluminescence spectra of our RCLEDs are shown in [Figure 8.1](#). Four nice emission spectra peaked at approximately 4.0 μm , 4.3 μm , 4.5 μm , and 4.6 μm each with narrow linewidths were obtained, showing the spectral range covered in this work.

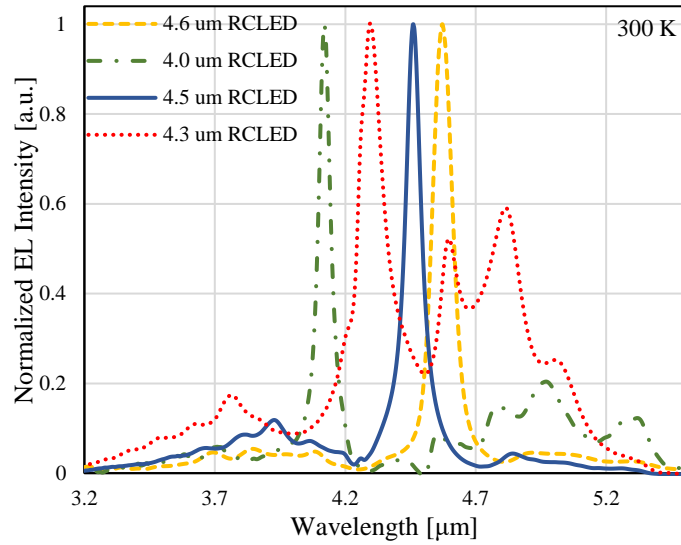


Figure 8.1: Room temperature electroluminescence spectra of the four RCLEDs grown and fabricated in the physics department at Lancaster University. The emission spectra were measured under quasi-CW conditions using 100 mA injection current and 30% Duty Cycle.

Owing to the increased brightness, narrower linewidth and improved temperature dependence our results indicate that these RCLED designs form an excellent basis for the further development of sources to be used in gas sensor instruments (CO_2 and N_2O gases) as well in spectroscopy and other applications.

8.2 Suggested future work

The RCLED structures developed and studied in this thesis exhibit significantly improved optical properties compared to non-resonant LEDs, but with higher series resistance and higher turn on voltage. Although we studied the features of these structures in details, there is still much to follow up. Therefore, the following suggested work could be investigated in the future:

- Design a mid-infrared RCLED grown on Si substrate for the low-cost next generation of mid-infrared applications. It can be designed to emit the light through the substrate by using a high-reflectivity gold mirror as a top mirror and a low-reflectivity AlAsSb/GaSb DBR as a bottom mirror.

- Interband cascade RCLEDs structures could be designed and developed to improve the optical output power and the efficiency. This is could be achieved by increasing the cavity order to increase the number of the electrical field antinodes inside the micro-cavity, enabling multi-stage active regions to be grown inside the cavity.
- Further investigation to improve the electrical properties of the RCLEDs by using other materials or fabrication methods to reduce the reverse current, the series resistance and the turn on voltage. The studies should include improvements to the electrical properties of the DBR mirror.
- Study the effect of the cavity order on the optical properties of the RCLEDs. Where the simulated results suggest that the enhancement factors and the emission linewidth could be effected when the cavity order increases. In our study we use cavity order equal 2 which corresponds to 1λ -thick cavity with one electrical field antinode.
- Develop our SLs and MQWs resonance cavity (RC) designs to investigate mid-infrared ($\lambda > 4 \mu\text{m}$) VCSELs using high reflectivity ($R \approx 99.9\%$) AlAsSb/Ga(As)Sb DBR as a bottom mirror and a dielectric DBR with reflectivity ($R > 99.0\%$) as a top mirror. Interband cascade mid-infrared VCSELs could be also designed based on InAs substrate using GaAsSb/InAs SLs as active region.
- Investigate strain balanced AlInAs/InAsSb MQWs, obtained by increasing the composition of Sb, which could be used to design RCLEDs and VCSELs for mid-infrared applications ($\lambda > 5 \mu\text{m}$).

References

- [1] C. N. Banwell. *Fundamentals of Molecular Spectroscopy*. McGrawHill, 1983.
- [2] B. A. Matveev, G. A. Gavrilov, V. V. Evstropov, N. V. Zotova, S. A. Karandashov, G. Y. Sotnikova, N. M. Stus', G. N. Talalakin and J. Malinen, "Mid-infrared (3-5 μ m) LEDs as sources for gas and liquid sensors," *Sensors and Actuators*, vol. 39, no. 1, pp. 339-343, 1997.
- [3] B. A. Matveev, N. Zotova, S. Karandashov, M. Remennyi, N. Il'inskaya, N. Stus', V. Shustov, G. Talalakin and J. Malinen, "InAsSbP/InAs LEDs for the 3.3-5.5 μ m spectral range," *IEE Proceedings – Optoelectronics*, vol. 145, no. 5, pp. 254-256, 1998
- [4] Y. Mao and A. Krier, "InAsSb p-n junction light emitting diodes grown by liquid phase epitaxy," *Journal of Physics and Chemistry of Solids*, vol. 56, no. 5, pp. 759-766, 1995.
- [5] Y. Mao and A. Krier, "Efficient 4.2 μ m light emitting diodes for detecting CO₂ at room temperature," *Electronics Letters*, vol. 32, no. 5, 1996.
- [6] Y. Mao and A. Krier, "Uncooled 4.2 μ m light emitting diodes based on InAs_{0.91}Sb_{0.09}/GaSb grown by LPE," *Optical Materials*, vol. 6, no. 1, pp. 55-61, 1996.
- [7] A. S. Golovin, A. P. Astakhova, S. S. Kizhaev, N. D. Il'inskaya, O. Y. Serebrennikova and Y. P. Yakovlev, "LEDs based on InAs/InAsSb heterojunctions for CO₂ spectroscopy," *Technical Physics Letters*, vol. 36, no. 1, pp. 47-49, 2010.
- [8] S. S. Kizhayev, N. V. Zotova, S. S. Molchanov and Y. P. Yakovlev, "High-power mid-infrared light emitting diodes grown by MOVPE," *IEE Proceedings - Optoelectronics*, vol. 149, no. 1, pp. 36-39, 2002.
- [9] H. H. Gao, A. Krier, V. Sherstnev and Y. Yakovlev, "InAsSb/InAsSbP light emitting diodes for the detection of CO and CO₂ at room temperature," *Journal of Physics D - Applied Physics*, vol. 32, no. 15, pp. 1768-1772, 1999.
- [10] A. A. Popov, M. V. Stepanov, V. V. Sherstnev and Y. P. Yakovlev, "InAsSb light-emitting diodes for the detection of CO₂ ($\lambda = 4.3\mu$ m)," *Technical Physics Letters*, vol. 24, no. 8, 1998.
- [11] X. Y. Gong, H. Kan, T. Makino, T. Lida, K. Watanabe, Y. Z. Gao, M. Aoyama, N. L. Rowell and T. Yamaguchi, "Room-temperature mid-infrared light-emitting diodes from liquid-phase epitaxial InAs/InAs_{0.89}Sb_{0.11}/InAs_{0.80}P_{0.12}Sb_{0.08} heterostructures," *Japanese Journal of Applied Physics*, vol. 39, no. 1, p. 9A, 2000.
- [12] P. J. P. Tang, M. J. Pullin, S. J. Chung, C. C. Phillips, R. A. Stradling, A. G. Norman, Y. B. Li and L. Hart, "4-11 μ m infrared-emission and 300 K light-emitting-diodes from arsenic-rich InAs_{1-x}Sb_x strained-layer superlattices," *Semiconductor Science and Technology*, vol. 10, no. 8, pp. 1177-1180, 1995.
- [13] H. Hardaway, J. Heber, P. Moeck, M. J. Pullin, T. Stradling, P. Tang and C. C. Phillips, "Optical studies of InAs/In(As,Sb) single quantum well (SQW) and strained-layer superlattice (SLS) LEDs for the mid-infrared (MIR) region," *SPIE Proceedings - Light emitting diodes: research, manufacturing and applications III*, vol. 3621, 1999.
- [14] M. J. Pullin, H. R. Hardaway, J. D. Heber, C. C. Phillips, W. T. Yuen and R. A. Stradling, "Room-temperature InAsSb strained-layer superlattice light-emitting diodes at 4.2 μ m with AlSb barriers for improved carrier confinement," *Applied Physics Letters*, vol. 74, no. 16, 1999.

- [15] V. V. Sherstnev, A. M. Monahov, A. Krier and G. Hill, "Superluminescence in InAsSb circular-ring-mode light-emitting diodes for CO gas detection," *Applied Physics Letters*, vol. 77, no. 24, pp. 3908-3910, 2000.
- [16] A. Krier, H. H. Gao, V. V. Sherstnev and Y. Yakovlev, "High power 4.6 μm light emitting diodes for CO detection," *Journal of Physics D: Applied Physics*, vol. 32, pp. 3117-3121, 1999.
- [17] L. Meriggi, M. J. Steer, Y. Ding, I.G. Thayne, C. MacGregor, Ch. N. Ironside, M. Sorel, *J. of Applied Physics* vol. 117, 063101, 2015.
- [18] H. Aït-Kaci, J. Nieto, J. B. Rodriguez, P. Grech, F. Chevrier, A. Salesse, A. Joullié, P. Christol, *Physica status solidi (a)* vol. 202, 647-651, 2005.
- [19] A. Krier, M. Stone, S. E. Krier, "Characterization of $\text{InAs}_{0.91}\text{Sb}_{0.09}$ for use in mid-infrared light-emitting diodes grown by liquid phase epitaxy from Sb-rich solution," *Semicond. Sci. Technol.*, vol. 22, 2007.
- [20] A. P. Craig, M. D. Thompson, Z. B. Tian, S. Krishna, A. Krier, A. R. J. Marshall, *Semi. Sci. and Tech.* vol. 30, 105011, 2015.
- [21] M. K. Haigh, G. R. Nash, S. J. Smith, L. Buckle, M. T. Emeny and T. Ashley, "Mid-infrared $\text{Al}_x\text{In}_{1-x}\text{Sb}$ light-emitting diodes," *Applied Physics Letters*, vol. 90, 2007.
- [22] P. J. Carrington, V. A. Solov'ev, Q. Zhuang, A. Krier, and S. V. Ivanov, *Applied Physics Letters* vol. 93, 091101, 2008.
- [23] M. J. Pullin, H. R. Hardaway, J. D. Heber, C. C. Phillips, W. T. Yuen and R. A. Stradling, "Room-temperature InAsSb strained-layer superlattice light-emitting diodes at 4.2 μm with AlSb barriers for improved carrier confinement," *Applied Physics Letters*, vol. 74, no. 16, 1999.
- [24] P. J. Carrington, Q. Zhuang, M. Yin and A. Krier, "Temperature dependence of mid-infrared electroluminescence in type II InAsSb/InAs multi-quantum well light-emitting diodes," *Semiconductor Science and Technology*, vol. 24, 2009.
- [25] A. Krier, M. Stone, Q. D. Zhuang, Po-Wei Liu, G. Tsai, and H. H. Lin, "Mid-infrared electroluminescence at room temperature from InAsSb multiquantum-well light-emitting diodes," *Applied Physics Letters*, vol. 89, 2006.
- [26] J. A. Keen, E. Repiso, Q. Lu, M. Kesaria, A. R. J. Marshall, A. Krier, "Electroluminescence and photoluminescence of type-II InAs/InAsSb strained-layer superlattices in the mid-infrared," *Infrared Physics and Technology*, vol. 93, 2018.
- [27] L. Meriggi, "Antimonide-based mid-infrared light-emitting diodes for low-power optical gas sensors," University of Glasgow, 2015.
- [28] D. Gibson and C. MacGregor, "A novel solid state non-dispersive infrared CO₂ gas sensor compatible with wireless and portable deployment," *Sensors* vol. 13, pp. 70797103, 2013.
- [29] A. R. Ravishankara, J. S. Daniel, R. W. Portmann, "Nitrous Oxide (N₂O): The Dominant Ozone-Depleting Substance Emitted in the 21st Century," *Science* vol. 326, pp.123-125, 2009.
- [30] Y. Zhao, A. S. Wexler, F. Hase, Y. Pan, F. M. A. Mitloehner, "Detecting Nitrous Oxide in Complex Mixtures Using FTIR Spectroscopy: Silage Gas," *Journal of Environmental Protection* vol. 7, pp. 1719-1729, 2016.

- [31] A. N. Hayburst, A. D. Lawrence, "Emissions of nitrous oxide from combustion sources," *Progress in ENERGY and Combustion Science* vol. 18, pp. 529-552, 1992.
- [32] J. M. Dasch, "Nitrous Oxide Emissions from Vehicles," *J. Air Waste Manage. Assoc.* vol. 42, pp. 63-67, 1992.
- [33] K. H. Becker, Lorzer, R. Kurtenbach, P. Wiesen, T. E. Jensen, T. J. Wallington, "Nitrous Oxide (N₂O) Emissions from Vehicles," *Environ. Sci. Technol.* vol. 33, pp. 4134-4139, 1999.
- [34] C. Wiesmann, K. Bergenek, N. Linder, U. T. Schwarz, "Photonic crystal LEDs – designing light extraction," *Laser & Photon. Rev.* vol. 3, pp. 262-286, 2009.
- [35] A. I. Zhmakin, "Enhancement of light extraction from light emitting diode," *Physics report* vol. 498, pp. 189-241, 2011.
- [36] Y. Zhou, Qi Lu, X. Chai, Z. Xu, A. Krier, L. He, "InAs/GaSb superlattice interband cascade light emitting diodes with high output power and high wall-plug efficiency," *Applied Physics Letters* vol. 114, 253507, 2019.
- [37] A. Krier, *Mid-infrared Semiconductor Optoelectronics*, Springer, 2007.
- [38] C. Wiesmann, K. Bergenek, N. Linder, U. T. Schwarz, *Laser & Photon. Rev.* vol. 3, 2009.
- [39] A. I. Zhmakin, *Physics report* vol. 498, 2011.
- [40] H. de Neve, J. Blondelle, P. van Daele, P. Demeester, R. Baets, G. Borghs, "Recycling of guided mode light emission in planar microcavity light emitting diodes," *Applied Physics Letters* vol. 70, 1997.
- [41] E. F. Schubert, Y.-H. Wang, A. Y. Cho, L.-W. Tu, G. J. Zydzik, "Resonant cavity light-emitting diode," *Applied Physics Letters* vol. 60, No.8, 1992.
- [42] N. E. J. Hunt, E. F. Schubert, R. A. Logan, G. J. Zydzik, *Applied Physics Letters* vol. 61, 1992.
- [43] E. Hadji, J. Bleuse, N. Magnea, J. L. Pautrat, "3.2 μm infrared resonant cavity light emitting diode," *Applied Physics Letters* vol. 67, pp. 2591-2593, 1998.
- [44] A. M. Green, D. G. Gevaux, Ch. Roberts, Ch. C. Phillips, "Resonant-cavity-enhanced photodetectors and LEDs in the mid-infrared," *Physica E: Low-dimensional Systems and Nanostructures* vol. 20, pp. 531-535, 2004.
- [45] A. Ducanhez, L. Cerutti, A. Gassenq, P. Grech, F. Genty, "Fabrication and Characterization of GaSb-Based Monolithic Resonant-Cavity Light-Emitting Diodes Emitting Around 2.3 μm and Including a Tunnel Junction," *IEEE J. of Sel. Top. in Quant. Electro.* vol. 14, pp. 1014-1021, 2008.
- [46] Ch. Grasse, P. Wiecha, T. Gruendl, S. Sprengel, R. Meyer, M-C. Amann, "InP-based 2.8–3.5 μm resonant-cavity light emitting diodes based on type-II transitions in GaInAs/GaAsSb heterostructures," *Applied Physics Letters* vol. 101, 221107, 2012.
- [47] A. Bachmann, Sh. Arafin, K. Kashani-Shirazi, "Single-mode electrically pumped GaSb-based VCSELs emitting continuous-wave at 2.4 and 2.6 μm ," *New J. of Phys.* vol. 11, 125014, 2009.

- [48] A. Andrejew, S. Sprengel, M-C. Amann, "GaSb-based vertical-cavity surface-emitting lasers with an emission wavelength at 3 μm ," *Opt. Lett.* vol. 41, pp. 2799-2802, 2016.
- [49]. L. Meriggi, M. J. Steer, Y. Ding, I. G. Thayne, C. MacGregor, Ch. N. Ironside, M. Sorel, "Development of mid-infrared light-emitting diodes for low-power optical gas sensors," *IEE 11th Conference on Ph.D. Research in Microelectronics and Electronics (PRIME)*, pp. 180-183 2015.
- [50] G. K. Veerabathran, S. Sprengel, A. Andrejew, M-C. Amann, "Room-temperature vertical-cavity surface-emitting lasers at 4 μm with GaSb-based type-II quantum wells," *Applied Physics Letters* vol. 110, 071104, 2017.
- [51] N. Dasgupta and A. Dasgupta, *Semiconductor devices: modelling and technology*. New Delhi: Prentice-Hall of India, 2004.
- [52] Y. P. Varshni, "Temperature dependence of the energy gap in semiconductors," *Physica Utrecht*, vol. 34, 1967.
- [53] S.M. Sze and K.K. Ng. *Physics of Semiconductor Devices*. John Wiley & Sons, 2006.
- [54] E. F. Schubert, *Light-emitting diodes*, Cambridge University Press, 2018.
- [55] M. P. C. M. Krijn, "Heterojunction band offsets and effective masses in III-V quaternary alloys," *Semicond. Sci. Technol.*, vol. 6, pp. 27–31, 1991.
- [56] K. M. Yu and M. Cardona, *Fundamentals of Semiconductors*. Springer, Berlin, 3rd ed., 2001.
- [57] P. M. Petroff, R. A. Logan, and A. Savage, "Nonradiative recombination at dislocations in III-V compound semiconductors," *Phys. Rev. Lett.*, vol. 44, p. 287, 1980.
- [58] J. W. Matthews and A. E. Bakeslee, "Defects in epitaxial multilayers: 1. misfit dislocations," *J. Cryst. Growth*, vol. 27, p. 118, 1974.
- [59] P. Bhattacharya, "Lattice-mismatched and pseudomorphic materials," in *Semiconductor Optoelectronic Devices*, 2nd ed, pp. 22-25, 1997.
- [60] R. People and J. C. Bean, "Calculation of critical layer thickness versus lattice mismatch for GexSi1-x/Si strained-layer heterostructures," *Appl. Phys. Lett.*, vol. 47, 1985.
- [61] S.-L. Chuang, *Physics of Photonic Devices*. Hoboken, New Jersey: Wiley, 2009.
- [62] F. Szmulowicz, E. R. Heller, K. Fisher and F. L. Madarasz, "Optimization of absorption in InAs/InxGa1-xSb superlattices for long-wavelength infrared detection," *Superlattices and Microstructures*, vol. 17, 1995.
- [63] C. G. Van de Walle, "Band lineups and deformation potentials in the model-solid theory," *Phys. Rev. B*, vol. 39, p. 1871, 1989.
- [64] F. Schubert, *Light emitting diodes*. Oxford University Press, 2003.
- [65] H. Kressel and J. Butler, *Semiconductor lasers and heterojunction LEDs*. London: Academic Press, 1977.
- [66] A. Rogalski and Z. Orman, "Band-to-band recombination in InAs1-xSbx ," *Infrared Phys.*, vol. 25, no. 3, pp. 551–560, 1985.
- [67] C. Smith, R.A. Abram, and M.G. Burt. "Auger recombination in a quantum well heterostructure." *Journal of Physics C: Solid State Physics*, vol. 16, 1983.
- [68] I. Hayashi, M. B. Panish, P. W. Foy, and S. Sumski, "Junction lasers which operate continuously at roomtemperature" *Appl. Phys. Lett.* , vol. 17, 1970.

- [69] R. N. Hall, G. E. Fenner, J. D. Kingsley, T. J. Soltys, and Carlson R. O. Carlson “Coherent light emission from GaAs junctions,” *Phys. Rev. Lett.*, vol. 9, 1962.
- [70] A. Yarive, *Theory and Applications of Quantum Mechanics*. John Wiley and Sons, New York, 1982.
- [71] H. Benisty, H. De Neve, and C. Weisbuc, “Impact of Planar Microcavity Effects on Light Extraction—Part I: Basic Concepts and Analytical Trends,” *IEEE Journal of Quantum Electronics*, vol. 34, 1998.
- [72] N. E. J. Hunt, E. F. Schubert, R. F. Kopf, D. L. Sivco, A. Y. Cho, and G. J. Zydzik, “Increased fiber communications bandwidth from a resonant cavity light emitting diode emitting at $\lambda = 940$ nm,” *Appl. Phys. Lett.*, vol. 63, 1993.
- [73] A. Yariv, *Quantum Electronics*. 3rd edition, John Wiley and Sons, New York, 1989.
- [74] M. Born and E. Wolf. *Principles of optics: electromagnetic theory of propagation, interference and diffraction of light*. Cambridge University Press, 1999.
- [75] N. E. J. Hunt, E. F. Schubert, D. L. Sivco, A. Y. Cho, R. F. Kopf, R. A. Logan, and G. J. Zydzik. “High efficiency, narrow spectrum resonant cavity light-emitting diodes” in *Confined Electrons and Photons* edited by E. Burstein and C. Weisbuch, Plenum Press, New York, 1995.
- [76] E. F. Schubert, N. E. J. Hunt, M. Micovic, R. J. Malik, D. L. Sivco, A. Y. Cho, and G. J. Zydzik, “Highly efficient light-emitting diodes with microcavities,” *Science*, vol. 26, 1994.
- [77] A. Krier and M. Fisher, “Comparison of light emission from room temperature light emitting diodes with InAs active regions grown by LPE,” *IEE Proceedings - Optoelectronics*, vol. 144, no. 5, pp. 287-294, 1997.
- [78] B. Matveev, N. Zotova, S. Karandashov, M. Remennyi, N. Il'inskaya, N. Stus', V. Shustov, G. Talalakin and J. Malinen, “InAsSbP/InAs LEDs for the 3.3-5.5 μ m spectral range,” *IEE Proceedings - Optoelectronics*, vol. 145, no. 5, pp. 254-256, 1998.
- [79] E. A. Grebenschikova, N. V. Zotova, S. S. Kizhaev, S. S. Molchanov and Y. P. Yakovlev, “InAs/InAsSbP light-emitting structures grown by gas-phase epitaxy,” *Technical Physics*, vol. 46, no. 9, pp. 1125-1127, 2001.
- [80] B. Grietens, S. Nemeth, C. Van Hoof, P. Van Daele and G. Borghs, “Growth and characterisation of mid-IR InAs_{0.9}Sb_{0.1}/InAs strained multiple quantum well light emitting diodes grown on InAs substrates,” *IEE Proceedings - Optoelectronics*, vol. 144, no. 5, pp. 295-298, 1997.
- [81] S. McCabe and B. D. MacCraith, “Novel midinfrared LED as a source for optical-fiber gas-sensing,” *Electronics Letters*, vol. 29, no. 19, pp. 1719-1721, 1993.
- [82] N. V. Zotova, S. S. Kizhaev, S. S. Molchanov, T. B. Popova and Y. P. Yakovlev, “Long-wavelength light-emitting diodes based on InAsSb/InAs heterostructures grown by vapor-phase epitaxy,” *Semiconductors*, vol. 34, no. 12, pp. 1402-1405, 2000.
- [83] G. R. Nash, M. K. Haigh, H. R. Hardaway, L. Buckle, A. D. Andreev, N. T. Gordon, S. J. Smith, M. T. Emeny and T. Ashley, “InSb/AlInSb quantum-well light-emitting diodes,” *Applied Physics Letters*, vol. 88, 2006.
- [84] I. Melngailis and R. H. Rediker, *Journal Applied Physics*, vol. 37, p. 899, 1966.
- [85] W. Dobbelaere, J. De Broek, C. Bruynseraede, R. Mertens and G. Borghs, “InAsSb light emitting diodes and their applications to infra-red gas sensors,” *Electronics Letters*, vol. 29, no. 10, 1993.

- [86] E. Delli, P. D. Hodgson, E. Repiso, A. P. Craig, J. P. Hayton, Q. Lu, A. R. J. Marshall, A. Krier, P. J. Carrington, "Heteroepitaxial Integration of Mid-Infrared InAsSb Light Emitting Diodes on Silicon," *IEE Photonic Journal*, vol. 11, 2019.
- [87] P. J. P. Tang, H. Hardaway, J. Heber, C. C. Phillips, M. J. Pullin, R. A. Stradling, W. T. Yuen and L. Hart, "Efficient 300 K light-emitting diodes at $\lambda \sim 5$ and ~ 8 μm from InAs/In($\text{As}_{1-x}\text{Sb}_x$) single quantum wells," *Applied Physics Letters*, vol. 72, no. 26, pp. 3473-3475, 1998.
- [88] J. D. Heber, D. Gevaux, X. Li and C. C. Phillips, "Room temperature InAs/InAs $_{1-x}$ Sb $_x$ single quantum well light emitting diodes with barriers for improved carrier confinement," *IEE Proceedings - Optoelectronics*, vol. 147, no. 6, pp. 407-411, 2000.
- [89] A. A. Allerman, S. R. Kurtz, R. M. Biefeld, K. C. Baucom, J. H. Burkhart, "Development of InAsSb-based light emitting diodes for chemical sensing systems," *SPIE Proceedings - The International Society for Optical Engineering*, vol. 3279, 1998.
- [90] V. V. Kuznetsov, G. W. Wicks "Molecular beam epitaxy growth of midinfrared "W" light emitting diodes on InAs," *J. Vac. Sci. Technol. B*, vol. 24, 2006.
- [91] P. J. Carrington, M. de laMare, K. J. Cheetham, Q. Zhuang, A. Krier "Midinfrared InAsSbN/InAs Multiquantum Well Light-Emitting Diodes," *Advances in OptoElectronics*, 2011.
- [92] M. Aziz, Ch. Xie, V. Pusino, A. Khalid, M. Steer, I. G. Thayne, D. R. S. Cumming "Multispectral mid-infrared light emitting diodes on a GaAs substrate," *Applied Physics Letters*, vol. 111, 2017.
- [93] S. R. Provence, R. Ricker, Y. Aytac, T. F. Boggess, J. P. Prineas, "High power cascaded mid-infrared InAs/GaSb light emitting diodes on mismatched GaAs," *Journal of Applied Physics*, vol. 118, 2015.
- [94] R. J. Ricker, S. R. Provence, D. T. Norton, T. F. Boggess, Jr., J. P. Prineas, "Broadband mid-infrared superlattice light-emitting diodes," *Journal of Applied Physics*, vol. 121, 2017.
- [95] A. J. Muhowski, R. J. Ricker, T. F. Boggess, J. P. Prineas "n-type anode layer, high-power MWIR superlattice LED," *Applied Physics Letters*, vol. 111, 243509, 2017.
- [96] "GaSb-Based Type-I Quantum Well 3–3.5- μm Cascade Light Emitting Diodes," *IEEE Photonics Technology Letters*, vol. 30, 2018.
- [97] C. S. Kim, W. W. Bewley, C. D. Merritt, C. L. Canedy, M. V. Warren, I. Vurgaftman, J. R. Meyer and M. Kim, "Improved mid-infrared interband cascade light-emitting devices," *Optical Engineering*, vol. 57, no. 1, 2018.
- [98] R. Bockstaele, J. Derluyn, C. Sys, S. Verstuyft, I. Moerman, P. Van Daele, R. Baets, "Realisation of highly efficient 850nm top emitting resonant cavity light emitting diodes," *Electronics Letters*, vol. 35, No.18, 1999.
- [99] M. Dumitrescu, L. Toikkanen, P. Sipila, V. Vilokkinen, P. Melanen, M. Saarinen, S. Orsila, P. Savolainen, M. Toivonen, M. Pessa, "Modeling and optimization of resonant cavity light-emitting diodes grown by solid source molecular beam epitaxy," *Microelectronic Engineering*, vol. 51-52, 2000.

- [100] T. Kato, Y. Mizuno, M. Hirotsu, T. Saka, H. Horinaka, "Resonant cavity light emitting diodes with two single quantum wells of different widths," *Journal of Applied Physics*, vol. 89, no.5, 2001.
- [101] J. J. Wierer, D. A. Kellogg, N. Holonyak, Jr., "Tunnel contact junction native-oxide aperture and mirror vertical-cavity surface-emitting lasers and resonant-cavity light-emitting diodes," *Applied Physics Letters*, vol. 74, no.7, 1999.
- [102] J.W. Gray, D. Childs, S. Malik, P. Sivers, C. Roberts, P.N. Stavrinou, M. Whitehead, R. Murray, G. Parry, "Quantum dot resonant cavity light emitting diode operating near 1300 nm," *Electronics Letters*, vol. 35, no.3, 1999.
- [103] B. Depreter, S. Verstuyft, I. Moerman, R. Baets, P. Van Daele, "InP-based microcavity light emitting diodes emitting at 1.3 μm and 1.55 μm ," *1 1th International Conference on Indium Phosphide and Related Materials*, Davos, Switzerland, 1999
- [104] F. Salomonsson, S. Rapp, K. Streubel, M. Hammar, J. Daleiden, "InP-based 1.55 μm Resonant Cavity Light-Emitting Diode with two Epitaxial Mirrors," *Physica Scripta*, vol. T79, 1999.
- [105] S. Orsila, J. Kongas, M. Toivonen, P. Savolainen, M. Jalonen, M. Pessa, "Solid source molecular beam epitaxy growth and characterization of resonant cavity light-emitting diodes," *Journal of Crystal Growth*, vol. 201/202, 1999.
- [106] M. V. Maximov, I. L. Krestnikov, YU. M. Shernyakov, A. E. Zhukov, N. A. Maleev, YU. G. Musikhin, V. M. Ustinov, ZH. I. Alferov, A. YU. Chernyshov, N. N. Ledentsov, D. Bimberg, T. Maka, C. M. S. Torres "InGaAs-GaAs Quantum Dots for Application in Long Wavelength (1.3 μm) Resonant Vertical Cavity Enhanced Devices," *Journal of electronic materials*, vol. 29, no. 5, 2000.
- [107] J. Muszalski, T. Ochalski, E. Kowalczyk, A. Wojcik, H. Wrzesinska, B. Mroziec, M. Bugajski, "InGaAs resonant cavity light emitting diodes (RC LEDs)," *9th Int. Symp. "Nanostructures: Physics and Technology"*, St Petersburg, Russia, June 18-22, 2001.
- [108] Y. K. Su, H. C. Yu, S. J. Changa, C. T. Lee, J. S. Wang, A. R. Kovsh, Y. T. Wu, K. F. Lin, C. Y. Huang, "1.3 μm InAs quantum dot resonant cavity light emitting diodes," *Materials Science and Engineering B*, vol. 110, 2004.
- [109] M. Ortsiefer, G.Bohm, M. Grau, K.Windhorn, E. Ronneberg, J. Roskopf, R. Shau, O. Dier, M.-C. Amann, "Electrically pumped room temperature CW VCSELs with 2.3 μm emission wavelength," *Electronics Letters*, vol. 42, no. 11, 2006.
- [110] L. Cerutti, A. Ducanhez, G. Narcy, P. Grech, G. Boissier, A. Garnache, E. Tournié, F. Genty, "GaSb-based VCSELs emitting in the mid-infrared wavelength range (2–3 μm) grown by MBE," *Journal of Crystal Growth*, vol. 311, 2009.
- [111] D. Sanchez, L. Cerutti, E. Tournié, "Single-Mode Monolithic GaSb Vertical-Cavity Surface-Emitting Laser," *Optics Express*, vol. 20, no. 14, 2012.
- [112] D. Sanchez, L. Cerutti, E. Tournié, "Mid-IR GaSb-based monolithic vertical-cavity surface-emitting lasers," *J. Phys. D: Appl. Phys.*, vol. 46, 2013.
- [113] F. Genty, L. Cerutti, A. Garnache, A. Ouvrard, A. Pérona, P. Grech, D. Romanini, F. Chevrier, "Room temperature Sb-based mid-infrared VCSELs." *phys. stat. sol. (c)*, vol. 4, no. 5, 2007.

- [114] A. Bachmann, K. Kashani-Shirazi, S. Arafin, M.-C. Amann, "GaSb-Based VCSEL With Buried Tunnel Junction for Emission Around 2.3 μm ," *IEEE Journal of Selected Topics in Quantum Electronics*, vol. 15, no. 3, 2009.
- [115] S. Arafin, A. Bachmann, M.-C. Amann, "Transverse-Mode Characteristics of GaSb-Based VCSELs With Buried-Tunnel Junctions" *IEEE Journal of Selected Topics in Quantum Electronics*, vol. 17, no. 6, 2011.
- [116] S. Sprengel, A. Andrejew, F. Federer, G. K. Veerabathran, G. Boehm, M.-C. Amann, "Continuous wave vertical cavity surface emitting lasers at 2.5 μm with InP-based type-II quantum wells," *Applied Physics Letters*, vol. 106, 151102, 2015.
- [117] S. Arafin, A. Bachmann, K. Kashani-Shirazi, M.-C. Amann, "Electrically pumped continuous-wave vertical-cavity surface-emitting lasers at $\sim 2.6 \mu\text{m}$," *Applied Physics Letters*, vol. 95, 131120, 2009.
- [118] A. Ducanhez, L. Cerutti, P. Grech, F. Genty, E. Tournié, "Mid-infrared GaSb-based EP-VCSEL emitting at 2.63 μm ," *Electronics Letters*, vol. 45, no. 5, 2009.
- [119] A. B. Ikyo, I. P. Marko, K. Hild, A. R. Adams, S. Arafin, M.-C. Amann, S. J. Sweeney, "Temperature stable mid-infrared GaInAsSb/GaSb Vertical Cavity Surface Emitting Lasers (VCSELs)," *Scientific Reports*, vol. 6, 2016.
- [120] W. W. Bewley, C. L. Canedy, C. S. Kim, C. D. Merritt, M. V. Warren, I. Vurgaftman, J. R. Meyer, M. Kim, "Room-temperature mid-infrared interband cascade vertical-cavity surface-emitting lasers," *Applied Physics Letters*, vol. 109, 151108, 2016.
- [121] I. Vurgaftman, R. Weih, M. Kamp, J. R. Meyer, C. L. Canedy, C. S. Kim, M. Kim, W. W. Bewley, C. D. Merritt, J. Abell, S. Höfling, "Interband cascade lasers," *J. Phys. D: Appl. Phys.*, vol. 48, 2015.
- [122] F. Zhao, H. Wu, A. Majumdar, Z. Shi "Continuous wave optically pumped lead-salt mid-infrared quantum-well vertical-cavity surface-emitting lasers," *Applied Physics Letters*, vol. 83, no. 25, 2003.
- [123] C. L. Felix, W. W. Bewley, I. Vurgaftman, J. R. Lindle, J. R. Meyer, "Low-threshold optically pumped $\lambda=4.4 \mu\text{m}$ vertical-cavity surface-emitting laser with a PbSe quantum-well active region," *Applied Physics Letters*, vol. 78, no. 24, 2001.
- [124] F. A. Al-Saymari, A. P. Craig, Y. J. Noori, Q. Lu, A. R. J. Marshall, A. Krier, "Electroluminescence enhancement in mid-infrared InAsSb resonant cavity light emitting diodes for CO₂ detection," *Applied Physics Letters*, vol. 114, 171103, 2019.
- [125] Furat A. Al-Saymari, Adam P. Craig, Qi Lu, Andrew R. J. Marshall, Peter J. Carrington, Anthony Krier, "Mid-infrared resonant cavity light emitting diodes operating at 4.5 μm ," *Optics express*, vol. 28, 23338, 2020.
- [126] P. J. Carrington, "Quantum nanostructures grown by molecular beam epitaxy for midinfrared applications (PhD thesis)," Lancaster University, 2009.
- [127] J. P. Hayton, "Development of mid-infrared light emitting diodes to replace incandescent airfield lighting (PhD thesis)," Lancaster University, 2016.
- [128] J. J. Dudley, D. L. Crawford, and J. E. Bowers "Temperature Dependence of the Properties of DBR Mirrors Used in Surface Normal Optoelectronic Devices", *IEEE PHOTONICS TECHNOLOGY LETTERS*, vol. 4, no. 4, 1992.
- [129] I. Vurgaftman, J. R. Meyer and L. R. Ram-Mohan, "band parameters for III-V compound semiconductors and their alloys," *Journal of Applied Physics*, vol. 89, 2001.

- [130] L. Piskorski, R. P. Sarzala “Material parameters of antimonides and amorphous materials for modelling the mid-infrared lasers,” *Optica Applicata* vol. XLVI, no. 2, 2016.
- [131] S. K. Tripathy “Refractive Indices of Semiconductors from Energy gaps,” *Optical Materials* vol. 46, 2015.
- [132] G. D. Gillen, Ch. DiRocco, P. Powers, and Sh. Guha “Temperature-dependent refractive index measurements of wafer-shaped InAs and InSb,” *Applied Optics*, vol. 47, no. 2, 2008.
- [133] P. J. L. Herve and L. K. J. Vandamme “Empirical temperature dependence of the refractive index of semiconductors,” *J. Appl. Phys.* vol. 77, 1995.
- [134] J. L. Shen, C. Y. Chang, W. C. Chou, M. C. Wu, Y. F. Chen “Temperature dependence of the reflectivity in absorbing Bragg reflectors,” *Optics Express* vol. 9, no. 6, 2001.
- [135] R. H. Birkner, J. Kaiser, W. Elsässer, and C. Jung “Resonant-cavity light-emitting diodes: quantum noise and spatial emission characteristics,” *Appl. Phys. B*, vol. 79, pp. 963–967, 2004.
- [136] N. V. Zotova, N. D. Il’inskaya, S. A. Karandashev, B. A. Matveev, M. A. Remennyi, and M. N. Stus “Flip-chip LEDs with deep mesa emitting at 4.2 μm ,” *Semiconductors*, vol. 40, p. 697, 2006.
- [137] http://www.roithner-laser.com/datasheets/led_midir/led46-pr.pdf
- [138] H. R. Hardaway, T. Ashley, L. Buckle, M. T. Emeny, G. Masterton, G. Pryce “Optimizing indium aluminum antimonide LEDs and photodiodes for gas sensing applications,” *SPIE Proceedings: Infrared Detector Materials and Devices*, 5564, 2004.
- [139] S. Elies, A. Krier, I. R. Cleverley, and K. Singer “Photoluminescence of MBE growth InAs_{1-x}Sb_x lattice matched to GaSb,” *J. Phys. D, Appl. Phys.*, vol. 26, pp. 159-162, 1993.
- [140] J. A. Keen, D. Lane, M. Kesaria, A. R. J. Marshall, and A. Krier “InAs/InAsSb type-II strained-layer superlattices for mid-infrared LEDs,” *J. Phys. D, Appl. Phys.*, vol. 51, 075103, 2018.
- [141] V. Letka, A. Bainbridge, A. P. Craig, F. Al-Saymari, A. R. J. Marshall, “Resonant cavity-enhanced photodetector incorporating a type-II superlattice to extend MWIR sensitivity,” *Optics Express*, vol. 27, 2019.